SYNTHESIS AND CHARACTERIZATION OF SILVER NANOPARTICLES FOR LIGHT TRAPPING APPLICATION IN THIN FILM SOLAR CELLS

A thesis submitted

by

MANVENDRA SINGH GANGWAR

Roll No: 166121104

In partial fulfillment of the requirement for the award of the degree of

DOCTOR OF PHILOSOPHY

DEPARTMENT OF PHYSICS

INDIAN INSTITUTE OF TECHNOLOGY GUWAHATI

GUWAHATI - 781039, ASSAM, INDIA

OCTOBER 2023

DECLARATION

The work contained in this thesis entitled "**Synthesis and characterization of silver nanoparticles for light trapping application in thin film solar cells"** has been carried out by me under the supervision of Dr. Pratima Agarwal, Professor, Department of Physics, Indian Institute of Technology, Guwahati, Assam, India. This thesis does not contain any materials previously submitted for the award of any degree or diploma.

Date: 25th October, 2023

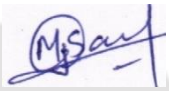

Manvendra Singh Gangwar
Roll No: 166121104
Department of Physics
Indian Institute of Technology Guwahati
Guwahati-781039, Assam, India

भारतीय प्रौद्योगिकी संस्थान गुवाहाटी
Indian Institute of Technology Guwahati
North Guwahati, Guwahati
PIN- 781 039, Assam State, INDIA
Phone: +91 361 2583000 Extn 2702, 2582702
Fax: +91 361 2690 762 (Institute), 2582749 (Department)

Dr. Pratima Agarwal
Professor
Department of Physics
E-mail:pratima@iitg.ernet.in

Dated: Oct 25, 2023

Certificate

This is certified that the work contained in this thesis entitled "**Synthesis and characterization of silver nanoparticles for light trapping application in thin film solar cells"** submitted by Mr. Manvendra Singh Gangwar, a Ph.D. student at Department of Physics, Indian Institute of Technology, Guwahati, Assam, India, for the award of the degree of Doctor of Philosophy has been carried out under my supervision. This work has not been submitted elsewhere for the award of any degree or diploma.

Pratima Agarwal

(Dr. Pratima Agarwal)

Dedicated

to

My Parents

(Late. Smt. Radha Devi and Shri. Mohan Swaroop Gangwar)

ACKNOWLEDGEMENTS

First and foremost, I would like to express my most sincere and heartfelt gratitude to my thesis supervisor, Prof. Pratima Agarwal, for her constant guidance, support, encouragement, and motivation throughout my Ph.D. research work. She gave me the freedom to pursue my interests while simultaneously keeping me on the research track. I am deeply thankful to her for giving the opportunity to learn various experimental techniques, and gain a comprehensive understanding of different topics. I would like to extend my gratitude to her for sharing her knowledge and valuable suggestions on numerous matters. She also helped me financially. I am profoundly thankful for the opportunity to conduct my doctoral study under her expert supervision. It is indeed a rare privilege to work under her guidance.

I extend my gratitude to my doctoral committee members: Prof. Alika Khare (Chairperson), Dr. Uday Narayan Maiti, and Prof. Harshal B. Nemade for their consistent review of my research work and their constructive suggestions and fruitful discussions at various stages of my research. Their valuable suggestions enriched my research and thesis. I would also like to express my sincere thanks to the former and present Heads of the Department of Physics, Prof. Poulose Poulose, Prof. Subradip Gosh, and Prof. Perumal Alagarsamy, for their encouragement and for granting me access to departmental facilities throughout my research. I am thankful to Prof. Saurabh Basu, Prof. Bosanta Ranjan Boruah, Dr. Udit Raha, Dr. Pankaj Kumar Mishra for their teaching during coursework, as well as all other faculty members of the Physics department. I appreciate Dr. Sidanada Sarma, scientific officer in the Department of Physics, for his assistance throughout my research. My thanks also go out to all the staff and technical officers of CIF, IIT Guwahati, for their help in utilizing CIF facilities.

I am grateful to the University Grants Commission (UGC), India, for providing financial support in the form of a scholarship under the NET-JRF scheme.

I acknowledge the contributions of my seniors and former lab mates, including Dr. Himanshu S. Jha, Dr. Asha Yadav, Dr. Ramakrishna Madaka, Dr. Venkanna Kanneboina, Dr. Pilik Basumatary, Mr. Vivek Ghritlahre, Ms. Shubhangi Bhardwaj, Ms. Niharika Gogoi, Mr. Ankit Kumar Singh, Mr. Gaurav Singh, Mr. Rohan Ghosh, Mr. Dharmendra Samota, and current lab members Ms. Juhi Kumari, Mr. Himangshu Deka, Ms. Jaishree Bharadwaj, Mr. Anterdipan Singh, Mr. Rahul, Mr. Tulsiram Madkami, Mr. Ashish Kumar Patel, and Ms. Keerthana B. K

for creating a friendly atmosphere and providing assistance throughout my research. I am also thankful to all the research scholars of the Department of Physics for their help and the wonderful moments we have shared.

My thanks extend to all my friends for their constant support and encouragement throughout my Ph.D.

I reserve a special place in my heart for my family and wish to thank my parents, Mr. Mohan Swaroop Gangwar and late Mrs. Radha Devi, for their unconditional support and blessings. I would like to express my gratitude to my brother, Mr. Satendra Kumar Gangwar, and my sisters, Mrs. Mamta Gangwar and Mrs. Reeta Gangwar, for everything they have done for me. This acknowledgment would remain incomplete without mentioning the support from my in-laws. I wish to thank my Father-in-law, Mr. Dharampal Gangwar, my mother-in-law, Mrs. Reshma Gangwar, and my brother-in-laws, Dr. Anukool Gangwar and Dr. Surendra Gangwar, for their constant support and motivation during my Ph.D.

Last but not least, I want to express my deep appreciation to my wife, Sonali Gangwar, for supporting me throughout my struggles and motivating me during my doctoral work.

Finally, I thank God for all His blessings.

Manvendra Singh Gangwar
IIT Guwahati, India

ABSTRACT

In the present thesis, silver nanoparticles have been synthesized by solid-state dewetting of the precursor silver films deposited at different deposition conditions (deposition time, rf power, substrate temperature) using rf sputtering technique. Surface morphology and growth dynamics of silver nanoparticles are studied using atomic force microscopy (AFM) with advanced statistical analysis. Height-height correlation function (HHCF) and power spectral density function (PSDF) are extracted from AFM data, and scaling exponents α_{local}, β, $1/z$ and α are determined using analysis. A direct correlation between morphology and the localized surface plasmon resonance (LSPR) properties of the silver nanoparticles studied using the absorbance spectroscopy is observed. The microstructure influence on dielectric function and plasmonic properties of silver nanoparticles (Ag NPs) is studied using spectroscopic ellipsometry (SE). Dielectric function and plasmonic properties of Ag NPs are investigated from spectroscopic ellipsometry (SE) data using a quite unique model in terms of the combination of different oscillators: Drude-Lorentz model along with two Gauss oscillators to account for intraband, interband transitions and different modes of localized surface plasmon resonance (LSPR) of Ag NPs. The influence of the substrate temperature on the growth of Ag NPs and their several properties like localized surface Plasmon resonance (LSPR), photoluminescence, and Raman spectroscopy is studied. Enhancement in PL peak intensity and Raman peak intensity is found to be in accordance with the LSPR of Ag NPs. Both simulation and experimental studies on single junction hydrogenated amorphous silicon (a-Si:H) thin film solar cells is done prior to the implementation of Ag NPs as a plasmonic back reflector in (a-Si:H) thin film solar cells. The effect of emitter layer (a-Si:H (p)) doping and absorber (a-Si:H (i)) layer thickness is studied. Further, simulation results are compared with the experimental results. A good match between simulation and experiment results is obtained. As an application part of this thesis, the role of silver nanoparticles as plasmonic back reflector for light trapping application in hydrogenated amorphous silicon (a-Si:H) thin film solar cells is explored. Excellent light trapping by plasmonic back reflector in solar cells is observed. A broadband enhancement in quantum efficiency is shown by a-Si:H thin film solar cells fabricated on the plasmonic back reflector with a gain of 47% in short circuit current density (J_{sc}) as compared to the flat back reflector. As a result, the improvement in the performance of the a-Si:H thin film solar with plasmonic back reflector is observed corresponding to an efficiency (η) of 8.4% against 5.6% efficiency of the a-Si:H thin-film solar cell with flat back reflector respectively.

LIST OF ABBREVIATIONS AND SYMBOLS

MNPs	Metal nanoparticles	**TEM**	Transmission electron microscopy
Ag	Silver		
Cu	Copper	**HRTEM**	High resolution transmission electron microscopy
Au	Gold		
NPs	Nanoparticles		
Ag NPs	Silver nanoparticles	**SAED**	Selective area electron diffraction
SSD	Solid state dewetting		
SPR	Surface plasmon resonance	**XRD**	X-Ray diffraction
LSPR	Localized surface plasmon resonance	**FWHM**	Full width at half maxima
		UV	Ultraviolet
PL	Photoluminescence	**UV-Vis-NIR**	Ultraviolet visible near infrared
SERS	Surface enhanced Raman spectroscopy		
		NIR	Near infrared
SE	Spectroscopic ellipsometry	**URA**	Universal reflectance accessory
SEA	Spectroscopy ellipsometry analyzer		
		DRS	Diffuse reflectance spectroscopy
RMSE	Root mean square error		
FCA	Free carrier absorption	**Si**	Silicon
CCD	Charge coupled device	**a-Si**	Amorphous silicon
BEMA	Bruggeman effective medium approximation	**a-Si:H**	Hydrogenated amorphous silicon
FESEM	Field emission scanning electron microscopy	**nc-Si:H**	Hydrogenated nano crystalline silicon
AFM	Atomic force microscopy	**CIGS**	Copper Indium Gallium Selenide
HHCF	Height-height correlation function	**CdTe**	Cadmium Telluride
		TF	Thin film
PSDF	Power spectral density function	**PV**	Photovoltaic
		RF	Radio frequency
RMS	Root mean square	**PVD**	Physical vapor deposition
FFT	Fast Fourier transform		

CVD	Chemical vapor deposition
RFPECVD	Radio frequency plasma enhanced chemical vapor deposition
RP	Rotary pump
TMP	Turbo molecular pump
AFORS-HET	Automated For simulation of hetrostructure
TCO	Transparent conducting oxide
ITO	Indium tin oxide
AZO	Aluminum doped zinc oxide
BR	Back reflector
PBR	Plasmonic back reflector
EQE	External quantum efficiency
SR	Spectral response
DI	Deionized water
Fig.	Figure
SCCM	Standard cubic centimeter per minute
RT	Room temperature
℃	Degree celcius
T_S	Substrate temperature
mbar	Milibar
nm	Nanometer
cm	Centimeter
Å	Angstrom
α	Global roughness exponent
α_{local}	Local roughness exponent
β	Growth exponent
$1/z$	Dynamic exponent
ξ	Lateral correlation length
w	Interface width
m	Local slop
β^*	Anomalous exponent
k	Spatial frequency
k_m	Characteristic peak
λ_m	Characteristic wavelength
$R_{diffuse}$	Diffuse reflectance
$R_{specular}$	Specular reflectance
R_T	Total reflectance
D	Average crystallite size
β_{hkl}	Full width at half maxima (FWHM) (in radian)
$< \varepsilon(E) >$	Pseudo dielectric function
$< \varepsilon_1(E) >$	Real part of pseudo dielectric function
$< \varepsilon_2(E) >$	Imaginary part of pseudo dielectric function
$\varepsilon_{eff}(E)$	Effective dielectric function
$\varepsilon_i(E)$	Dielectric function of i^{th} phase
ε_∞	Residual polarization
f_i	Volume fraction of i^{th} phase
ψ	Amplitude ratio
Δ	Phase difference
n	Refractive index
k	Extinction coefficient
ρ	Polarization ratio
r_p **and** r_s	Complex Fresnel reflection coefficients of *p*- and *s*-polarized light
θ_0	Angle of incidence.
E	Photon energy
E_0	Oscillator position

f	Strength of oscillator	FF	Fill factor
A	Amplitude of oscillator	η	Efficiency
σ	FWHM of the oscillator	P_{in}	Input power density
ω_p	Plasma frequency	b_s	Incident spectral photon flux density
E_p	Plasma energy		
J	Current density	q	Electron charge
V	Voltage	λ	Wavelength
J_{sc}	Short circuit current density	h	Planks constant
V_{oc}	Open circuit voltage	c	Speed of light

TABLE OF CONTENTS

		Page
Declaration		**i**
Certificate		**ii**
Dedication		**iii**
Acknowledgements		**iv**
Abstract		**vi**
List of abbreviations and symbols		**vii**
Table of content		**x**
List of figures		**xiv**
List of tables		**xix**
Chapter 1: Introduction		**1-26**
1.1	Introduction	1
1.2	Optical properties of metal nanoparticles	2
1.3	Dielectric properties of metal nanoparticles	4
1.4	Photoluminescence properties of metal nanoparticles	5
1.5	SERS properties of metal nanoparticles	6
1.6	Light trapping properties of metal nanoparticles	7
1.6.1	a-Si:H thin film solar cells	7
1.6.2	Light trapping in a-Si:H thin film solar cells	9
1.7	Synthesis methods of silver nanoparticles	11
1.8	Motivation, objective and content of thesis	12
1.9	References	16
Chapter 2: Experimental details		**27-49**
2.1	Introduction	27
2.2	Synthesis of silver nanoparticles by solid state dewetting	27
2.1.1	Substrate cleaning	29
2.1.2	RF sputtering	30
2.3	Fabrication of solar cells	31
2.3.1	Radio frequency plasma enhanced chemical vapour deposition technique	31

2.4 Characterization techniques…… 34
2.4.1 Silver nanoparticle characterization…….. 34
2.4.1.1 Surface profilometer ……..... 34
2.4.1.2 Field emission scanning electron microscopy (FESEM)….. 34
2.4.1.3 Atomic force microscopy (AFM)…….. 34
2.4.1.4 Transmission electron microscopy (TEM)…… 35
2.4.1.5 X-Ray Diffraction (XRD)…….. 35
2.4.1.6 UV-Vis-NIR spectroscopy……. 35
2.4.1.7 Raman Scattering spectroscopy……..... 36
2.4.1.8 Photoluminescence (PL) spectroscopy…….. 36
2.4.1.9 Spectroscopic Ellipsometry (SE)……... 36
2.4.2 Solar cell characterization……. 39
2.4.2.1 Current density – Voltage (*J-V*) measurement…….. 39
2.4.2.2 External quantum efficiency (EQE) measurement…… 40
2.5 Simulation details of hydrogenated amorphous silicon (a-Si:H) thin film solar cells using AFORS-HET software…….. 42
2.6 References……. 43

Chapter 3: Growth of silver thin films and nanoparticles and its correlation with the plasmonic properties…… 50-75

3.1 Introduction ……..... 50
3.2 Theoretical details for AFM analysis …… 52
3.3 Experimental details……..... 53
3.4 Results and discussion…… 54
3.4.1 Field emission scanning electron microscopy (FESEM) analysis…… 54
3.4.2 X-ray diffraction (XRD) analysis…….. 56
3.4.3 Atomic force microscopy (AFM) analysis…… 57
3.4.4 UV-Vis-NIR analysis…… 66
3.5 Conclusions…… 68
3.6 References…….. 69

Chapter 4: Influence of the microstructure on the dielectric and plasmonic properties of silver nanoparticles …….. 76-95

4.1 Introduction ……..... 76
4.2 Experimental details …….. 78

4.3 Ellipsometry modeling……... 78
4.3.1 Choice of suitable model for SE data fitting……. 78
4.3.2 Formation of layer structure for SE data fitting……..... 80
4.4 Results and discussion…… 81
4.4.1 Field emission scanning electron microscopy (FESEM) analysis…… 81
4.4.2 X-ray diffraction (XRD) analysis……. 83
4.4.3 Atomic force microscopy (AFM) analysis…….. 83
4.4.4 Spectroscopic ellipsometry (SE) analysis …… 85
4.4.5 UV-Vis-NIR analysis……... 89
4.5 Conclusions…… 90
4.6 References……..... 90

Chapter 5: Plasmon enhanced photoluminescence and Raman spectroscopy of silver nanoparticles…….. 96-114

5.1 Introduction ……... 96
5.2 Experimental details……... 97
5.3 Results and discussion……..…….. 98
5.3.1 Field emission scanning electron microscopy (FESEM) analysis…… 98
5.3.2 Transmission electron microscopy (TEM) analysis……. 100
5.3.3 X-ray diffraction analysis……. 102
5.3.4 UV-Vis-NIR analysis…… 103
5.3.5 Photoluminescence (PL) spectroscopy analysis...…… 104
5.3.6 Raman spectroscopy analysis……..... 106
5.4 Conclusions…… 108
5.5 References…….. 108

Chapter 6: Simulation and fabrication of a-Si:H thin film solar cells..... 115-130

6.1 Introduction……..... 115
6.2 Simulation details……..……...…….. 116
6.3 Experimental details……... 118
6.4 Results and discussion…… 119
6.4.1 Influence of emitter layer doping……..... 119
6.4.2 Influence of *i*- layer thickness……... 123
6.5 Conclusions…… 125

6.6 References……... 126

Chapter 7: Implementaion of silver nanoparticle as plasmonic back reflector to improve the performance of a-Si:H thin film solar cells..... 131-147

7.1 Introduction……... 131

7.2 Experimental details……... 132

7.3 Results and discussion…… 135

7.3.1 Field emission scanning electron microscopy (FESEM) analysis…… 135

7.3.2 Atomic force microscopy (AFM) analysis……..... 136

7.3.3 UV-Vis-NIR analysis…… 137

7.3.4 Current density – Voltage (*J-V*) and External quantum efficiency (EQE) measurement on a-Si:H thin film solar cells…….. 140

7.4 Conclusions…… 141

7.5 References…….. 142

Chapter 8: Summary, conclusion and future scope……..... 148-151

8.1 Thesis summary……..... 148

8.2 Thesis conclusion……... 151

8.3 Scope of future works……..... 151

Appendix ……..... 152-155

List of publications ……..... 156

LIST OF FIGURES

Figure No.	Description	Page No.
1.1	Schematic of the applications of metal nanoparticles……..	2
1.2	Schematic of localized surface plasmon resonance of metal nanoparticles…..	3
1.3	Schematic diagram of superstrate-type (*p-i-n*) and substrate-type (*n-i-p*) hydrogenated amorphous silicon thin film solar cells…….	8
1.4	Schematic diagram of thin-film silicon solar cells with and without light trapping…….....	9
1.5	Schematic of different plasmonic light-trapping geometries for thin-film solar cells…….	10
1.6	Schematic of different synthesis methods of silver nanoparticles……	12
2.1	Schematic of solid-state dewetting, thin films dewet to form isolated islands..	28
2.2	Schematic of island shape on the rigid substrate…….	28
2.3	Schematic and photograph of RF sputtering system……	31
2.4	Photograph of multi-chamber PECVD system……	33
2.5	Schematic of the ellipsometry spectroscopy measurement technique…….	37
2.6	Photograph of spectroscopic ellipsometry system……...	37
2.7	Current density- Voltage (*J-V*) curve of a-Si:H thin film solar cell…….	39
2.8	Schematic of external quantum efficiency setup…….	41
2.9	Screenshot of AFORS-HET input window to define the structure and perform the measurement…….	42
3.1	SEM images of Ag NPs on corning glass formed by annealing at 400 ℃ for 1 h of Ag precursor films of different thickness on 200 nm scale. (a) 12 nm, (b) 21 nm, (c) 34 nm and (d) 50 nm……..	55
3.2	The histogram of NPs' size on corning glass substrate formed by annealing at 400 ℃ for 1 h of Ag precursor films having different thickness……..	55
3.3	XRD spectra of Ag NPs formed by post annealing of precursor film of different thickness; 12-50 nm……...	56
3.4	AFM images with 5 $\mu m \times 5\ \mu m$ area of as deposited films having different thickness, (a) for 12 nm, (b) for 21 nm, (c) for 34 nm and (d) for 50 nm…….	57

3.5 AFM images with $5\ \mu m \times 5\ \mu m$ area of annealed films (Ag NPs) (a)-(d) and their particle size distribution (a_1)-(d_1) having different thickness, (a)&(a_1) for 12 nm, (b)&(b_1) for 21 nm, (c)&(c_1) for 34 nm and (d)&(d_1) for 50 nm……... 58

3.6 Log-log plot of Height-Height correlation function (HHCF) as function of distance (r) of as-deposited and annealed films of different thickness: 12-50 nm…… 59

3.7 (a)Variation in local roughness exponent α_{local} (b) interface width w, and (c) correlation length ξ with the precursor Ag film thickness, (d) interface width w vs correlation length ξ…… 60

3.8 Variation of local slope m with the thickness (growth time) for as-deposited and annealed films, fitting of this curve give the anomalous exponent β^*…… 62

3.9 (a) Log-log plot of power spectrum density function $P(k)$ as function of k (reciprocal space) of as-deposited and annealed films of different thickness: 12-50 nm, (b) variation in cutoff frequency k_{cutoff} and correlation length ξ of as deposited and annealed films with the precursor Ag precursor film thickness……..... 63

3.10 Power spectrum density function $P(k)$ as function of k (reciprocal space) and corresponding 2D FFT images (inset) of as deposited and annealed films of different thickness (a) 12 nm, (b) 21 nm, (c) 34 nm and (d) 50 nm…….. 64

3.11 (a) Log-log plot of characteristic wavelength as a function of thickness (growth time), (b) variation in peak position (k_m) and FWHM of the corresponding peak of the mound surface (Ag NPs)…… 65

3.12 (a) Absorption spectra of Ag NPs and as deposited films (inset), (b) variation in LSPR peak position with thickness, (c), (d) variation in LSPR peak and bandwidth with correlation length and interface width…… 67

4.1 Optical model for the spectroscopic ellipsometry data fitting……. 80

4.2 SEM images of Ag NPs on corning glass at different RF power on 200 nm scale. (a) for 40 Watt, (b) for 50 Watt, (c) for 60 Watt (d) for 70 Watt, and (e) for 80 Watt…….. 82

4.3 Histogram images of Ag NPs at different RF power. (a) for 40 Watt, (b) for 50 Watt, (c) for 60 Watt (d) average particle size, surface coverage by the particles and RMS roughness (from AFM) for 40, 50 and 60 Watt……... 82

4.4	XRD spectra of Ag NPs on corning glass at different RF power: 40-80 Watt...	83
4.5	AFM images of Ag NPs on $5\mu m \times 5\mu m$ square region for different RF power. (a) For 40 Watt, (b) for 50 Watt, (c) for 60 Watt, (d) for 70 Watt, (e) for 80 Watt, (f) RMS roughness, surface roughness and void fraction plot for RF power variation……...	84
4.6	$\tan\psi$ (a), and $\cos\Delta$ (b) spectra of Ag NPs at different RF power: 40-80 Watt…….	85
4.7	The measured and fitted real ($< \varepsilon_1 >$) (a), and the imaginary ($< \varepsilon_2 >$) part (b) of the pseudo dielectric function spectra of Ag NPs on corning glass deposited at different RF power: 40-80 Watt……..	86
4.8	Refractive index (a), and extinction coefficient spectra (b) of Ag NPs for different RF power: 40-80 Watt……...	88
4.9	Absorbance spectra of Ag NPs at different RF power: 40-80 Watt (a), and LSPR peak position and peak width from UV and SE (b)…….	89
5.1	FESEM images of Ag NPs on corning glass substrate at different substrate temperatures on 200 nm scale. (a) for RT, (b) for 100, (c) for 200, (d) 300, and (e) for 400 ℃……..	99
5.2	(a-e) Histogram images of Ag NPs on corning glass substrate at different substrate temperatures, (f) variation in particle size and surface coverage (from FESEM images) with substrate temperature…….	99
5.3	TEM images of Ag NPs on carbon-coated copper TEM grid deposited at different substrate temperatures on a 200 nm scale. (a) for RT, (b) for 100, (c) for 200, (d) 300, and (e) for 400 ℃, (f) particle size from TEM v/s substrate temperature……...	100
5.4	HRTEM images of Ag NPs on carbon-coated copper TEM grid at different substrate temperatures on a 5 nm scale. (a) for RT, (b) for 100, (c) for 200, (d) 300, and (e) for 400 ℃, (f) SAED pattern of Ag NPs for 200 ℃ substrate temperature……..	101
5.5	XRD spectra of Ag NPs with substrate temperature variation……..	102
5.6	(a) Absorbance spectra of Ag NPs at different substrate temperatures, (b) Variation in LSPR peak and particle size from FESEM with substrate temperature……..	103

5.7 (a) PL spectra of Ag NPs with substrate temperature variation, (b) variation in peak intensity and particle size from FESEM with substrate temperature… 104
5.8 (a-e) De-convoluted PL spectra of Ag NPs with substrate temperature variation, (f) variation in peaks intensity ratio with substrate temperature….. 105
5.9 Raman spectra of Ag NPs with substrate temperature variation……... 106
5.10 (a) De-convoluted Raman spectra of Ag NPs, (b) variation in peak 1 height and particles size from FESEM with the substrate temperature…….. 107
6.1 Solar cell structure to be simulated……... 117
6.2 Density of the states of a-Si:H n-i-p layers (a) n-layer (b) i-layer (c) p-layer 117
6.3 Solar cell structure to be experimentally fabricated……. 118
6.4 The simulated *J-V* characteristic and spectral response of solar cell with variation in emitter layer doping and 200 nm absorber layer thickness **(**a) *J-V* curve and (b) External quantum efficiency…….. 119
6.5 The measured *J-V* characteristic and spectral response of fabricated solar cell with variation in B_2H_6 flow rate in emitter layer and 200 nm absorber layer thickness **(**a) *J-V* curve and (b) External quantum efficiency……. 120
6.6 The variation of short circuit current density (J_{sc}), open circuit voltage (V_{oc}), fill factor (*FF*), and power conversion efficiency (*PCE*) as a function of emitter layer doping **(**a) simulated results (b) experimental results……... 120
6.7 Measured and simulated *J-V* characteristic and spectral response of single-junction n-i-p solar cell with 10 sccm B_2H_6 flow rate and 7.6×10^{19} cm^{-3} doping concentration in emitter layer **(**a) *J-V* curve and (b) External quantum efficiency curve……... 122
6.8 The simulated *J-V* characteristic and spectral response of simulated solar cell with variation in absorber layer thickness and 7.6×10^{19} cm^{-3} p layer doping concentration **(**a) *J-V* curve and (b) External quantum efficiency……. 123
6.9 The measured *J-V* characteristic and spectral response of fabricated solar cell with variation in absorber layer thickness and 10 sccm B_2H_6 flow rate in p layer **(**a) J-V curve and (b) External quantum efficiency……. 123

6.10 The variation of short circuit current density (J_{sc}), open circuit voltage (V_{oc}), fill factor (*FF*), and power conversion efficiency (*PCE*) as a function of absorber layer thickness **(**a) simulated results (b) experimental results……... 124

7.1 (a) Ag NPs on corning glass substrate, (b) Ag NPs on corning glass/AZO substrate, (c) plasmonic back reflector, and (d) flat back reflector……... 133

7.2 Solar cell structure with (a) flat BR and (b) plasmonic BR……. 134

7.3 (a) Photograph and (b) cross section SEM image of the fabricated solar cell with plasmonic BR……... 134

7.4 FESEM images of Ag NPs on corning glass (a) and corning glass /AZO (b) formed by annealing at 400 ℃ for 1 h of Ag precursor films of thickness 21 nm on 200 nm scale…….. 136

7.5 Histogram images of Ag NPs on corning glass (a) and corning glass/AZO (b) formed by annealing at 400 ℃ for 1 h of Ag precursor films of thickness 21 nm……... 136

7.6 3D AFM images of Ag NPs on corning glass (a) and corning glass/AZO (b) substrate with $5\ \mu m \times 5\ \mu m$ area formed by annealing at 400 ℃ for 1 h of Ag precursor films of thickness 21 nm……. 137

7.7 Absorbance spectra of Ag NPs on corning glass substrate and corning glass/AZO…… 138

7.8 (a) Specular reflectance, (b) diffuse reflectance spectra, (c) total reflectance, and (d) haze in reflection of flat plasmonic BRs and Ag NPs on corning glass substrate……... 139

7.9 (a) J-V curve and (b) External quantum efficiency curve of a-Si:H solar cells with flat BR and plasmonic BR……... 140

LIST OF TABLES

Table No.	Description	Page No.
3.1	Experimental parameters and thickness of silver precursor films measured by stylus profilometer…….	54
3.2	Roughness exponent (α_{local}), interface width (w), lateral correlation length (ξ) calculated using the HHCF from AFM images of as deposited films (Ag precursor films) and annealed films (Ag NPs)…….	61
4.1	The thickness of Ag precursor films (as deposited films) measured by stylus profilometer, average particle size, and surface coverage (post annealing) from FESEM images calculated by *ImageJ* software…….	81
4.2	The values of crystallite size calculated from XRD, roughness calculated from AFM and SE measurement, void fraction from SE measurement……..	84
4.3	The values of plasma energy, and central energy of Lorentz and Gauss oscillator, obtained from SE fitting……..	87
4.4	The average particle size from FESEM, LSPR peak position and peak width calculated from UV-Vis-NIR and SE measurement……	89
6.1	Input parameters used for simulation……...	117
6.2	Deposition parameters for each layer of a-Si:H thin film solar cells……	119
6.3	Calculated values of J_{sc}, V_{oc}, FF, and power conversion efficiency of fabricated and simulated single junction n-i-p solar cells with 10 sccm B_2H_6 flow rate and 7.6×10^{19} cm^{-3} doping concentration in emitter layer…….....	122
7.1	Deposition parameters for each layer of a-Si:H thin film solar cells……	134
7.2	Calculated values of J_{sc}, V_{oc}, FF, and power conversion efficiency with flat BR and plasmonic BR……..	141

Chapter 1

Introduction

1.1. Introduction

Metal nanoparticles (MNPs) are extensively used nanomaterials due to their broad range of applications in plasmonics, photonics, electronics, energy, biomedical fields and information technologies [1–5]. When these metal NPs interact with incoming light, they initiate a collective movement of free electrons, termed plasmons, which lead to the rise of surface plasmon resonance. The surface plasmon resonance from these free electrons of metal NPs results in strong absorption, scattering, and near-field enhancement at the resonance frequency of metal NPs [6]. The noble metal NPs have been extensively studied due to their localized surface plasmon resonance (LSPR) in the both visible and near-infrared (NIR) regions, which find the applications in the advance fields such as biomedicine, energy applications, and information technologies, photovoltaics, photo catalysis, and data storage [3,7–11]. To tune the LSPR properties for specific applications, the physical characteristics of noble metal NPs such as size, morphology, and composition must be precisely designed while considering the surrounding medium's permittivity [12–14]. A comprehensive knowledge of the underlying physics dictating LSPR effects holds a pivotal role in fabricating and employing plasmonic NPs for a range of applications, including biological sensors, solar cells, and surface-enhanced Raman spectroscopy (SERS) [8,9,15–18].

Noble metal nanoparticles (NPs), such as gold (Au), copper (Cu), and silver (Ag), stand out from other nanomaterials due to their tunable localized surface plasmon resonance (LSPR) properties [4]. Their optical characteristics, characterized by notable absorption, scattering, and field enhancement capacities, bring up a wide range of applications focused on improved optical and chemical signal responses for imaging and sensing [6]. Furthermore, because of the good correlation between plasmonic structures and optical characteristics of noble metal NPs, their consistently repeatable production processes and modifiable optical features are unique [18]. Noble metals' unique and important optical characteristics can be examined using exact plasmonic theories, which aid in the synthesis of application-oriented plasmonic nanomaterials. Fig. 1.1 illustrates the different optical properties and applications of metal NPs which are

related with factors like, shape, size, composition, permittivity of nanoparticles, and the surrounding medium as well [12–14]. These applications are based on their capacity for light absorption, scattering, and field enhancement [4]. The utilization of plasmonic properties to advance energy technologies (e.g., photovoltaics) by capitalizing on their substantial scattering cross section and surface field enhancement represents a notable potential of plasmonic NPs [15,17,19,20].

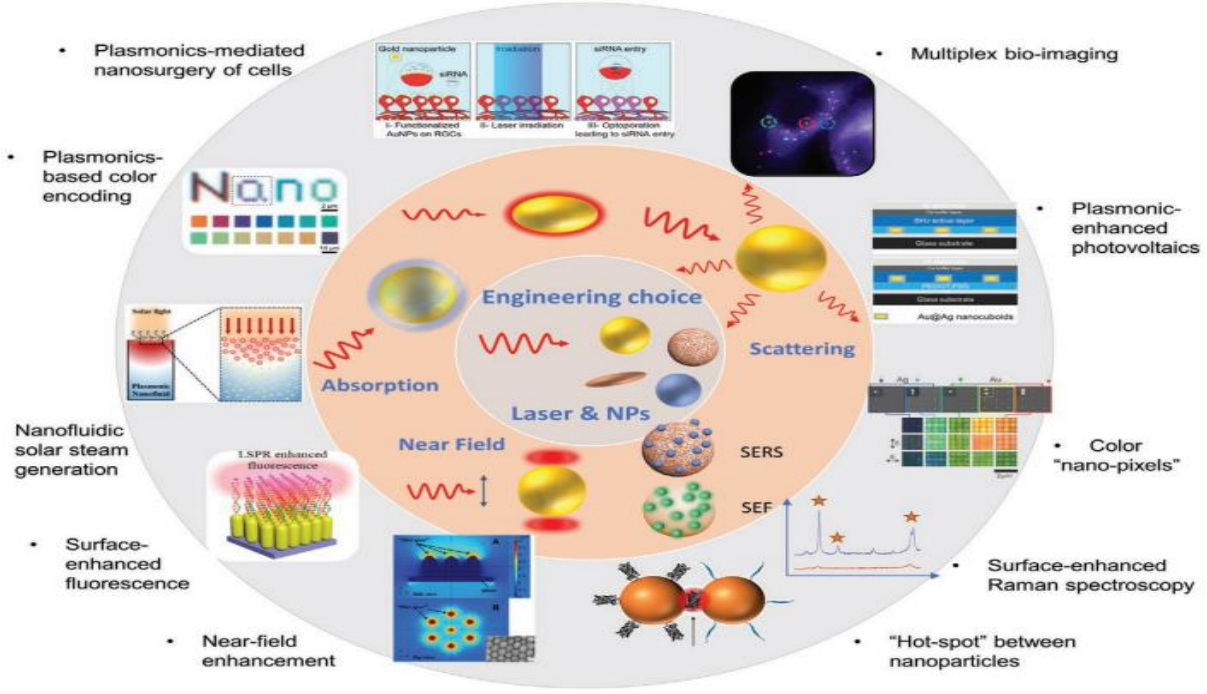

Fig.1.1. Schematic of the applications of metal nanoparticles, adapted from [4].

The noble metal NPs, Au, Cu, and Ag are mostly used in the plasmonic applications. Au due to its chemical inertness and biocompatibility has been in high demand in many applications [2]. Application of Cu NPs in plasmonics is comparatively limited due to its reactive nature. But the low cost of copper has been motivating factor for researcher to explore its potential in plasmonic applications. Ag is the another very important noble metal, and due to the strongest LSPR compared to other noble metal (Au and Cu) nanoparticles, Ag NPs have generated more interest in silicon-based thin film solar cells, glucose biosensors, and photodetectors [6,8,15,21].

1.2. Optical absorption properties of metal nanoparticles: Localised surface plasmon resonance (LSPR)

Nanoparticles (NPs) differ greatly from bulk materials in terms of their optical properties. Continuous electron bands become discrete as the size of the bulk material decreases to the

nanoscale. As a result, the optical properties of metal nanoparticles (MNPs) such as localized surface plasmon resonance (LSPR) is greatly influenced by the size, shape, and aggregation level of the nanoparticles. An optical phenomenon known as localized surface plasmon resonance (LSPR) occurs when light waves are contained within conductive nanoparticles (NPs) that have the smaller size than the wavelengths of incident light. Surface electrons inside the conduction band of nanoparticles interact with incoming light to produce this phenomenon [4,6]. This interaction causes localized plasmons to oscillate coherently at a predetermined resonance frequency.

Fig. 1.2 illustrates the formation of localized surface plasmon oscillations in a straightforward manner. The oscillating electric field causes conduction electrons to flow in a coherent manner when a small NP is activated by a plane wave. Therefore, this process causes polarisation charges to build up on the NP's surface [4,6].

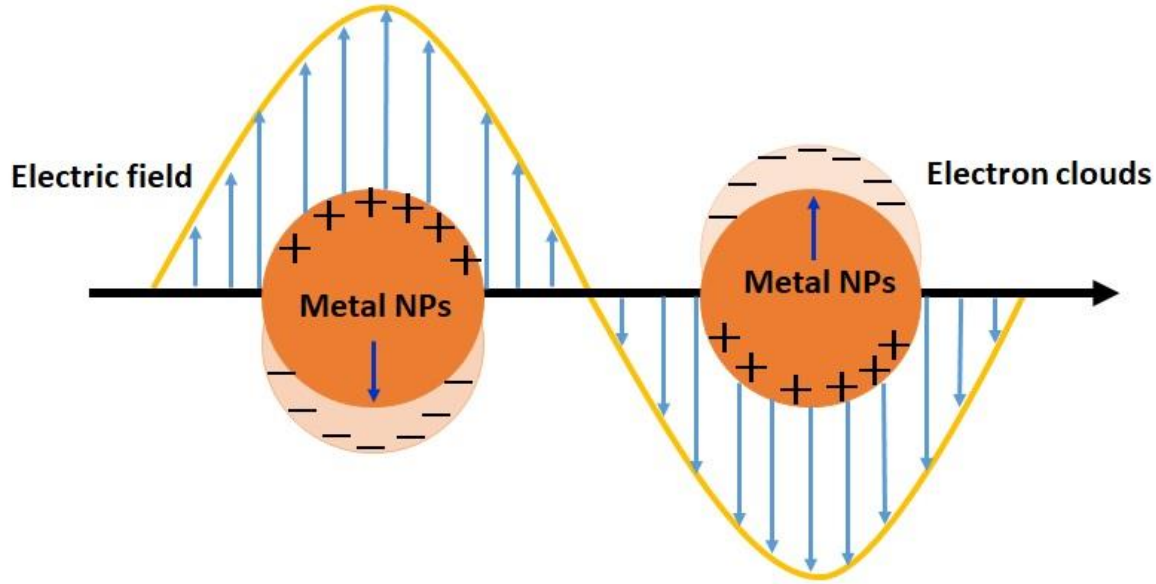

Fig.1.2. Schematic of localized surface plasmon resonance of metal nanoparticles.

The spectrum for well-separated NPs can be calculated using Mie's solution of Maxwell's equation when only dipole oscillations contribute to the extinction cross-section (σ_{ext}) [22,23].

$$\sigma_{ext}(\omega) = \frac{9V\omega\varepsilon_m^{3/2}}{c}\frac{\varepsilon_2(\omega)}{[\varepsilon_1(\omega)+2\varepsilon_m]^2+(\varepsilon_2)^2} \quad (1.1)$$

Where V is the particle volume, ω is the angular frequency of the exciting light, c is the speed of light, and ε_m and $\varepsilon(\omega) = \varepsilon_1(\omega) + i\varepsilon_2(\omega)$ are the dielectric functions of the surrounding medium and the material itself respectively. The resonance condition is met when $\varepsilon_1(\omega) = -2\varepsilon_m$, assuming that ε_2 is either small or exhibits only weak dependence on ω [22,23].

The characteristics of the localized surface plasmon resonance (LSPR) spectra, including peak position, bandwidth, and intensity, are influenced by various factors such as the size, shape, composition, surrounding medium, and inter-particle distance of nanoparticles (NPs) [15,24]. According to the Mie theory, the LSPR peak's position shifts towards the red end of the spectrum as the size of spherical nanoparticles increases, and towards the blue end as it decreases [25]. The aggregation and wide distribution of NPs sizes also contribute to a red shift in the LSPR peak. Simultaneously, the LSPR bandwidth broadens with larger particle sizes. This bandwidth holds significance in determining the specific applications of nanostructured metallic thin films [22]. For instance, a broader bandwidth is advantageous for plasmonic solar cells, enhancing absorption efficiency, while a narrower bandwidth is more suitable for plasmonic sensing applications. While size and environmental effects are pivotal, the impact of shape appears to be even more pronounced in the optical absorption spectrum of nanoparticles [26]. In the case of nanorods, the plasmon resonance absorption band splits into two bands [22]. The high-energy band corresponds to electron oscillation perpendicular to the major rod axis, termed transverse plasmon absorption. This absorption is relatively unaffected by the nanorod's aspect ratio [26]. The second absorption band at lower energies results from electron oscillation along the major rod axis, known as longitudinal surface plasmon absorption [6]. The maximum of the longitudinal plasmon band shifts towards the red end of the spectrum with increasing aspect ratio, while the maximum of the transverse absorption band remains relatively stable [23,27]. As the aspect ratio grows, the energy difference between the resonance frequencies of the two plasmon bands widens. The surface indeed plays a pivotal role in observing the surface plasmon resonance.

1.3. Permitivity of metals: Dielectric properties of the metal nanoparticles

As discussed above the permittivity/dielectric function, $\varepsilon(\omega) = \varepsilon_1(\omega) + i\varepsilon_2(\omega)$, which is composed of both real $\varepsilon_1(\omega)$ and imaginary parts $\varepsilon_2(\omega)$ play a crucial role in the optical properties of metal NPs. The variation in size-dependent surface plasmon absorption can be explained by the dielectric function, which combines the effects of free conduction electrons and interband transitions. The Drude model serves as the basic approach to describe the permittivity of metals, wherein conduction electrons are treated as free electrons [28,29]. Therefore, it can be expressed as

$$\varepsilon_D(\omega) = 1 - \frac{\omega_p^2}{\omega^2 + i\gamma\omega} \tag{1.2}$$

In this context, $\omega_p^2 = {ne^2}/{\varepsilon_0 m_{eff}}$ represents the bulk plasmon frequency, which is formulated in relation to the free electron density *n* and the charge of an electron *e*. Here, ε_0 signifies the vacuum permittivity, and m_{eff} stands for the effective mass of an electron. The parameter γ is introduced as a damping constant, and in the scenario of free electrons, it is equal to the bandwidth of the localized surface plasmon resonance (LSPR), denoted as (Γ). This bandwidth (Γ) is interconnected with the lifetime of various electron scattering processes in bulk materials, including electron-electron, electron-phonon, and electron-defect scattering. For nanoparticles that are smaller than the average free path of conduction electrons, electron-surface scattering assumes significance due to the dominant collisional interaction between conduction band electrons and the particle surface. This interaction diminishes the effective mean free path. The mean free path is influenced by multiple factors, including phonons and impurities. The mean free path of electrons in silver and gold, for instance, is around 40-50 nm [30]. The bandwidth shows a linear increase with electron density and is inversely proportional to particle size. The relation between bandwidth of LSPR and the particle size is given by following equation [30]

$$\Gamma(d) = \Gamma_0 + \frac{Av_f}{d} \tag{1.3}$$

Here, Γ_0 represents the damping constant at the bulk level, while A is a parameter that relies on the specifics of the scattering process, considering factors such as whether the scattering is isotropic or diffuse [29,31]. Additionally, v_f stands for the velocity of electrons at the Fermi energy. This theory offers a robust explanation for the relationship between the particle's dielectric constant and its size. Subsequently, the absorption spectrum of metal nanoparticles within a transparent non-interacting host medium can be readily computed. This is achievable because the dielectric constant is linked to the optical refractive index (*n*) and the absorption coefficient (*k*) in the subsequent manner [27]

$$\varepsilon = n^2 = \varepsilon_1 + i\varepsilon_2 \tag{1.4}$$

$$\varepsilon_1 = n^2 - k^2 \tag{1.5}$$

$$\varepsilon_2 = 2nk \tag{1.6}$$

1.4. Photoluminescence properties of the metal nanoparticles

Photolumniscense (PL) of metal nanostructure has gained more interest due to its promising

application in bioimaging and optical recording. The noble metal nanoparticles emit light at their LSPR band [32–34]. The LSPR strongly depends upon the size, morphology, and spatial orientation of the nanoparticles, the resonant wavelength and width of the LSPR can be tuned through the size, shape, and environmental control of the nanoparticles. However unlike semiconductor materials, the probability of radiative transitions for the luminescence from the metal nanoparticles is very low as metals do not have a forbidden energy gap between the occupied and unoccupied states in the conduction band [35,36]. Due to this, the luminescence from noble metal nanoparticles has been studied very sparsely [36,37]. In metals, photoluminescence is originated from the radiative recombination of hot excited core holes and conduction band electrons [35], but in the metal nanoparticles, PL is enhanced due to the surface plasmon effect [38]. During the last decades, PL from various plasmonic structures, including spherical nanoparticles [39–41], and nanorods [42,43], has been studied. The PL from the noble metal nanoparticles has been reported for gold, silver, and copper [32,36,44]. Due to the strongest LSPR compared to other noble metal (Au and Cu) nanoparticles, and luminescence enhancement property of Ag NPs is used to enhance the sensitivity of radiation detector, and the photodetectors [45–47]. Notably, the surface of the metal NPs palys a crucial role, and luminescence on rough metal surfaces was found to be amplified by several orders of magnitude [38,48,49]. This enhancement can be understood by viewing the rough metal surface as a collection of randomly oriented nanometer-sized hemispheroids on a smooth surface. These hemispheroids exhibit a surface plasmon resonance, thereby amplifying the incoming and outgoing electric fields due to the local field induced around them by plasmon resonances [38,48,49]. Based on theoretical studies of photoinduced luminescence from rough surfaces of noble metals, it is proposed that incoming and outgoing fields are amplified through coupling with local plasmon resonances [38]. The notable enhancement in luminescence efficiency arises from the substantial augmentation of the field of incoming exciting light and the emitted outgoing light due to coupling with surface plasmon resonance.

1.5. Surface enhanced Raman spectroscopy (SERS) properties of the metal nanoparticles

Since the discovery of Surface-Enhanced Raman Spectroscopy (SERS) spectroscopy by Fleischmann in 1976, it has been extensively explored to serve as a valuable tool for enhancing the sensitivity of inherently weak Raman signals [50]. In terms of identification of various species, although the traditional Raman spectroscopy is very efficient technique but it suffers

from the disadvantage of poor signal due to the low cross section for Raman scattering. This disadvantage of Raman spectroscopy has been effectively resolved by the introduction of SERS [51]. SERS is one such vibrational spectroscopic approach that uses the LSPR feature of noble metals to enhance the inherently weak Raman signal received from a sample by many orders of magnitude [51,52]. The electromagnetic effect from the concentrated electric field in the Localized Surface Plasmon Resonance (LSPR) around plasmonic NPs results into Raman signal enhancement. The SERS properties from the metal NPs is very sensitive to the shape, size, and interparticles separation of the implemented nanostructures. The surface of the metal nanostructure which amplified the electromagnetic fields near the NP surface, also play a crucial role to enhanced the Raman scattering [12,53,54]. The use of SERS in identifying various species and getting structural information is widely accepted. This is reflected in the application of SERS in the fields of material science, biomedical engineering, electrochemistry, etc [51,54].

While many advancements have been made in the development of high-performance SERS substrates, there is still a quest for more reliable and cost-effective substrates. Some plasmonic nanostructures, including nano-islands and nanoparticles serves as a high-performance SERS substrates and creates a highly sensitive platform for chemical and biological analyte detection [16]. The reproducibility of these highly effective SERS substrates based on periodic nanostructures is very challenging and limiting a variety of sensing applications. The precise control of fabrication parameters in the assembly of plasmonic nanostructures is essential for tailoring SERS substrates to meet specific requirements. Well-designed substrates, with carefully arranged nanostructures, offer improved predictability, sensitivity, and cost-effectiveness in SERS applications [54–56]. The combination of theoretical predictions and well-established synthesis techniques has confirmed the substantial potential of plasmonic assembled nanoarrays for surface-enhanced Raman spectroscopy (SERS) applications. These enhancements have a broad range of applications in fields like analytical chemistry, biosensing, and materials science.

1.6. Light trapping by metal nanoparticles in hydrogenated amorphous silicon (a-Si:H) thin film solar cells

1.6.1 Hydrogenated amorphous silicon (a-Si:H) thin film solar cells

Over the last three decades, hydrogenated amorphous silicon (a-Si:H) thin film solar cells are extensively explored as an alternative of crystalline silicon (c-Si) solar cells fabricated by

diffusion of *p-n* junction at high temperature [57–60]. However, due to structural disorder, a-Si:H materials possess high defect densities of dangling bond defect states and band tail defect states resulting in short diffusion length and low mobility of charge carriers [61]. These poor electrical properties of a-Si:H compared to c-Si leads to need of an extra layer in a-Si:H thin film solar compared to the conventional *p-n* junction structure [61]. a-Si:H thin film solar cells adopt *n-i-p* or *p-i-n* cell structure as shown in Fig. 1.3, where *i*-layer (intrinsic a-Si:H layer) is the absorber layer inserted between thin a-Si:H doped layers (p and n layer). The carrier lifetime in doped a-Si:H layer is very short, and photo carriers generated in these layers do not contribute to photocurrent. Therefore, the thickness of these layers is kept thin to reduce parasitic absorption losses [61]. In contrast, the intrinsic layer (a-Si:H i- layer) is the most essential part of a-Si:H thin film solar cells, where the process of electron-hole generation takes place, and these charge carriers get separated by the internal electric field prevailing within the whole i layer [62]. The first experimental demonstration of a-Si:H solar cell with *p-i-n* cell structure is given by Carlson and Wronski in 1976. They were able to achieve 2.4% efficiency in AM 1.0 sun light [63].

Based on the sequence of doped and undoped layers, in hydrogenated amorphous silicon thin film solar cells two cell structures are commonly used; (1) *p-i-n* structure (superstrate structure), (2) *n-i-p* structure (substrate structure). The schematic diagram of *p-i-n* and *n-i-p* structures is shown in Fig. 1.3 (Superstrate and substrate). In *p-i-n* structure, the *p, i, and n* layers are sequentially deposited on transparent conducting oxide (TCO) coated substrate.

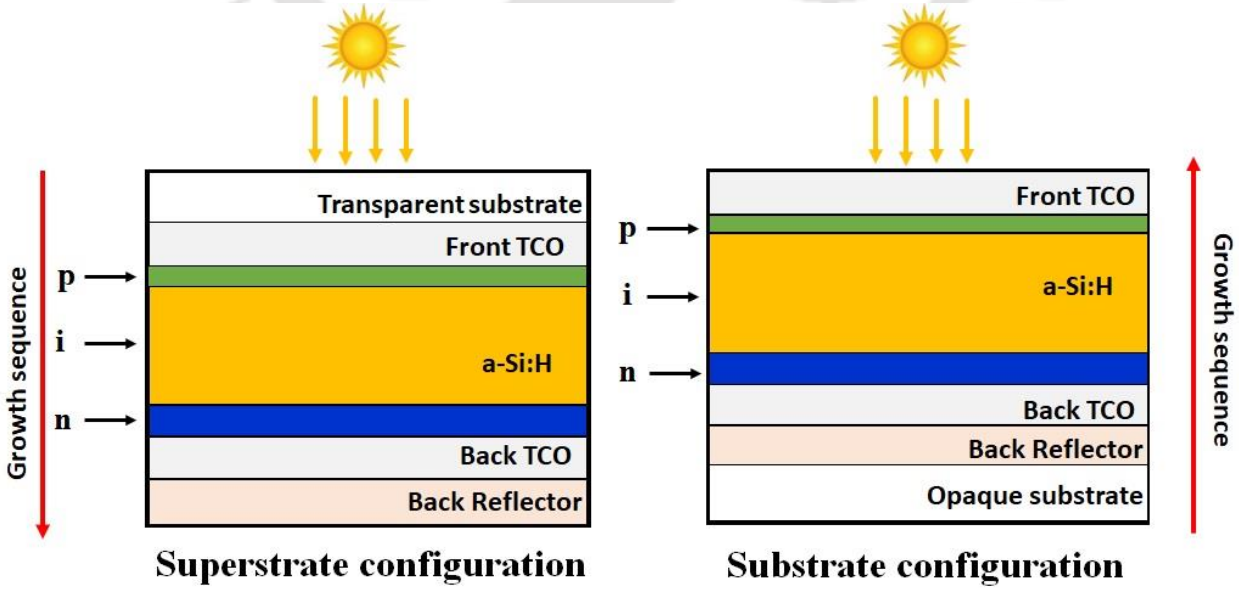

Fig. 1.3 Schematic diagram of superstrate-type (*p-i-n*) and substrate-type (*n-i-p*) hydrogenated amorphous silicon thin film solar cells.

In this structure, front contact and substrate should be transparent. In the case of *n-i-p* structure, the sequence of *n, i, and p* layers is grown on the opaque substrate. In both structures, *i-* layer is the main absorber layer which is inserted between *p-* and *n-* layer for optimum utilization of incident light. In this thesis a-Si:H thin film solar cells with *n-i-p* cell structure are used to explore the performance of the plasmonic back reflector.

1.6.2 Light trapping for hydrogenated amorphous silicon (a-Si:H) thin film solar cells

Despite having several advantages; the relatively low fabrication cost due to processing at low temperatures [64] and large area deposition on different substrates [65], including the flexible substrate, which are relatively cheaper than the silicon wafer, a-Si:H thin film solar cells suffer with the a relatively low efficiency compared to c-Si solar cells due to low absorption coefficient near the bandgap [66]. To overcome this problem, efficient light trapping is very essential in order to increase the absorption in the device [67–70]. Random texturing is the most common and widely used method of light trapping. The surface texturing of the front transparent conducting oxides (TCO) and the rear contact/mirror is generally used in superstrate (*p-i-n*) and substrate (*n-i-p*) configuration respectively [71–73]. Fig. 1.4 shows the light trapping mechanism by the texturing.

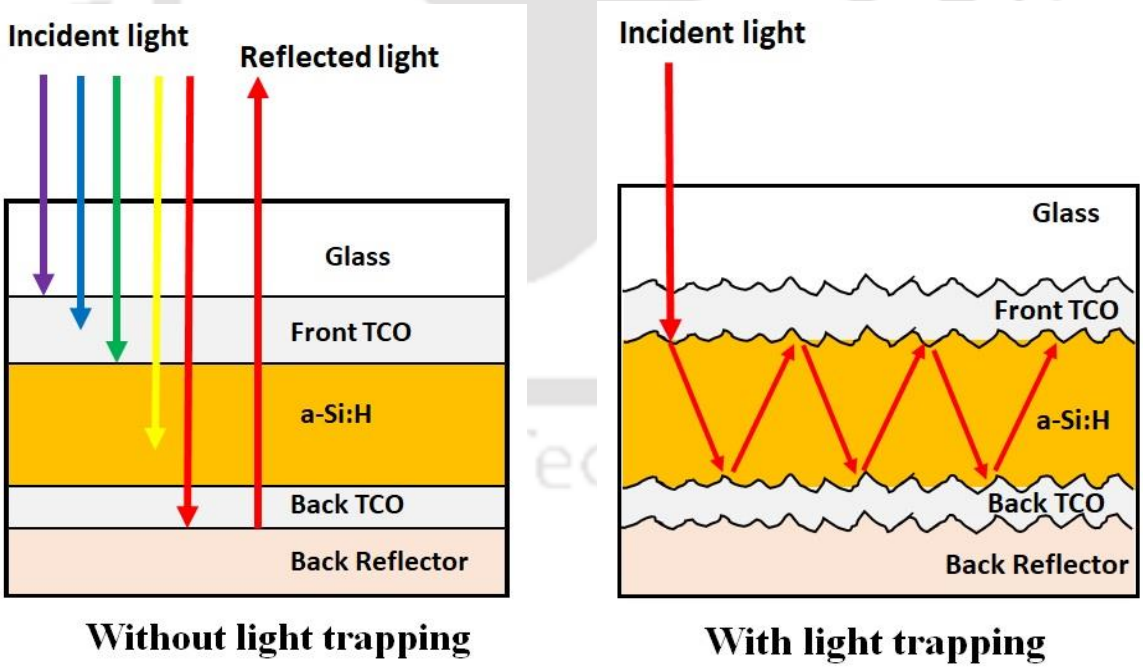

Fig. 1.4 Schematic diagram of thin-film silicon solar cells with and without light trapping

Left Fig. shows the when the light incident on the solar cells, the light passes through the absorber layer without being absorbed in the initial pass, it exists the solar cells in the absence of the any light-trapping mechanism. Whereas solar cells with the texturing surface in the right

Fig. show that incident light scattered at the rear contact and TCO interface and results in the absorption enhancement in the absorber layer. This texturing approach however often leads to high surface roughness, contributing the formation of bulk and surface defects, which in turn increase the recombination in the silicon layer and degrades the performance of device [74].

To address this issue, unconventional light trapping geometries based on periodic and random nanostructures such as nanowire, nanocones, nanorods, nanodomes , nanoparticles and nanocavity have been explored [75–81]. The use of metal nanoparticles provides low surface roughness, and efficient light trapping from the noble metal nanoparticles excited their surface plasmon resonance [82–85]. Surface plasmon resonance is a collective oscillation of the conduction electrons in the metal. The resonance of metallic nanoparticles strongly depends on factors like size, shape, spacing of the metallic particles, and the dielectric properties of the surrounding medium [4,86,87]. Light interaction with these nanoparticles at plasmonic resonance results in both scattering and absorption. These absorptions and scattering properties of metal nanoparticles are utilized for light trapping. Among the other noble nanoparticles, silver nanoparticles (Ag NPs) are popular choice due to their strongest plasmon resonance and large scattering cross-section in the visible and near infrared (NIR) region [87,88].

The location of the metal NPs array in the solar cells is very important which play a crucial role in light management. Metal NPs can be incorporated in the thin film solar cells in three different locations as shown in Fig. 1.5: (1) at the front surface, (2) embedded into the absorber layer, (3) at the back surface.

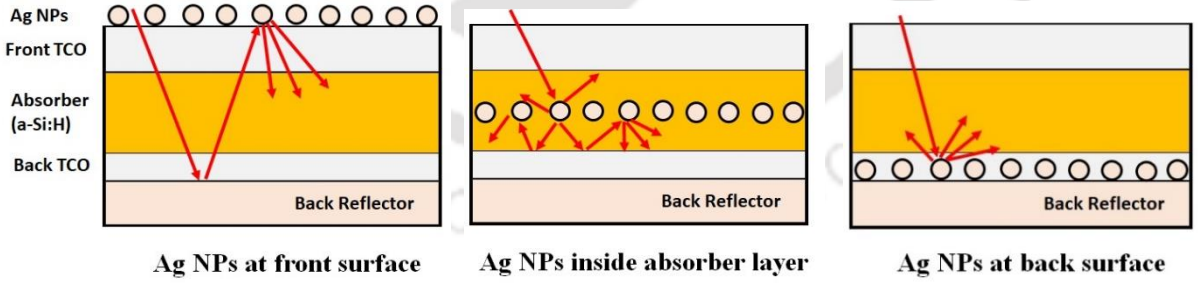

Fig. 1.5 Different plasmonic light-trapping geometries for a-Si:H thin-film solar cells.

The front surface placement of Ag NPs serves as an antireflection coating to reduce the reflection from the top surface and scatter the light by forward scattering into the absorber layer. However, these anti reflection properties of Ag NPs are not much effective in comparison conventional anti reflection coating, and state of the art light trapping performance has not been reported in this configuration. Furthermore, this configuration leads to parasitic absorption losses with the Ag NPs. Integration of Ag NPs inside the absorber layer results in the

contamination in the absorber layer which can lower the material quality. Placing the Ag NPs rear side of the cell is more beneficial arrangement. In this arrangement, Ag NPs are embedded in thin transparent conducting oxide (TCO) layer located between silicon absorber layer and a flat Ag mirror (rear contact). This configuration is termed as plasmonic back reflector and offer great potential to achieve effective light trapping cells [89–92].

1.7. Synthesis methods of silver nanoparticles

The synthesis of nanoparticles (NPs) is a dynamic and complex process with various methods available, each with its own advantages and disadvantages. Several routes for synthesizing silver nanostructures have been introduced, including physical, chemical, biological, and mechanical methods, as depicted in Fig. 1.6 [3,10]. Starting with mechanical techniques, high energy ball milling with the aid of high speed rotating balls is often used to produce nanoparticles from bulk material. The synthesis of intermetallic NPs are commonly done by this method [93]. However, this ball milling method requires substantial energy and time for milling. In the biological synthesis, Ag NPs are produced by microorganisms (bacteria, fungi, yeast), microbial reduction, and plants (lemongrass, Aloe vera, seaweed, mustard, safeda, lotus alfalfa, tea, neem, and tulsi) [94–96]. Microorganism-based nanoparticle synthesis is not a practical option since it calls for strict aseptic conditions to be maintained. The mechanisms for biological synthesis can include enzymatic and non-enzymatic reduction. These biological methods have safety risks and do not offer precise control on the shape and size [94,95]. The synthesis of silver nanoparticle by chemical methods can be divided into three main category; chemical reduction [97], electrochemical techniques [98], and solgel technique [93]. Chemical reduction methods involve the use of specific chemicals as reducing agents to convert silver ions into silver nanoparticles. Common reducing agents include borohydride, sodium citrate, ascorbic acid, alcohol, and hydrazine compounds [99]. Electrochemical methods use electrical currents and reactions at electrodes to reduce silver ions into nanoparticles. Sol-gel chemistry involves the synthesis of nanoparticles from a solution that undergoes a transition from a liquid "sol" to a solid "gel"[93]. Most of these methods produce the nanoparticles in liquid phases in which due to the colloidal solution, it is very challenging to organize the nanoparticles in the systematic array for their use in applications, especially in nanophotonics and solar cells. The fabrication of the metallic nanoparticles on the solid substrate with the desired shape and size and low-cost methodology is the main critical issue in using these nanoparticles in solid-state devices [100]. Physical methods, in contrast, often have short processing times and do not use hazardous chemicals. Such methods include solid state dewetting, laser ablation method, pulse

laser deposition, and thermal evaporation. Among the physical methods, solid-state dewetting (SSD) technique is a simple, low-cost physical method that can fabricate the metallic nanoparticles with control on the shape and size on the different substrates. In the SSD process, a thin film is transformed into an array of droplets or nanoparticles by thermal annealing through the minimization the surface energies of films, substrate and film substrate interface [101]. This method is relatively easier, more reproducible, and more reliable in fabricating these structures. Moreover, in this method, the nanoparticles can be fabricated on a large scale for Nano photonics, Nano electronics, plasmonics and photovoltaic devices.

The choice of nanoparticle synthesis method depends on the specific application's requirements, including control over nanoparticle size, shape, and distribution, as well as considerations of toxicity and environmental impact. The SSD method stands out as a promising approach for certain applications, including those in photovoltaics.

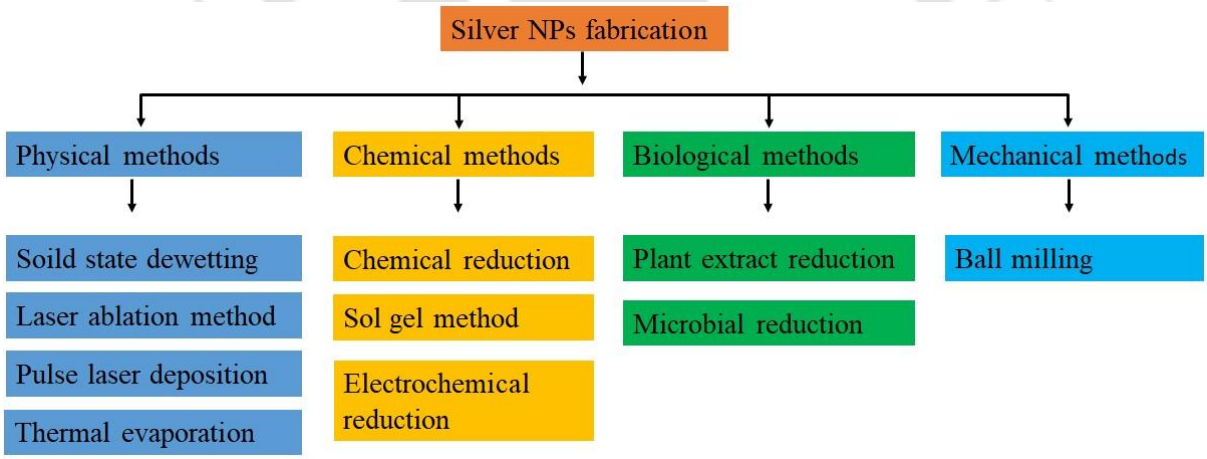

Fig.1.6. Schematic of different synthesis methods of silver nanoparticles.

1.8. Motivation, Objective and Contents of Thesis

In recent years, the field of plasmonics has rapidly grown as a new and expanding area for materials and device research. Among various types of nanoparticles, noble metals like Au, Ag, and Cu stand out due to their ability to exhibit localized surface plasmon resonance (LSPR), which has applications in biological sensors, solar cells, and surface-enhanced Raman spectroscopy (SERS). This has encouraged significant research into the fundamental properties and applications of metallic nanoparticles, particularly in integrated optics and biosensing. Among these noble metals, Ag nanoparticles have garnered considerable interest in silicon-based thin-film solar cells, glucose biosensors, and photodetectors due to their exceptionally

strong LSPR compared to other metals like Au and Cu. Most studies involve synthesizing Ag nanoparticles through solution-based methods, followed by deposition on substrates using techniques like drop-casting for various applications. However, a major challenge in employing these nanoparticles in solid-state devices lies in their controlled growth on solid substrates with specific shapes and sizes.The aim of this thesis work is to address this challenge by synthesizing silver nanoparticles through a physical approach known as solid-state dewetting (SSD). This involves depositing a thin silver film using radiofrequency (rf) sputtering and then subjecting it to thermal annealing to induce the growth of nanoparticles. By employing this method, the research seeks to investigate different properties of the resulting Ag nanoparticles for potential device applications. As thin-film silicon solar cells have gained importance due to their ability to reduce manufacturing costs while maintaining comparable efficiencies with other types of solar cells. However, these cells heavily rely on effective light trapping to reduce transmission losses and enhance performance, particularly as absorber layers become thinner. Achieving effective light trapping in thin-film solar cells, especially for indirect semiconductor silicon, presents a significant challenge. One promising way for improving light trapping is through the integration of metal nanoparticles of various shapes and sizes. These nanoparticles can serve as antireflection coatings on the surface, back reflectors on the rear side, or embedded within the medium of the solar cell. The incorporation of silver nanoparticles into thin-film silicon solar cells is driven by the motivation to enhance light trapping within the cells and subsequently improve their overall efficiency across a wide range of the electromagnetic spectrum.With this motivation, the following objectives have been set for this thesis work.

1. Synthesis and optimization of deposition parametrs of silver nanoparticles by solid state dewetting method.

2. Extensive growth study, structural, morphological, dielectric, optical, and surface enhanced Raman spectroscopy (SERS) properties of silver nanoparticles by Field emission scanning electron microscopy (FESEM), atomic force microscopy (AFM), Field emission transmission electron microscopy (FETEM), X-Ray Diffraction (XRD), Spectroscopic Ellipsometry (SE), Photoluminescence (PL), and UV-Vis-NIR spectroscopy, Raman spectroscopy.

3. Simulation and fabrication of hydrogenated amorphous silicon (a-Si:H) thin film solar cells using AFORS-HET software and radio frequency plasma enhanced chemical vapour deposition (RF-PECVD) multi-chamber system.

4. Integration of silver nanoparticles as a plasmonic back reflector into hydrogenated amorphous silicon (a-Si:H) thin film solar cells to improve the light trapping inside the cells and enhance its efficiency.

Proposed chapters in the present thesis

This thesis contains eight chapters as briefed below

Chapter 1 "Introduction" briefly introduces metal nanoparticles, a short literature review, and the advantages of thin film-based solar cells. The motivation and objectives of the thesis work are also included in this chapter.

Chapter 2 "Experimental details" briefly describes the synthesis method of silver nanoparticles and the deposition process of (n-i-p) a-Si:H thin film solar cells. This chapter also briefly describes different characterization techniques used to study silver nanoparticles' structural, morphological, optical, and dielectric properties and the performance of (n-i-p) a-Si:H thin film solar cells.

Chapter 3 "Growth dynamics of silver thin films and nanoparticles and its correlation with plasmonic properties of silver nanoparticles" presents the the correlation bewteen the growth dynamics and the optical properties of silver nanoparticles (Ag NPs). Ag NPs were grown onto the corning glass 1737 substrate by solid state dewetting of the silver precursor films deposited at different deposition time varying from 30-120 seconds by rf sputtering. Atomic force Microscopy (AFM) characterization with advanced data analysis is used to describe the surface characteristics. The height-height correlation function (HHCF) and power spectral density function (PSDF) are extracted from AFM images for the calculation of scaling exponents; local roughness exponent (α_{local}), growth exponents (β), dynamic exponent ($1/z$), and global roughness exponent (α) and to know the scaling behavior and growth model of the surface.

Chapter 4 "Influence of the microstructure on dielectric and plasmonic properties of silver nanoparticles" presents the dielectric and plasmonic properties of silver nanoparticles studied by Spectroscopic Ellipsometry. Ag NPs were grown on corning glass 1737 substrate by solid-state dewetting (SSD) of silver precursor thin film deposited at different RF power varying from 40-80 Watt by rf sputtering. Dilectric function and plasmonic properties of Ag NPs were investigated from spectroscopic ellipsometry (SE) data over a broad spectral range from 1.0 - 4.5 eV. The measured SE data was fitted by applying the Drude-Lorentz model to account for intraband and interband transitions in metallic films along with two Gaussian oscillators

corresponding to LSPR due to nanostructures. The BEMA was also simultaneously applied to calculate the void fraction arising due to the conversion of the continuous film into nanostructures and the top layer's roughness. The results of SE studies have been correlated with the microstructure and LSPR properties probed using FESEM, AFM, XRD, and UV-Vis-NIR absorbance spectroscopy.

Chapter 5 "Plasmon enhanced photoluminescence and Raman spectroscopy of silver nanoparticles" presents photoluminescence and Raman study of the silver nanoparticles. Ag NPs were grown on corning glass substrate by solid-state dewetting (SSD) of silver precursor thin film deposited at different substrate temperatures varying from RT- 400 ℃ by rf sputtering. The influence of the substrate temperature on the growth of Ag NPs and their several properties like localized surface Plasmon resonance (LSPR), photoluminescence (PL), and Raman spectroscopy is studied.

Chapter 6 "Simulation and fabrication of (*n-i-p*) a-Si:H thin film solar cells" presents both simulation and fabrication of single junction hydrogenated amorphous silicon (a-Si:H) thin film solar cells to study the performance of plasmonic back reflectors. Hydrogenated amorphous silicon (a-Si:H) thin film solar cells with *n-i-p* structure are simulated using AFORS-HET (Automated For Simulation of Heterostructure) software and fabricated using radio-frequency plasma enhanced chemical vapor deposition (RF-PECVD) (13.56 MHz) multi-chamber system at low temperature of 180℃. The influence of the emitter layer doping and absorber layer thickness was studied. Further, simulation results are compared with the experimental results.

Chapter 7 "Implementation of silver nanoparticles as plasmonics back reflector in (*n-i-p*) a-Si:H thin film solar cells" presents the integration of silver nanoparticles in thin film solar cells. Ag NPs were fabricated using optimized parameters on different substrate configuration to incorporate them plasmonic back reflector (PBR) in thin film solar cells. The structural and optical properties of Ag NPs grown on these substrates configuration were studied. Ag NPs were integrated as plasmonic back reflector into the a-Si:H thin film solar cells (corning *glass/Ag/AZO/AgNPs/AZO/n-i-p a-Si:H/ITO/Ag* structure) using using radio-frequency plasma enhanced chemical vapor deposition (RF-PECVD).

Chapter 8 "Summary, conclusion and future scopes" presents a summary and highlights of studies on silver nanoparticles, (*n-i-p*) a-Si:H thin film solar cells and implementation of silver

nanoparticles as plasmonic back reflector in (*n-i-p*) a-Si:H thin film solar cells. The future scope of this research area is also included in this chapter.

1.9 References

[1] I. Khan, K. Saeed, I. Khan, Nanoparticles: Properties, applications and toxicities, Arab. J. Chem. 12 (2019) 908–931. https://doi.org/10.1016/j.arabjc.2017.05.011.

[2] A. Gentile, F. Ruffino, M.G. Grimaldi, Complex-morphology metal-based nanostructures: Fabrication, characterization, and applications, Nanomaterials. 6 (2016). https://doi.org/10.3390/nano6060110.

[3] J. Natsuki, A Review of Silver Nanoparticles: Synthesis Methods, Properties and Applications, Int. J. Mater. Sci. Appl. 4 (2015) 325. https://doi.org/10.11648/j.ijmsa.20150405.17.

[4] L. Wang, M. Hasanzadeh Kafshgari, M. Meunier, Optical Properties and Applications of Plasmonic-Metal Nanoparticles, Adv. Funct. Mater. 30 (2020) 2005400. https://doi.org/https://doi.org/10.1002/adfm.202005400.

[5] A. Zada, P. Muhammad, W. Ahmad, Z. Hussain, S. Ali, M. Khan, Q. Khan, M. Maqbool, Surface Plasmonic-Assisted Photocatalysis and Optoelectronic Devices with Noble Metal Nanocrystals: Design, Synthesis, and Applications, Adv. Funct. Mater. 30 (2020) 1–29. https://doi.org/10.1002/adfm.201906744.

[6] E. Petryayeva, U.J. Krull, Localized surface plasmon resonance: Nanostructures, bioassays and biosensing-A review, Anal. Chim. Acta. 706 (2011) 8–24. https://doi.org/10.1016/j.aca.2011.08.020.

[7] F.J. Beck, S. Mokkapati, A. Polman, K.R. Catchpole, Asymmetry in photocurrent enhancement by plasmonic nanoparticle arrays located on the front or on the rear of solar cells, Appl. Phys. Lett. 96 (2010). https://doi.org/10.1063/1.3292020.

[8] A. Loiseau, V. Asila, G. Boitel-Aullen, M. Lam, M. Salmain, S. Boujday, Silver-Based Plasmonic Nanoparticles for and Their Use in Biosensing, Biosensors. 9 (2019). https://doi.org/10.3390/bios9020078.

[9] J. Divya, S. Selvendran, A.S. Raja, A. Sivasubramanian, Surface plasmon based

plasmonic sensors: A review on their past, present and future, Biosens. Bioelectron. X. 11 (2022) 100175. https://doi.org/10.1016/j.biosx.2022.100175.

[10] P.G. Jamkhande, N.W. Ghule, A.H. Bamer, M.G. Kalaskar, Metal nanoparticles synthesis: An overview on methods of preparation, advantages and disadvantages, and applications, J. Drug Deliv. Sci. Technol. 53 (2019) 101174. https://doi.org/10.1016/j.jddst.2019.101174.

[11] L. Wei, J. Lu, H. Xu, A. Patel, Z.S. Chen, G. Chen, Silver nanoparticles: Synthesis, properties, and therapeutic applications, Drug Discov. Today. 20 (2015) 595–601. https://doi.org/10.1016/j.drudis.2014.11.014.

[12] K. Kamakshi, K.C. Sekhar, A. Almeida, J. Agostinho Moreira, M.J.M. Gomes, Tuning the surface plasmon resonance and surface-enhanced Raman scattering of pulsed laser deposited silver nanoparticle films by ambience and deposition temperature, J. Opt. 16 (2014) 55002. https://doi.org/10.1088/2040-8978/16/5/055002.

[13] C. Guillén, J. Herrero, Surface-properties relationship in sputtered Ag thin films: Influence of the thickness and the annealing temperature in nitrogen, Appl. Surf. Sci. 324 (2015) 245–250. https://doi.org/https://doi.org/10.1016/j.apsusc.2014.10.076.

[14] O.A. Yeshchenko, I.M. Dmitruk, A.M. Dmytruk, A.A. Alexeenko, Influence of annealing conditions on size and optical properties of copper nanoparticles embedded in silica matrix, Mater. Sci. Eng. B. 137 (2007) 247–254. https://doi.org/https://doi.org/10.1016/j.mseb.2006.11.030.

[15] A. Ali, F. El-Mellouhi, A. Mitra, B. Aïssa, Research Progress of Plasmonic Nanostructure-Enhanced Photovoltaic Solar Cells, Nanomaterials. 12 (2022) 788. https://doi.org/10.3390/nano12050788.

[16] X. Xie, H. Pu, D.W. Sun, Recent advances in nanofabrication techniques for SERS substrates and their applications in food safety analysis, Crit. Rev. Food Sci. Nutr. 58 (2018) 2800–2813. https://doi.org/10.1080/10408398.2017.1341866.

[17] K. Nakayama, K. Tanabe, H.A. Atwater, Plasmonic nanoparticle enhanced light absorption in GaAs solar cells, Appl. Phys. Lett. 93 (2008) 121904. https://doi.org/10.1063/1.2988288.

[18] S. Morawiec, M.J. Mendes, S. Mirabella, F. Simone, F. Priolo, I. Crupi, Self-assembled

silver nanoparticles for plasmon-enhanced solar cell back reflectors: correlation between structural and optical properties, Nanotechnology. 24 (2013) 265601. https://doi.org/10.1088/0957-4484/24/26/265601.

[19] H. Tan, R. Santbergen, A.H.M. Smets, M. Zeman, Plasmonic Light Trapping in Thin-film Silicon Solar Cells with Improved Self-Assembled Silver Nanoparticles, Nano Lett. 12 (2012) 4070–4076. https://doi.org/10.1021/nl301521z.

[20] V.E. Ferry, L.A. Sweatlock, D. Pacifici, H.A. Atwater, Plasmonic Nanostructure Design for Efficient Light Coupling into Solar Cells, Nano Lett. 8 (2008) 4391–4397. https://doi.org/10.1021/nl8022548.

[21] S. Li, J. He, Q.H. Xu, Aggregation of Metal-Nanoparticle-Induced Fluorescence Enhancement and Its Application in Sensing, ACS Omega. 5 (2020) 41–48. https://doi.org/10.1021/acsomega.9b03560.

[22] S. Link, M.A. El-Sayed, Shape and size dependence of radiative, non-radiative and photothermal properties of gold nanocrystals, Int. Rev. Phys. Chem. 19 (2000) 409–453. https://doi.org/10.1080/01442350050034180.

[23] P.J. Dobson, Absorption and Scattering of Light by Small Particles, Phys. Bull. 35 (1984) 104. https://doi.org/10.1088/0031-9112/35/3/025.

[24] B. Khodashenas, H.R. Ghorbani, Synthesis of silver nanoparticles with different shapes, Arab. J. Chem. 12 (2019) 1823–1838. https://doi.org/10.1016/j.arabjc.2014.12.014.

[25] H. Horvath, Gustav Mie and the scattering and absorption of light by particles: Historic developments and basics, J. Quant. Spectrosc. Radiat. Transf. 110 (2009) 787–799.

[26] X. Lu, M. Rycenga, S.E. Skrabalak, B. Wiley, Y. Xia, Chemical Synthesis of Novel Plasmonic Nanoparticles, (2009). https://doi.org/10.1146/annurev.physchem.040808.090434.

[27] G.C. Papavassiliou, Optical properties of small inorganic and organic metal particles, Prog. Solid State Chem. 12 (1979) 185–271. https://doi.org/https://doi.org/10.1016/0079-6786(79)90001-3.

[28] U. Kreibig, Kramers Kronig analysis of the optical properties of small silver particles, Zeitschrift Für Phys. 234 (1970) 307–318. https://doi.org/10.1007/BF01394718.

[29] U. Kreibig, L. Genzel, Optical absorption of small metallic particles, Surf. Sci. 156 (1985) 678–700. https://doi.org/https://doi.org/10.1016/0039-6028(85)90239-0.

[30] U. Kreibig, C. v. Fragstein, The limitation of electron mean free path in small silver particles, Zeitschrift Für Phys. 224 (1969) 307–323. https://doi.org/10.1007/BF01393059.

[31] U. Kreibig, M. Vollmer, Optical properties of metal clusters, Springer Science & Business Media, 2013.

[32] J.P. Wilcoxon, J.E. Martin, F. Parsapour, B. Wiedenman, D.F. Kelley, Photoluminescence from nanosize gold clusters, J. Chem. Phys. 108 (1998) 9137–9143. https://doi.org/10.1063/1.476360.

[33] W.S. Chang, B. Willingham, L.S. Slaughter, S. Dominguez-Medina, P. Swanglap, S. Link, Radiative and nonradiative properties of single plasmonic nanoparticles and their assemblies, Acc. Chem. Res. 45 (2012) 1936–1945. https://doi.org/10.1021/ar200337u.

[34] M. Yorulmaz, S. Khatua, P. Zijlstra, A. Gaiduk, M. Orrit, Luminescence quantum yield of single gold nanorods, Nano Lett. 12 (2012) 4385–4391. https://doi.org/10.1021/nl302196a.

[35] P. Apell, R. Monreal, S. Lundqvist, Photoluminescence of noble metals, Phys. Scr. 38 (1988) 174–179. https://doi.org/10.1088/0031-8949/38/2/012.

[36] A. Zhang, J. Zhang, Y. Fang, Photoluminescence from colloidal silver nanoparticles, J. Lumin. 128 (2008) 1635–1640. https://doi.org/10.1016/j.jlumin.2008.03.014.

[37] H. Mertens, A. Polman, Plasmon-enhanced erbium luminescence, Appl. Phys. Lett. 89 (2006). https://doi.org/10.1063/1.2392827.

[38] G.T. Boyd, Z.H. Yu, Y.R. Shen, Photoinduced luminescence from the noble metals and its enhancement on roughened surfaces, Phys. Rev. B. 33 (1986) 7923–7936. https://doi.org/10.1103/PhysRevB.33.7923.

[39] A. Lin, D.H. Son, I.H. Ahn, G.H. Song, W.-T. Han, Visible to infrared photoluminescence from gold nanoparticles embedded in germano-silicate glass fiber, Opt. Express. 15 (2007) 6374–6379. https://doi.org/10.1364/OE.15.006374.

[40] M. Eichelbaum, K. Rademann, A. Hoell, D.M. Tatchev, W. Weigel, R. Stößer, G.

Pacchioni, Photoluminescence of atomic gold and silver particles in soda-lime silicate glasses, Nanotechnology. 19 (2008) 135701. https://doi.org/10.1088/0957-4484/19/13/135701.

[41] M. Eichelbaum, B.E. Schmidt, H. Ibrahim, K. Rademann, Three-photon-induced luminescence of gold nanoparticles embedded in and located on the surface of glassy nanolayers, Nanotechnology. 18 (2007) 355702. https://doi.org/10.1088/0957-4484/18/35/355702.

[42] K. Imura, H. Okamoto, Properties of photoluminescence from single gold nanorods induced by near-field two-photon excitation, J. Phys. Chem. C. 113 (2009) 11756–11759. https://doi.org/10.1021/jp9018074.

[43] D.-S. Wang, F.-Y. Hsu, C.-W. Lin, Surface plasmon effects on two photon luminescence of gold nanorods, Opt. Express. 17 (2009) 11350. https://doi.org/10.1364/oe.17.011350.

[44] O.A. Yeshchenko, I.M. Dmitruk, A.M. Dmytruk, A.A. Alexeenko, Influence of annealing conditions on size and optical properties of copper nanoparticles embedded in silica matrix, Mater. Sci. Eng. B Solid-State Mater. Adv. Technol. 137 (2007) 247–254. https://doi.org/10.1016/j.mseb.2006.11.030.

[45] J.S. Cho, S. Baek, S.H. Park, J.H. Park, J. Yoo, K.H. Yoon, Effect of nanotextured back reflectors on light trapping in flexible silicon thin-film solar cells, Sol. Energy Mater. Sol. Cells. 102 (2012) 50–57. https://doi.org/10.1016/j.solmat.2012.03.031.

[46] J.N. Anker, W.P. Hall, O. Lyandres, N.C. Shah, J. Zhao, R.P. Van Duyne, Biosensing with plasmonic nanosensors, Nat. Mater. 7 (2008) 442–453. https://doi.org/10.1038/nmat2162.

[47] P. Berini, Surface plasmon photodetectors and their applications, Laser Photon. Rev. 8 (2014) 197–220. https://doi.org/https://doi.org/10.1002/lpor.201300019.

[48] C.K. Chen, T.F. Heinz, D. Ricard, Y.R. Shen, Surface-enhanced second-harmonic generation and Raman scattering, Phys. Rev. B. 27 (1983) 1965–1979. https://doi.org/10.1103/PhysRevB.27.1965.

[49] G.T. Boyd, T. Rasing, J.R.R. Leite, Y.R. Shen, Local-field enhancement on rough surfaces of metals, semimetals, and semiconductors with the use of optical second-harmonic generation, Phys. Rev. B. 30 (1984) 519–526.

https://doi.org/10.1103/PhysRevB.30.519.

[50] M. Fleischmann, P.J. Hendra, A.J. McQuillan, Raman spectra of pyridine adsorbed at a silver electrode, Chem. Phys. Lett. 26 (1974) 163–166. https://doi.org/https://doi.org/10.1016/0009-2614(74)85388-1.

[51] D. Cialla-May, X.-S. Zheng, K. Weber, J. Popp, Recent progress in surface-enhanced Raman spectroscopy for biological and biomedical applications: from cells to clinics, Chem. Soc. Rev. 46 (2017) 3945–3961. https://doi.org/10.1039/C7CS00172J.

[52] K. Chaudhari, T. Ahuja, V. Murugesan, V. Subramanian, M.A. Ganayee, T. Thundat, T. Pradeep, Appearance of SERS activity in single silver nanoparticles by laser-induced reshaping, Nanoscale. 11 (2019) 321–330. https://doi.org/10.1039/C8NR06497K.

[53] A. Gentile, F. Ruffino, M.G. Grimaldi, Complex-Morphology Metal-Based Nanostructures: Fabrication, Characterization, and Applications, Nanomaterials. 6 (2016). https://doi.org/10.3390/nano6060110.

[54] Z. Fusco, R. Bo, Y. Wang, N. Motta, H. Chen, A. Tricoli, Self-assembly of Au nano-islands with tuneable organized disorder for highly sensitive SERS, J. Mater. Chem. C. 7 (2019) 6308–6316. https://doi.org/10.1039/C9TC01231A.

[55] H. Dies, A. Bottomley, D.L. Nicholls, K. Stamplecoskie, C. Escobedo, A. Docoslis, Electrokinetically-Driven Assembly of Gold Colloids into Nanostructures for Surface-Enhanced Raman Scattering, Nanomaterials. 10 (2020). https://doi.org/10.3390/nano10040661.

[56] M. Rycenga, M.H. Kim, P.H.C. Camargo, C. Cobley, Z.-Y. Li, Y. Xia, Surface-Enhanced Raman Scattering: Comparison of Three Different Molecules on Single-Crystal Nanocubes and Nanospheres of Silver, J. Phys. Chem. A. 113 (2009) 3932–3939. https://doi.org/10.1021/jp8101817.

[57] M. Okil, M.S. Salem, T.M. Abdolkader, A. Shaker, From Crystalline to Low-cost Silicon-based Solar Cells: a Review, Silicon. 14 (2022) 1895–1911. https://doi.org/10.1007/s12633-021-01032-4.

[58] M. Stuckelberger, R. Biron, N. Wyrsch, F. Haug, C. Ballif, Review : Progress in solar cells from hydrogenated amorphous silicon, Renew. Sustain. Energy Rev. 76 (2017) 1497–1523. https://doi.org/10.1016/j.rser.2016.11.190.

[59] F. Meillaud, M. Boccard, G. Bugnon, M. Despeisse, S. Ha, F. Haug, M. Stuckelberger, C. Ballif, J. Persoz, J. Schu, Recent advances and remaining challenges in thin-film silicon photovoltaic technology, 18 (2015). https://doi.org/10.1016/j.mattod.2015.03.002.

[60] A. Lambertz, F. Finger, R.E.I. Schropp, U. Rau, V. Smirnov, Preparation and measurement of highly efficient a-Si:H single junction solar cells and the advantages of μc-SiOx:H n-layers, Prog. Photovoltaics Res. Appl. 23 (2015) 939–948. https://doi.org/https://doi.org/10.1002/pip.2629.

[61] A. Shah, Thin-film silicon solar cells, EPFL press, 2010.

[62] I. Benigno, D. Darminto, Effect of Intrinsic Layer Energy Gap and Thicknesses Optimization on the Efficiency of p-i-n Amorphous Silicon Solar Cell, IPTEK J. Sci. 2 (2017). https://doi.org/10.12962/j23378530.v2i3.a3184.

[63] D.E. Carlson, C.R. Wronski, Amorphous silicon solar cell, Appl. Phys. Lett. 28 (1976) 671–673. https://doi.org/10.1063/1.88617.

[64] J. Ramanujam, D.M. Bishop, T.K. Todorov, O. Gunawan, J. Rath, R. Nekovei, E. Artegiani, A. Romeo, Flexible CIGS, CdTe and a-Si:H based thin film solar cells: A review, Prog. Mater. Sci. 110 (2020) 1–20. https://doi.org/10.1016/j.pmatsci.2019.100619.

[65] R. Madaka, V. Kanneboina, P. Agarwal, Exploring the photo paper as flexible substrate for fabrication of a-Si:H based thin film solar cells at low temperature (110 °C): Influence of radio frequency power on opto-electronic properties, Thin Solid Films. 662 (2018) 155–164. https://doi.org/10.1016/j.tsf.2018.07.043.

[66] M.A. Green, E.D. Dunlop, M. Yoshita, N. Kopidakis, K. Bothe, G. Siefer, X. Hao, Solar cell efficiency tables (version 62), Prog. Photovoltaics Res. Appl. (2023) 651–663. https://doi.org/10.1002/pip.3726.

[67] C. Sun, Z. Wang, X. Wang, J. Liu, A Surface Design for Enhancement of Light Trapping Efficiencies in Thin Film Silicon Solar Cells, Plasmonics. 11 (2016) 1003–1010. https://doi.org/10.1007/s11468-015-0135-8.

[68] P.M. Voroshilov, C.R. Simovski, P.A. Belov, A.S. Shalin, Light-trapping and antireflective coatings for amorphous Si-based thin film solar cells, J. Appl. Phys. 117

(2015). https://doi.org/10.1063/1.4921440.

[69] C. Haase, H. Stiebig, Thin-film silicon solar cells with efficient periodic light trapping texture, Appl. Phys. Lett. 91 (2007). https://doi.org/10.1063/1.2768882.

[70] R.H. Franken, R.L. Stolk, H. Li, C.H.M. Van Der Werf, J.K. Rath, R.E.I. Schropp, Understanding light trapping by light scattering textured back electrodes in thin film n-i-p -type silicon solar cells, J. Appl. Phys. 102 (2007). https://doi.org/10.1063/1.2751117.

[71] X. Yan, S. Venkataraj, A.G. Aberle, Modified surface texturing of aluminium-doped zinc oxide (AZO) transparent conductive oxides for thin-film silicon solar cells, Energy Procedia. 33 (2013) 157–165. https://doi.org/10.1016/j.egypro.2013.05.053.

[72] F.J. Haug, A. Naqavi, C. Ballif, Diffraction and absorption enhancement from textured back reflectors of thin film solar cells, J. Appl. Phys. 112 (2012). https://doi.org/10.1063/1.4737606.

[73] U. Palanchoke, V. Jovanov, H. Kurz, R. Dewan, P. Magnus, H. Stiebig, D. Knipp, Influence of back contact roughness on light trapping and plasmonic losses of randomly textured amorphous silicon thin film solar cells, Appl. Phys. Lett. 102 (2013). https://doi.org/10.1063/1.4793415.

[74] C. Battaglia, J. Escarré, K. Söderström, L. Erni, L. Ding, G. Bugnon, A. Billet, M. Boccard, L. Barraud, S. De Wolf, F.J. Haug, M. Despeisse, C. Ballif, Nanoimprint lithography for high-efficiency thin-film silicon solar cells, Nano Lett. 11 (2011) 661–665. https://doi.org/10.1021/nl1037787.

[75] J. Kim, J.H. Yun, H. Kim, Y. Cho, H.H. Park, M.M.D. Kumar, J. Yi, W.A. Anderson, D.W. Kim, Transparent conductor-embedding nanocones for selective emitters: Optical and electrical improvements of Si solar cells, Sci. Rep. 5 (2015) 1–8. https://doi.org/10.1038/srep09256.

[76] P.S. Chandrasekhar, H. Elbohy, B. Vaggensmith, A. Dubey, K.M. Reza, V.K. Komarala, Q. Qiao, Plasmonic silver nanowires for higher efficiency dye-sensitized solar cells, Mater. Today Energy. 5 (2017) 237–242. https://doi.org/10.1016/j.mtener.2017.07.005.

[77] M. Law, L.E. Greene, J.C. Johnson, R. Saykally, P. Yang, Nanowire dye-sensitized solar cells, Nat. Mater. 4 (2005) 455–459. https://doi.org/10.1038/nmat1387.

[78] J. Zhu, C.M. Hsu, Z. Yu, S. Fan, Y. Cui, Nanodome solar cells with efficient light management and self-cleaning, Nano Lett. 10 (2010) 1979–1984. https://doi.org/10.1021/nl9034237.

[79] M.J. Mendes, S. Morawiec, I. Crupi, F. Simone, F. Priolo, Colloidal self-assembled nanosphere arrays for plasmon-enhanced light trapping in thin film silicon solar cells, Energy Procedia. 44 (2014) 184–191. https://doi.org/10.1016/j.egypro.2013.12.026.

[80] M.J. Mendes, A. Araújo, A. Vicente, H. Águas, I. Ferreira, E. Fortunato, R. Martins, Design of optimized wave-optical spheroidal nanostructures for photonic-enhanced solar cells, Nano Energy. 26 (2016) 286–296. https://doi.org/10.1016/j.nanoen.2016.05.038.

[81] Z. Xu, H. Qiao, H. Huangfu, X. Li, J. Guo, H. Wang, Optical absorption of several nanostructures arrays for silicon solar cells, Opt. Commun. 356 (2015) 526–529. https://doi.org/10.1016/j.optcom.2015.08.069.

[82] Y.H. Jang, Y.J. Jang, S. Kim, L.N. Quan, K. Chung, D.H. Kim, Plasmonic Solar Cells: From Rational Design to Mechanism Overview, Chem. Rev. 116 (2016) 14982–15034. https://doi.org/10.1021/acs.chemrev.6b00302.

[83] V.E. Ferry, A. Polman, H.A. Atwater, Light trapping in plasmonic solar cells, Opt. InfoBase Conf. Pap. 18 (2011) 237–245. https://doi.org/10.1364/ls.2011.lwe3.

[84] K.R. and Catchpole, A. Polman, Plasmonic solar cells, Opt. Express. 16 (2008) 21793–21800.

[85] H.A. Atwater, A. Polman, Plasmonics for improved photovoltaic devices, Nat. Mater. 9 (2010) 205–213. https://doi.org/10.1038/nmat2629.

[86] M. Singh, P. Agarwal, Growth dynamics and its correlation with plasmonic properties of silver nanoparticles grown by solid state dewetting, Mater. Res. Bull. 167 (2023) 112380. https://doi.org/10.1016/j.materresbull.2023.112380.

[87] S. Morawiec, M.J. Mendes, S. Mirabella, F. Simone, F. Priolo, I. Crupi, Self-assembled silver nanoparticles for plasmon-enhanced solar cell back reflectors: Correlation between structural and optical properties, Nanotechnology. 24 (2013). https://doi.org/10.1088/0957-4484/24/26/265601.

[88] A. Araújo, M.J. Mendes, T. Mateus, A. Vicente, D. Nunes, T. Calmeiro, E. Fortunato,

H. Águas, R. Martins, Influence of the Substrate on the Morphology of Self-Assembled Silver Nanoparticles by Rapid Thermal Annealing, J. Phys. Chem. C. 120 (2016) 18235–18242. https://doi.org/10.1021/acs.jpcc.6b04283.

[89] S. Cao, D. Yu, Y. Lin, C. Zhang, L. Lu, M. Yin, X. Zhu, X. Chen, D. Li, Light Propagation in Flexible Thin-Film Amorphous Silicon Solar Cells with Nanotextured Metal Back Re fl ectors, (2020). https://doi.org/10.1021/acsami.0c05330.

[90] S. Morawiec, M.J. Mendes, F. Priolo, I. Crupi, Materials Science in Semiconductor Processing Plasmonic nanostructures for light trapping in thin- fi lm solar cells, Mater. Sci. Semicond. Process. 92 (2019) 10–18. https://doi.org/10.1016/j.mssp.2018.04.035.

[91] A. Araújo, M.J. Mendes, T. Mateus, J. Costa, D. Nunes, E. Fortunato, H. Águas, R. Martins, Ultra-fast plasmonic back re fl ectors production for light trapping in thin Si solar cells, Sol. Energy. 174 (2018) 786–792. https://doi.org/10.1016/j.solener.2018.08.068.

[92] H. Tan, R. Santbergen, A.H.M. Smets, M. Zeman, Plasmonic light trapping in thin-film silicon solar cells with improved self-assembled silver nanoparticles, Nano Lett. 12 (2012) 4070–4076. https://doi.org/10.1021/nl301521z.

[93] N. Rajput, Methods of preparation of nanoparticles-a review, Int. J. Adv. Eng. Technol. 7 (2015) 1806.

[94] N. Pantidos, L.E. Horsfall, Biological synthesis of metallic nanoparticles by bacteria, fungi and plants, J. Nanomed. Nanotechnol. 5 (2014) 1.

[95] A. Ahmad, P. Mukherjee, S. Senapati, D. Mandal, M.I. Khan, R. Kumar, M. Sastry, Extracellular biosynthesis of silver nanoparticles using the fungus Fusarium oxysporum, Colloids Surfaces B Biointerfaces. 28 (2003) 313–318. https://doi.org/https://doi.org/10.1016/S0927-7765(02)00174-1.

[96] P. Kuppusamy, M.M. Yusoff, G.P. Maniam, N. Govindan, Biosynthesis of metallic nanoparticles using plant derivatives and their new avenues in pharmacological applications – An updated report, Saudi Pharm. J. 24 (2016) 473–484. https://doi.org/https://doi.org/10.1016/j.jsps.2014.11.013.

[97] Q. Zhang, N. Li, J. Goebl, Z. Lu, Y. Yin, A Systematic Study of the Synthesis of Silver Nanoplates: Is Citrate a "Magic" Reagent?, J. Am. Chem. Soc. 133 (2011) 18931–

18939. https://doi.org/10.1021/ja2080345.

[98] M. Roldán, N. Pellegri, O. de Sanctis, Electrochemical method for Ag-PEG nanoparticles synthesis, J. Nanoparticles. 2013 (2013).

[99] S.M. Landage, A.I. Wasif, P. Dhuppe, Synthesis of nanosilver using chemical reduction methods, Int. J. Adv. Res. Eng. Appl. Sci. 3 (2014) 14–22.

[100] J.A. Badán, E. Navarrete-Astorga, R. Henríquez, F. Martín Jiménez, D. Ariosa, J.R. Ramos-Barrado, E.A. Dalchiele, Silver Nanoparticle Arrays onto Glass Substrates Obtained by Solid-State Thermal Dewetting: A Morphological, Structural and Surface Chemical Study, Nanomaterials. 12 (2022). https://doi.org/10.3390/nano12040617.

[101] C. V. Thompson, Solid-state dewetting of thin films, Annu. Rev. Mater. Res. 42 (2012) 399–434. https://doi.org/10.1146/annurev-matsci-070511-155048.

Chapter 2

Experimental details

2.1. Introduction

This chapter presents the brief discussion on synthesis and characterization techniques for Ag NPs and fabrication of the a-Si:H thin film solar cells. In this thesis work, Ag NPs were grown by solid state dewetting process of the precursor films deposited by rf sputtering technique. Surface morphology of the films was studied by Atomic force microscope (AFM) and Field emission scanning electron microscope (FESEM) technique. For structural evaluation of Ag NPs, X-ray and Transmission electron microscopy (TEM) measurements have been carried out. Plasmonic properties of Ag NPs were studied using UV-Vis-NIR spectroscopy. Spectroscopic ellipsometry (SE) technique was used to study dielectric and optical properties of the films. The performance of n-i-p a-Si:H thin film solar cells with flat back reflector and the plasmonic back reflector was evaluated by current-voltage and external quantum efficiency measurements.

2.2. Synthesis of silver nanoparticles by solid state dewetting

In this thesis, we have used solid-state dewetting (SSD) technique, which is a simple, low-cost method that can be used to fabricate the metallic nanoparticles with control on the shape and size on the different substrates including glass, sapphire, silicon etc [1–5]. After adequate annealing, a continuous metallic thin film on a surface spontaneously rearranges into a array of isolated islands or droplets in SSD process [6,7], as illustrated in Fig. 2.1. Dewetting is the process by which the continuous film separates into many particles in a way similar to how a water layer would behave on a hydrophobic surface [8–10]. The film dewettes in the following stages: hillock development during the incubation phase; film pinch off followed by hole formation, growth, and percolation; and, lastly, the formation and aggregation of islands producing distinct structures as a result of Rayleigh instability [11,12]. According to the aforementioned scheme, the development of such nanostructures on oxide matrices can be described using the Volmer-Weber growth mode [13], where the morphological change and dewetting process are influenced by the annealing parameters (annealing temperature and time)

and film thickness [1,12,13]. Legrand et al. were the first to show that, in the case of silicon-on-insulator (SOI) thin films, solid-state dewetting is controlled by the initial film thickness [14,15]. As a result, the dimensions and distribution of the nanocrystals are also entirely governed by the film thickness if no special preparation is applied to the film.

The SSD process can be triggered by thermal annealing [16–19], pulsed laser heating [20–22], combined thermal annealing and pulsed laser heating [23], ion beam irradiation [24,25], electron beam irradiation [26], and inductively coupled plasma discharge [27]. However, when working on large areas, thermal annealing is generally the easiest method for dewetting. For thinner films, the dewetting temperature is lower, and the island size increases with film thickness [28]. This method is relatively easier, more reproducible and reliable in fabricating these structures. Furthermore, the size of nanoparticles can be monitored more effectively and reproducibly on a large scale using this technology for Nano photonics, Nano electronics, plasmonics, and photovoltaic devices [6,29,30].

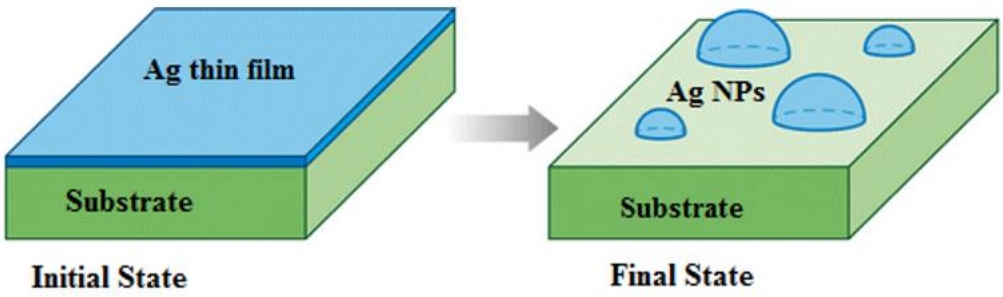

Fig.2.1 solid-state dewetting, thin films dewet to form isolated islands.

The equilibrium shape of an island on a rigid substrate is that of a spherical cap with contact angle θ as shown in Fig. 2.2. For islands with isotropic surface energy per unit area (γ_f) on a rigid substrate with surface energy per area (γ_s), the energy minimization of dewetting is given by the Young-Laplace equation [31]

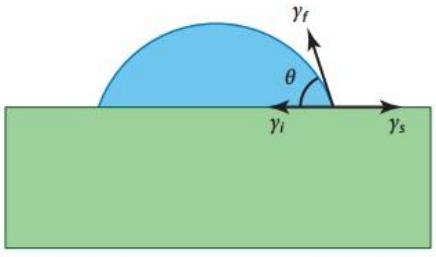

Fig.2.2 Schematic of island shape on the rigid substrate adapted from [6].

$$\gamma_s = \gamma_i + \gamma_f \cos\theta \tag{2.1}$$

Where γ_i is the energy per unit area of the island-substrate interface and θ is the equilibrium contact angle. If $\gamma_s > \gamma_i + \gamma_f$, a film is stable and will not dewet. If this condition is not satisfied, the film will dewet when the rates of the necessary kinetic processes are sufficiently high.

The main driving force for dewetting is minimization of the total energy of the free surfaces of the film and substrate, and of the film-substrate interface. More precisely, from a thermodynamic point of view, dewetting may occur when the driving force defined as

$$E_s = \gamma_A + \gamma_{AB} - \gamma_B \tag{2.2}$$

is positive where γ_A, γ_B γ_{AB} is the surface energy density of substrate, film and film substrate interface. The driving force for dewetting increases as the film thickness decreases. This means that thinner films are more prone to dewetting, and the process occurs more rapidly in thinner films. As a result, the temperature at which dewetting takes place decreases with decreasing film thickness. This behavior allows the precise control of the solid-state dewetting (SSD) process by adjusting key parameters such as annealing temperature, annealing time, and the initial thickness of the precursor films. By carefully tuning these parameters, it becomes possible to achieve nanoparticles with specific, predetermined sizes and spatial distributions. This control is highly advantageous as it eliminates the need for complex and costly lithographic or subtractive processes, providing a more efficient and cost-effective means of nanoparticle fabrication.

SSD is a two step process; first a precursor film is deposited by sputtering/thermal evaporation on a substrate and subsequently post deposition film was annealed under vacuum to grow silver nanoparticles. In this thesis the precursor silver films were deposited on corning glass 1737 substrate using rf sputtering system and post deposition annealing was done in the same system at high vacuum.

2.2.1. Substrate cleaning

The cleaning process for the Corning Glass 1737 substrates involved several steps to ensure its cleanliness before further processing. Here are the steps involved:

- The glass substrates were initially soaked in a soap solution for a duration of 10 minutes. This step was intended to remove any dust or fingerprints present on surface.

- After the soap soak, the glass substrates were rinsed thoroughly with deionized (DI) water. This step helps to remove any soap residue or contaminants from the surface.
- The glass substrates were subjected to ultrasonic wave sonication for a period of 10 minutes. Sonication is an effective method for removing particles and contaminants from the surface of the substrate.
- Following the DI water rinse, the glass substrates were sonicated once more, but this time in isopropanol. Isopropanol is commonly used as a cleaning solvent to ensure the substrate is free from any remaining impurities.
- To complete the cleaning process, the substrates were dried using nitrogen gas. A nitrogen gun was used to blow dry nitrogen gas over the surface of the substrate, ensuring that it was thoroughly dried and free from any residual moisture

2.2.2. RF sputtering technique

Sputtering is a widely used physical vapour deposition (PVD) technology to deposit thin films in a plasma environment. In sputtering process, the ejection of atoms from a solid source target is caused by the bombardment of powerful gas ions. Prior to the deposition procedure, a high vacuum (10^{-6}-10^{-7} mbar) is established within the chamber. During the deposition, a controlled flow of an inert gas, typically Argon (Ar) gas, is injected in chamber. Furthermore, a high voltage is supplied between the cathode and the anode, with the target and the substrate acting as the cathode and anode, respectively. This high voltage excites Ar^+ ions, causing them to accelerate towards the negatively biased target. The target atoms are then ejected when intense Ar^+ ions impact the target surface. Sputtered atoms are deposited on the substrate, forming a thin coating [32]. Secondary electrons are ejected as a result of the intense ion bombardment of the target. To attract secondary electrons to the target, a strong magnetic field is needed. This magnetic field confines the plasma to a small area around the target. Because of their charge neutrality, sputtered atoms are unaffected by the magnetic field [32,33]. For pure metals, DC power supplies are employed, whereas RF power supplies are used for semiconductors and insulators.

RF (13.56 MHz) magnetron sputtering system (EXCEL instruments, Mumbai, India) has been used to deposit the Ag precursor thin films to grow Ag NPs, transparent conducting oxide and metal contact for the solar cells. The schematic of sputtering and real image RF sputtering system is shown in Fig. 2.3. The sputtering chamber is connected to a turbo-molecular pump (TMP) (Pfieffer, HIPAC 300) with a CF100 gate valve between them. The TMP is backed by

a two-stage rotary pump (Pfieffer, PASCAL 2020SD). The target is connected with a RF gun and the substrate holder is attached with a heater.

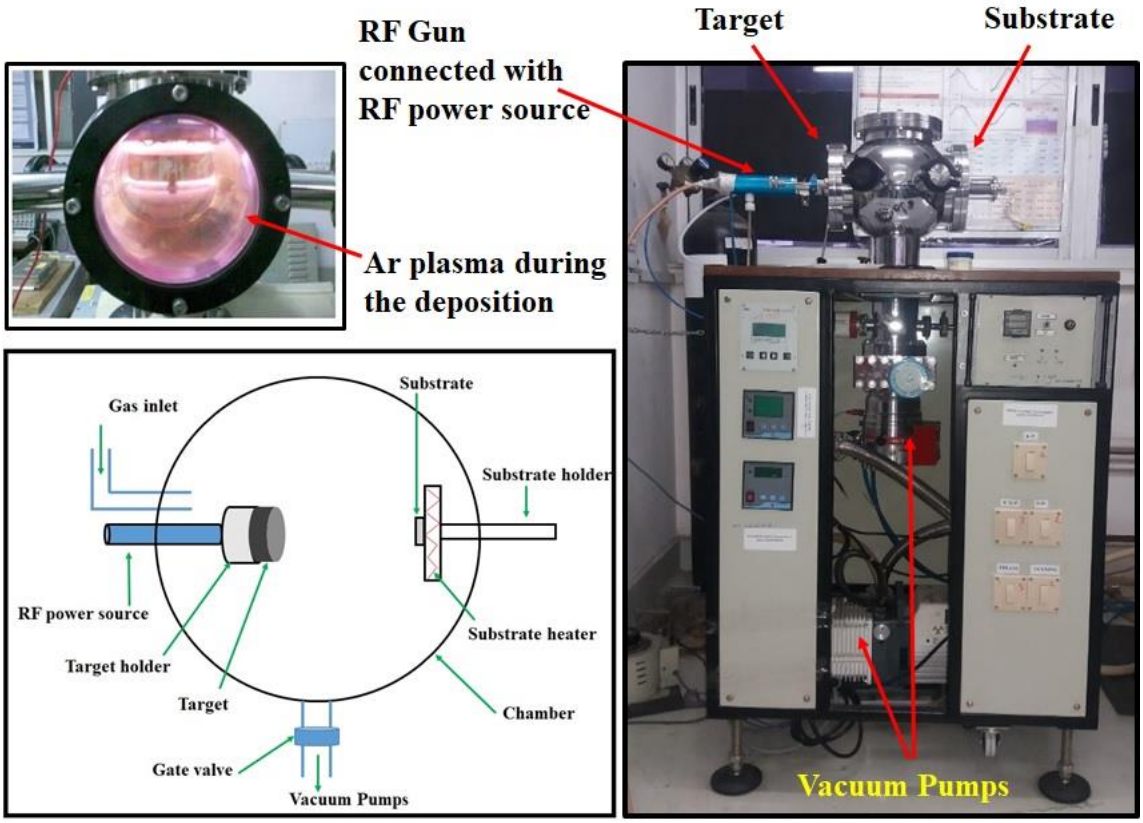

Fig.2.3 Schematic and photograph of RF sputtering system.

After cleaning the substrate, the silver precursor thin films were deposited on corning 1737 glass substrate using RF magnetron sputtering technique. A silver target of 2-inch diameter and 0.125-inch thickness with a purity of 99.99% was used as a sputtering target for the deposition of the silver precursor films. Argon gas with a purity of 99.999% was used as a sputtering gas.

2.3. Fabrication of solar cells

The a-Si:H heterojunction solar cells were fabricated by RF-PECVD in multi-chamber system. The corning glass 1737 substrate (Corning Incorporated, Danville) of 1 mm thickness have been used for cell fabrication.

2.3.1. Radio frequency plasma enhanced chemical vapour deposition technique

Radio frequency plasma-enhanced chemical vapor deposition (RF-PECVD) is a well-established technique and commonly used in the industry for fabricating thin-film amorphous silicon (a-Si:H) based solar cells. In RF-PECVD, a plasma is generated between two parallel plates using a radio frequency (RF) power source, typically operating at a frequency of 13.56

MHz. The two plates serve as electrodes. One electrode is connected to the RF power source, while the other electrode, which holds the substrate, is grounded. A mixture of gases, typically silane (SiH4) and hydrogen (H2), is introduced into the deposition chamber. This gas mixture is the precursor for depositing a-Si:H thin film. The RF power source applies an oscillating electric field between the two parallel plates. This electric field causes the gas in the chamber to become ionized, creating a plasma. Within the plasma, electrons gain sufficient kinetic energy from the electric field to dissociate gas molecules into various species, including free radicals, atoms, positive and negative ions, and additional electrons. The various species generated within the plasma undergo secondary reactions. These reactions can have a significant impact on the electronic and structural properties of the deposited thin film [32,33]. It's in this stage that the chemical reactions responsible for depositing a-Si:H thin films take place. Near the grounded electrode (substrate holder), electrons are easily transported to the electrode surface, creating an electric field region known as the sheath. In this region, positive ions from the plasma are attracted toward the substrate, leading to ion bombardment of the substrate surface. On the substrate surface, surface reactions occur as a result of the ion bombardment and the presence of various species from the plasma. These reactions contribute to the deposition of the a-Si:H thin film. During the deposition process, hydrogen molecules may be released from the film, and the silicon matrix of the a-Si:H thin film undergoes relaxation to form the amorphous structure [32,33].

Radio frequency plasma enhanced chemical vapour deposition (RF-PECVD) (13.56 MHz) multi-chamber system (EXCEL instruments, Mumbai, India) has been used for the fabrication of a-Si:H thin film solar cells. Fig. 2.4 shows the real image of RF-PECVD multi-chamber. The system consists of four stainless steel (SS304 grade) cylindrical chambers. Three of them are dedicated to Plasma-Enhanced Chemical Vapor Deposition (PECVD): one for depositing intrinsic amorphous silicon films, and the other two for depositing n-type and p-type a-Si:H with phosphine and diborane as dopant gases, respectively. These chambers are equipped with CF100 gate valves for isolation. The central chamber serves as both a load lock and Hot Wire Chemical Vapor Deposition (HWCVD) chamber, facilitating substrate transfer between PECVD chambers without breaking the vacuum to prevent contamination. Each process chamber, including the load lock, is connected to a Pfieffer HIPAC 300 turbo-molecular pump (TMP) with gate valves for separation. A Pfieffer PASCAL 2020SD two-stage rotary pump supports the TMPs. The exhaust lines from the rotary pumps lead to a burn box maintained at 700°C to ensure complete burning of residual gases before release into the atmosphere. Burnt

gases are dissolved in soapy water before disposal. To prevent overheating, fans are attached to each TMP, and cold water is supplied to both the TMPs and the burn box. Pressure inside the chambers is monitored using Pirani and Penning gauges to maintain the necessary vacuum conditions for the deposition process. Distinct gas lines are employed for precise control of reactant gas flow rates and mixing during thin film deposition, crucial for achieving high-quality results.

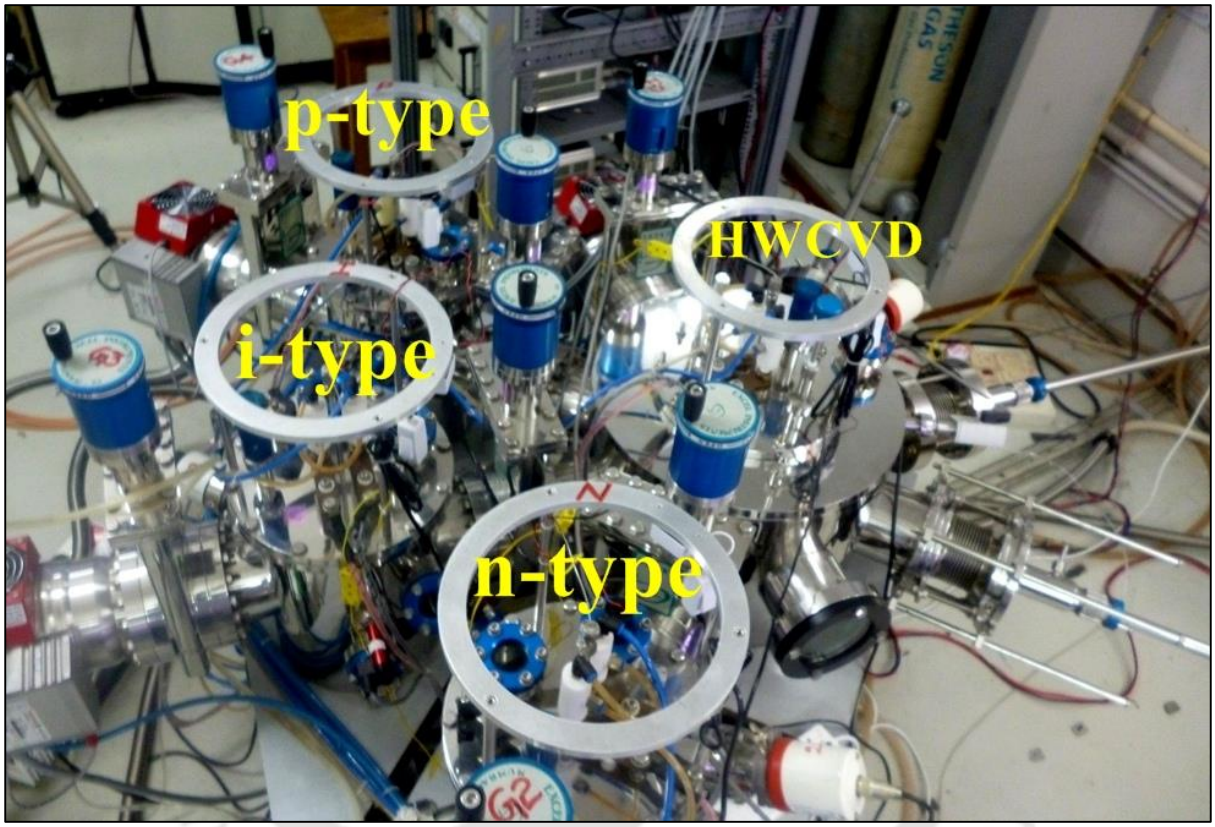

Fig.2.4 Photograph of multi-chamber PECVD system.

a-Si:H thin film solar cells were fabricated on the corning glass substrates with the following structure *corning glass/Ag/AZO/a-Si:H(n)/a-Si:H(i)/a-Si:H(p)/ITO/Ag* using Radio Frequency Plasma Enhanced Chemical Vapor Deposition (RF-PECVD) multi-chamber system. After cleaning the corning glass 1737 substrate, a silver layer of 100 nm thickness was deposited using rf sputtering system. To prevent the diffusion of silver in solar cells, a thin buffer layer of AZO of 40 nm thickness was deposited over the Ag films using rf sputtering system. After that, the n-i-p layer of a-Si:H were fabricated at 180 ^{o}C substrate temperature in different (n), (i), (p) chambers. In addition, for doping, phosphine (PH_3) and diborane (B_2H_6) gases were introduced for a-Si:H(n) layer, and a-Si:H(p) layer. On top of that, 100 nm of ITO layer was deposited using a circular mask of 4 mm diameter (cell area of 0.12 cm^2) by rf sputtering.

Finally, front metal grid electrodes were made on cells with silver paste. All the fabricated solar cells were annealed at 150 ℃ for 1 hour to improve the performance of the solar cells.

2.4. Characterization techniques

The Ag NPs grown using above-mentioned methods were characterized for studying its structural, optical and electrical properties using different experimental techniques described below.

2.4.1 Silver nanoparticle characterization

2.4.1.1 Surface profilometer

The thickness of as-deposited silver precursor films is measured using a surface profilometer. It has a scanning area of tens of millimeters and a vertical range of hundreds of microns to a few nanometers. The measurements in this thesis were taken with a stylus profilometer (Make: Veeco, Model: Dektak 150). Each film's thickness was measured on Corning 1737 glass at three distinct mask sites, and the data were averaged to determine the thickness.

2.4.1.2 Field emission scanning electron microscopy (FESEM)

Field emission scanning electron microscopy (FESEM) (Make: Zeiss Model: Sigma 300) was used to examine the surface morphology of Ag NPs [34]. In this approach, a field emission cathode generates a narrow, high-energy electron beam that is focused on the sample, improving picture resolution. To eliminate charging effects during measurement, FESEM was operated with an accelerating voltage of 2 to 10 KeV. Surface coverage *ImageJ* software was used to determine particle size.

2.4.1.3 Atomic force microscopy (AFM)

Atomic force microscopy (AFM) is one of the useful tool to observe surface topography of the films. AFM consists of a microscale cantilever with a sharp tip at its end that is used to scan the surface of the film. Cantilever is generally made with silicon or silicon nitride. When the tip is brought close to the film surface, the force between film and tip leads to a deflection of the cantilever. The deflection is measured using a laser spot reflected from the top surface of the cantilever into an array of photodiodes. In this thesis, AFM measurements were done on 5μm×5μm square region by atomic force microscope (Make: Oxford, Model: Cypher) with silicon probe (n-type, 0.1-0.4 ohm. cm) to study the dynamic scaling behavior and growth mechanism of as-deposited Ag films and Ag NPs. The cantilever has an Al reflex coating. All the measurements were performed in the non-contact mode in the air with 256 pixel × 256-

pixel resolution at room temperature and relative humidity of 54%. All AFM images were taken using an Olympus Micro Cantilever tip (OMCL-AC160TS-R3) with a spring constant of 26 N/m, resonant frequency of 300 kHz, and a tip radius of 7 nm. Gwyddion software (v 2.60) was used for the AFM data analysis [35].

2.4.1.4 Transmission electron microscopy technique (TEM)

To analyse the structure of the Ag NPs, transmission electron microscopy (TEM) studies were performed. The JEOL-2100 was used to capture TEM, selective area electron diffraction (SAED) patterns, and high resolution TEM (HRTEM) pictures. The Ag NPs structure and crystallinity were determined using TEM in dark field mode with a 200 kV acceleration voltage and LaB6 filament. For measurement, the Ag NPs were grown directly on a copper (Cu) mesh grid. Using ImageJ software, the HRTEM picture was utilised to quantify lattice spacing (d-spacing) of distinct crystallographic planes of Ag NPs [32,34].

2.4.1.5 X-Ray Diffraction (XRD)

A high power X-ray diffractometer (Make: Rigaku Technology, Model: Smart lab, 9 kW) was used to investigate the microstructure of Ag NPs at a wavelength of 1.54 Å of CuK_{α}. XRD analysis was carried out on Ag NPs fabricated on a Corning 1737 glass substrate at a glancing incidence angle ω=0.2° and scan 2θ in the range of 30° to 80° in an angular step of 0.02° steps. The crystallite size in the film was calculated using Scherrer's formula [36,37] (Eq. 2.3) as follows

$$d_{XRD} = \frac{0.9\,\lambda}{\beta_{hkl} cos\theta_{hkl}} \tag{2.3}$$

Where, d_{XRD} is crystallite size, λ is wavelength of X-ray radiation, β_{hkl} is full width at half maxima (FWHM) (in Radians), 0.94 is proportionality constant (scherrer constant) for spherical crystals with cubic symmetry and θ_{hkl} is the peak position corresponding to the (hkl) plane.

2.4.1.6. UV-Vis-NIR spectroscopy

The plasmonic characteristics of metal nanoparticles were studied using UV-Vis-NIR spectroscopy [38]. The absorbance spectra of Ag NPs were measured using a twin beam UV-Vis-NIR spectrometer (Perkin Elmer, Lambda 950) in the 300-1500 nm range. While the reflectance and scattering properties of the Ag NPs were measured using an Universal reflectance accessory (URA) unit and a diffuse reflectance spectroscopy (DRS) unit with an

integrating sphere of 60 nm respectively and, both of them were associated with the UV-Vis-NIR spectrometer.

2.4.1.7 Raman Scattering Spectroscopy

Raman spectroscopy is a non-destructive and extremely powerful instrument for studying a material's vibrational modes in order to discover the crystal structure and many other fundamental features. Raman scattering is an inelastic scattering phenomenon of photons in a material caused by fluctuations such as atomic vibrations, charge density, spin density, and so on. The peaks' positions are connected to inter-atomic forces and distances, as well as their masses and chemical surroundings [39–41]. In this thesis, Raman spectroscopy of Ag NPs on corning glass substrates were done in the range of 200 cm^{-1} to 2000 cm^{-1} using a 514 nm wavelength Ar-ion laser by Laser Micro Raman spectrometer (Horiba Jobin Vyon, LabRam HR). The laser beam's spot size was 1 μm in diameter, and the incidence laser power on the sample was less than 1 mW. These experiments were conducted at room temperature (RT).

2.4.1.8. Photoluminescence (PL) spectroscopy

Photoluminescence (PL) is a non-destructive, contactless method for determining the electrical structure of a material. The incoming light is absorbed by the material in PL spectroscopy, and then photoexcitation occurs, followed by relaxation and photon emission [42,43]. The emitted spectrum is collected by a charge coupled device (CCD) camera for each studied location on the sample. To capture the PL data in this thesis, a Fluorescence Spectrophotometer (Horiba, Fluoromax-4C) coupled with a Xenon lamp was employed. At room temperature, the photoluminescence emission spectra of Ag NPs grown on corning glass were recorded using an excitation wavelength of 320 nm.

2.4.1.9. Spectroscopic ellipsometry (SE)

Spectroscopic ellipsometry (SE) is a non-destructive and highly accurate powerful optical technique used to investigate the optical properties and determine various parameters of thin films, such as thickness, refractive index, and surface roughness, with high precision. The technique relies on measuring the change in the polarization state of light after it reflects from a sample's surface. The unpolarized light coming from Xenon lamp is passed through a polarizer, which linearly polarizes the light. Linear polarization means that the oscillations of the electric field of the light occur in a specific direction. The linearly polarized light is directed onto the surface of the sample under investigation. Some of the incident light gets reflected

from the surface of the sample, and some of it penetrates the sample, interacting with various interfaces within the film. The light that is reflected from the surface and interfaces of the sample undergoes changes in both amplitude and phase, leading to elliptical polarization. This means that the orientation of the electric field vector of the light changes as it interacts with the sample. The elliptically polarized light is then directed to a detector, which measures its properties, including changes in phase and amplitude. Two compensators are used in SE to adjust the phase delay of the light. The schematic of SE and spectroscopic ellipsometer instrument (Semilab, Sopra, GES-5E) used for the studies are shown in Fig. 2.5 and 2.6 respectively.

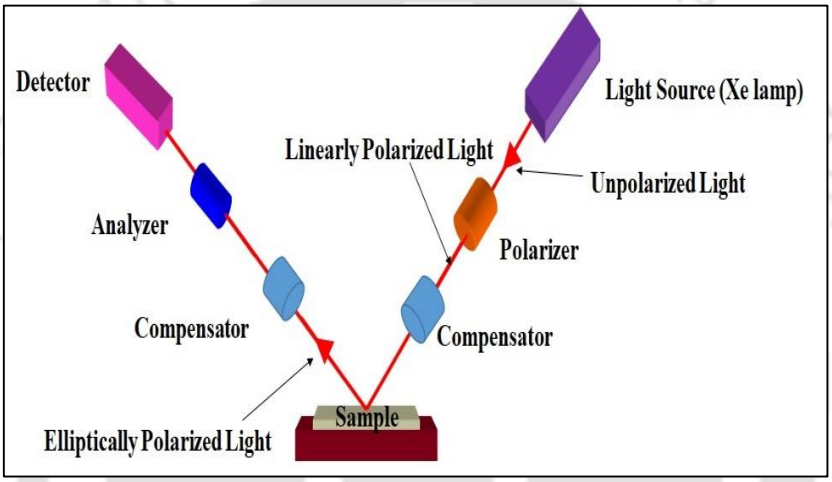

Fig.2.5 Schematic of the ellipsometry spectroscopy measurement technique.

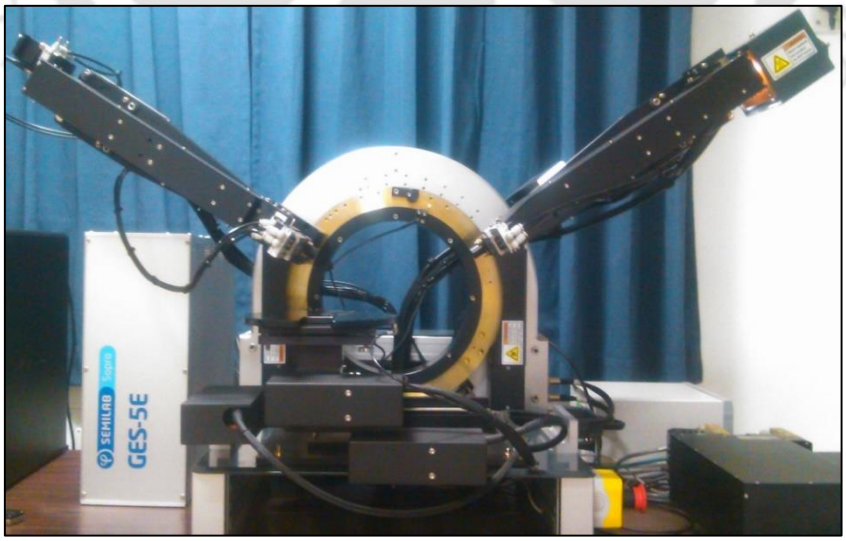

Fig.2.6 Photograph of spectroscopic ellipsometry system.

Ellipsometry measures the polarization change ρ which is the ratio of reflectance of p polarized (r_p) and s polarized (r_s) light [44]

$$\rho = \frac{r_p}{r_s} = (\tan\psi)e^{i\Delta} \tag{2.4}$$

With amplitude ratio $\tan\psi$ and the phase difference $\Delta = \phi_p - \phi_s$.

The pseudo dielectric function ($< \varepsilon >$) of material is directly related to the ρ and can be drived from the ellipsometry measurement using Fresnel's equation and is given by Eq.2.5 [44]

$$< \varepsilon > = < \varepsilon_1 > + i < \varepsilon_2 > = \sin^2(\theta_0)\left[1 + \left(\frac{1-\rho}{1+\rho}\right)^2 \tan^2(\theta_0)\right] \tag{2.5}$$

Where ε_1 and ε_2 are real and imaginary parts of the pseudo dielectric function and θ_0 is the angle of the incidence. The pseudo dielectric function is therefore directly determined from the measurement of the ψ and Δ using equations (2.4). The pseudo dielectric function relates to the complex refractive index through

$$N = n + ik = \sqrt{\varepsilon} \tag{2.6}$$

where n and k are the refractive index and extinction coefficient respectively.

In the present thesis, spectroscopic ellipsometry (SE) measurements were done in the photon energy range of 1.0 - 4.5 eV at an incidence angle of 60° by spectroscopic ellipsometer (Semilab SOPRA, GES-5E). The spot size of The spectroscopy ellipsometry analyzer (SEA v1.5.26) software was used to analyze the SE data. This software uses a standard regression based Levenberg-Marquardt algorithm (LMA) to minimize the value of the root means square error (RMSE). RMSE which should be the least for the best fitting, can be defined as [44]

$$RMSE = \sqrt{\frac{1}{2N-M}\sum_{i=1}^{N}\left[\left(\frac{f_{1,meas}^{i} - f_{1,calc}^{i}}{\sigma_{1,meas}^{i}}\right)^2 w_1 + \left(\frac{f_{2,meas}^{i} - f_{2,calc}^{i}}{\sigma_{2,meas}^{i}}\right)^2 w_2\right]} \tag{2.5}$$

Where N is the number of measured data points, M is the number of fitted model parameters, $f_{1,meas}^{i}$ and $f_{1,calc}^{i}$ are the i^{th}measured and calculated ellipsometric quantities which was taken from the set of ($< \varepsilon_1 >, < \varepsilon_2 >$), $\sigma_{1,meas}^{i}$ and $\sigma_{2,meas}^{i}$ are pointwise experimental error belongings to the i^{th} $f_1$and f_2 measurements, w_1 and w_2 are user-defined weight factors.

The dielectric, plasmonic properties, and roughness of the Ag NPs films are deduced from measured (ψ, Δ) values as a function of energy applying suitable optical models using single

or multilayer structures having minimum RMSE value. The best fitted model and the structure are described in chapter 4.

2.4.2 Solar cell characterization

2.4.2.1 Current density (*J*) – Voltage (*V*) measurement

The electrical performance of the fabricated a-Si:H solar cells was assessed through current density-voltage (J-V) characteristic measurements under standard testing conditions (AM 1.5G, 100 mW/cm^2) using a solar simulator (Make: Sciencetech, Model: SL-50A-WS) and Keithley 2450 source meter controlled by a computer to provide voltage sweeps and record the corresponding current. Current density-voltage characteristic of solar cell is illustrated in Fig. 2.7.

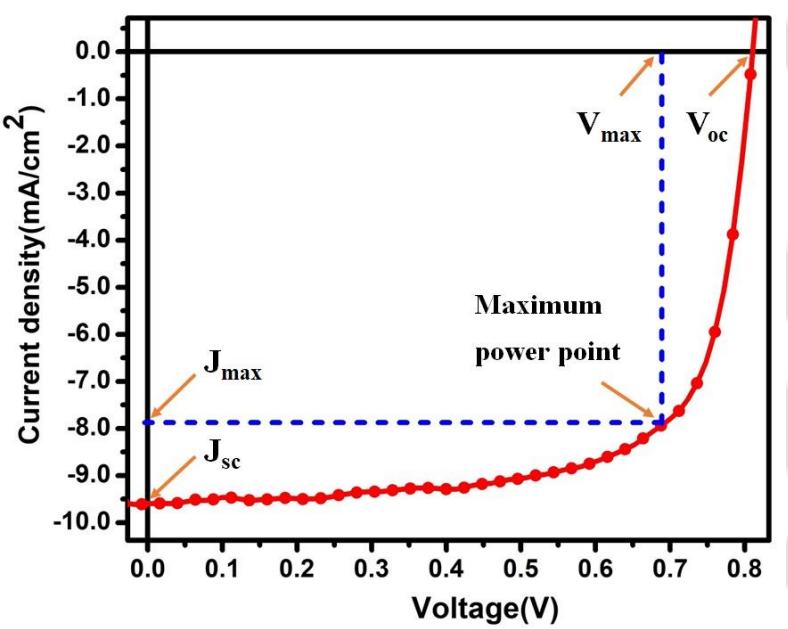

Fig. 2.7 Current density- Voltage (*J-V*) curve of a-Si:H thin film solar cell.

From the *J-V* curve, short-circuit current density (J_{sc}), open-circuit voltage (V_{oc}) and fill factor (*FF*) are obtained. The solar cell efficiency (η) is defined as the ratio of maximum electrical energy output to the incident solar energy on the cell. The η (%) is determined by the following Eq. 2.7. [33,45,46]

$$\eta\,(\%) = \frac{J_{sc} \times V_{oc} \times FF}{P_{in}} \times 100 \qquad (2.7)$$

$$\text{where} \quad FF = \frac{J_{\max} \times V_{\max}}{J_{sc} \times V_{oc}}$$

where J_{sc}, V_{oc}, FF and P_{in} are short-circuit current density, open-circuit voltage, fill factor and input power. The V_{oc} is the voltage at which no current flows through the external circuit; that is at $J = 0$. On the other hand, J_{sc} is current density at which voltage drop is zero across the solar cell. The FF is the ratio of the maximum power that can be obtained from the cell to the product of J_{sc} and V_{oc}. It is a measure of 'squareness' of the J-V curve and describes the operating point at which the solar cell gives maximum power to the attached load.

2.4.2.2 External quantum efficiency (*EQE*)

External quantum efficiency (EQE) tests were carried out in the wavelength range 300-900 nm at room temperature utilizing an in house built dual beam setup. The schematic diagram of the quantum efficiency measurement apparatus is shown in Fig. 2.8. The system's initial component, the light source for the EQE measurements, was a xenon lamp fed through a monochromator (Horiba Jovin Yvon-Triax). Before taking any measurements, the lamp was turned on for at least 30 minutes. This was shown to be adequate for producing a steady current output from an a-Si: H solar cell. The incident beam was separated into two beams using a beam splitter, one for the reference calibrated diode and the other for the solar cell. To achieve optimal alignment, optical lenses were utilized during measurements to focus the light from the monochromator onto the reference photodiode and solar cell. The incision width was kept constant at 3 mm in diameter. When the sample was exposed to light at longer wavelengths, second order filters with cutoff wavelengths of 400 nm and 610 nm were utilized to prevent second harmonics. An optical chopper (Stanford Research Systems Model SR540) was utilised to disrupt the light beam on a regular basis. To accurately maintain the chopping speed and phase relative to the reference signal, the controller employs a phase locked loop motor speed control architecture. A chopper was put in front of the monochromator entry slit in our measurement. We employed a 6-slot blade set with a 17-Hz chopper frequency. Two lock-in amplifiers (Stanford Research Systems Model SR-810) were connected to the optical chopper outputs. One lock-in amplifier was linked to the reference photodiode, while the other was linked to the solar cell. A lock-in amplifier monitors a single output, a signal component at a defined reference frequency. Noise signals at frequencies other than the reference frequency are disregarded, and the measurements are unaffected. The LabVIEW programme was used to operate the monochromator, two lock-in amplifiers, and the output signals from the reference diode and solar cell in terms of volts through a general purpose interface bus (GPIB) card and wires [47–49].

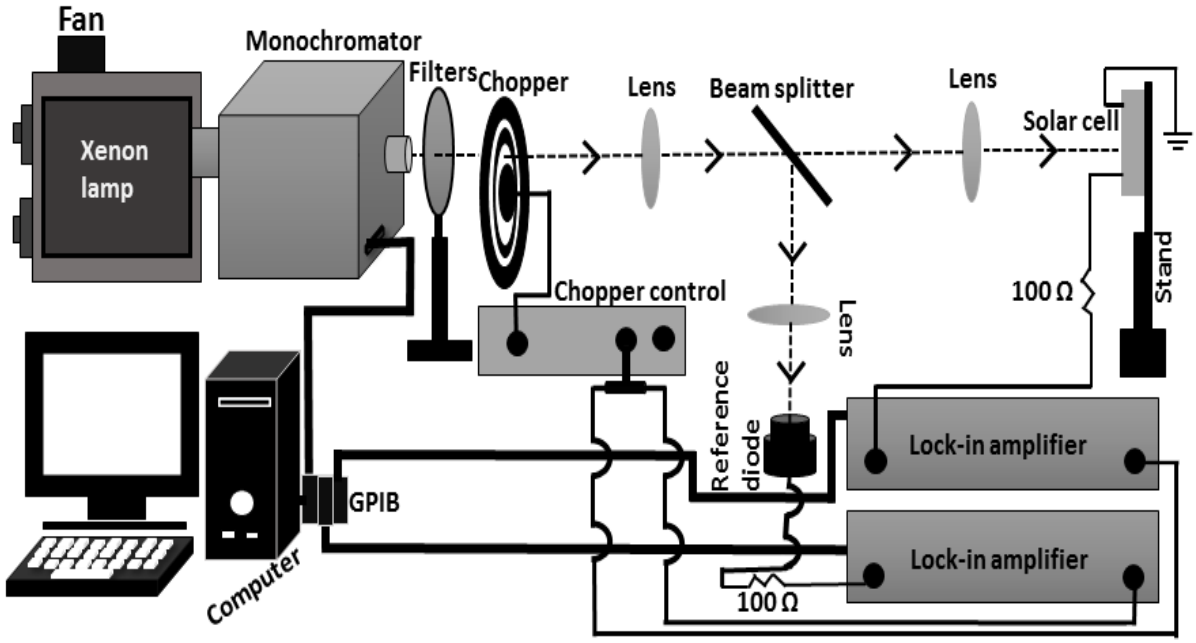

Fig.2.8 Schematic of external quantum efficiency setup.

External quantum efficiency can be obtained from Eq. 2.8

$$EQE\ (\%) = \frac{h \times c}{q \times \lambda} \times SR_{cell} \times 100 \tag{2.8}$$

where h,c,q,λ and SR_{cell} are planks constant, velocity of light, charge of electron, wave length of light and spectral response of the measured solar cell respectively.

Spectral response of the measured solar cell can be obtained from the following Equation 2.9

$$SR_{cell} = SR_{ref} \times \left(\frac{V_{cell}}{V_{std}}\right) \times \left(\frac{V_{ref/std}}{V_{ref/cell}}\right) \tag{2.9}$$

where SR_{ref}, V_{cell}, V_{std}, $V_{ref/std}$ and $V_{ref/cell}$ are respectively the spectral response of standard diode, voltage of the test cell, voltage of a standard diode, reference diode voltage when standard diode voltage was measured and reference diode voltage when test cell voltage respectively.

The short circuit current density of solar cells estimated from EQE is given by Eq.2.10 [33,50]

$$J_{sc} = \int_{\lambda}^{\lambda+\Delta\lambda} b_s EQE(\lambda) d\lambda \tag{2.10}$$

Where b_s is incident spectral photon flux density, λ is wavelength.

2.5. Simulation details of hydrogenated amorphous silicon (a-Si:H) thin film solar cells using AFORS-HET software

The single junction n-i-p hydrogenated amorphous silicon (a-Si:H) thin film solar cells were simulated using well-practiced AFORS-HET (Automated For Simulation of Heterostructure, v 2.5) software developed by Helmholtz- Zentrum Berlin (HZB) to accurately evaluate the effect of various parameters on solar cells performance [51–54]. Fig. 2.9 shows the input window of the AFORS-HET software. AFORS-HET software is a handy tool for modeling homojunction and heterojunction solar cells. This software solves 1-D Poisson's equation and the continuity equation for the electrons and holes using Shockley-Read-Hall (SRH) recombination statistics [55–57]. Also, the e-h generation in the absorber layer is estimated with the Beer-Lambert absorption equation using the optical model in the AFORS-HET. Moreover, the AFORS-HET simulator is good enough for an amorphous structure since it considers different types of defects in materials and also at interfaces between different layers. Each layer consists of band tail defect states described as conduction and valance band tails with exponential distribution while mid band dangling bond defect states described as acceptor-like dangling bond and donor-like dangling bond with Gaussian distribution.

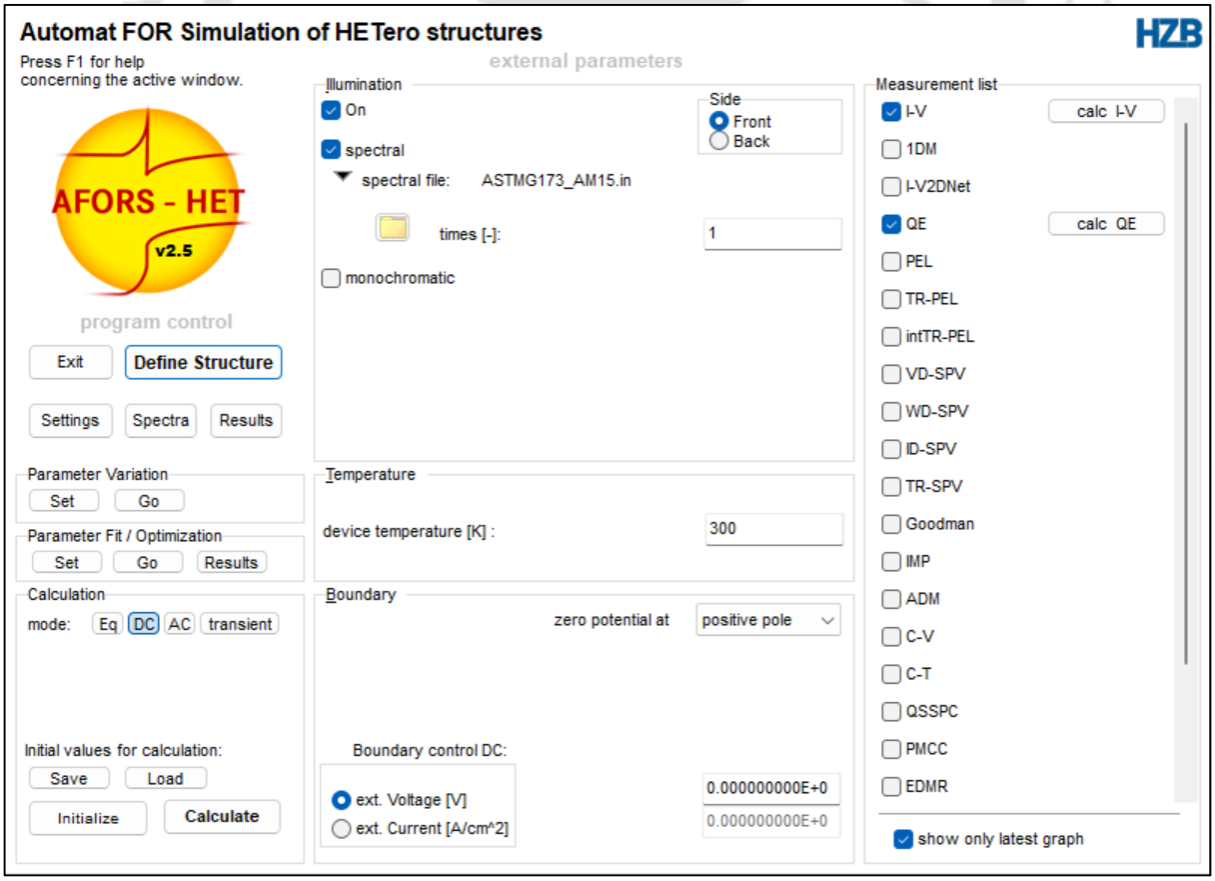

Fig.2.9. Afors-HET input window to define the structure and perform the measurement.

Throughout the optimization, flat band was chosen as a front and back contact. No front and back surface texturing was done. The surface recombination velocity of electrons and holes was set 10^7 cm/s. The global radiation AM 1.5 spectrum with an incident power density of 100 mW/cm^2 was used as the illuminating source in the present simulation, while the operational temperature was 300K.

2.6. References

[1] A. Serrano, O. Llorca-Hernando, A. Del Campo, F. Rubio-Marcos, O. Rodríguez de La Fuente, J.F. Fernández, M.A. García, Ag-AgO nanostructures on glass substrates by solid-state dewetting: From extended to localized surface plasmons, J. Appl. Phys. 124 (2018). https://doi.org/10.1063/1.5049651.

[2] A. Araújo, M.J. Mendes, T. Mateus, A. Vicente, D. Nunes, T. Calmeiro, E. Fortunato, H. Águas, R. Martins, Influence of the Substrate on the Morphology of Self-Assembled Silver Nanoparticles by Rapid Thermal Annealing, J. Phys. Chem. C. 120 (2016) 18235–18242. https://doi.org/10.1021/acs.jpcc.6b04283.

[3] P. Herre, J. Will, M. Dierner, D. Wang, T. Yokosawa, T. Zech, M. Wu, T. Przybilla, S. Romeis, T. Unruh, W. Peukert, E. Spiecker, Rapid fabrication and interface structure of highly faceted epitaxial Ni-Au solid solution nanoparticles on sapphire, Acta Mater. 220 (2021) 117318. https://doi.org/https://doi.org/10.1016/j.actamat.2021.117318.

[4] A. Serrano, J. Rubio-Zuazo, J. López-Sánchez, E. Enríquez, E. Salas-Cólera, G.R. Castro, Nanostructured Au(111)/Oxide Epitaxial Heterostructures with Tailoring Plasmonic Response by a One-Step Strategy, J. Phys. Chem. C. 123 (2019) 25294–25302. https://doi.org/10.1021/acs.jpcc.9b04768.

[5] J.A. Badán, E. Navarrete-Astorga, R. Henríquez, F.M. Jiménez, D. Ariosa, J.R. Ramos-Barrado, E.A. Dalchiele, Silver Nanoparticle Arrays onto Glass Substrates Obtained by Solid-State Thermal Dewetting: A Morphological, Structural and Surface Chemical Study, Nanomaterials. 12 (2022). https://doi.org/10.3390/nano12040617.

[6] C. V. Thompson, Solid-state dewetting of thin films, Annu. Rev. Mater. Res. 42 (2012) 399–434. https://doi.org/10.1146/annurev-matsci-070511-155048.

[7] M.T. Sultan, A. Manolescu, H.G. Svavarsson, A. Valfells, Solid-state dewetting of

silver-thin films : self- assembled nano-geometries Solid-state dewetting of silver-thin fi lms : self-assembled nano- geometries, (2020).

[8] J. Ye, D. Zuev, S. Makarov, Dewetting mechanisms and their exploitation for the large-scale fabrication of advanced nanophotonic systems, Int. Mater. Rev. 64 (2019) 439–477. https://doi.org/10.1080/09506608.2018.1543832.

[9] A. Le Bris, F. Maloum, J. Teisseire, F. Sorin, Self-organized ordered silver nanoparticle arrays obtained by solid state dewetting, Appl. Phys. Lett. 105 (2014) 203102. https://doi.org/10.1063/1.4901715.

[10] P. Jacquet, R. Podor, J. Ravaux, J. Lautru, J. Teisseire, I. Gozhyk, J. Jupille, R. Lazzari, On the solid-state dewetting of polycrystalline thin films: Capillary versus grain growth approach, Acta Mater. 143 (2018) 281–290. https://doi.org/https://doi.org/10.1016/j.actamat.2017.08.070.

[11] R. Liu, F. Zhang, C. Con, B. Cui, B. Sun, Lithography-free fabrication of silicon nanowire and nanohole arrays by metal-assisted chemical etching, Nanoscale Res. Lett. 8 (2013) 155. https://doi.org/10.1186/1556-276X-8-155.

[12] P. Jacquet, R. Podor, J. Ravaux, J. Teisseire, I. Gozhyk, J. Jupille, R. Lazzari, Grain growth: The key to understand solid-state dewetting of silver thin films, Scr. Mater. 115 (2016) 128–132. https://doi.org/https://doi.org/10.1016/j.scriptamat.2016.01.005.

[13] S. Kunwar, M. Sui, Q. Zhang, P. Pandey, M.-Y. Li, J. Lee, Various Silver Nanostructures on SapphireUsing Plasmon Self-Assembly and Dewetting of Thin Films, Nano-Micro Lett. 9 (2016) 17. https://doi.org/10.1007/s40820-016-0120-6.

[14] B. Legrand, V. Agache, T. Mélin, J.P. Nys, V. Senez, D. Stiévenard, Thermally assisted formation of silicon islands on a silicon-on-insulator substrate, J. Appl. Phys. 91 (2002) 106–111. https://doi.org/10.1063/1.1420761.

[15] B. Legrand, V. Agache, J.P. Nys, V. Senez, D. Stievenard, Formation of silicon islands on a silicon on insulator substrate upon thermal annealing, Appl. Phys. Lett. 76 (2000) 3271–3273. https://doi.org/10.1063/1.126603.

[16] M. Łapiński, R. Kozioł, A. Cymann, W. Sadowski, B. Kościelska, Substrate Dependence in the Formation of Au Nanoislands for Plasmonic Platform Application,

Plasmonics. 15 (2020) 101–107. https://doi.org/10.1007/s11468-019-01021-9.

[17] A.N. Chaika, S.I. Bozhko, A.M. Ionov, I. Sveklo, E.Y. Postnova, V.N. Semenov, A. Bisht, E. Rabkin, The role of defects in solid state dewetting of ultrathin Ag film on Si(557), Scr. Mater. 194 (2021) 113655. https://doi.org/https://doi.org/10.1016/j.scriptamat.2020.113655.

[18] F. Ruffino, M.G. Grimaldi, Nano-shaping of gold particles on silicon carbide substrate from solid-state to liquid-state dewetting, Surfaces and Interfaces. 24 (2021) 101041. https://doi.org/https://doi.org/10.1016/j.surfin.2021.101041.

[19] M. Berni, I. Carrano, A. Kovtun, A. Russo, A. Visani, C. Dionigi, A. Liscio, F. Valle, A. Gambardella, Monitoring morphological and chemical properties during silver solid-state dewetting, Appl. Surf. Sci. 498 (2019) 143890. https://doi.org/https://doi.org/10.1016/j.apsusc.2019.143890.

[20] H.K. Lin, C.W. Huang, Y.H. Lin, W.S. Chuang, J.C. Huang, Effects of Accumulated Energy on Nanoparticle Formation in Pulsed-Laser Dewetting of AgCu Thin Films, Nanoscale Res. Lett. 16 (2021) 110. https://doi.org/10.1186/s11671-021-03564-5.

[21] Y.-H. Lin, J.-J. Wang, Y.-T. Wang, H.-K. Lin, Y.-J. Lin, Antifungal Properties of Pure Silver Films with Nanoparticles Induced by Pulsed-Laser Dewetting Process, Appl. Sci. 10 (2020). https://doi.org/10.3390/app10072260.

[22] S. Yadavali, R. Kalyanaraman, Fabricating Metal Nanostructures with Pulsed Laser Dewetting Self-Assembly, Adv. Mater. Process. 171 (2013) 22–26. https://doi.org/10.31399/asm.amp.2013-07.p022.

[23] H. Oh, A. Pyatenko, M. Lee, A hybrid dewetting approach to generate highly sensitive plasmonic silver nanoparticles with a narrow size distribution, Appl. Surf. Sci. 542 (2021) 148613. https://doi.org/https://doi.org/10.1016/j.apsusc.2020.148613.

[24] X. Hu, D.G. Cahill, R.S. Averback, Nanoscale pattern formation in Pt thin films due to ion-beam-induced dewetting, Appl. Phys. Lett. 76 (2000) 3215–3217. https://doi.org/10.1063/1.126633.

[25] X. Hu, D.G. Cahill, R.S. Averback, R.C. Birtcher, In situ transmission electron microscopy study of irradiation induced dewetting of ultrathin Pt films, J. Appl. Phys.

93 (2002) 165–169. https://doi.org/10.1063/1.1527712.

[26] Y. Kojima, T. Kato, Nanoparticle formation in Au thin films by electron-beam-induced dewetting, Nanotechnology. 19 (2008) 255605. https://doi.org/10.1088/0957-4484/19/25/255605.

[27] G. Rusciano, A. Capaccio, A. Martinez, A. Sasso, Nanoporous silver films produced by solid-state dewetting for SERS applications, 2021. https://doi.org/10.1117/12.2592391.

[28] R. Nuryadi, Y. Ishikawa, Y. Ono, M. Tabe, Thermal agglomeration of single-crystalline Si layer on buried SiO2 in ultrahigh vacuum, J. Vac. Sci. Technol. B Microelectron. Nanom. Struct. Process. Meas. Phenom. 20 (2002) 167–172. https://doi.org/10.1116/1.1431956.

[29] D. Gentili, G. Foschi, F. Valle, M. Cavallini, F. Biscarini, Applications of dewetting in micro and nanotechnology, Chem. Soc. Rev. 41 (2012) 4430–4443. https://doi.org/10.1039/c2cs35040h.

[30] J. Ye, D. Zuev, S. Makarov, Dewetting mechanisms and their exploitation for the large-scale fabrication of advanced nanophotonic systems, Int. Mater. Rev. 64 (2019) 439–477. https://doi.org/10.1080/09506608.2018.1543832.

[31] F. Spaepen, Substrate curvature resulting from the capillary forces of a liquid drop, J. Mech. Phys. Solids. 44 (1996) 675–681. https://doi.org/https://doi.org/10.1016/0022-5096(96)00005-1.

[32] M. Ohring, Materials Science of Thin Films, Second Edition, 2001.

[33] A. Shah, Thin-film silicon solar cells, EPFL press, 2010.

[34] I. Khan, K. Saeed, I. Khan, Nanoparticles: Properties, applications and toxicities, Arab. J. Chem. 12 (2019) 908–931. https://doi.org/10.1016/j.arabjc.2017.05.011.

[35] M. Pelliccione, T.-M. Lu, Evolution of Thin Film Morphology: Modeling and Simulations, 2008. https://doi.org/10.1007/978-0-387-75109-2.

[36] E. Atkins, Elements of X-ray Diffraction, Phys. Bull. 29 (1978) 572. https://doi.org/10.1088/0031-9112/29/12/034.

[37] A.L. Patterson, The Scherrer Formula for X-Ray Particle Size Determination, Phys. Rev.

56 (1939) 978–982. https://doi.org/10.1103/PhysRev.56.978.

[38] S. Morawiec, M.J. Mendes, S. Mirabella, F. Simone, F. Priolo, I. Crupi, Self-assembled silver nanoparticles for plasmon-enhanced solar cell back reflectors: correlation between structural and optical properties, Nanotechnology. 24 (2013) 265601. https://doi.org/10.1088/0957-4484/24/26/265601.

[39] K. Chaudhari, T. Ahuja, V. Murugesan, V. Subramanian, M.A. Ganayee, T. Thundat, T. Pradeep, Appearance of SERS activity in single silver nanoparticles by laser-induced reshaping, Nanoscale. 11 (2019) 321–330. https://doi.org/10.1039/C8NR06497K.

[40] X. Xie, H. Pu, D.-W. Sun, Recent advances in nanofabrication techniques for SERS substrates and their applications in food safety analysis, Crit. Rev. Food Sci. Nutr. 58 (2018) 2800–2813. https://doi.org/10.1080/10408398.2017.1341866.

[41] K. Kamakshi, K.C. Sekhar, A. Almeida, J. Agostinho Moreira, M.J.M. Gomes, Tuning the surface plasmon resonance and surface-enhanced Raman scattering of pulsed laser deposited silver nanoparticle films by ambience and deposition temperature, J. Opt. 16 (2014) 55002. https://doi.org/10.1088/2040-8978/16/5/055002.

[42] M. Manoth, K. Manzoor, M.K. Patra, P. Pandey, S.R. Vadera, N. Kumar, Dendrigraft polymer-based synthesis of silver nanoparticles showing bright blue fluorescence, Mater. Res. Bull. 44 (2009) 714–717. https://doi.org/10.1016/j.materresbull.2008.06.033.

[43] O.A. Yeshchenko, I.S. Bondarchuk, M.Y. Losytskyy, Surface plasmon enhanced photoluminescence from copper nanoparticles: Influence of temperature, J. Appl. Phys. 116 (2014). https://doi.org/10.1063/1.4892432.

[44] H. Fujiwara, Spectroscopic Ellipsometry: Principles and Applications, 2007. https://doi.org/10.1002/9780470060193.

[45] J.L. Gray, The Physics of the Solar Cell, in: Handb. Photovolt. Sci. Eng., 2010: pp. 82–129. https://doi.org/https://doi.org/10.1002/9780470974704.ch3.

[46] A. Luque, S. Hegedus, Handbook of Photovoltaic Science and Engineering, 2011. https://doi.org/10.1002/9780470974704.

[47] D. Berrian, M. Fathi, M. Kechouane, Numerical Optimization of a Bifacial Bi-Glass

Thin-Film a-Si:H Solar Cell for Higher Conversion Efficiency, J. Electron. Mater. 47 (2018) 1140–1150. https://doi.org/10.1007/s11664-017-5828-7.

[48] R. Madaka, V. Kanneboina, P. Agarwal, Enhanced performance of amorphous silicon solar cells (110 °c) on flexible substrates with a-SiC:H(p) window layer and H2 plasma treatment at n/i and i/p interface, Semicond. Sci. Technol. 33 (2018). https://doi.org/10.1088/1361-6641/aac8ca.

[49] R. Madaka, V. Kanneboina, P. Agarwal, Low-Temperature Growth of Amorphous Silicon Films and Direct Fabrication of Solar Cells on Flexible Polyimide and Photo-Paper Substrates, J. Electron. Mater. 47 (2018) 4710–4720. https://doi.org/10.1007/s11664-018-6344-0.

[50] H. Antonio, S. Hegedus, Handbook of photovoltaic science and engineering, Willey. (2003). https://doi.org/10.1002/9780470974704.

[51] R.A. Stangl, a numerical computer program for simulation of (thin film) heterojunction solar cells, (2014) 1–3.

[52] R. Stangl, C. Leendertz, J. Haschke, Numerical Simulation of Solar Cells and Solar Cell Characterization Methods: the Open-Source on Demand Program AFORS-HET, 2010. https://doi.org/10.5772/8073.

[53] R. Stangl, C. Leendertz, General Principles of Solar Cell Simulation and Introduction to AFORS-HET BT - Physics and Technology of Amorphous-Crystalline Heterostructure Silicon Solar Cells, in: W.G.J.H.M. van Sark, L. Korte, F. Roca (Eds.), Springer Berlin Heidelberg, Berlin, Heidelberg, 2012: pp. 445–458. https://doi.org/10.1007/978-3-642-22275-7_13.

[54] R. Varache, C. Leendertz, M.E. Gueunier-Farret, J. Haschke, D. Muñoz, L. Korte, Investigation of selective junctions using a newly developed tunnel current model for solar cell applications, Sol. Energy Mater. Sol. Cells. 141 (2015) 14–23. https://doi.org/10.1016/j.solmat.2015.05.014.

[55] A. Belfar, B. Amiri, H. Aït-kaci, Optimization of band gap and thickness for the development of efficient n-i-p+ solar cell, J. Nano- Electron. Phys. 7 (2015) 1–7.

[56] S. Singh, S. Kumar, N. Dwivedi, Band gap optimization of p-i-n layers of a-Si:H by

computer aided simulation for development of efficient solar cell, Sol. Energy. 86 (2012) 1470–1476. https://doi.org/10.1016/j.solener.2012.02.007.

[57] M. Sharma, S. Kumar, N. Dwivedi, S. Juneja, A.K. Gupta, S. Sudhakar, K. Patel, Optimization of band gap, thickness and carrier concentrations for the development of efficient microcrystalline silicon solar cells: A theoretical approach, Sol. Energy. 97 (2013) 176–185. https://doi.org/10.1016/j.solener.2013.08.012.

Chapter 3

Growth dynamics of silver thin films and nanoparticles and its correlation with plasmonic properties of silver nanoparticles

3.1. Introduction

The surface morphology of thin films has a considerable influence on its optical, mechanical, and electrical properties [1–3]. The surface roughness of thin films affects the performance of the optical devices, plasmonic devices, biological sensor and solar cells [4]. In the solar cells, the surface roughness of thin films controls the fraction of incident light in the absorber layer, which influences the efficiency of solar cell [5]. Though the increase in front surface roughness decreases the conversion efficiency of solar cell [6,7], it has been shown that more rough surface is desirable to enhance the diffuse light reflection at back contact electrode of the thin film photovoltaic devices [8]. The textured back reflector in thin film solar cells enhances the optical path length of incident light within the absorber layer and consequently increases the photocurrent and efficiency [2,9]. Therefore, the importance of surface morphology cannot be ignored and it is necessary to study the surface properties of the thin films before the actual device fabrication. The morphology of thin films and the nanostructures strongly depend on the deposition method (chemical method and physical method) and growth condition [10,11] and the final structure depends upon the mechanism of its formation [12] which influence the optical properties of the nanostructure materials[13]. The nanoparticles of the noble metals (Ag, Au, Cu) exhibit the localized surface plasmon resonance (LSPR) properties which is useful for surface enhanced Raman spectroscopy, sensor, solar cells etc. [14–20]. The LSPR properties of the metallic nanostructures strongly depend upon the shape and size of the nanoparticles and other related parameters e.g., roughness, correlation length and the film growth mechanism etc. [21–23]. The surface roughness of the film and the nanostructure also affect the LSPR properties [24–26]. These properties of surface boost

the interest for surface evolution study to obtain a better understanding of the essential growth process of metallic nanomaterials and help to fabricate nanostructures with desirable properties in a controlled way.

In the last few decades, the interest to study growth dynamics of the films and its dependency on the deposition process, parameters and the post deposition processing has increased for potential nanotechnology applications. Research work, both experimental and theoretical have been reported on the growth of thin films and the nanostructures using different methods based on the statistical analysis [27–35]. Several analyses like steriometric, kinetic roughening, fractal, and multifractal have been carried out by the researchers to characterize the thin film surfaces [36–41]. Beside these analysis, Height-height correlation function and power spectral density function with advance data analysis are generally used to perform quantitative study of the surfaces using a dynamic scaling methods [38,39,42]. For this purpose, Atomic Force Microscopy (AFM) is considered a suitable tool to describe the surface characteristic from the AFM images. AFM technique provides real space imaging and can be employed to characterize surface and its growth kinetics which is involved in the growth mechanism [43–46]. The analysis of surface morphology provides the information of its scaling behavior and growth model which is helpful for better understanding of the growth mechanism and also helps in correlating the morphological properties with the optical properties of the thin films and nanostructure materials [1,31–33,47,48].

As discussed in the chapter 1 and 2, several methods have been reported to synthesize the Ag NPs [49–53]. The solid state dewetting (SSD) is a physical method commonly used for the growth of the nanoparticles. In SSD a thin film is transformed into an array of droplets or nanoparticles by the thermal annealing [54]. Moreover, in this method, the size of the nanoparticles can be controlled more effectively and reproducibly on a large scale for Nano photonics, Nano electronics, plasmonics and photovoltaic devices [53].

With this motivation, in this chapter, we have investigated the growth dynamics of silver nanoparticles, grown onto the corning glass 1737 substrate by solid state dewetting of the silver precursor films, and correlated the growth dynamics with the evolution of optical properties of silver nanoparticles. AFM characterization with advanced data analysis is used to describe the surface characteristics. The height-height correlation function and power spectral density function are extracted from AFM images for the calculation of scaling exponents; local roughness exponent

(α_{local}), growth exponents (β), dynamic exponent ($1/z$), and global roughness exponent (α) and to know the scaling behavior and growth model of the surface. The microstructure of the Ag NPs was probed by field emission scanning electron microscopy and X-ray diffraction. The LSPR properties of the Ag NPs were studied by UV-Vis-NIR spectroscopy. A correlation between the growth exponents with the optical properties of the silver nanoparticle is also established. The aim of this study is to understand the influence of the dewetting parameter (thickness of precursor film) on growth dynamics and its correlation with the plasmonic properties of Ag NPs for application in plasmonic devices.

3.2. Theoretical details for AFM analysis

An important quantity for knowing the surface morphology and dynamic scaling behavior is height-height correlation function (HHCF). It can be defined as the statistical average of the mean square of height difference between the two points, separated by distance r, and is written as [47],

$$H(r,t) = \langle |h(r+r',t) - h(r',t)|^2 \rangle \tag{3.1}$$

Where $h(r',t)$ is the surface height at position r' and time t measured by AFM and $h(r+r',t)$ is that at point $(r+r',t)$.

For self-affine surface, HHCF can be expressed by exponential correlation model in the scaling form [47]

$$H(r,t) = 2w^2\left[1 - \exp\left\{-\left(\frac{r}{\xi}\right)^{2\alpha}\right\}\right] \tag{3.2}$$

Where w is the interface width (or RMS roughness), ξ is lateral correlation length and α is roughness exponents. Further w and ξ follow the power law dependence with deposition time (here equivalent precursor film thickness) as $w \sim t^{\beta}$, $\xi \sim t^{1/z}$ respectively, where β is growth exponent and $1/z$ is dynamic exponent. Here β signifies the pace of the surface roughening while $1/z$ represents the rate of the lateral growth . The growth exponent β and dynamic exponent $1/z$ are related to α as $\beta = \alpha/z$.

HHCF behaves differently for the two different regions (for $r \ll \xi$ and $r \gg \xi$) depending on the relative value of r and correlation length ξ. Now $eq.2$ can be expressed as

$$H(r,t)\sim\begin{cases}2w^2 & {}^{r}/_{\xi}\gg 1\\ (mr)^{\,2\alpha_{local}} & {}^{r}/_{\xi}\ll 1\end{cases} \tag{3.3}$$

Here m is the local slope, which identifies the mode of growth (stationary/non-stationary) and is related to interface width w and lateral correlation length ξ as $m=\left(\sqrt{2}w\right)^{1/\alpha_{local}}/\xi$. Further local slope (m) follows the power law dependence with the growth time (or film thickness) as $m\sim t^{\beta^*}$, where β^* is the anomalous exponent, representing the anomalous scaling behavior of growth (for $\beta^*\neq 0$). The anomalous exponent can be defined as $\beta^*=\beta-\beta_{local}$, and $\beta_{local}={}^{\alpha_{local}}/_{z}$. Here α_{local} is the local roughness exponent. The roughness exponent is local (α_{local}) for the region $r\ll\xi$ and is global (α) for the region $r\gg\xi$.

The power spectral density function (PSDF) of a surface profile is Fourier transform of the surface heights. A suitable model for the PSDF of a self-affine surface is given by [47],

$$P(k,t)=\frac{1}{(2\pi)^d}\left|\langle h(r,t)e^{-ikr}\rangle\right|^2 \tag{3.4}$$

Where $P(k,t)$ is PSDF in reciprocal space and $h(r,t)$ is the surface height at position r and time t measured by AFM, d is the dimension of surface.

3.3. Experimental details

The silver nanoparticles (Ag NPs) were grown on corning glass 1737 substrate by solid state dewetting of sputtered silver precursor films using RF magnetron sputtering technique as described in section 2.1, chapter 2. The silver precursor thin films were deposited for 30, 60, 90 and 120 s time duration at a substrate temperature of 50 ℃, process pressure of 5×10^{-2} mbar, RF power of 40 Watt. The flow rate of Ar was kept constant at 5 sccm and source to substrate distance was fixed at 8 cm. For the growth of the silver nanoparticles by SSD process, post deposition annealing was performed under vacuum at a base pressure $\sim 10^{-6}$ mbar at 400 ℃ for 1h. Thickness of Ag precursors thin films (as deposited samples) were measured by stylus profilometer. Surface morphology of Ag NPs (annealed samples) was characterized by Field Emission Scanning Electron Microscope. For the structural analysis, X ray diffractometer was used. AFM measurements were done by atomic force microscope to study the dynamic scaling behavior and growth mechanism of as deposited Ag films and Ag NPs. Gwyddion software was used for the

AFM data analysis [56]. Optical properties of Ag NPs were recorded by UV-Vis-NIR spectrometer. All details of these characterization techniques are given in chapter 2.

3.4. Results and discussion

The thickness of Ag precursor thin films deposited on glass substrate by rf sputtering is measured by the stylus profilometer. A linear increase in thickness with deposition time is observed. Experimental parameters and thickness of silver precursor films are listed in table 3.1.

Table 3.1. Experimental parameters and thickness of silver precursor films measured by stylus profilometer.

Deposition time (s)	Ar Flow Rate (sccm)	Process Pressure (mbar)	Substrate Temperature (℃)	RF Power (W)	Thickness (nm)
30	5	5×10^{-2}	50	40	12 ± 2
60					21 ± 1
90					34 ± 3
120					50 ± 3

3.4.1. FESEM analysis

The FESEM images of Ag NPs formed by post annealing of Ag precursor films of the different thickness (12 nm, 21 nm, 34 nm and 50 nm) are shown in Fig. 3.1. From the SEM images, it is clear that the size of NPs as well as inter particle spacing has increased with the increase in the thickness of the precursor films. Initially as the precursor film thickness increases from 12 nm to 21 nm, the particles size is regular with nearly circular shape but for higher thickness, the particles transform in to irregular shape and formation of island of silver agglomerates instead of Ag NPs is observed. For this shape and size irregularity, solid state dewetting (SSD) process, which minimize the surface free energies of the film, substrate and film-substrate interface [54] is responsible. SSD process depends upon several deposition parameters like the thickness of the precursor film, annealing temperature, and annealing time [53,57,58]. The driving force for solid state dewetting process is more for the thinner films and hence the rate of dewetting is higher for thinner films. The particles grown via the SSD process have the broad distribution of size. Therefore, a statistical approach is required for the analysis and its correlation with optical properties, which can be commonly realized by histograms of NPs size. The histogram for low

thickness films are shown in Fig. 3.2. These histograms reveal that with the increase in thickness, the number of small particles decreases and average particle size increases from 45 nm to 87 nm.

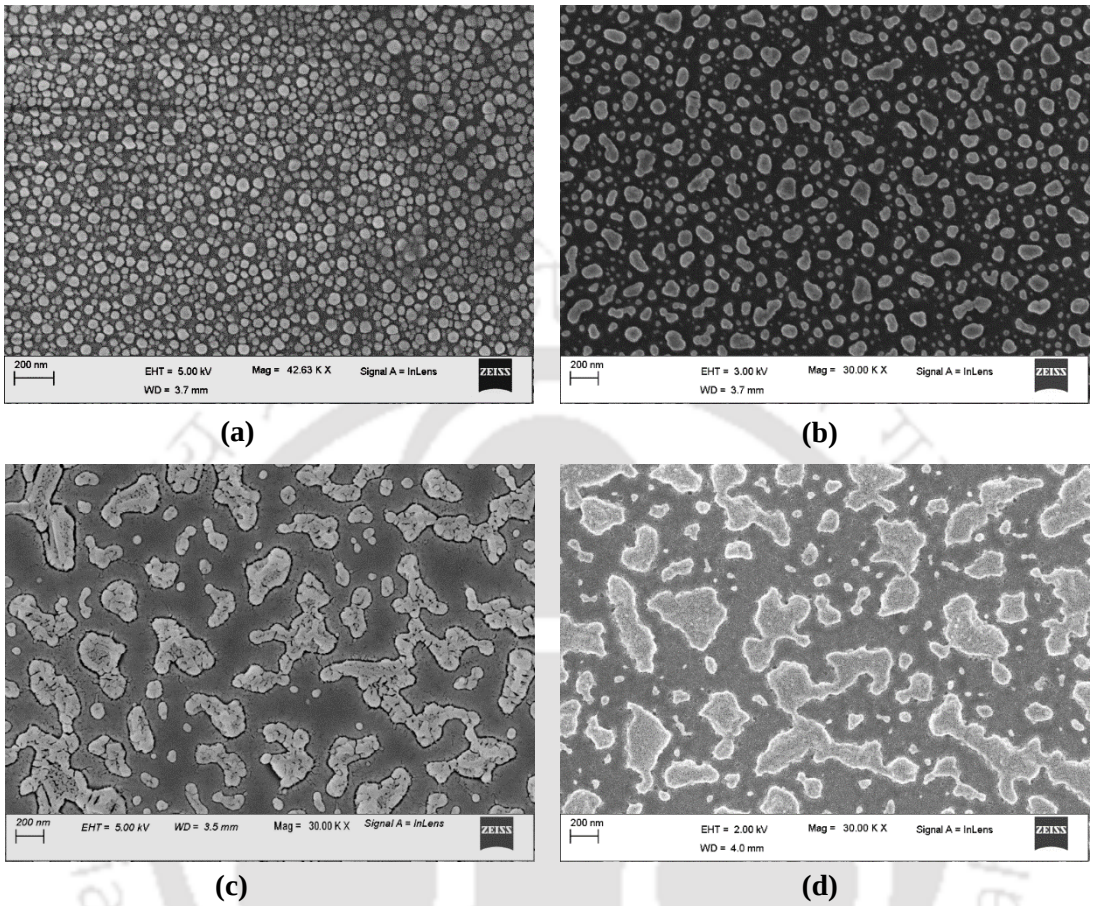

Fig. 3.1 SEM images of Ag NPs on corning glass formed by annealing at 400 ℃ for 1 h of Ag precursor films of different thickness on 200 nm scale. (a) 12 nm, (b) 21 nm, (c) 34 nm and (d) 50 nm**.**

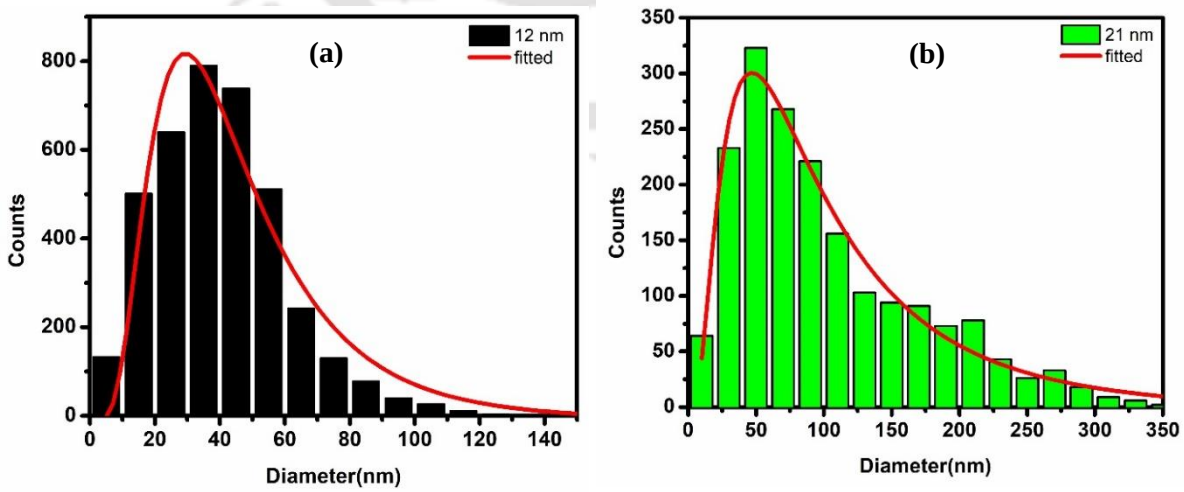

Fig. 3.2 The histogram of NPs' size on corning glass substrate formed by annealing at 400 ℃ for 1 h of Ag precursor films having different thickness.

The surface area covered by NPs is increased from 26% to 40% with film thickness increasing from 12 to 21 nm. For the higher thickness ($> 21\ nm$) of Ag precursor films, the formation of the irregular shaped clusters is observed, and due to uncertainties in definition of particle size, histograms are not available.

3.4.2. XRD analysis

The XRD spectra of films of Ag NPs are shown in Fig. 3.3. The XRD peaks at 38.2°, 44.2°, 64.5°and 77.4° corresponding to the (111), (200), (220) and (311) planes of silver respectively (JCPDS 4-0783) are observed for all the samples. The peak corresponding to (111) plane becomes more intense with the thickness of the precursor films. The crystallite sizes of the silver nanostructured films were estimated using the Debye -Scherrer's formula, defined as $D = 0.9\lambda/\beta \cos\theta$, where D is the average crystallite size and λ is the X-ray wavelength (1.5406 Å); β and θ are the full width at half maxima of the XRD peak and the diffraction angle of the corresponding XRD peak.

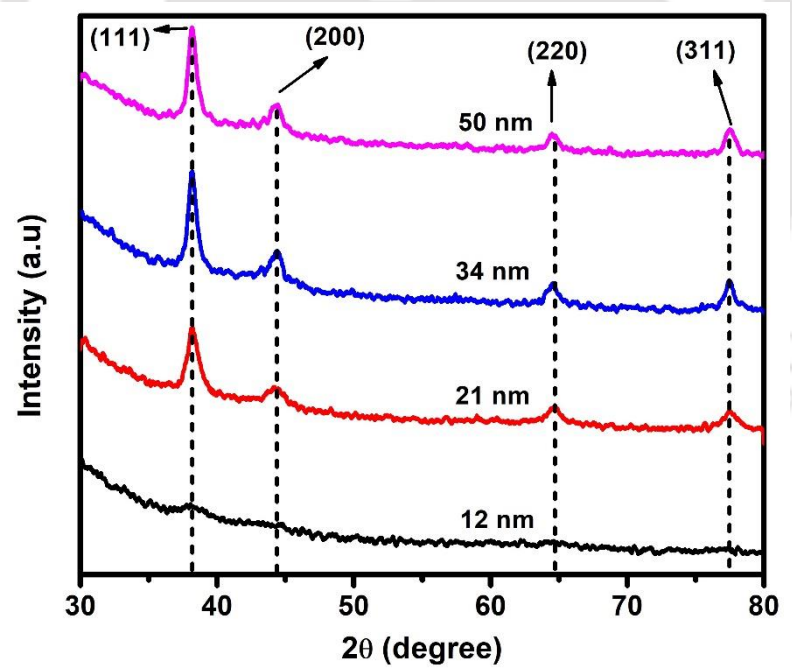

Fig. 3.3 XRD spectra of Ag NPs formed by post annealing of precursor film of different thickness; 12-50 nm.

The most intense peak corresponding to (111) plane was taken for of calculation of the crystallite size. The average crystallite size increases from 4.2 to 8.4 nm with increase in the thickness from 12 to 50 nm. The values of inter-planar distance d are 2.35, 2.04, 1.44, and 1.23 Å corresponding to (111), (200), (220) and (311) planes of silver respectively.

3.4.3. AFM analysis

The surface morphology (AFM images) of as deposited films (Ag precursor films) and annealed films (Ag NPs) are shown in Fig. 3.4, and Fig. 3.5 respectively. Multiple 2D/3D AFM images were taken at different locations/scan area of the film surface to check the surface morphology. These AFM images indicate that as-deposited films are uniform having very low surface roughness, though the roughness is slightly more for thicker films deposited for long duration (Fig.3.4). No grain formation is observed for the as-deposited silver films. After the films are annealed at 400 ℃, continuous thin films changed into the array of nanoparticles [59,60] and increase in roughness is observed. Large increase in roughness for the thicker films is due to the irregularity in shape and large size of the nanoparticles/island for these samples. The initial visualization of AFM images (Fig.3.5) of the annealed silver films indicate the uniform distribution of the small nanoparticles over the surface. For the lower thickness of the precursor film, the shape of nanoparticles is nearly spherical. With increase in thickness or growth time of the precursor film, particle shape changes from circular to elongated due to formation of islands.

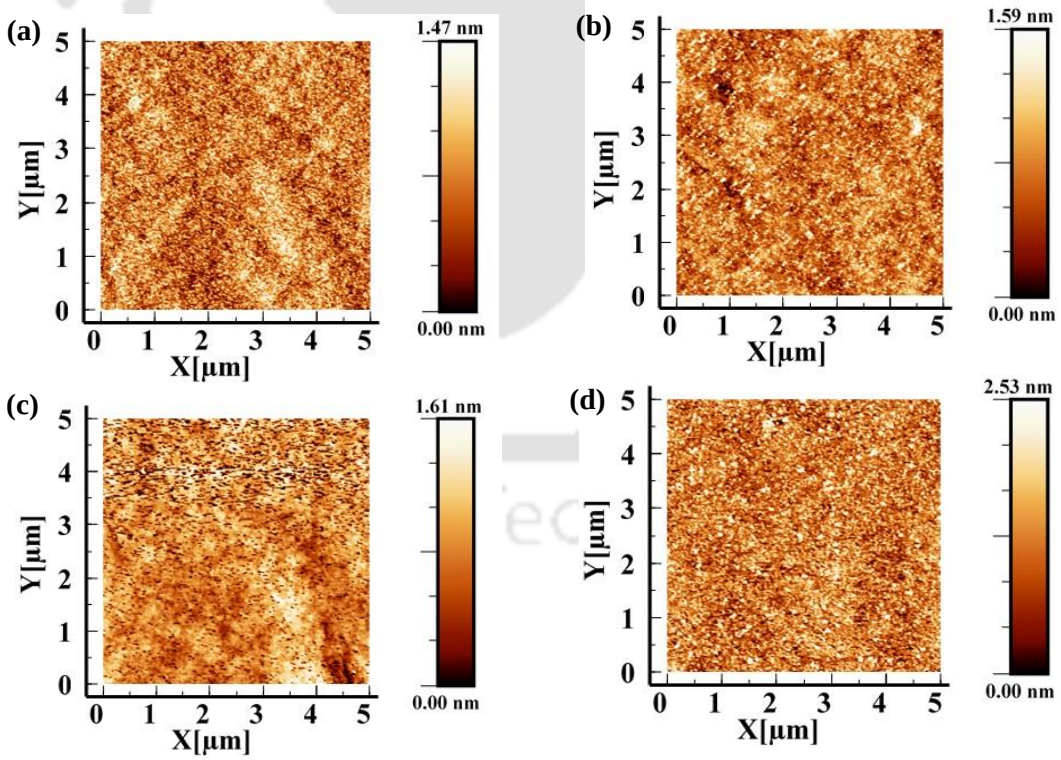

Fig. 3.4 AFM images with 5 $\mu m \times 5\ \mu m$ area of as deposited films having different thickness, (a) for 12 nm, (b) for 21 nm, (c) for 34 nm and (d) for 50 nm.

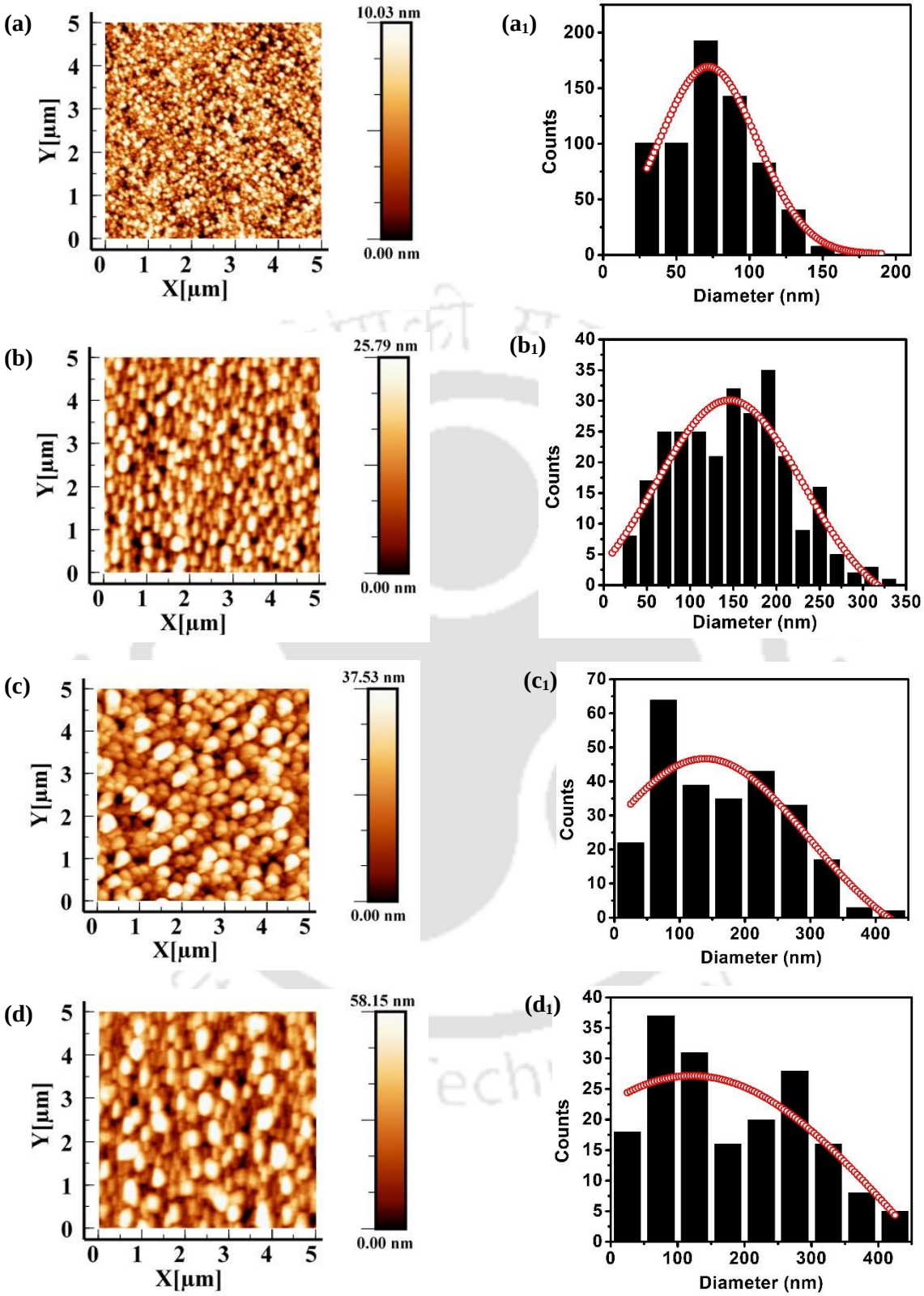

Fig. 3.5 AFM images with 5 $\mu m \times 5\ \mu m$ area of annealed films (Ag NPs) (a)-(d) and their particle size distribution (a_1)-(d_1) having different thickness, (a)&(a_1) for 12 nm, (b)&(b_1) for 21 nm, (c)&(c_1) for 34 nm and (d)&(d_1) for 50 nm.

To measure the particle size from the AFM images, watershed-based segmentation algorithm was used [61]. The average particles size is obtained as 57, 90, 140, and 160 nm for the precursor film thickness of 12, 21,34, and 50 nm respectively. The particle size distribution from AFM images is shown in Fig. 3.5 (a_1-d_1).

The height-height correlation function (HHCF) extracted from AFM images for as deposited and annealed samples having different thickness is plotted in log scale and shown in Fig. 3.6. The curve fitted using $Eq.3.2$ is shown as a solid line in the same Fig. 3.6. The measured data fit well to $eq.2$ (R^2=0.96-0.99) for as deposited films, whereas for annealed films with Ag NPs, fitting deviated for $r \gg \xi$. From Fig. 3.6, It is observed that HHCF shifted upward as the film thickness is increased for both as deposited and the annealed samples; for the annealed samples the magnitude of HHCF is higher by nearly one order than that for corresponding precursor films. The behavior of HHCF is different for two regions; $r \ll \xi$ and $r \gg \xi$.

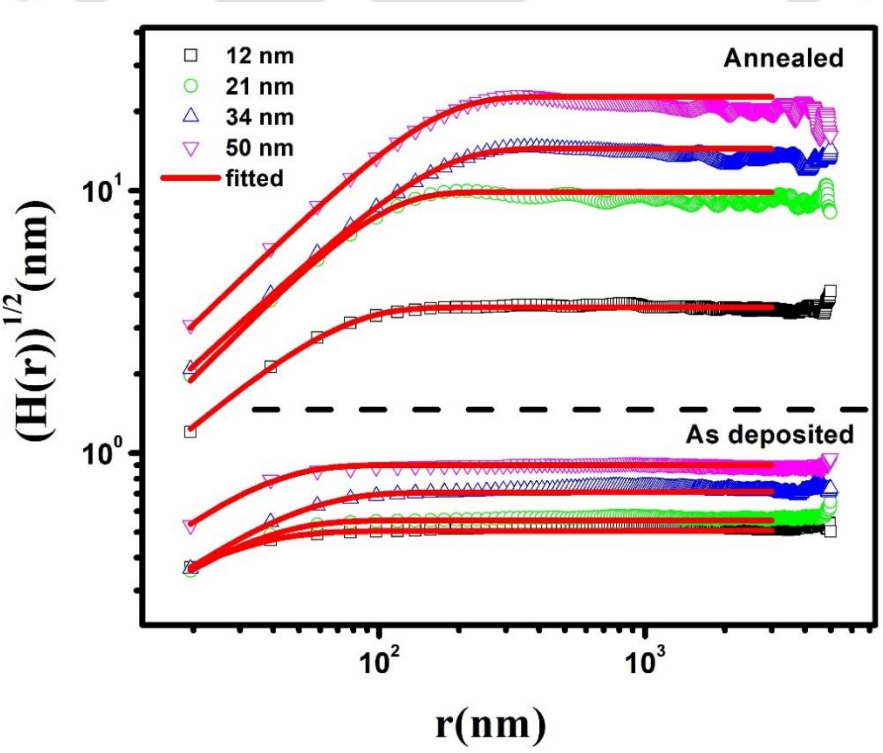

Fig. 3.6 Log-log plot of Height-Height correlation function (HHCF) as function of distance (r) of as-deposited and annealed films of different thickness: 12-50 nm.

For the as-deposited samples, HHCF remains constant in the region $r \gg \xi$ which is indicating the nature of the surfaces as self-affine while for the annealed samples, an oscillatory behavior is observed for $r \gg \xi$ indicating the formation of mound on the surfaces for thicker films [47]. For

the region $r \ll \xi$, HHCF follows a power law trend and is proportional to $r^{2\alpha_{local}}$ whereas for the region $r \gg \xi$, HHCF is close to $2w^2$. The short range (for $r \ll \xi$) and long range (for $r \gg \xi$) behavior of the rough surface are distinguished by lateral correlation length ξ.

Parameters α_{local}, w, and ξ were estimated from the best fitting of experimental curves with $eq.2$ and the values of these parameters are listed in table 3.2. The variation of the α_{local}, w, and ξ as a function of the thickness for as deposited and annealed samples on the log-log scale is shown in Fig. 3.7 (a), (b) and (c) respectively. From Fig. 3.7 (a), It is found that the value of the α_{local} for the annealed sample is higher than that for as-deposited sample due to the formation of the nanostructure. A larger value of α_{local} corresponds to more rough surface while the smaller α_{local} value corresponds to comparatively smooth surface.

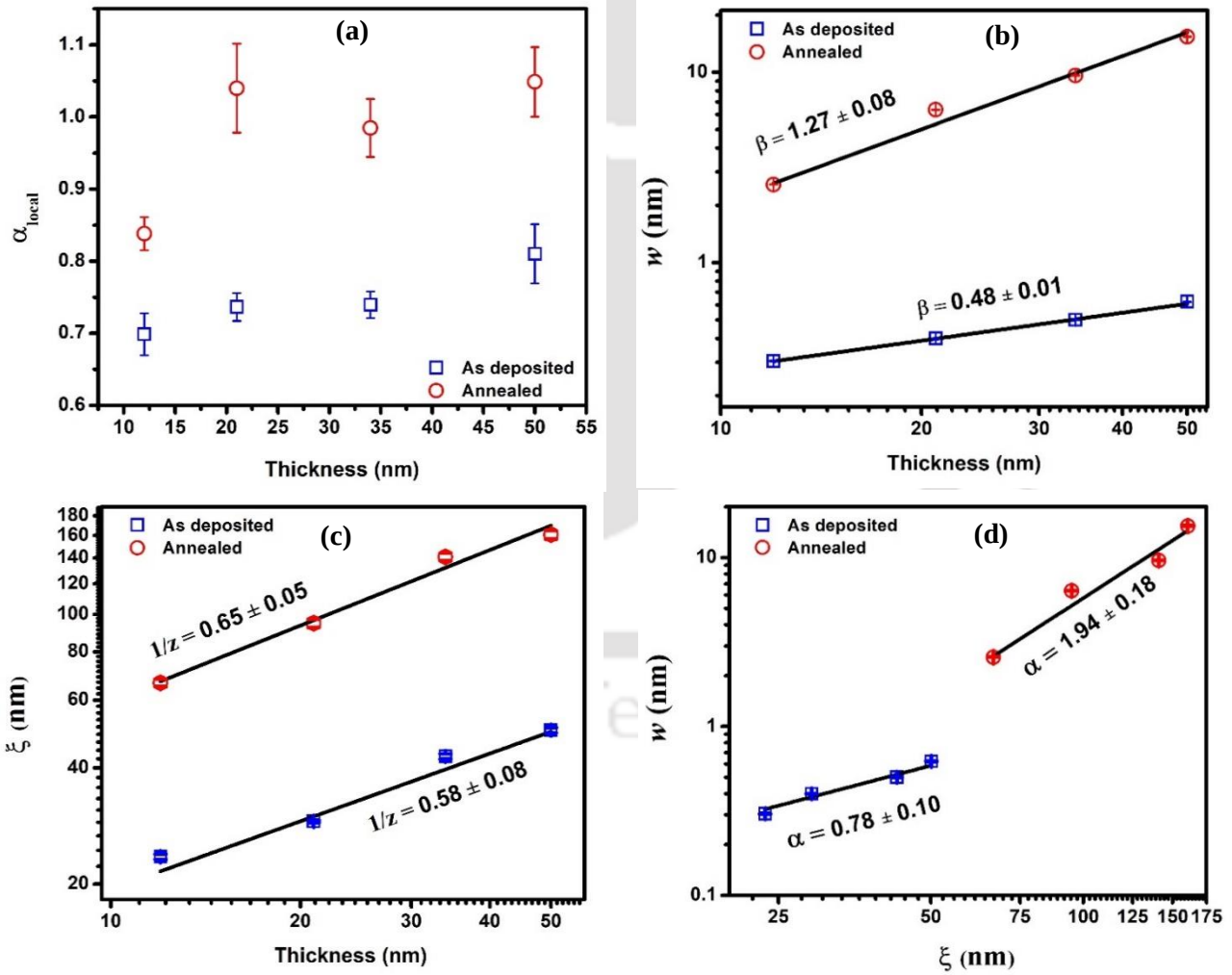

Fig. 3.7 (a)Variation in local roughness exponent α_{local} (b) interface width w, and (c) correlation length ξ with the precursor Ag film thickness, (d) interface width w vs correlation length ξ.

Table 3.2. Roughness exponent (α_{local}), interface width (w), lateral correlation length (ξ) calculated using the HHCF from AFM images of as deposited films (Ag precursor films) and annealed films (Ag NPs).

Thickness (nm)	Roughness exponent (α_{local})		Interface width (w) (nm)		Correlation length (ξ) (nm)	
	As-deposited	Annealed (Ag NPs)	As-deposited	Annealed (Ag NPs)	As-deposited	Annealed (Ag NPs)
12	0.69±0.02	0.83±0.02	0.30±0.002	2.5±0.02	23.5±0.38	66.4±1.5
21	0.73±0.02	1.03±0.06	0.39±0.002	6.3±0.02	29.0±0.19	94.8±2.4
34	0.74±0.02	0.98±0.04	0.50±0.003	9.6±0.03	42.8±0.66	140.9±3.2
50	0.81±0.04	1.04±0.05	0.62±0.004	15.3±0.05	50.0±0.80	160.8±4.1

It can also be seen from the Fig. 3.7 (b), that the interface width w increases with the thickness for all the samples however the values of interface width for the annealed samples are comparatively higher, further confirming the increase in roughness due to formation of the silver nanoparticles [1]. Fig. 3.7 (c) shows that the increase of film thickness affects the correlation length (ξ); and its ξ value is increased with the thickness for both as-deposited and annealed samples. Due to the uniform surface for thinner films, values of lateral correlation length ξ are found to be lower in the case of as-deposited samples compared to the annealed samples. In the annealed samples lateral correlation length ξ also indicates the size of the nanoparticles (mounds) and increase in correlation length is due to lateral growth of the island [1]. The correlation length estimated from HHCF matches with the particle size calculated from the AFM images. The parameters w and ξ show the power law dependence as $w \sim t^{\beta}$ and $\xi \sim t^{1/z}$ respectively having values $\beta = 0.48 \pm 0.01$ and $1/z = 0.58 \pm 0.08$ for as deposited samples, and $\beta = 1.27 \pm 0.08$ and $1/z = 0.65 \pm 0.05$ for annealed samples. In order to quantify the dynamics of roughness, ξ versus w for all the samples were plotted on log-log scale and is shown in Fig. 3.7(d). The relation between w and ξ can be worked out as $w \sim \xi^{\alpha}$ [47], where α is found to be 0.78 ± 0.10 and 1.94 ± 0.18 for as deposited and annealed samples which is well matched with that of calculated value from the relation $\alpha = \beta z$ within the measurement error. The validation of the relation confirms the presence of the dynamic scaling [47]. The measured values of $\alpha, \beta, 1/z$ for the annealed samples are comparable with the literature in the case of the mound surfaces [42,48]. We observed the value of $\alpha > 1$ in

the case of annealed samples which is the indication of the faster vertical growth compared to the lateral growth and is also related to the roughness of the precursor silver thin films.

The local slope (m) calculated using the relation $m = \left(\sqrt{2}w\right)^{1/\alpha_{local}}/\xi$ [47], is plotted as a function of film thickness and shown in Fig. 3.8. The local slope evolved with thickness and followed power law dependence with the thickness as $m(t) \sim t^{\beta*}$.

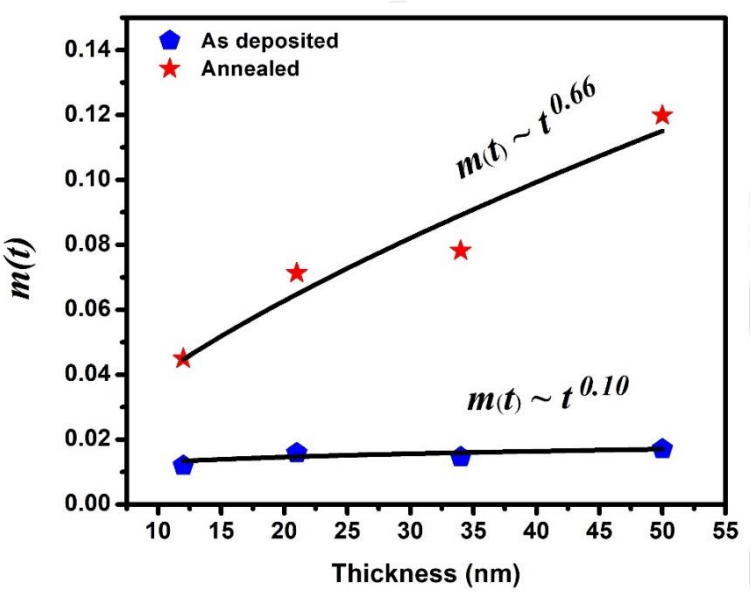

Fig. 3.8 Variation of local slope m with the thickness (growth time) for as-deposited and annealed films, fitting of this curve give the anomalous exponent β^*.

Very weak dependence ($\beta^* = 0.10 \pm 0.01$) with the thickness is observed for as deposited films indicating a near stationary growth whereas for annealed films the exponents is significantly higher ($\beta^* = 0.66 \pm 0.03$) indicating the non-stationary growth of nanoparticles during annealing. The non-stationary growth is also confirmed by HHCF as it is shifting upward with thickness for the region $r \ll \xi$ [47]. The anomalous exponent β^* is calculated by the power law fitting of local slope curve which matched very well with that of calculate values from the relation $\beta^* = \beta - \beta_{local}$. The value $\beta^* \neq 0$ further confirms that the anomalous scaling has occurred [10,36].

Fig. 3.9 (a) shows the power spectrum density function (PSDF) plots of as deposited and annealed samples of different thickness in logarithmic scale. Power spectrum density function of as deposited samples has lower intensity at each spatial frequency compared with those of annealed samples for all the thicknesses, which is related to lesser roughness of as deposited films.

However, the intensity of power spectrum increases with the thickness or growth time. Like HHCF, the PSDF exhibits two different regimes, a correlated regime (frequency dependent) and non-correlated regime (constant value); PSDF spectra bend at higher frequencies for all the samples.

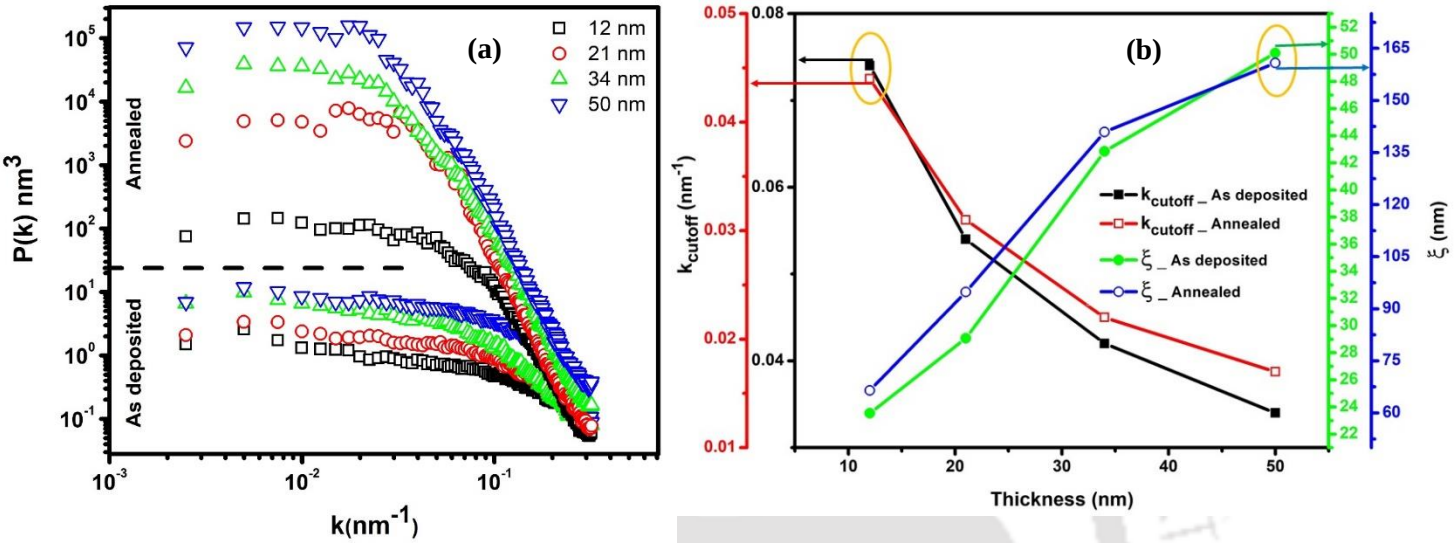

Fig. 3.9 (a) Log-log plot of power spectrum density function $P(k)$ as function of k (reciprocal space) of as-deposited and annealed films of different thickness: 12-50 nm, (b) variation in cutoff frequency k_{cutoff} and correlation length ξ of as deposited and annealed films with the precursor Ag precursor film thickness.

These two behaviors of the PSDF are differentiated by cut off frequency (k_{cutoff}), which can be determined by the turning point of the PSDF spectra. The cutoff frequency (k_{cutoff}) is shifted towards lower k with increase of the film thickness for all the samples and shown in Fig. 3.9 (b). This is in agreement with increase in correlation length ξ for thicker silver precursor films, $k_{cutoff} \sim 1/\xi$. The anomalous scaling is also confirmed by the plots of HHCF and PSDF (see Fig. 6 and Fig. 9a) as HHCF and PSDF curves are shifted upwards with increase in thickness [10].

From the PSDF shown in Fig. 3.10, it is also found that for as deposited sample no characteristic peak is observed which is characteristic of a smooth surface with self-affine growth while for the annealed samples, when nanoparticle formation has taken place, PSDF spectrum has a characteristic peak suggesting the formation of mounds on the surface [55]. For the annealed samples, this characteristic peak become more prominent with increase in the thickness of the precursor films. These observations are in agreement with literature for mound surfaces [47].

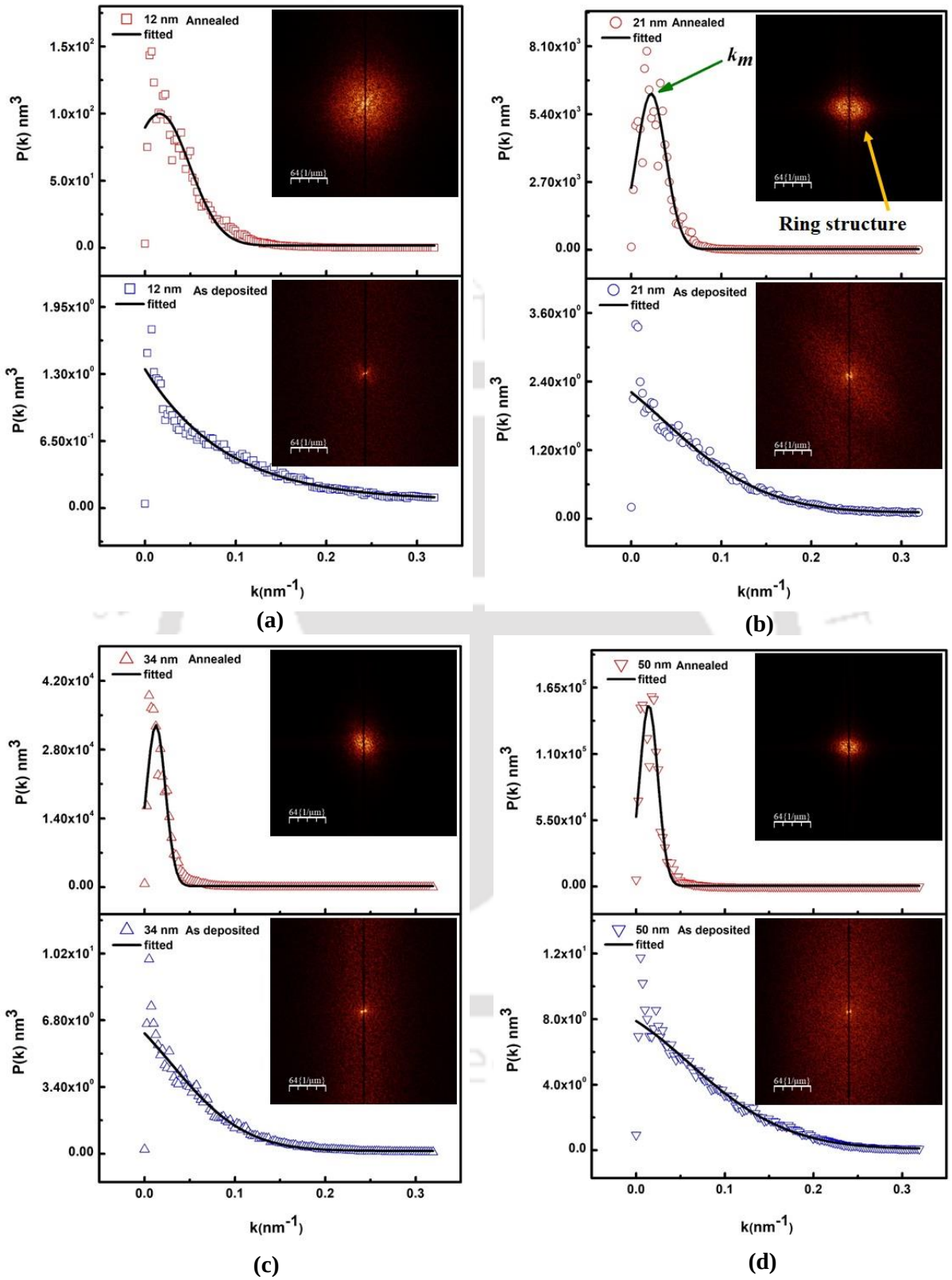

Fig. 3.10 Power spectrum density function $P(k)$ as function of k (reciprocal space) and corresponding 2D FFT images (inset) of as deposited and annealed films of different thickness (a) 12 nm, (b) 21 nm, (c) 34 nm and (d) 50 nm.

The 2D Fast Fourier Transform (FFT) of AFM images for as-deposited and annealed samples are shown as inset image in Fig. 3.10. A bright ring like structure in k- space is observed for the annealed samples, which further supports presence of mounds on the surface [48].The fitting for the all-PSDF curves with Gaussian function was done to estimate the peak position k_m and FWHM of the peak. The peak position of the PSDF is given by $k_m = 2\pi/\lambda$ and has a power law dependence with time (or film thickness) $k_m \sim t^{-p}$, where p is the wavelength exponent. This implies a similar behavior for the wavelength (λ_m) (see Fig. 3.11a). A linear variation in λ_m with thickness is observed for these annealed films with growth of Ag NPs.

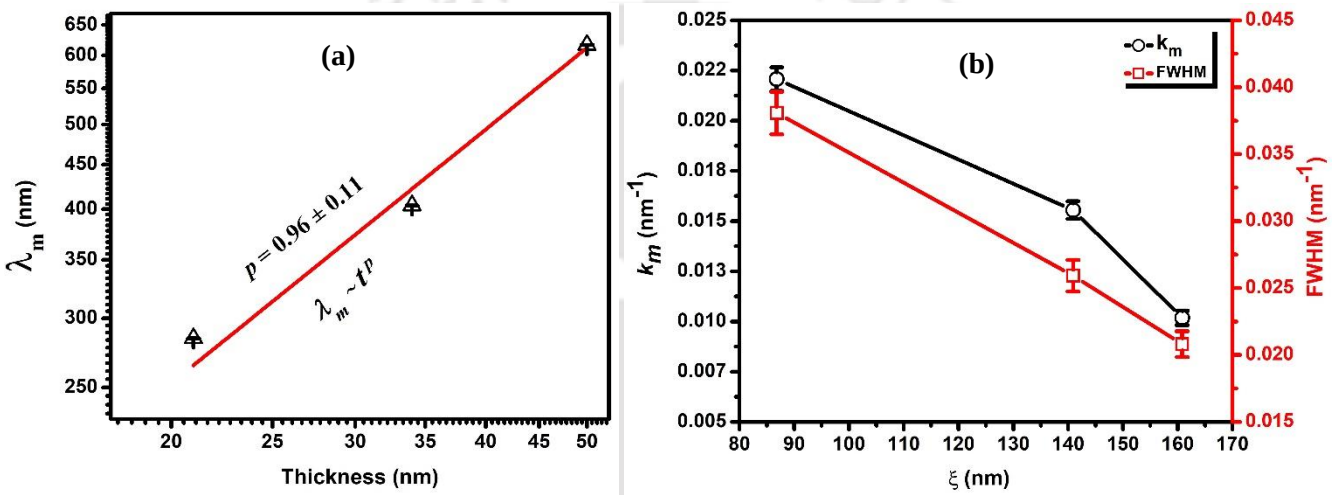

Fig. 3.11 (a) Log-log plot of characteristic wavelength as a function of thickness (growth time), (b) variation in peak position (k_m) and FWHM of the corresponding peak of the mound surface (Ag NPs) .

From the Fig. 3.11 (b), it is observed that characteristic peak (k_m) is shifted towards the lower k in the reciprocal space with the increase in the correlation length indicating increase in separation of island or the size of the mounds. The full width at half maxima (FWHM) of the PSDF also follows an inversely proportional relation with the correlation length (ξ). This behavior of k_m and FWHM is the agreement with literature for the mound surfaces [33,47].

Above observations show that the growth of as-deposited films result in self-affine surface but after the annealing, the surface becomes mounded with the well-defined characteristic wavelength which is due to the transformation of continuous film into nanoparticles [55]. The mound formation on any surface is caused by the different growth effects such as shadowing, reemission, diffusion. In the present work solid state dewetting process occurs via surface diffusion below the melting points of the films and promotes the mound formation [1,55,62].

3.4.4. UV-Vis-NIR analysis

To correlate the growth dynamics of the silver thin films and the silver nanoparticles with the optical properties, the absorbance spectra for all the samples is measured in the wavelength range from 300-1500 nm (Fig. 3.12). For as deposited films, absorbance spectra are nearly flat in the wavelength range from 300-800 nm (inset of Fig. 3.12 a) without any peak in the absorbance spectra. Absence of any LSPR peak in the spectra for the as deposited films (Ag Precursor films) indicates that nanoparticles formation has not taken place at this stage. These observations are in agreement with the AFM studies indicating the self-affine growth for as deposited films with low roughness and small growth exponents in HHCF. For annealed films, the absorbance spectra is characterized by a peak in the wavelength range 400-600 nm corresponding to the LSPR nature due to formation of nanoparticles on the surface. This peak in absorbance spectra for the annealed films is more symmetric with low FWHM and nearly zero absorbance value in the high wavelength range (>600-800 nm) for films having low thickness prior to the annealing. The significant decrease in absorbance to nearly zero value beyond the LSPR peak range indicates that as deposited films are fully converted in to the nanoparticles. A shift in peak position towards longer wavelength is also observed with increase in thickness of the as deposited films, which is related to the increase in size of the nanoparticle. For films with higher thickness (~35 nm or more), the LSPR peak in absorbance spectra is asymmetric with larger FWHM and nonzero absorbance value in the high wavelength range due to formation of silver island instead of Ag nanoparticles. In the case of thick precursor films, the entire thickness of the precursor film is not converted, resulting into island formation on top of continuous film after annealing. The absorbance spectra in these cases have the background effect (in 800-1400 nm range) due to presence of continuous film. The asymmetric nature of LSPR peak is due to broad distribution and irregularity in shape of Ag NPs grown via SSD process. The fact that for thicker films, the part of the film is not converted in to nanoparticles upon annealing is the due to requirement of larger driving force for solid state dewetting process when the film thickness is more. The absorbance spectra are fitted with Lorentz function to calculate the position and bandwidth of the peak; these fitted curves are shown in Fig. 3.12 (a) as solid lines. Although the fitting for the higher thickness of the films ($> 21\ nm$) is not as good due to more broadening, asymmetric nature and finite background absorbance, however one could get a reasonably good estimate of peak position and bandwidth of the peak. The LSPR peak shifts to longer wavelength side from 475 nm to 548 nm with increase in thickness of

precursor films due to change in size and shape of the particles as shown in Fig. 3.12 (b). This is an agreement with the Mie theory [63], according to Mie theory, metal nanoparticles exhibit red shift in λ_{LSPR}, with increase of the particle size [17].

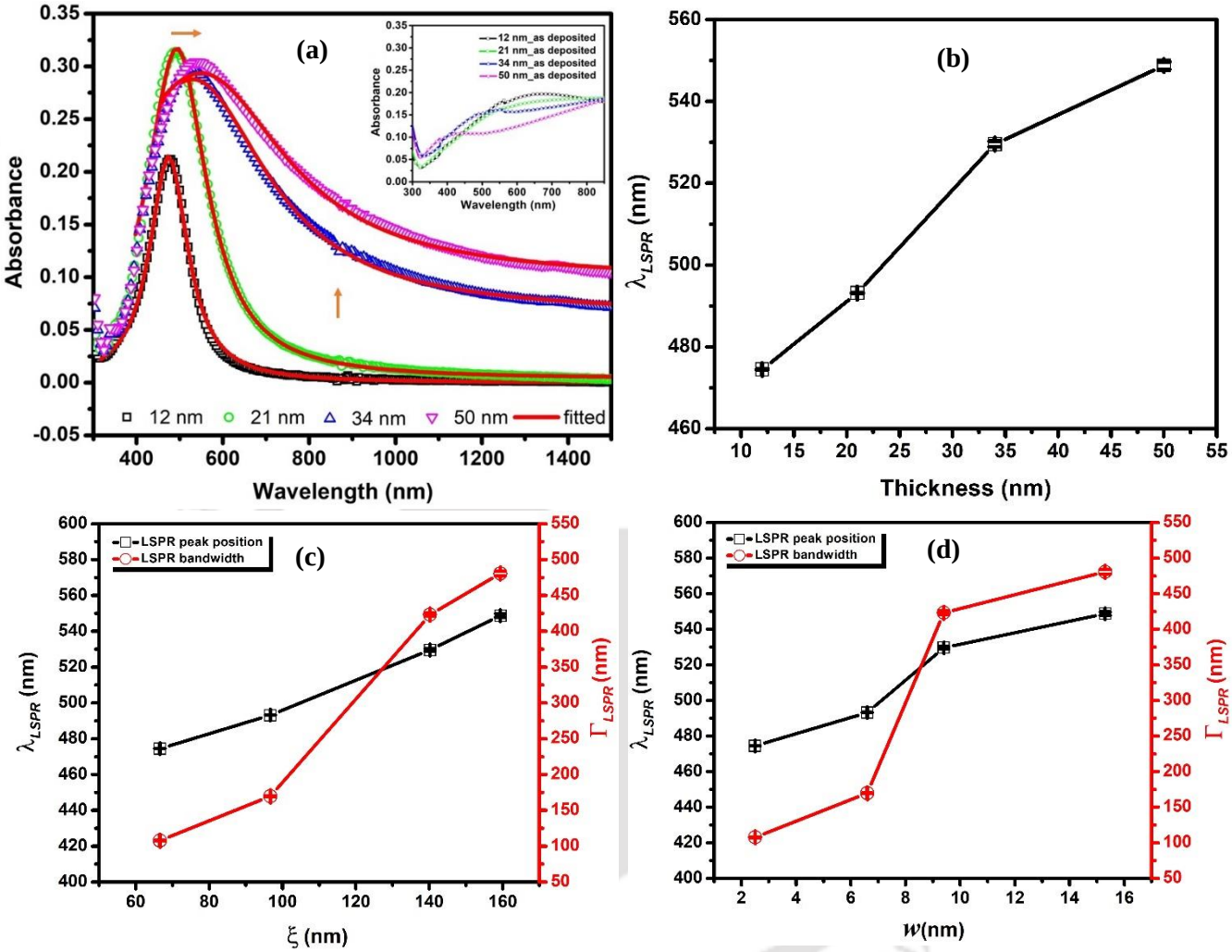

Fig. 3.12 (a) Absorption spectra of Ag NPs and as deposited films (inset), (b) variation in LSPR peak position with thickness, (c), (d) variation in LSPR peak and bandwidth with correlation length and interface width.

Fig. 3.12 (c), (d) shows the correlation between the interface width *w* and lateral correlation length ξ with the LSPR properties of the Ag NPs. From Fig. 3.12 (c), it is observed that LSPR peak (λ_{LSPR}) is red shifted from 475 nm to 548 nm with increase in the correlation length ξ from 66 to 160 nm-[48]. The results are in agreement with the fact that both LSPR peak position in absorbance spectra and correlation length in HHCF derived from AFM analysis depend upon the particle size; the peak position is red shifted with increase in particle size, whereas the correlation length is directly proportional to the particle size. The correlation length is also responsible for the

broadening of the LSPR peak as shown in Fig 3.12(c); both have direct relationship with the particle size [17]. Fig. 3.12 (d) shows the dependence of LSPR peak position and peak width (FWHM) on the interface width w estimated from AFM analysis. Both LSPR peak position λ_{LSPR} and Peak width (FWHM) increase as the interface width w increases from 2.5 to 15.3 nm [26,48]. The direct correlation suggests that in solid state dewetting process, as the nanoparticles grow, the distribution in size is observed resulting in an increase in surface roughness and asymmetric broadening of LSPR peak. Further, the characteristic peak (k_m) in PSDF is red shifted (shifted towards lower k values in k space) and became broader (FWHM decreased in k space) with increase in the lateral correlation length. This behavior of characteristic peak is quite similar to the LSPR peak, which demonstrate a good correlation between the growth dynamics and the LSPR properties of Ag NPs.

3.5. Conclusions

Surface morphology and growth dynamics of the Ag NPs grown by solid state dewetting has been investigated as a function of thickness of the precursor silver films and a correlation between the growth exponents and optical properties of the Ag NPs is established. The thickness of the as deposited films (Ag precursor silver films) is found to range from 12 to 50 nm for the deposition time 30-120 seconds respectively. For lower precursor film thickness deposited for shorter time, the particles size is regular with nearly circular shape, but for higher thickness, the particles transform into irregular shapes and formation of island of silver agglomerates instead of Ag NPs is observed. The XRD spectra of Ag NPs (annealed films) is characterized by a dominating peak at 38° corresponding to (111) and relatively weak peaks at 44°, 64° and 78° corresponding to (200), (220) and (311) planes of silver respectively. The surface morphology of as deposited films (Ag precursor films) and annealed films (Ag NPs) has been studied with scaling analysis of AFM data. From HHCF analysis, the interface width w and lateral correlation length ξ are found to follow the power law dependence with the thickness (or deposition time) as $w \sim t^{\beta}$, $\xi \sim t^{1/z}$ respectively. From the comparative analysis of HHCF, PSDF and 2D FFT, it is observed that the as deposited samples (Ag precursor films) show self-affine surface while annealed samples (Ag NPs) follow the mounded surface due to the formation of the nanoparticles by the solid state dewetting. The LSPR peak (λ_{LSPR}) of the Ag NPs is red shifted and become broader with the increase in the ξ and

w. This shows a good correlation between the growth exponents and the optical properties of Ag NPs.

3.6. References

[1] C. Guillén, J. Herrero, Surface-properties relationship in sputtered Ag thin films: Influence of the thickness and the annealing temperature in nitrogen, Appl. Surf. Sci. 324 (2015) 245–250. https://doi.org/10.1016/j.apsusc.2014.10.076.

[2] J. Bhattacharya, N. Chakravarty, S. Pattnaik, W. Dennis Slafer, R. Biswas, V.L. Dalal, A photonic-plasmonic structure for enhancing light absorption in thin film solar cells, Appl. Phys. Lett. 99 (2011) 131114. https://doi.org/10.1063/1.3641469.

[3] L. Wang, M. Hasanzadeh Kafshgari, M. Meunier, Optical Properties and Applications of Plasmonic-Metal Nanoparticles, Adv. Funct. Mater. 30 (2020) 2005400. https://doi.org/https://doi.org/10.1002/adfm.202005400.

[4] T. Yoshinobu, A. Iwamoto, H. Iwasaki, Scaling Analysis of***SiO*₂**/Si Interface Roughness by Atomic Force Microscopy, Jpn. J. Appl. Phys. 33 (1994) 383–387. https://doi.org/10.1143/jjap.33.383.

[5] Ľ. Scholtz, L. Ladányi, J. Mullerova, Influence of Surface Roughness on Optical Characteristics of Multilayer Solar Cells, Adv. Electr. Electron. Eng. 12 (2015). https://doi.org/10.15598/aeee.v12i6.1078.

[6] K.M. Byun, S.J. Yoon, D. Kim, Effect of surface roughness on the extinction-based localized surface plasmon resonance biosensors, Appl. Opt. 47 (2008) 5886–5892. https://doi.org/10.1364/AO.47.005886.

[7] V.E. Ferry, L.A. Sweatlock, D. Pacifici, H.A. Atwater, Plasmonic Nanostructure Design for Efficient Light Coupling into Solar Cells, Nano Lett. 8 (2008) 4391–4397. https://doi.org/10.1021/nl8022548.

[8] J.S. Cho, S. Baek, S.H. Park, J.H. Park, J. Yoo, K.H. Yoon, Effect of nanotextured back

reflectors on light trapping in flexible silicon thin-film solar cells, Sol. Energy Mater. Sol. Cells. 102 (2012) 50–57. https://doi.org/10.1016/j.solmat.2012.03.031.

[9] D. Madzharov, R. Dewan, D. Knipp, Influence of front and back grating on light trapping in microcrystalline thin-film silicon solar cells, Opt. Express. 19 (2011) A95–A107.

[10] G. Nabiyouni, B.J. Farahani, Anomalous scaling in surface roughness evaluation of electrodeposited nanocrystalline Pt thin films, Appl. Surf. Sci. 256 (2009) 674–682. https://doi.org/https://doi.org/10.1016/j.apsusc.2009.08.041.

[11] M.F. Al-Kuhaili, Characterization of thin films produced by the thermal evaporation of silver oxide, J. Phys. D. Appl. Phys. 40 (2007) 2847–2853. https://doi.org/10.1088/0022-3727/40/9/027.

[12] F. Ruffino, V. Torrisi, G. Marletta, M.G. Grimaldi, Atomic force microscopy investigation of the kinetic growth mechanisms of sputtered nanostructured Au film on mica: towards a nanoscale morphology control, Nanoscale Res. Lett. 6 (2011) 112. https://doi.org/10.1186/1556-276X-6-112.

[13] P. Jacquet, B. Bouteille, R. Dezert, J. Lautru, R. Podor, A. Baron, J. Teisseire, J. Jupille, R. Lazzari, I. Gozhyk, Periodic Arrays of Diamond-Shaped Silver Nanoparticles: From Scalable Fabrication by Template-Assisted Solid-State Dewetting to Tunable Optical Properties, Adv. Funct. Mater. 29 (2019) 1901119. https://doi.org/https://doi.org/10.1002/adfm.201901119.

[14] J. Zhang, L. Zhang, W. Xu, Surface plasmon polaritons: Physics and applications, J. Phys. D. Appl. Phys. 45 (2012). https://doi.org/10.1088/0022-3727/45/11/113001.

[15] S. Law, V. Podolskiy, D. Wasserman, Towards nano-scale photonics with micro-scale photons: the opportunities and challenges of mid-infrared plasmonics, 2 (2013) 103–130. https://doi.org/doi:10.1515/nanoph-2012-0027.

[16] V.N. Rai, A.K. Srivastava, C. Mukherjee, S.K. Deb, Surface enhanced absorption and transmission from dye coated gold nanoparticles in thin films, Appl. Opt. 51 (2012) 2606–2615. https://doi.org/10.1364/AO.51.002606.

[17] S. Link, M.A. El-Sayed, Shape and size dependence of radiative, non-radiative and

photothermal properties of gold nanocrystals, Int. Rev. Phys. Chem. 19 (2000) 409–453. https://doi.org/10.1080/01442350050034180.

[18] R. Chang, Surface enhanced Raman scattering, Springer Science & Business Media, 2013.

[19] W. Zi, X. Ren, F. Xiao, H. Wang, F. Gao, S.F. Liu, Ag nanoparticle enhanced light trapping in hydrogenated amorphous silicon germanium solar cells on flexible stainless steel substrate, Sol. Energy Mater. Sol. Cells. 144 (2016) 63–67. https://doi.org/10.1016/j.solmat.2015.08.024.

[20] M.S. Gangwar, P. Agarwal, Plasmon-enhanced photoluminescence and Raman spectroscopy of silver nanoparticles grown by solid state dewetting, J. Phys. Condens. Matter. 35 (2023) 325301. https://doi.org/10.1088/1361-648X/acd1cd.

[21] J.P. Huang, L. Gao, Z.Y. Li, Temperature effect on nonlinear optical response of metal–dielectric composite with interfacial layers, Solid State Commun. 115 (2000) 347–352. https://doi.org/https://doi.org/10.1016/S0038-1098(00)00199-X.

[22] C. Noguez, Surface Plasmons on Metal Nanoparticles: The Influence of Shape and Physical Environment, J. Phys. Chem. C. 111 (2007) 3806–3819. https://doi.org/10.1021/jp066539m.

[23] M.M. Miller, A.A. Lazarides, Sensitivity of Metal Nanoparticle Surface Plasmon Resonance to the Dielectric Environment, J. Phys. Chem. B. 109 (2005) 21556–21565. https://doi.org/10.1021/jp054227y.

[24] C. Lee, C.S. Robertson, A.H. Nguyen, M. Kahraman, S. Wachsmann-Hogiu, Thickness of a metallic film, in addition to its roughness, plays a significant role in SERS activity OPEN, (2015). https://doi.org/10.1038/srep11644.

[25] D. Lepage, D. Carrier, A. Jiménez, J. Beauvais, J.J. Dubowski, Plasmonic propagations distances for interferometric surface plasmon resonance biosensing, Nanoscale Res. Lett. 6 (2011) 388. https://doi.org/10.1186/1556-276X-6-388.

[26] M. Kanso, S. Cuenot, G. Louarn, Roughness effect on the SPR measurements for an optical fibre configuration: experimental and numerical approaches, J. Opt. A Pure Appl. Opt. 9 (2007) 586–592. https://doi.org/10.1088/1464-4258/9/7/008.

[27] J.M. López, Scaling Approach to Calculate Critical Exponents in Anomalous Surface Roughening, Phys. Rev. Lett. 83 (1999) 4594–4597. https://doi.org/10.1103/PhysRevLett.83.4594.

[28] J.H. Yao, H. Guo, Shadowing instability in three dimensions, Phys. Rev. E. 47 (1993) 1007–1011. https://doi.org/10.1103/PhysRevE.47.1007.

[29] J.H. Yao, C. Roland, H. Guo, Interfacial dynamics with long-range screening, Phys. Rev. A. 45 (1992) 3903–3912. https://doi.org/10.1103/PhysRevA.45.3903.

[30] J.T. Drotar, Y.-P. Zhao, T.-M. Lu, G.-C. Wang, Surface roughening in shadowing growth and etching in $2+1$ dimensions, Phys. Rev. B. 62 (2000) 2118–2125. https://doi.org/10.1103/PhysRevB.62.2118.

[31] J.H. Jeffries, J.-K. Zuo, M.M. Craig, Instability of Kinetic Roughening in Sputter-Deposition Growth of Pt on Glass, Phys. Rev. Lett. 76 (1996) 4931–4934. https://doi.org/10.1103/PhysRevLett.76.4931.

[32] G. Palasantzas, J. Krim, Scanning Tunneling Microscopy Study of the Thick Film Limit of Kinetic Roughening, Phys. Rev. Lett. 73 (1994) 3564–3567. https://doi.org/10.1103/PhysRevLett.73.3564.

[33] M. Pelliccione, T. Karabacak, C. Gaire, G.-C. Wang, T.-M. Lu, Mound formation in surface growth under shadowing, Phys. Rev. B. 74 (2006) 125420. https://doi.org/10.1103/PhysRevB.74.125420.

[34] D. Siniscalco, M. Edely, J.F. Bardeau, N. Delorme, Statistical analysis of mounded surfaces: Application to the evolution of ultrathin gold film morphology with deposition temperature, Langmuir. 29 (2013) 717–726. https://doi.org/10.1021/la304621k.

[35] C. Tang, S. Alexander, R. Bruinsma, B.E. Shaw, Scaling theory for the growth of amorphous films, Phys. Rev. Lett. 64 (1990) 772–775. https://doi.org/10.1103/PhysRevLett.64.772.

[36] M. Nasehnejad, M. Gholipour Shahraki, G. Nabiyouni, Atomic force microscopy study, kinetic roughening and multifractal analysis of electrodeposited silver films, Appl. Surf. Sci. 389 (2016) 735–741. https://doi.org/10.1016/j.apsusc.2016.07.134.

[37] Ş. Ţălu, R.S. Matos, E.P. Pinto, S. Rezaee, M. Mardani, Stereometric and fractal analysis of sputtered Ag-Cu thin films, Surfaces and Interfaces. 21 (2020) 100650. https://doi.org/10.1016/j.surfin.2020.100650.

[38] R. Shakoury, R.S. Matos, H.D. da Fonseca Filho, S. Rezaee, A. Arman, A. Boochani, S. Jurečka, A. Zelati, M. Mardani, Ş. Ţălu, Investigation of deposition temperature effect on spatial patterns of MgF2 thin films, Microsc. Res. Tech. 86 (2023) 169–180. https://doi.org/10.1002/jemt.24246.

[39] L. Dejam, J. Sabbaghzadeh, A. Ghaderi, S. Solaymani, R.S. Matos, Ștefan Țălu, H.D. da Fonseca Filho, A.H. Sari, H. Kiani, A.H.S. Shayegan, M.A. Doudaran, Advanced nano-texture, optical bandgap, and Urbach energy analysis of NiO/Si heterojunctions, Sci. Rep. 13 (2023) 6518. https://doi.org/10.1038/s41598-023-33713-y.

[40] R.S. Matos, N.S. Ferreira, Ş. Ţălu, A. Ghaderi, S. Solaymani, M.A. Pires, E.A. Sanches, H.D. da Fonseca Filho, Percolative, Multifractal, and Symmetry Properties of the Surface at Nanoscale of Cu-Ni Bimetallic Thin Films Deposited by RF-PECVD, Symmetry (Basel). 14 (2022). https://doi.org/10.3390/sym14122675.

[41] R.S. Matos, H.D. da Fonseca Filho, A. Das, S. Kumar, V. Chawla, Ş. Ţălu, Stereometric analysis of Ti1−xAlxN thin films deposited by direct current/radio frequency magnetron sputtering, Microsc. Res. Tech. 85 (2022) 296–307. https://doi.org/https://doi.org/10.1002/jemt.23905.

[42] M. Nasehnejad, G. Nabiyouni, M.G. Shahraki, Dynamic scaling study of nanostructured silver films, J. Phys. D. Appl. Phys. 50 (2017) 375301. https://doi.org/10.1088/1361-6463/aa7d78.

[43] G. Zhang, B.L. Weeks, M. Holtz, Application of dynamic scaling to the surface properties of organic thin films: Energetic materials, Surf. Sci. 605 (2011) 463–467. https://doi.org/https://doi.org/10.1016/j.susc.2010.11.018.

[44] H. Yoshino, A. Abbas, P.M. Kaminski, R. Smith, J.M. Walls, D. Mansfield, Measurement of thin film interfacial surface roughness by coherence scanning interferometry, J. Appl. Phys. 121 (2017) 105303. https://doi.org/10.1063/1.4978066.

[45] T. V Vorburger, E.C. Teague, Optical techniques for on-line measurement of surface topography, Precis. Eng. 3 (1981) 61–83. https://doi.org/https://doi.org/10.1016/0141-6359(81)90038-6.

[46] M. Sadeghi, A. Zelati, S. Rezaee, C. Luna, R.S. Matos, M.A. Pires, N.S. Ferreira, H.D. da Fonseca Filho, A. Ahmadpourian, Ş. Ţălu, Evaluating the Topological Surface Properties of Cu/Cr Thin Films Using 3D Atomic Force Microscopy Topographical Maps, Coatings. 12 (2022) 1–13. https://doi.org/10.3390/coatings12091364.

[47] M. Pelliccione, T.-M. Lu, Evolution of thin film morphology, Springer, 2008.

[48] R. Kesarwani, P.P. Dey, A. Khare, Correlation between surface scaling behavior and surface plasmon resonance properties of semitransparent nanostructured Cu thin films deposited via PLD, RSC Adv. 9 (2019) 7967–7974. https://doi.org/10.1039/C9RA00194H.

[49] S. Kunwar, M. Sui, Q. Zhang, P. Pandey, M.Y. Li, J. Lee, Various silver nanostructures on sapphire using plasmon self- assembly and dewetting of thin films, Nano-Micro Lett. 9 (2017) 1–17. https://doi.org/10.1007/s40820-016-0120-6.

[50] B. Khodashenas, H.R. Ghorbani, Synthesis of silver nanoparticles with different shapes, Arab. J. Chem. 12 (2019) 1823–1838. https://doi.org/10.1016/j.arabjc.2014.12.014.

[51] J. García-Barrasa, J.M. López-De-luzuriaga, M. Monge, Silver nanoparticles: Synthesis through chemical methods in solution and biomedical applications, Cent. Eur. J. Chem. 9 (2011) 7–19. https://doi.org/10.2478/s11532-010-0124-x.

[52] A. Gambardella, M. Berni, G. Graziani, A. Kovtun, A. Liscio, A. Russo, A. Visani, M. Bianchi, Nanostructured Ag thin films deposited by pulsed electron ablation, Appl. Surf. Sci. 475 (2019) 917–925. https://doi.org/10.1016/j.apsusc.2019.01.035.

[53] J.A. Badán, E. Navarrete-Astorga, R. Henríquez, F. Martín Jiménez, D. Ariosa, J.R. Ramos-Barrado, E.A. Dalchiele, Silver Nanoparticle Arrays onto Glass Substrates Obtained by Solid-State Thermal Dewetting: A Morphological, Structural and Surface Chemical Study, Nanomaterials. 12 (2022) 1–27. https://doi.org/10.3390/nano12040617.

[54] C. V Thompson, Solid-State Dewetting of Thin Films, (2012). https://doi.org/10.1146/annurev-matsci-070511-155048.

[55] M. Berni, I. Carrano, A. Kovtun, A. Russo, A. Visani, C. Dionigi, A. Liscio, F. Valle, A. Gambardella, Monitoring morphological and chemical properties during silver solid-state dewetting, Appl. Surf. Sci. 498 (2019) 143890. https://doi.org/10.1016/j.apsusc.2019.143890.

[56] D. Nečas, P. Klapetek, Gwyddion: An open-source software for SPM data analysis, Cent. Eur. J. Phys. 10 (2012) 181–188. https://doi.org/10.2478/s11534-011-0096-2.

[57] F. Leroy, Ł. Borowik, F. Cheynis, Y. Almadori, S. Curiotto, M. Trautmann, J.C. Barbé, P. Müller, How to control solid state dewetting : A short review, Surf. Sci. Rep. 71 (2016) 391–409. https://doi.org/10.1016/j.surfrep.2016.03.002.

[58] A. Serrano, O. Llorca-Hernando, A. Del Campo, F. Rubio-Marcos, O. Rodríguez de La Fuente, J.F. Fernández, M.A. García, Ag-AgO nanostructures on glass substrates by solid-state dewetting: From extended to localized surface plasmons, J. Appl. Phys. 124 (2018). https://doi.org/10.1063/1.5049651.

[59] H.C. Kim, T.L. Alford, D.R. Allee, Thickness dependence on the thermal stability of silver thin films, Appl. Phys. Lett. 81 (2002) 4287–4289. https://doi.org/10.1063/1.1525070.

[60] P. Dutheil, A.L. Thomann, T. Lecas, P. Brault, M. Vayer, Sputtered Ag thin films with modified morphologies: Influence on wetting property, Appl. Surf. Sci. 347 (2015) 101–108. https://doi.org/10.1016/j.apsusc.2015.04.052.

[61] T. Gredig, E.A. Silverstein, M.P. Byrne, Height-height correlation function to determine grain size in iron phthalocyanine thin films, J. Phys. Conf. Ser. 417 (2013) 1–5. https://doi.org/10.1088/1742-6596/417/1/012069.

[62] V. Ioannou-Sougleridis, V. Constantoudis, M. Alexe, R. Scholz, G. Vellianitis, A. Dimoulas, Effects on surface morphology of epitaxial Y2O3 layers on Si (001) after postgrowth annealing, Thin Solid Films. 468 (2004) 303–309. https://doi.org/10.1016/j.tsf.2004.05.076.

[63] Q. Fu, W. Sun, Mie theory for light scattering by a spherical particle in an absorbing medium, Appl. Opt. 40 (2001) 1354–1361. https://doi.org/10.1364/AO.40.001354.

Chapter 4

Influence of microstructure on dielectric function and plasmonic properties of silver nanoparticles

4.1 Introduction

The dielectric and surface plasmon resonance properties of the metal nanoparticles play a crucial role in metallic nanostructure-based devices [1–4]. The metallic nanostructure is affected by its deposition process parameters (substrate temperature, deposition time), deposition techniques [5–11], and post-deposition treatment such as annealing temperature, and annealing time [12,13]. The deposition parameters and post-deposition treatment also affect other properties like voids, grains size, and surface roughness as well. Over the years, researchers have been studying the dielectric function of very thin silver films or nanoparticles synthesized using various techniques [14–17] and many theoretical and experimental research works have been done to study the optical properties of noble metal nanoparticles owing to their significant utility across various applications in electronics and optical devices [18–21]. It has been proven by many researchers that the optical constants of the films are dependent on the film thickness [22,23]. The optical and dielectric properties of ultra-thin films or nanostructures significantly differ from the bulk material. Due to the island structure or nanostructure, very thin silver films exhibit a free electron-like dispersion of the complex dielectric function with optical plasma resonance [24]. Generally, the applications based on surface plasmon use Ag films with the nanoparticles [25]. Optical techniques such as spectrophotometry, prism coupling, ellipsometry, etc., are typically used to investigate the optical characteristics of metal nanoparticles [26–28]. Spectroscopy ellipsometry (SE) is a powerful non-destructive measuring technique that provides accurate results even for very thin films. It can be easily used to investigate the optical and localized surface plasmon resonance (LSPR) properties of the nanostructured film. Optical constants in spectroscopic ellipsometry are often calculated by fitting experimental data to a parametric dispersion model. However, choosing a precise dispersion model for metallic films often requires a substantial foundation of prior information. Moreover, simultaneously fitting both thickness and dielectric function using the dispersion equation becomes notably challenging due to the profound connection

between thickness and the dispersion model, particularly in the case of ultra-thin films. Thus, choosing an appropriate dispersion model is crucial when using the SE approach [29].

Previously in the literature, the dielectric constant of the novel metallic films and their nanostructures (Ag, Au, Cu) have been measured using SE with different dispersion models. The dielectric function of silver nanoparticles and silver nanorods on silicon substrate have been calculated using variable angle ellipsometry by applying the combination of one Lorentz oscillator for the main LSPR, and one Tauc-Lorentz oscillator for the bulk silver [30]. The dielectric constant of the silver island on a glass substrate has been measured by the aid of ellipsometry using the combination of three Gauss and one Tanguy oscillators: Two Gauss Oscillator for the main LSPR, one Gauss oscillator for the bulk plasmon and one Tanguy oscillator for the interband transitions [31]. The dielectric constant for the gold island on glass substrate has been determined using Muller matrix ellipsometry and got the best fitting with the help four Gauss oscillators: one Gauss oscillator for main LSPR, two Gauss oscillator for the interband transition of the gold, and one Gauss oscillator for inhomogeneous broadening of LSPR [32]. The dielectric constant of the Cu nanostructure thin film has been measured using the combination of one Lorentz and three Gauss oscillators; Lorentz oscillator was used for the interband transition, two Gauss oscillators for the transverse and the longitudinal mode of surface plasmon resonance (SPR), and one Gauss oscillator was used for the copper oxides layers (top and interfacial) [33]. The optical constant of the silver thin films has been investigated by applying the combination of the Drude and Lorentz oscillators with the Bruggeman Effective Medium Approximation (BEMA) for the porosity study [34]. Ellipsometry is an indirect method of measuring the film structure (thickness, optical constant etc.). Therefore, it is necessary to choose the physical model in which the optical response will best match with the experimental data to determine the film parameters using spectroscopic ellipsometry.

With this motivation, in this chapter we have used a combination of Drude, Lorentz model and Gauss oscillators with the Bruggeman effective medium approximation (BEMA) to determine the dielectric constants of Ag NPs and continuous films by SE measurements. This model is more suitable for the metallic films/nanostructure to account for all the characteristics related to their surface, bulk and optical properties. The measured SE data was fitted using four-layer structure by applying the Drude-Lorentz model to account for intraband and interband transitions in metallic films along with two Gaussian oscillators which correspond to LSPR due to the presence of nanostructures. The BEMA was also simultaneously applied to calculate

the void fraction arising due to the conversion of the continuous film into nanostructures and top layer's roughness. The results of SE studies have been correlated with the microstructure and LSPR properties probed using FESEM, AFM, XRD and UV-Vis-NIR absorbance spectroscopy.

4.2 Experimental details

The silver nanoparticles (Ag NPs) were grown on corning glass 1737 substrate by solid state dewetting of sputtered silver precursor films using RF magnetron sputtering technique as described in section 2.1, chapter 2. The silver precursor thin films were deposited at different RF power of 40, 50, 60, 70, 80 Watt for 60 s time duration keeping other parameters constant as mentioned in section 3.2 of chapter 3. For the growth of the silver nanoparticles by SSD process, post deposition annealing was performed under vacuum at a base pressure $\sim 10^{-6}$ mbar at 400 ℃ for 1h [35]. Thickness of deposited Ag precursors thin films were measured by stylus profilometer. The microstructure of annealed silver films (Ag NPs) were characterized by Field Emission Scanning Electron Microscope. Atomic force microscopy (AFM) was done for the surface roughness. Structure of films was probed using X-ray diffractometer. The optical absorbance spectra of silver nanoparticles were recorded by UV-Vis-NIR spectrometer. Spectroscopic ellipsometry (SE) measurements were done in the photon energy range of 1.0 - 4.5 eV at an incidence angle of 60° by spectroscopic ellipsometer. The spectroscopy ellipsometry analyzer (SEA) software was used to analyze the SE data. This software used a standard regression based Levenberg-Marquardt algorithm (LMA) to minimize the value of the root means square error (RMSE). All details of these characterization techniques are given in chapter 2.

4.3 Ellipsometry modeling

4.3.1 Choice of suitable model for SE data fitting

SE directly measures the amplitude ratio (ψ) and phase difference (Δ) of the reflected light oriented in the parallel (p-) and perpendicular (s-) directions with respect to plane of incidence as a function of wavelength or energy [36]. The polarization change ρ which is the ratio of reflectance of p polarized (r_p) and s polarized (r_s) light is given by Eq. 4.1

$$\rho = \frac{r_p}{r_s} = (\tan\psi)e^{i\Delta} \tag{4.1}$$

With amplitude ratio $\tan\psi$ and the phase difference $\Delta = \phi_p - \phi_s$.

The relative dielectric function for a uniform, isotropic, and optically opaque material with a smooth surface is directly related to the ρ and can be derived from the ellipsometry measurement using Fresnel's equation through [36]

$$< \varepsilon_r >=< \varepsilon_1 > + i < \varepsilon_2 >= \sin^2(\theta_0)\left[1 + \left(\frac{1-\rho}{1+\rho}\right)^2 \tan^2(\theta_0)\right] \quad (4.2)$$

Where ε_1 and ε_2 are real and imaginary parts of the dielectric function and θ_0 is the angle of incidence. The dielectric function is therefore directly determined from the measurement of the ψ and Δ using equation (4.1). The relative dielectric function relates to the complex refractive index N through

$$N = n + ik = \sqrt{\varepsilon_r} \quad (4.3)$$

For the metallic thin films, the dielectric function is dominated by the intraband transitions of free electrons which can be described by the Drude model [37]

$$\varepsilon_{Drude}(E) = \varepsilon_\infty - \frac{{E_p}^2}{E^2 + iE\Gamma_{\text{Drude}}} \quad (4.4)$$

Where $E_p = \hbar\omega_p$ and Γ_{Drude} are plasma energy and broadening which are related to the scattering. Here ω_p is the plasma frequency which is related to the effective mass of the electron (m^*) and free electron density (N_e) and can be defined as $\omega_p = \sqrt{N_e e^2/\varepsilon_0 m^*}$. The parameter ε_∞ accounts for the net contribution from the positive ion cores and the value of the ε_∞ varies in the range from 1-10. Though the Drude model describe the free electron contribution with the plasma frequency and the damping constant. However it neglects the band structure effects which describes the interband transitions of electron from *d* band to *sp* band and also contribute to the dielectric function. A Lorentz oscillator was added to account for the interband transitions [37]

$$\varepsilon_{Lorentz}(E) = \frac{f{E_0}^2}{({E_0}^2 - E^2 - iE\Gamma_{\text{Lorentz}})} \quad (4.5)$$

Where f is the oscillator strength E_0 is the oscillator position and Γ_{Lorentz} is the oscillator width.

LSPR properties of the metal nanoparticles are well described by the Gauss oscillator. The contribution to the dielectric constant due to the Gauss oscillator is defined as [31,36].

$$\varepsilon_{1Gauss}(E) = \frac{2A}{\sqrt{\pi}}\left[D\left(\frac{E+E_0}{\sigma}\right) - D\left(\frac{E-E_0}{\sigma}\right)\right] \quad (4.6\ a)$$

$$\varepsilon_{2Gauss}(E) = A\left[exp\left\{-\left(\frac{E-E_0}{\sigma}\right)^2\right\} - exp\left\{-\left(\frac{E+E_0}{\sigma}\right)^2\right\}\right] \qquad (4.6\ b)$$

Where A is the amplitude of the oscillator, E_0 is the oscillator peak position and D is the operator (Dawson function) [36]. The broadening (B_r) of the peak is related to Full width at Half maxima (FWHM) $\sigma = B_r/2\sqrt{\ln 2}$.

Since the LSPR contribution to the dielectric constant depends upon the shape and size of nanoparticle and therefore two gauss oscillators were added in the model to account LSPR properties of Ag NPs.

Now the effective relative dielectric constant can be written as combinations of all the oscillators:

$$\varepsilon_{effective} = \varepsilon_{\infty} + \varepsilon_{Drude} + \varepsilon_{Lorentz} + \sum_{i=1,2} \varepsilon_{iGauss} \qquad (4.7)$$

The silver nanostructure layer is having mixed volume fraction of void and silver therefore to calculate the void fraction and surface roughness, an effective medium approximation (EMA) was used [46].

$$\sum_{i=1}^{n} f_i \frac{\varepsilon_i(E) - \varepsilon(E)}{\varepsilon_i(E) + 2\varepsilon(E)} = 0 \qquad (4.8)$$

Where f_i is the volume fraction and $\varepsilon_i(E)$ is the dielectric function of the i^{th} phase. In our SE modelling, the two phases are Ag NPs and voids respectively.

4.3.2 Formation of layer structure for data fitting

Optical model for SE data fitting is shown in Fig. 4.1. A four-layer structure consisting of void, corning glass of 1 mm thickness, main layer of Ag NPs with voids, and a surface roughness layer was used for the SE analysis of experimental data.

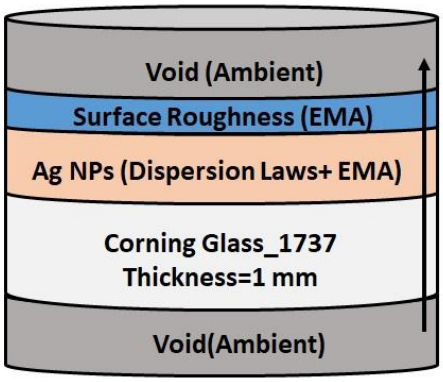

Fig. 4.1 Optical model for the spectroscopic ellipsometry data fitting.

For the calculation of the dielectric constant and LSPR properties, proposed model was applied on main Ag NPs layer. BEMA was used to calculate the void fraction in Ag NPs layer and surface roughness of the top layer.

4.4 Results and Discussion

Using a stylus profilometer, the thickness of the as-deposited silver films was measured, and found to range from 15 nm to 65 nm due to increase in the deposition rate by changing the rf power from 40 to 80 Watt. The results are shown in table 4.1.

Table 4.1 The thickness of Ag precursor films (as deposited) measured by stylus profilometer, average particle size of Ag NPs, and surface coverage (post annealing) from FESEM images calculated by *ImageJ* software.

RF Power (Watt)	Thickness (nm)	Average Particle Size (nm)	Surface Coverage (%)
40	15±2	50±2	27
50	25±3	70±6	30
60	40±3	100±10	34
70	50±4	-	-
80	65±5	-	-

4.4.1 FESEM Analysis

The continuous films converted into nanoparticles after annealing due to solid state dewetting (SSD) [35,38]. Fig. 4.2 displays the FESEM pictures of the Ag NPs produced by SSD on a corning glass substrate from Ag precursor films deposited at different RF powers. Using *ImageJ* software and thresholding method, the average particle size and surface coverage from FESEM pictures were estimated and values are listed in table 4.1. It was observed that the Ag nanoparticles of 50±2 nm size with uniform distribution and near spherical shape were formed for rf power of 40 Watt. However, with increasing the rf power (50 and 60W), the particle size was increased with mixed spherical and oval shapes and non-uniform distribution on the surface. An increase in the Ag NPs size with increasing rf power is due to the higher thickness of the corresponding films. Furthermore, no clear formation of Ag NPs is seen for thick films (> 50 nm) deposited at RF power of 70 Watt, and FESEM pictures are identical to those for uniformly deposited films. Histograms are plotted using FESEM data to determine particle size and distribution, as illustrated in Fig. 4.3 (a)-(c).

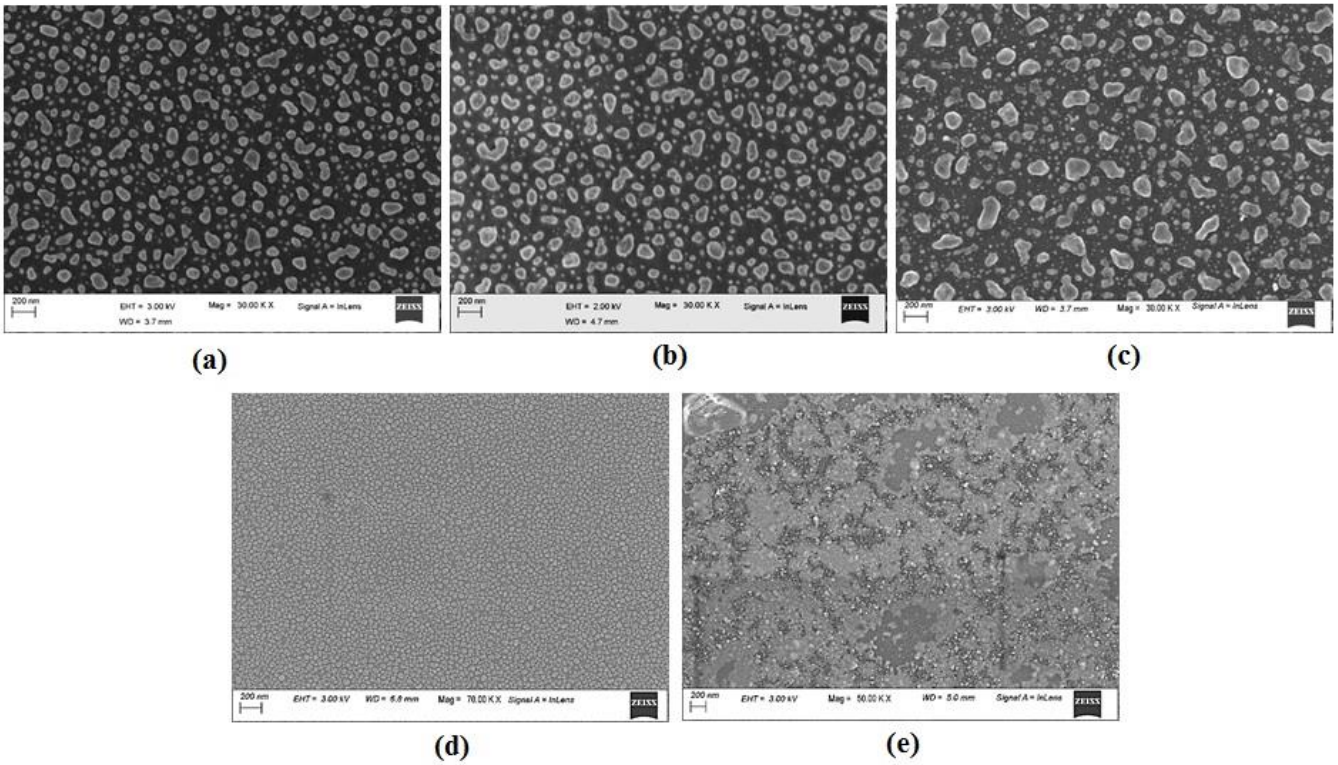

Fig. 4.2 SEM images of Ag NPs on corning glass at different RF power on 200 nm scale. (a) for 40 Watt, (b) for 50 Watt, (c) for 60 Watt (d) for 70 Watt, and (e) for 80 Watt.

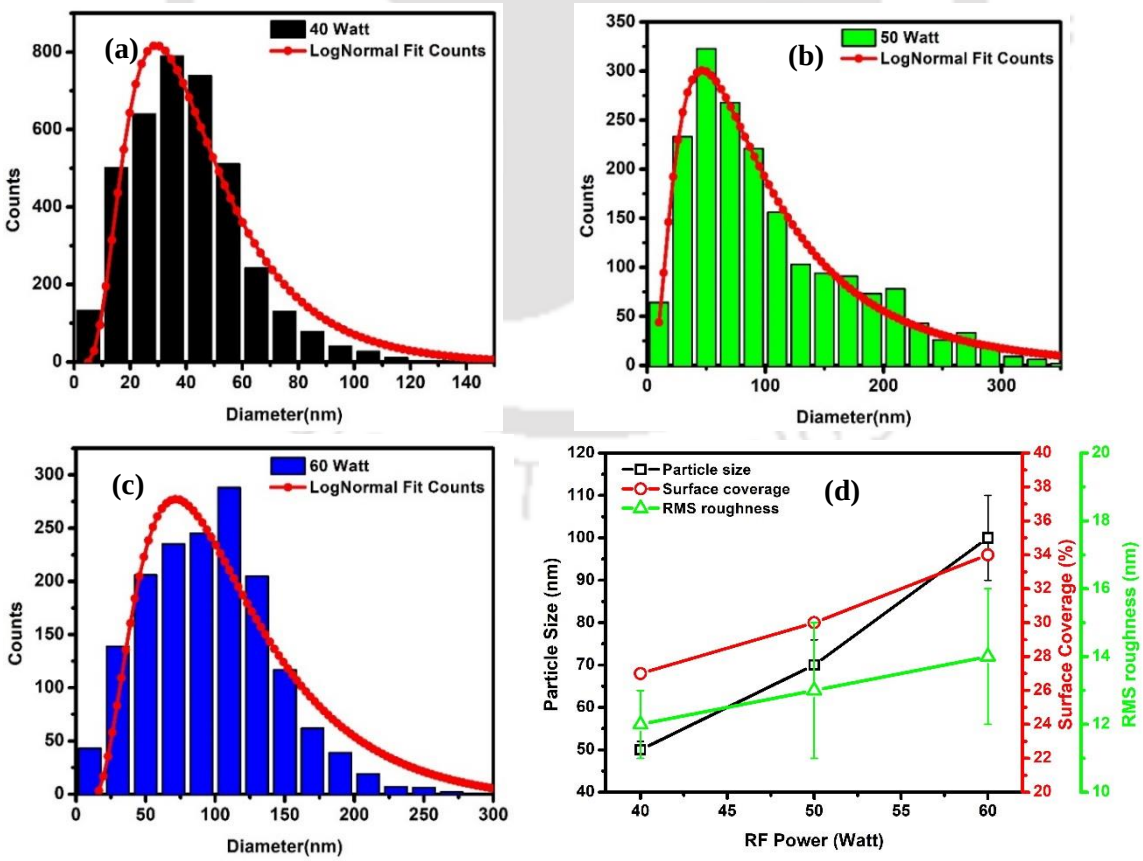

Fig. 4.3 Histogram images of Ag NPs at different RF power. (a) for 40 Watt, (b) for 50 Watt, (c) for 60 Watt (d) average particle size, surface coverage by the particles and RMS roughness (from AFM) for 40,50 and 60 Watt.

Fig. 4.3 (d) shows the variation in average particle size, surface coverage determined by FESEM, and RMS roughness evaluated by AFM (explained later) with rf power. Surface coverage and the RMS roughness linearly increase with the particle size.

4.4.2 XRD Analysis

Fig. 4.4 displays the XRD spectra of Ag NPs at different RF power. The polycrystalline nature of the films is demonstrated by the presence of XRD peaks at 38.2°, 44.2°, 64.5°, and 77.4° which correspond to the (111), (200), (220), and (311) planes of silver (JCPDS 4-0783), respectively for all films. An increase in the intensity for (111) peaks with the RF power is seen owing to the increase in the average particle size or thickness of the precursor film. Debye-Scherrer's formula ($D = 0.9\lambda/\beta\cos\theta$) was used to estimate the crystallite size. In this formula, D represents the average crystallite size, λ stands for the X-ray wavelength, β and θ correspond to the FWHM of the XRD peak, and the diffraction angle of the respective XRD peak. The crystallite size was determined by considering the most prominent peak associated with the (111) plane. A linear increase in the crystallite size (D) with the RF power is observed, and the corresponding values can be found in Table 4.2. The interplanar distance (d) values for (111), (200), (220) and (311) planes of silver are 2.35, 2.04, 1.44, and 1.23 Å respectively.

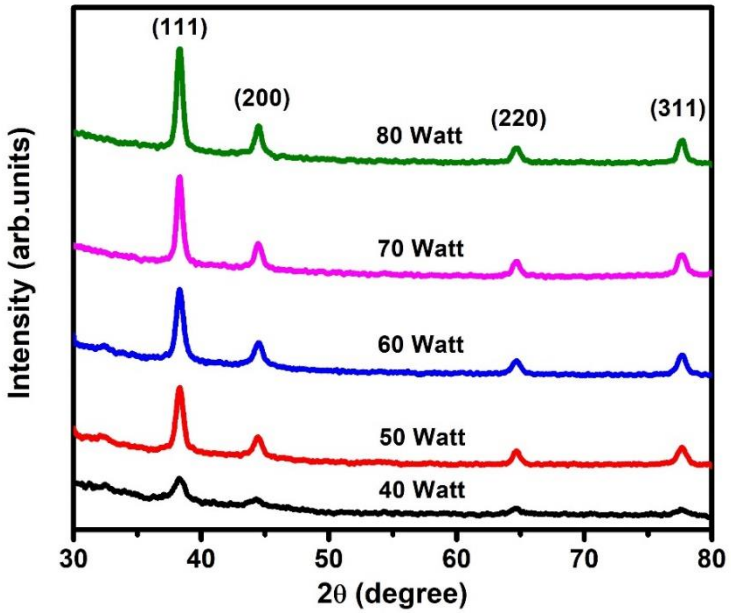

Fig. 4.4 XRD spectra of Ag NPs on corning glass at different RF power: 40-80 Watt.

4.4.3 AFM Analysis

The surface morphology of Ag NPs for different rf power is shown in Fig. 4.5. AFM image for the low rf power shows the uniform and well-separated nanoparticles. As the rf power is increased from 40 Watt to 60 Watt, the size of the nanoparticles became bigger and a further

increase in rf power resulted in a smooth surface with small grains. These observations from AFM are similar to those from FESEM images. Due to increase in nanoparticle size and irregularity in shape, the root-mean-square (RMS) roughness of the Ag NPs is increased with the increase in rf power from 40-60 Watt.

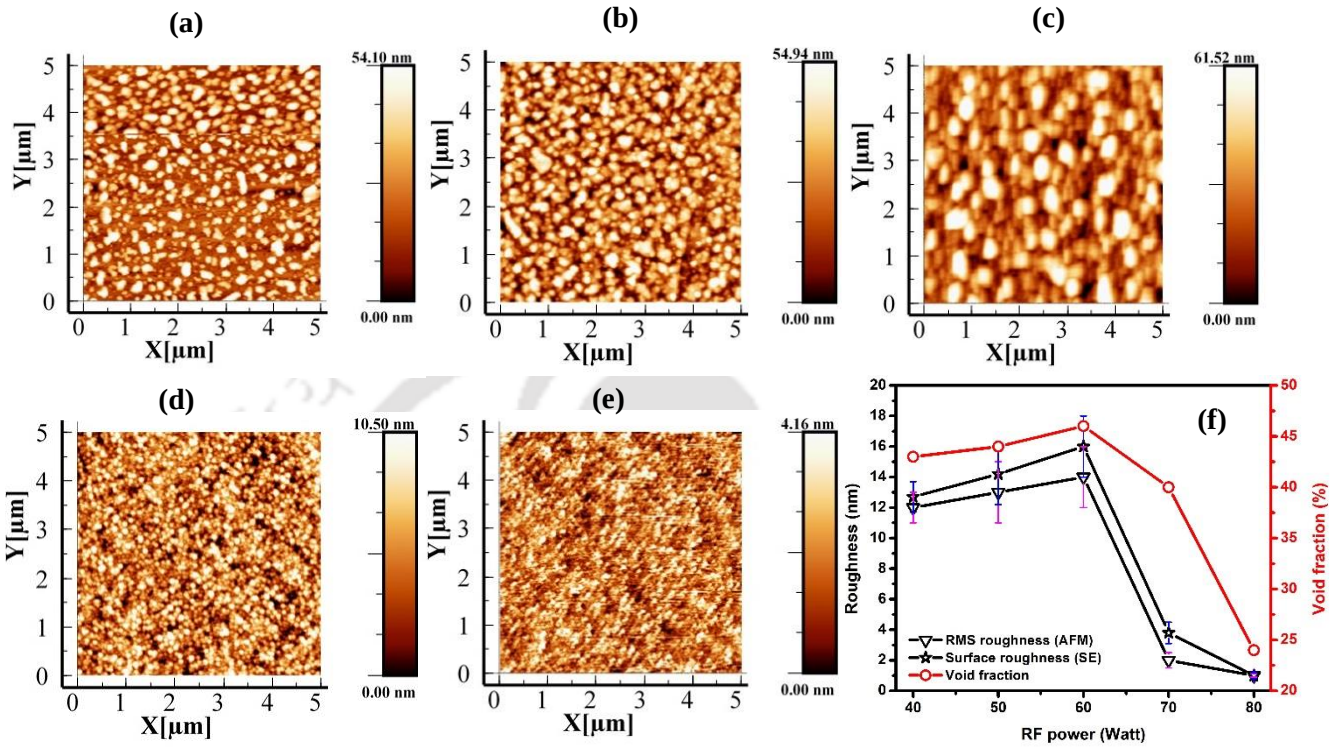

Fig. 4.5 AFM images of Ag NPs on $5\mu m \times 5\mu m$ square region for different RF power. (a) For 40 Watt, (b) for 50 Watt, (c) for 60 Watt, (d) for 70 Watt, (e) for 80 Watt, (f) RMS roughness, surface roughness and void fraction plot for RF power variation.

Table 4.2 The values of crystallite size calculated from XRD, roughness calculated from AFM and SE measurement, void fraction from SE measurement.

RF Power (Watt)	Crystallite size *(D)* (nm)	Roughness (nm)		Void fraction (%)
		AFM	SE	
40	6.2	12±1	12.7±1	43
50	11.7	13±2	14.2±2	44
60	13.1	14±2	16.0±2	46
70	14.3	2±0.5	3.8±0.7	40
80	14.0	1±0.1	1.0±0.2	24

However, for the higher rf power (70, 80 Watt), AFM images have low values of root-mean-square (RMS) roughness indicating the smooth surface due to the continuous film and also

confirm that no isolated particle formation took place for these films. The RMS roughness of Ag NPs estimated from AFM, surface roughness, and void fraction determined from SE (explained later) are shown together in Fig. 4.5 (f) to link the void fraction with the roughness. These results are provided in table 4.2. A linear relation between surface roughness and void fraction is observed.

4.4.4 Spectroscopic ellipsometry Analysis

The spectroscopic ellisopmeter directly measures the $\tan\psi$ and $\cos\Delta$, which are used to extract the optical constants. The variation of $\tan\psi$ and $\cos\Delta$ with rf power is shown in Fig. 4.6. A sharp transition in $\tan\psi$ observed around ~3.60-3.77 eV is due to the interband transition in silver thin films and nanostructures. The position is slightly below the reported value of 3.9 eV for bulk silver films, however this edge shifts toward the higher energy due to microstructral change from nanoparticles to continuous films at higher rf power Moreover, an upward shift in $\tan\psi$ with an increase in RF power from 40- 80 Watt is due to increase in surface reflection. The lower values of $\tan\psi$ for films with nanoparticles is attributed to the lower thickness of the films and the nonuniform surface coverage. The values of Phase shift $\cos\Delta$ (Fig 4.6 b) varies from -1 to 1 with photon energy, indicating the change in phase difference from 180° to 0°. A peak is observed at around ~ 3.71-3.85 eV, which is close to the transition energy in $\tan\psi$ plot. Furthermore, the peak in $\cos\Delta$ shifts to higher energy side with an increase in rf power.

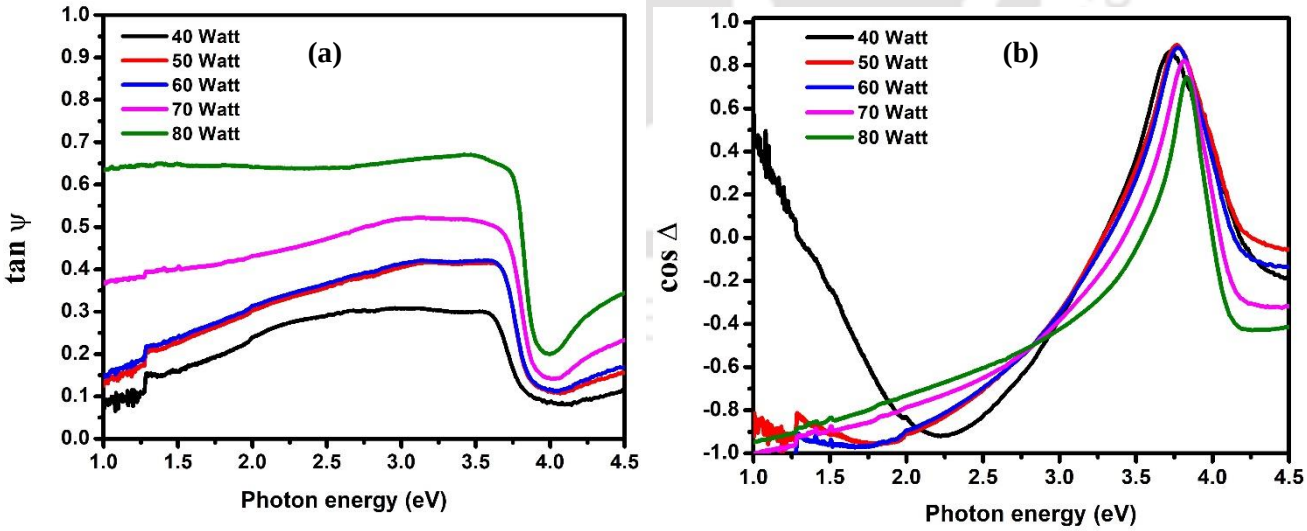

Fig. 4.6 $\tan\psi$ (a), and $\cos\Delta$ (b) spectra of Ag NPs at different RF power: 40-80 Watt.

Fig. 4.7 shows the measured real ($< \varepsilon_1 >$) and imaginary ($< \varepsilon_2 >$) part of the pseudo dielectric function along with the curve fitted using proposed model. A good fit with low value of RMSE validates the proposed model. The fitting parameters with RMSE values are listed in Table 4.3.

It can be seen from Fig. 4.7 (a) that the behavior of the real part ($< \varepsilon_1 >$) of the pseudo dielectric function is completely different for the silver nanoparticle (low rf power < 70 Watt) and the silver films with the relatively higher thickness (high rf power > 60 Watt). For the Ag NPs at 40 Watt, a peak at 2.26 eV is observed due to the contribution of the bound electrons [10] and the peak shifted toward the lower energy as the particle size increased. But for the thick silver films (70 & 80 Watt), as the nanoparticles are not present in the sample, free carrier absorption (FCA) is dominant over the bound electrons and no peak in $< \varepsilon_1 >$ spectra is observed. Furthermore, the real part $< \varepsilon_1 >$ has the positive values for the Ag NPs while it shows negative values for the continuous film at higher rf power, indicating the metallic nature for these films.

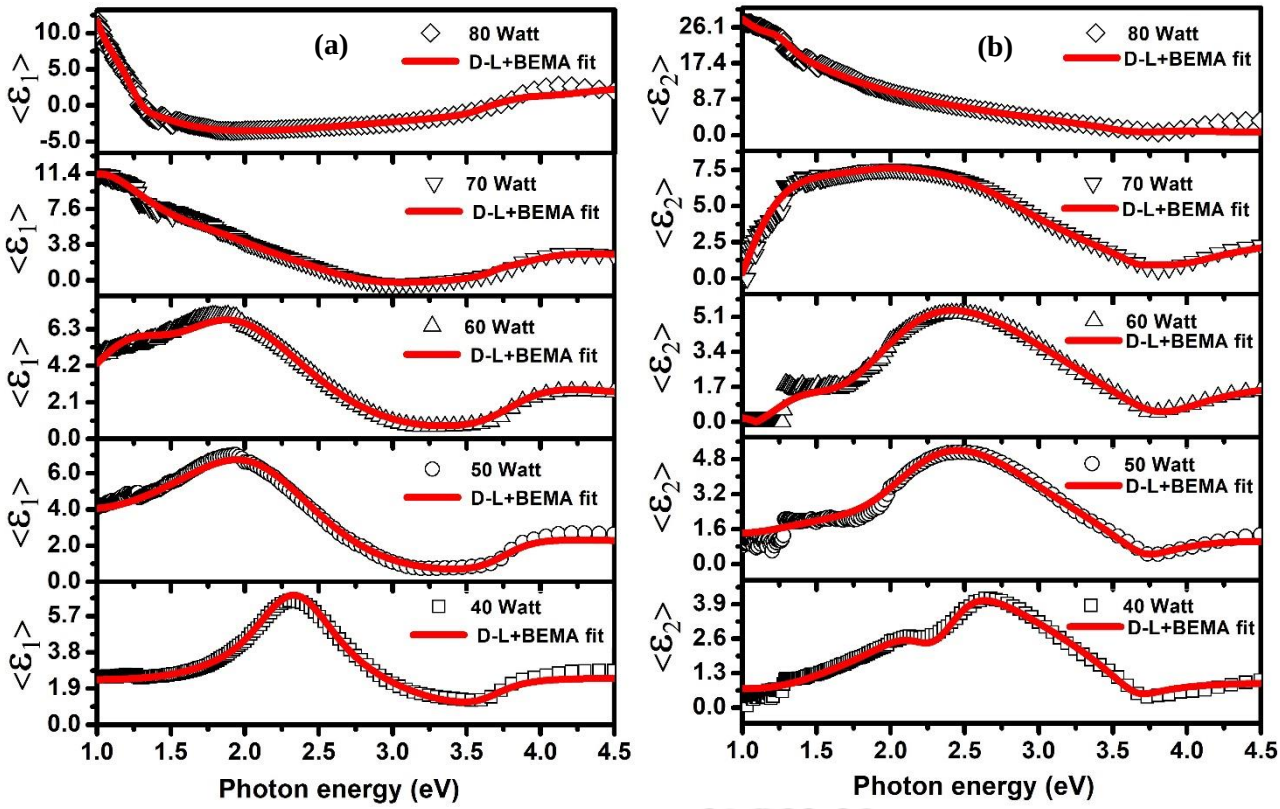

Fig. 4.7 The measured and fitted real ($< \varepsilon_1 >$) (a), and the imaginary ($< \varepsilon_2 >$) part (b) of the pseudo dielectric function spectra of Ag NPs on corning glass deposited at different RF power: 40-80 Watt.

The imaginary ($< \varepsilon_2 >$) part of the pseudo dielectric function shown in Fig. 4.7 (b) also shows the peak at 2.41 eV for the Ag NPs at 40 Watt due to the LSPR and the peak position is shifted towards the lower energy as the particle size is increased. For the thicker films, no peak is observed in $< \varepsilon_2 >$ due to the absence of the nanoparticles and their LSPR nature. Additionally, an enhancement in peak amplitude is observed due to the LSPR of Ag NPs of different sizes.Simlar thickness dependent features in SE data have also been reported for nano

metal thin films. [39,40]. From the fitting parameters of SE data listed in table 4.3, it is observed that plasma energy/frequency corresponding the intraband transition (Drude model) increases with increase in rf power used for deposition of Ag films. Plasma energy increases from 2.04 eV to 4.14 eV with an increase in nanoparticles size for the rf power 40-60 Watt. Furthermore, for 80 Watt films, plasma energy attains a high value of 8.63 eV due to an increase in free electron density at higher rf power. This value (8.63 eV) is close to the reported value for bulk silver [18,36]. This increase in plasma energy for 80 Watt indicates that the formation of nanoparticles did not take place so efficiently for these thick films and films behaves like the bulk Ag films [41–44]. This is in agreement with the metallic nature for 80 Watt film observed from the real part of the pseudo dielectric function. The Lorentz model describes the interband transitions of electron from $4d\ to\ 5s$ for the silver which occurs ~ 3.9 eV for bulk silver. [10]. In our case, the peak energy for the interband transition shifts from 3.7 eV towards 4.10 eV with an increase in the rf power due to the transition from the nanostructure to the bulk silver. Two Gauss oscillators are used corresponding to the main LSPR and the energy of the oscillators varies towards the lower energy with an increase in the particle size. The LSPR mode is very sensitive to the shape of the particles; Spherical Ag NPs have only one LSPR peak while the silver rods have longitudinal and transverse modes of the LSPR [45,46]. In our case, the peak positions for the two gauss oscillators (table 3) are only slightly different for low rf films due to formation of near spherical shaped nanoparticles as observed in FESEM images. The peak position is however significantly different for 60 Watt film due to formation of irregular shaped large particles and increase in interparticle separation. From the effective medium approximation, we observed that the void fraction has increased with the increase in the rf power.

Table 4.3 The values of plasma energy, and central energy of Lorentz and Gauss oscillator, obtained from SE fitting.

RF Power (Watt)	Drude E_p(eV)	Lorentz E_0(eV)	$Gauss_1$ E_0(eV)	$Gauss_2$ E_0(eV)	ε_∞	RMSE
40	2.04±0.18	3.70±0.24	2.41±0.20	2.26±0.08	3.35	0.20
50	2.94±0.25	3.80±0.30	2.30±0.12	2.37±0.10	3.41	0.19
60	4.14±0.33	3.85±0.27	1.89±0.15	2.30±0.20	4.50	0.21
70	7.75±1.74	4.06±0.63	2.88±0.17	2.10±0.27	8.40	0.20
80	8.63±3.14	4.10±0.14	2.46±0.10	2.38±0.05	8.70	0.14

The surface roughness of the top layer first increased with rf power up to 60 Watt and then it started to decrease which is again due to the smooth surface of these films. This trend in surface roughness variation from SE modeling, shown in Fig. 4.5 (f) and table 4.2, are consistent with rms roughness values obtained from AFM measurements.

The Refractive index (n) and the extinction coefficient (k) extracted from the SE fitting are shown in Fig. 4.8. For comparison, the refractive index and extinction coefficient of bulk Ag from Palik's database is also plotted [47]. The refractive index for lower thickness films at low RF power show a peak, which is not typically observed in bulk Ag, indicating a nonmetallic behavior (Fig. 4.8 a) [48]. On the other hand, for high RF power, this peak is absent, revealing the metallic nature of these films. The extinction coefficient increases monotonically with the increase in RF power and follows a similar trend as the imaginary part of the pseudo-dielectric function (Fig. 4.8 b). Thick films deposited at high RF power exhibit behavior more closely resembling to bulk Ag films. Similar behavior of refractive index and extinction coefficient with thickness has also been reported for metal nanoparticles/thin films [48]. The difference in (*n*,*k*) spectra between the thick samples deposited at high RF power and the data reported by Palik is primarily attributed to the post-annealing treatment of these films, which can lead to significant changes in the optical properties. We have also compared our refractive index and extinction coefficient spectra with the silver oxide films prepared in different oxygen-gas ratio conditions and annealed at different temperatures [49]. The comparison revealed a significant difference in refractive index and extinction coefficient values, confirming that no oxidation of Ag NPs/films occurred. This finding is further supported by X-ray diffraction (XRD) data, which showed no diffraction peak corresponding to silver oxide, providing additional evidence of the absence of oxidation in the Ag NPs/films.

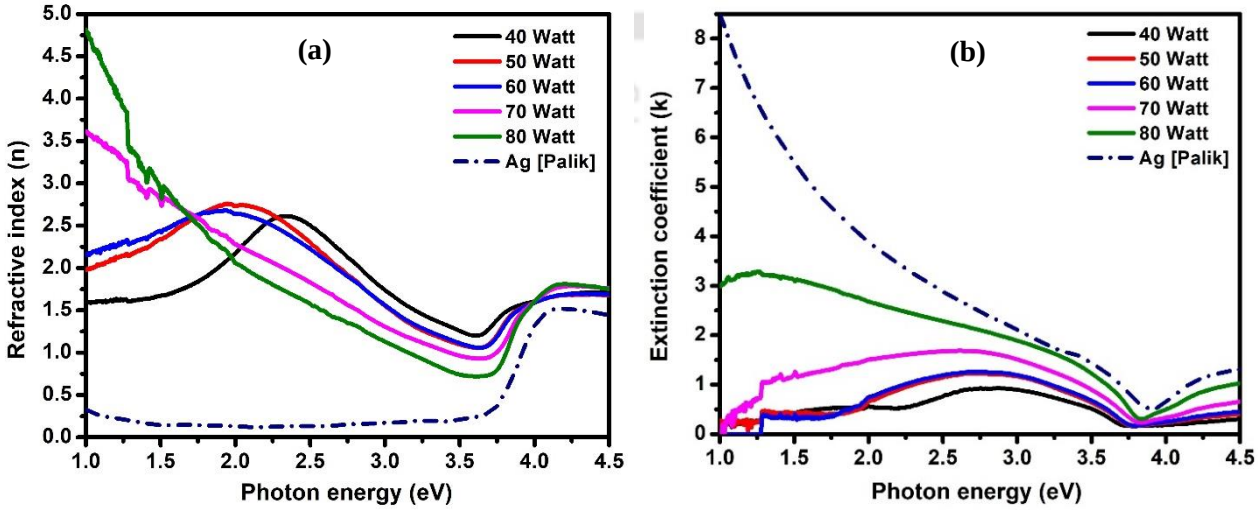

Fig. 4. 8 Refractive index (a), and extinction coefficient spectra (b) of Ag NPs for different RF power: 40-80 Watt.

4.4.5 UV-Vis-NIR analysis

To validate the SE measurement, plasmonic properties of Ag NPs, in terms of their absorbance, were measured with a double beam UV-Vis-NIR spectrometer Lambda 950 in the photon energy range of 1.0-4.5 eV and are shown in Fig 4.9 (a). The spectra show the characteristics of the Ag NPs only after excluding the background influence of the glass substrate from the raw optical observations. From the absorbance spectra, it can be observed that for RF power of 40 Watt, the LSPR peak position of Ag NPs is around 2.47 eV, and with the increase in RF power from 40 Watt to 60 Watt, the LSPR peak is shifted towards lower energy at 2.11 eV due to formation of large size nanoparticles. There is no LSPR peak for the RF power of 70 and 80 Watt. These findings are in good accordance with the findings of the SE. It is also observed that absorbance has enhanced with increase in the RF power. The change in Ag NPs morphology results in the improvement of their optical performance.

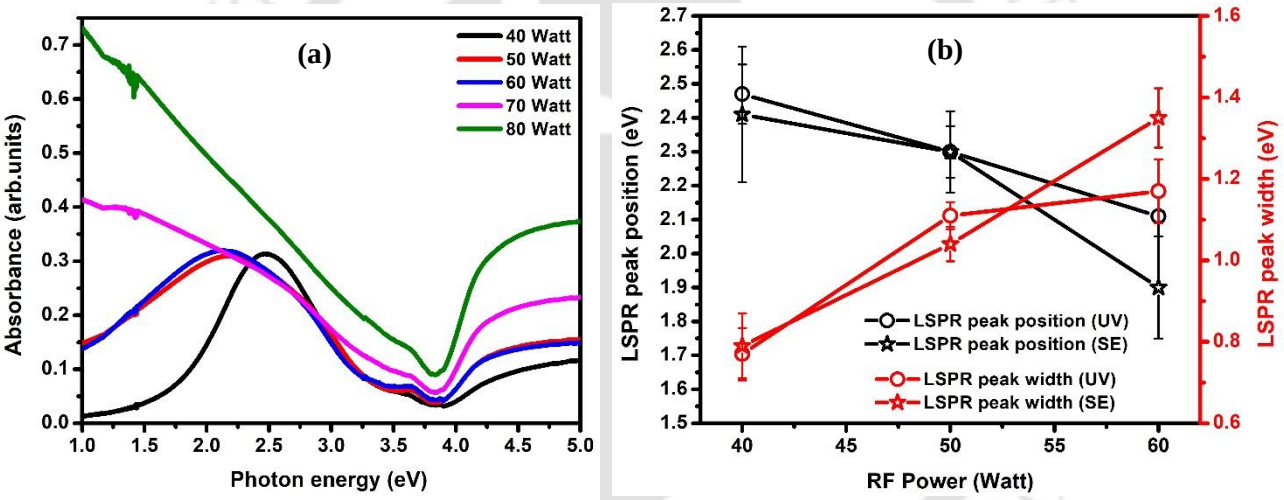

Fig. 4.9 Absorbance spectra of Ag NPs at different RF power: 40-80 Watt (a), and LSPR peak position and peak width from UV and SE (b).

Table 4.4 The average particle size from FESEM, LSPR peak position and peak width calculated from UV-Vis-NIR and SE measurement.

RF power (Watt)	Average Particle Size (nm)	LSPR peak position (eV)		LSPR peak width (eV)	
		UV	SE	UV	SE
40	50±2	2.47	2.41	0.77	0.79
50	70±6	2.30	2.30	1.11	1.04
60	100±10	2.11	1.89	1.17	1.25

LSPR peak position and LSPR peak width calculated from UV and for the Gauss oscillator in our model are shown in Fig. 4.9 (b), and the values are listed in table 4.4 along with the

corresponding average particle size estimated from FESEM. LSPR peak position values and the broadening of the peak from the UV matched well with the SE.

4.5 Conclusions

In summary, influence of microstructure on dielectric and plasmonic properties of Ag NPs is studied using spectroscopic ellipsometry over a broad spectral range from 1.0 - 4.5 eV. The effective dielectric function and plasmonic properties of Ag NPs are well described using a multiple oscillator approach that can take into account the different light-matter interaction phenomenon which occur in the investigated spectral range. The dispersion model containing one Drude-Lorentz model and two Gauss oscillators is found suitable to describe the intraband, interband and the LSPR contribution to the dielectric function respectively. The Bruggeman effective medium approximation is simultaneously applied to measure the void fraction and the surface roughness. The microstructural changes, induced by rf power variation, affect the intraband, interband transitions and LSPR properties of Ag NPs. The plasma energy evaluated from the Drude model, corresponding to intraband transition, shows an increase with the increase in the rf power due to the structural transition from the nanoparticles to the bulk film. This change in microstructure from nanoparticle formation to continuous films is also reflected in the values of void fraction and surface roughness, calculated from SE using Bruggeman Effective Medium Approximation (BEMA). More importantly the proposed model for SE data analysis has successfully demonstrated the strong correlation between the microstructure and the LSPR properties of Ag NPs with the accurate output comparable to the results obtained by the AFM, and UV-Vis-NIR spectroscopy.

4.6 References

[1] B. Karthikeyan, M. Anija, C.S. Suchand Sandeep, T.M. Muhammad Nadeer, R. Philip, Optical and nonlinear optical properties of copper nanocomposite glasses annealed near the glass softening temperature, Opt. Commun. 281 (2008) 2933–2937. https://doi.org/10.1016/J.OPTCOM.2008.01.032.

[2] J. Zhang, L. Zhang, W. Xu, Surface plasmon polaritons: Physics and applications, J. Phys. D. Appl. Phys. 45 (2012). https://doi.org/10.1088/0022-3727/45/11/113001.

[3] J. Jana, M. Ganguly, T. Pal, Enlightening surface plasmon resonance effect of metal nanoparticles for practical spectroscopic application, RSC Adv. 6 (2016) 86174–86211.

https://doi.org/10.1039/c6ra14173k.

[4] A. Parretta, M.K. Jayaraj, A. Di Nocera, S. Loreti, L. Quercia, A. Agati, Electrical and Optical Properties of Copper Oxide Films Prepared by Reactive RF Magnetron Sputtering, Phys. Status Solidi. 155 (1996) 399–404. https://doi.org/https://doi.org/10.1002/pssa.2211550213.

[5] B. Prével, J. Lermé, M. Gaudry, E. Cottancin, M. Pellarin, M. Treilleux, P. Mélinon, A. Perez, J.L. Vialle, M. Broyer, Optical properties of nanostructured thin films containing noble metal clusters: AuN, (Au0.5Ag0.5)N and AgN, Scr. Mater. 44 (2001) 1235–1238. https://doi.org/https://doi.org/10.1016/S1359-6462(01)00852-1.

[6] M. Yano, M. Fukui, M. Haraguchi, Y. Shintani, In situ and real-time observation of optical constants of metal films during growth, Surf. Sci. 227 (1990) 129–137. https://doi.org/https://doi.org/10.1016/0039-6028(90)90400-3.

[7] H.T.G. Hentzell, B. Andersson, S.-E. Karlsson, Grain size and growth of Ni-Rich Ni-Al alloy films, Acta Metall. 31 (1983) 2103–2111. https://doi.org/https://doi.org/10.1016/0001-6160(83)90029-9.

[8] A.L. Lereu, F. Lemarchand, M. Zerrad, M. Yazdanpanah, A. Passian, Optical properties and plasmonic response of silver-gallium nanostructures, J. Appl. Phys. 117 (2015) 063110. https://doi.org/10.1063/1.4906950.

[9] O. Peña-Rodríguez, M. Caro, A. Rivera, J. Olivares, J.M. Perlado, A. Caro, Optical properties of Au-Ag alloys: An ellipsometric study, Opt. Mater. Express. 4 (2014) 403–410. https://doi.org/10.1364/OME.4.000403.

[10] H. Ehrenreich, H.R. Philipp, Optical Properties of Ag and Cu, Phys. Rev. 128 (1962) 1622–1629. https://doi.org/10.1103/PhysRev.128.1622.

[11] B.R. Cooper, H. Ehrenreich, H.R. Philipp, Optical Properties of Noble Metals. II., Phys. Rev. 138 (1965) A494–A507. https://doi.org/10.1103/PhysRev.138.A494.

[12] A.N. Belov, S. V Bulyarsky, D.G. Gromov, L.M. Pavlova, O. V Pyatilova, Study of silver cluster formation from thin films on inert surface, Calphad. 44 (2014) 138–141. https://doi.org/https://doi.org/10.1016/j.calphad.2013.07.017.

[13] E. Thouti, N. Chander, V. Dutta, V.K. Komarala, Optical properties of Ag nanoparticle layers deposited on silicon substrates, J. Opt. 15 (2013) 35005.

https://doi.org/10.1088/2040-8978/15/3/035005.

[14] T. Yamaguchi, S. Yoshida, A. Kinbara, Continuous Ellipsometric Determination of the Optical Constants and Thickness of a Silver Film during Deposition, Jpn. J. Appl. Phys. 8 (1969) 559–567. https://doi.org/10.1143/jjap.8.559.

[15] P.B. Johnson, R.W. Christy, Optical Constants of the Noble Metals, Phys. Rev. B. 6 (1972) 4370–4379. https://doi.org/10.1103/PhysRevB.6.4370.

[16] T. Yamaguchi, S. Yoshida, A. Kinbara, Effects of Optical Anisotropy of Aggregated Silver Films on Ellipsometric Determination of n, k, and d, J. Opt. Soc. Am. 62 (1972) 634–638. https://doi.org/10.1364/JOSA.62.000634.

[17] U. Kreibig, Electronic properties of small silver particles: the optical constants and their temperature dependence, J. Phys. F Met. Phys. 4 (1974) 999–1014. https://doi.org/10.1088/0305-4608/4/7/007.

[18] M.A. Ordal, L.L. Long, R.J. Bell, S.E. Bell, R.R. Bell, R.W. Alexander, C.A. Ward, Optical properties of the metals Al, Co, Cu, Au, Fe, Pb, Ni, Pd, Pt, Ag, Ti, and W in the infrared and far infrared, Appl. Opt. 22 (1983) 1099–1119. https://doi.org/10.1364/AO.22.001099.

[19] M. Bergmair, K. Hingerl, P. Zeppenfeld, Spectroscopic Ellipsometry on Metallic Gratings, in: 2013: pp. 257–311. https://doi.org/10.1007/978-3-642-33956-1_7.

[20] J. Lv, Effect of wettability on surface morphologies and optical properties of Ag thin films grown on glass and polymer substrates by thermal evaporation, Appl. Surf. Sci. 273 (2013) 215–219. https://doi.org/https://doi.org/10.1016/j.apsusc.2013.02.015.

[21] S. Baba, A. Kinbara, M. Adachi, Island structure of sputter-deposited Ag thin films, Vacuum. 42 (1991) 279–282. https://doi.org/https://doi.org/10.1016/0042-207X(91)90037-J.

[22] O.S. Heavens, Optical properties of thin films, Reports Prog. Phys. 23 (1960) 1–65. https://doi.org/10.1088/0034-4885/23/1/301.

[23] A. Lehmuskero, M. Kuittinen, P. Vahimaa, Refractive index and extinction coefficient dependence of thin Al and Ir films on deposition technique and thickness, Opt. Express. 15 (2007) 10744–10752. https://doi.org/10.1364/OE.15.010744.

[24] T. Yamaguchi, H. Takahashi, A. Sudoh, Optical behavior of a metal island film, J. Opt. Soc. Am. 68 (1978) 1039–1044. https://doi.org/10.1364/JOSA.68.001039.

[25] O. Nicoletti, F. de la Peña, R.K. Leary, D.J. Holland, C. Ducati, P.A. Midgley, Three-dimensional imaging of localized surface plasmon resonances of metal nanoparticles, Nature. 502 (2013) 80–84. https://doi.org/10.1038/nature12469.

[26] L. Ward, Contours of constant Δ and Ψ in the ε 2– ε 4 plane for the ellipsometric functions, Opt. Laser Technol. - OPT LASER TECHNOL. 34 (2002) 513–521. https://doi.org/10.1016/S0030-3992(02)00051-8.

[27] D. Dalacu, L. Martinu, Optical properties of discontinuous gold films: finite-size effects, J. Opt. Soc. Am. B. 18 (2001) 85–92. https://doi.org/10.1364/JOSAB.18.000085.

[28] D.E. Aspnes, Spectroscopic ellipsometry of solids, Opt. Prop. Solids New Dev. (1976).

[29] A. Vial, T. Laroche, Description of dispersion properties of metals by means of the critical points model and application to the study of resonant structures using the FDTD method, J. Phys. D. Appl. Phys. 40 (2007) 7152–7158. https://doi.org/10.1088/0022-3727/40/22/043.

[30] T.W.H. Oates, M. Ranjan, S. Facsko, H. Arwin, Highly anisotropic effective dielectric functions of silver nanoparticle arrays, Opt. Express. 19 (2011) 2014–2028. https://doi.org/10.1364/OE.19.002014.

[31] M.N.M.N. Perera, D. Schmidt, W.E.K. Gibbs, S. Juodkazis, P.R. Stoddart, Effective optical constants of anisotropic silver nanoparticle films with plasmonic properties, Opt. Lett. 41 (2016) 5495–5498. https://doi.org/10.1364/OL.41.005495.

[32] M. Lončarić, J. Sancho-Parramon, H. Zorc, Optical properties of gold island films—a spectroscopic ellipsometry study, Thin Solid Films. 519 (2011) 2946–2950. https://doi.org/10.1016/j.tsf.2010.12.068.

[33] R. Kesarwani, A. Khare, Assessment of interfacial layer thickness of pulsed laser deposited plasmonic copper thin films via spectroscopic ellipsometer, Opt. Mater. (Amst). 93 (2019) 98–102. https://doi.org/10.1016/j.optmat.2019.05.009.

[34] M. Zhou, Y.-P. Li, S. Zhou, D.-Q. Liu, Optical Properties and Surface Morphology of Thin Silver Films Deposited by Thermal Evaporation, Chinese Phys. Lett. 32 (2015) 77802. https://doi.org/10.1088/0256-307x/32/7/077802.

[35] C. V. Thompson, Solid-state dewetting of thin films, Annu. Rev. Mater. Res. 42 (2012) 399–434. https://doi.org/10.1146/annurev-matsci-070511-155048.

[36] H. Fujiwara, Spectroscopic Ellipsometry: Principles and Applications, 2007. https://doi.org/10.1002/9780470060193.

[37] J. Liu, J. Lin, H. Jiang, H. Gu, X. Chen, C. Zhang, G. Liao, S. Liu, Characterization of dielectric function for metallic thin films based on ellipsometric parameters and reflectivity, Phys. Scr. 94 (2019). https://doi.org/10.1088/1402-4896/ab1606.

[38] F. Leroy, Ł. Borowik, F. Cheynis, Y. Almadori, S. Curiotto, M. Trautmann, J.C. Barbé, P. Müller, How to control solid state dewetting : A short review, Surf. Sci. Rep. 71 (2016) 391–409. https://doi.org/10.1016/j.surfrep.2016.03.002.

[39] J. Gong, R. Dai, Z. Wang, Z. Zhang, Thickness Dispersion of Surface Plasmon of Ag Nano-thin Films: Determination by Ellipsometry Iterated with Transmittance Method, (n.d.). https://doi.org/10.1038/srep09279.

[40] E.-T. Hu, Q.-Y. Cai, R.-J. Zhang, Y.-F. Wei, W.-C. Zhou, S.-Y. Wang, Y.-X. Zheng, W. Wei, L.-Y. Chen, Effective method to study the thickness-dependent dielectric functions of nanometal thin film, Opt. Lett. 41 (2016) 4907–4910. https://doi.org/10.1364/OL.41.004907.

[41] A.J. de Vries, E.S. Kooij, H. Wormeester, A.A. Mewe, B. Poelsema, Ellipsometric study of percolation in electroless deposited silver films, J. Appl. Phys. 101 (2007) 53703. https://doi.org/10.1063/1.2654234.

[42] M. Hövel, B. Gompf, M. Dressel, Dielectric properties of ultrathin metal films around the percolation threshold, Phys. Rev. B. 81 (2010) 35402. https://doi.org/10.1103/PhysRevB.81.035402.

[43] R.L. Olmon, B. Slovick, T.W. Johnson, D. Shelton, S.-H. Oh, G.D. Boreman, M.B. Raschke, Optical dielectric function of gold, Phys. Rev. B. 86 (2012) 235147. https://doi.org/10.1103/PhysRevB.86.235147.

[44] M.-L. Thèye, Investigation of the Optical Properties of Au by Means of Thin Semitransparent Films, Phys. Rev. B. 2 (1970) 3060–3078. https://doi.org/10.1103/PhysRevB.2.3060.

[45] V. Amendola, O. Bakr, F. Stellacci, A Study of the Surface Plasmon Resonance of Silver

Nanoparticles by the Discrete Dipole Approximation Method: Effect of Shape, Size, Structure, and Assembly, Plasmonics. 5 (2010) 85–97. https://doi.org/10.1007/s11468-009-9120-4.

[46] Z. Jiang, G. Wen, Y. Luo, X. Zhang, Q. Liu, A. Liang, A new silver nanorod SPR probe for detection of trace benzoyl peroxide, Sci. Rep. 4 (2014) 5323. https://doi.org/10.1038/srep05323.

[47] E.D. Palik, Handbook of optical constants of solids, Academic press, 1998.

[48] J. Gong, R. Dai, Z. Wang, Z. Zhang, Thickness Dispersion of Surface Plasmon of Ag Nano-thin Films: Determination by Ellipsometry Iterated with Transmittance Method, Sci. Rep. 5 (2015) 9279. https://doi.org/10.1038/srep09279.

[49] X.Y. Gao, S.Y. Wang, J. Li, Y.X. Zheng, R.J. Zhang, P. Zhou, Y.M. Yang, L.Y. Chen, Study of structure and optical properties of silver oxide films by ellipsometry, XRD and XPS methods, Thin Solid Films. 455–456 (2004) 438–442. https://doi.org/10.1016/j.tsf.2003.11.242.

Chapter 5

Plasmon-enhanced photoluminescence and Raman spectroscopy of silver nanoparticles

5.1. Introduction

The metal nanoparticles' size-dependent optical and electronic properties make them suitable for technological applications [1–3] in plasmonics, photonics, electronics, biology, and medicines [4,5]. Therefore, the size-controlled synthesis of metallic nanoparticles has gained the attention of researchers. The size and shape of the nanoparticles strongly depend on the growth conditions and the final structure depends upon the mechanism of its formation, which influence the optical properties of the nanostructure materials [6]. Among the nanoparticles of different metals, the noble metal (Au, Ag, Cu) nanoparticles exhibit localized surface plasmon resonance (LSPR) [7,8], which finds applications in biological sensors, solar cells, and surface-enhanced Raman spectroscopy (SERS) [9–12]. Since the LSPR strongly depends upon the size, morphology, and spatial orientation of the nanoparticles, the resonant wavelength and width of the LSPR can be tuned through the size, shape, and environmental control of the nanoparticles [3,13,14]. Fine-tuning of the surface plasmon wavelength makes the metallic nanostructure more attractive for various applications, including biosensors and photovoltaic devices [12,13,15,16]. The noble metal nanoparticles can also emit light at their LSPR band [17–19]. The metal nanostructure's PL has gained more interest due to its promising application in bioimaging and optical recording [20–22]. However unlike semiconductor materials, the probability of radiative transitions for the luminescence from the metal nanoparticles is very low as metals do not have a forbidden energy gap between the occupied and unoccupied states in the conduction band [23,24]. Due to this, the luminescence from noble metal nanoparticles has been studied very sparsely [24,25]. In metals, photoluminescence is originated from the radiative recombination of hot excited core holes and conduction band electrons [23] but in the metal nanoparticles, PL is enhanced due to the surface plasmon effect [26]. During last decades, PL from various plasmonic structures, including

spherical nanoparticles [27–29], and nanorods [30,31], has been studied. The PL from the noble metal nanoparticles has been reported for gold, silver, and copper [17,24,32]. Due to the strongest LSPR compared to other noble metal (Au and Cu) nanoparticles, Ag NPs have generated more interest in silicon-based thin film solar cells, glucose biosensors, and the photodetectors [33–35].

The strong local field induced by LSPR of metal nanoparticles can also boost the Raman signal by enhancing the Raman scattering on the surface of the nanoparticles or close to a rough metal surface by the localized field enhancement [10,12]; as a result, the noble metal nanoparticles have been grown to use these as SERS substrate [36,37]. Preparation of a specific substrate suitable for various surface-enhanced phenomena such as surface-enhanced Raman spectroscopy and surface-enhanced photoluminescence is very challenging for their use in various devices [38–40]. Many reports are available on the photoluminescence, Raman spectroscopy of Ag NPs and synthesis of Ag NPs for SERS substrates. But in most of these reports, photoluminescence and Raman study have been done on Ag nanoparticles dispersed in a solvent or Ag nanoparticles were synthesised by the solution process and later deposited on the substrate by drop casting [41–43]. However, when nanoparticles are in liquid phases, it difficult to organize them in a systematic array for usage in many applications, including solar cells and nanophotonics [44].

With this motivation, in this chapter we have fabricated the Ag NPs on the glass substrate by the solid-state dewetting of the sputtered silver thin films deposited at different substrate temperatures. The influence of the substrate temperature on the growth of Ag NPs and their several properties, such as localized surface Plasmon resonance, photoluminescence, and Raman spectroscopy is studied. The enhancement in PL and Raman intensities is in linear relation with the LSPR properties of Ag NPs measured from the absorbance spectroscopy.

5.2. Experimental details

The silver nanoparticles (Ag NPs) were grown on corning glass 1737 substrate by solid state dewetting of sputtered silver precursor films using RF magnetron sputtering technique as described in section 2.1, chapter 2. The silver precursor thin films were deposited at different substrate temperature varying from RT- 400 ℃ for 60 s time duration at RF power of 40 Watt keeping other parameters constant mentioned in section 3.2, 4.2 in chapter 3 and 4. For the growth of the silver nanoparticles by SSD process, post deposition annealing was performed under vacuum at a base pressure $\sim 10^{-6}$ mbar at 400 ℃ for 1h. Thickness of Ag precursors thin films were measured by

stylus profilometer. Surface morphology of Ag NPs was characterized by FESEM. FETEM was used for high resolution transmission electron microscopy (HRTEM) and selected area electron diffraction (SAED). For quantitative estimation of size of NPs, their size distribution and surface coverage from FESEM images and *d* spacing from HRTEM images, *ImageJ* software was used. For the structural analysis, X ray diffractometer. Absorbance spectra of Ag NPs were recorded with a double beam UV-Vis-NIR spectrometer in the wavelength range of 300-1500 nm. Photoluminescence emission spectra of the Ag NPs grown at different substrate temperature under the excitation wavelength of 320 nm was measured using Fluorescence Spectrophotometer. Raman spectroscopy of Ag NPs on corning glass substrate was done in the range of 200 cm^{-1} to 2000 cm^{-1} using a 514 nm wavelength laser by Laser Micro Raman spectrometer. All details of these characterization techniques are given in chapter 2.

5.3. Results and Discussion

5.3.1 FESEM Analysis

The FESEM images of Ag NPs on corning glass substrate are shown in Fig. 5.1. It is observed that at all substrate temperatures (T_S), Ag NPs are distributed uniformly over the entire substrate surface. Though the thickness of all films in as deposited state is nearly same (~18-21 nm), a variation in size of NPs is observed as a result of solid state dewetting [45]. Since thin films grown by rf sputtering technique are away from the thermal equilibrium condition, as deposition conditions are varied, films can be in different metastable state. Annealing results in the transition from one metastable state to other metastable state. In SSD, growth of the NPs is affected by deposition parameters (deposition time and substrate temperature) and post deposition parameters (annealing temperature and annealing time). During deposition, the adsorbed and absorbed species may modify the surface properties of the film due to change in mobility of adatoms at film/substrate interface which can control the dewetting process. As the substrate temperature is increased, the mobility of adatoms reaching the substrate is enhanced and atoms moves on the surface to minimize the energy. The histograms showing the size distribution of Ag NPs as obtained using *ImageJ* software are shown in Fig. 5.2. These histograms reveal that the increase in substrate temperature of as deposited films increases the number of large particles after SSD. The average particle size varies in the range 25-70 nm for different substrate temperature.

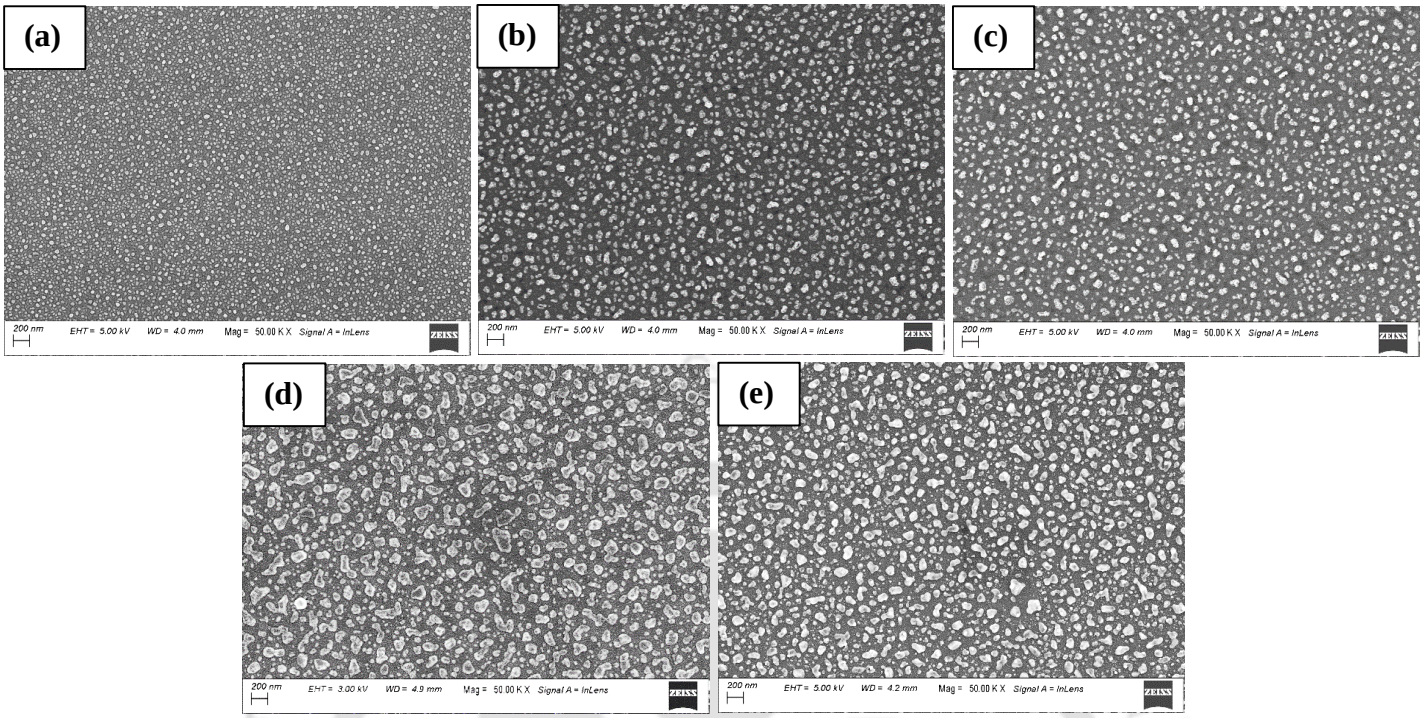

Fig. 5.1. FESEM images of Ag NPs on corning glass substrate at different substrate temperatures on 200 nm scale. (a) for RT, (b) for 100, (c) for 200, (d) 300, and (e) for 400 ℃.

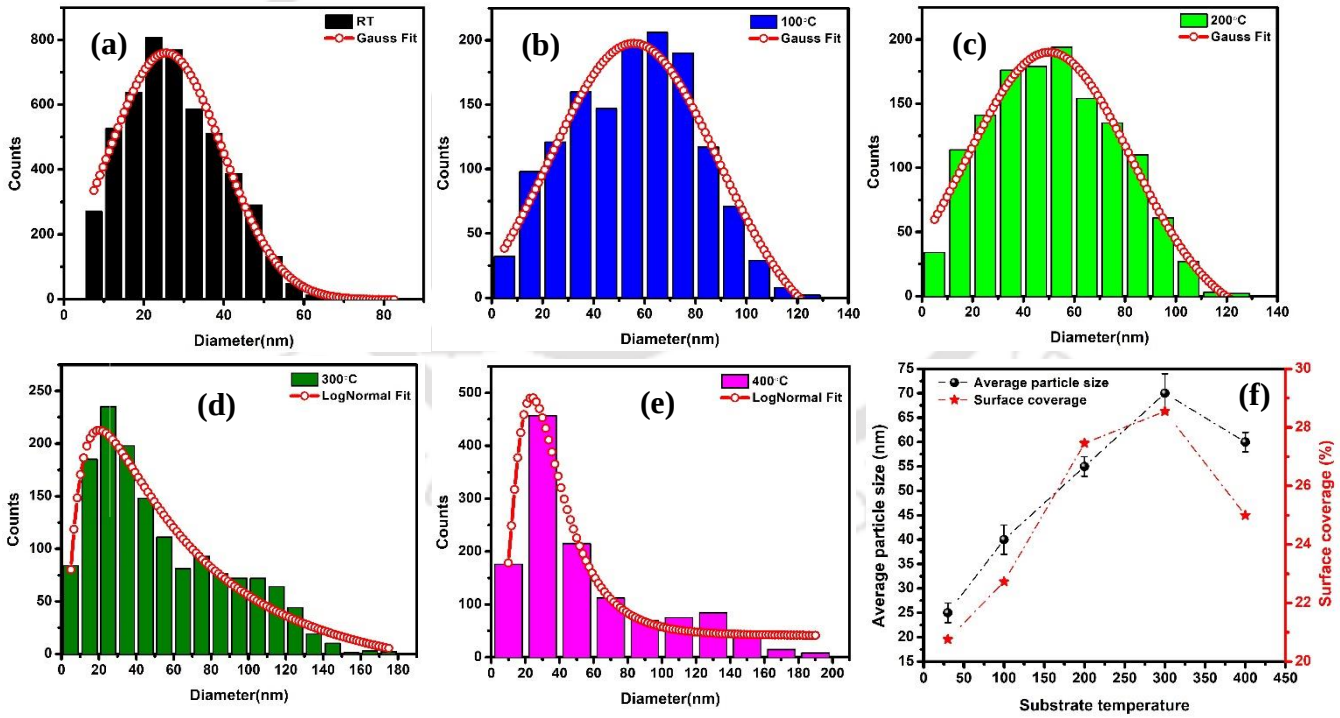

Fig. 5.2. (a-e) Histogram images of Ag NPs on corning glass substrate at different substrate temperatures, (f) variation in particle size and surface coverage (from FESEM images) with substrate temperature.

The smallest particle size (25±2 nm) with very high size uniformity is obtained for room temperature (RT) deposited silver precursor film. Due to constant film thickness, the particle size

and inter particle separation has increased with increasing the substrate temperature while the particles number of uniform size has decreased. Moreover, the substrate temperature has its influence on the NPs size distribution which can be seen from Fig. 5.2(a-e). For films deposited at low T_S ($\leq$ 200 ℃), the NPs size has a Gaussian distribution where average particle size increasing with increase in T_S of precursor films. However, for higher T_S ($\geq$ 300 ℃) which is close to the annealing temperature, a log normal distribution is observed though a large number of particles have size in the range of 20-30 nm. A much larger variation in size is obtained resulting in increase in average particle size. The size of NPs and surface area covered by NPs' are 25 ± 2 nm, 40 ± 3 nm, 55 ± 2 nm, 70 ± 4 nm, and 60 ± 2 nm and 20%, 22%, 27%, 29%, and 25% for RT, 100, 200, 300, and 400 ℃ respectively.

5.3.2 FETEM Analysis

Fig. 5.3 shows FETEM images of Ag NPs deposited on carbon-coated copper TEM grids. These observations also suggest that the substrate temperature variation has a pronounced effect on the size of Ag NPs.

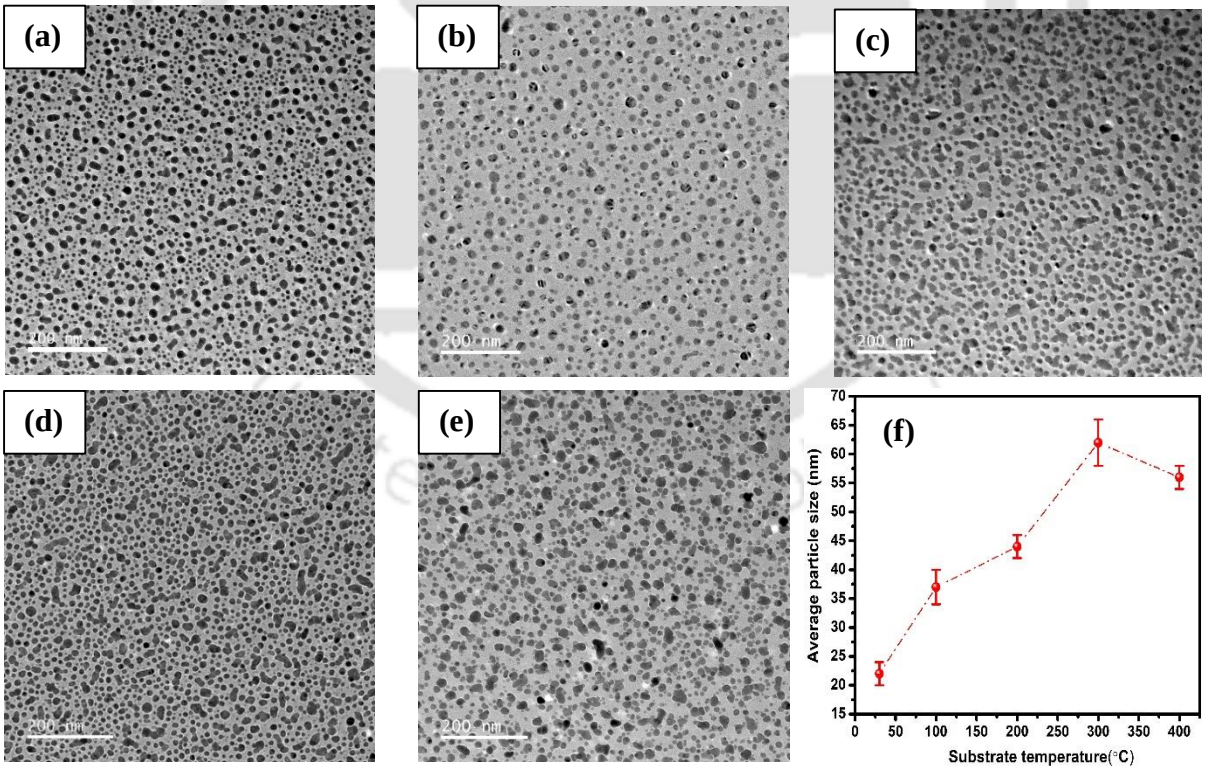

Fig. 5.3. TEM images of Ag NPs on carbon-coated copper TEM grid deposited at different substrate temperatures on a 200 nm scale. (a) for RT, (b) for 100, (c) for 200, (d) 300, and (e) for 400 ℃, (f) particle size from TEM v/s substrate temperature.

The smallest particle size (22 ± 2 nm) with very high size uniformity is obtained for precursor films deposited at room temperature. However, with increasing the substrate temperature, the particle size has increased while size uniformity decreased. The size of the particles is 22 ± 2 nm, 37 ± 3 nm, 44 ± 2 nm, 62 ± 4 nm, and 56 ± 2 nm for the substrate temperature RT, 100, 200, 300, and 400 ℃ respectively. These values are similar to those obtained from FESEM images on glass substrate and follow a similar trend. Fig. 5.4(a)-(e) show the HRTEM image representing the crystalline structure of the Ag NPs for different substrate temperature. The calculated *d* spacing from the HRTEM images is 0.265 nm, 0.277 nm, 0.250 nm, 0.245 nm, and 0.245 nm for RT, 100, 200, 300, and 400 ℃, respectively. The *d* spacing values are corresponding to the (110), (110), (111), (111), and (111) facet planes of the face-centered cubic (fcc) structure of silver [44]. Selective area electron diffraction (SAED) pattern shows an intense ring for (111) plane and rings of diminishing intensity for (200), (220), and (311) (see Fig. 5.4f). These rings are indexed to face centered cubic (fcc) crystal structure of silver.

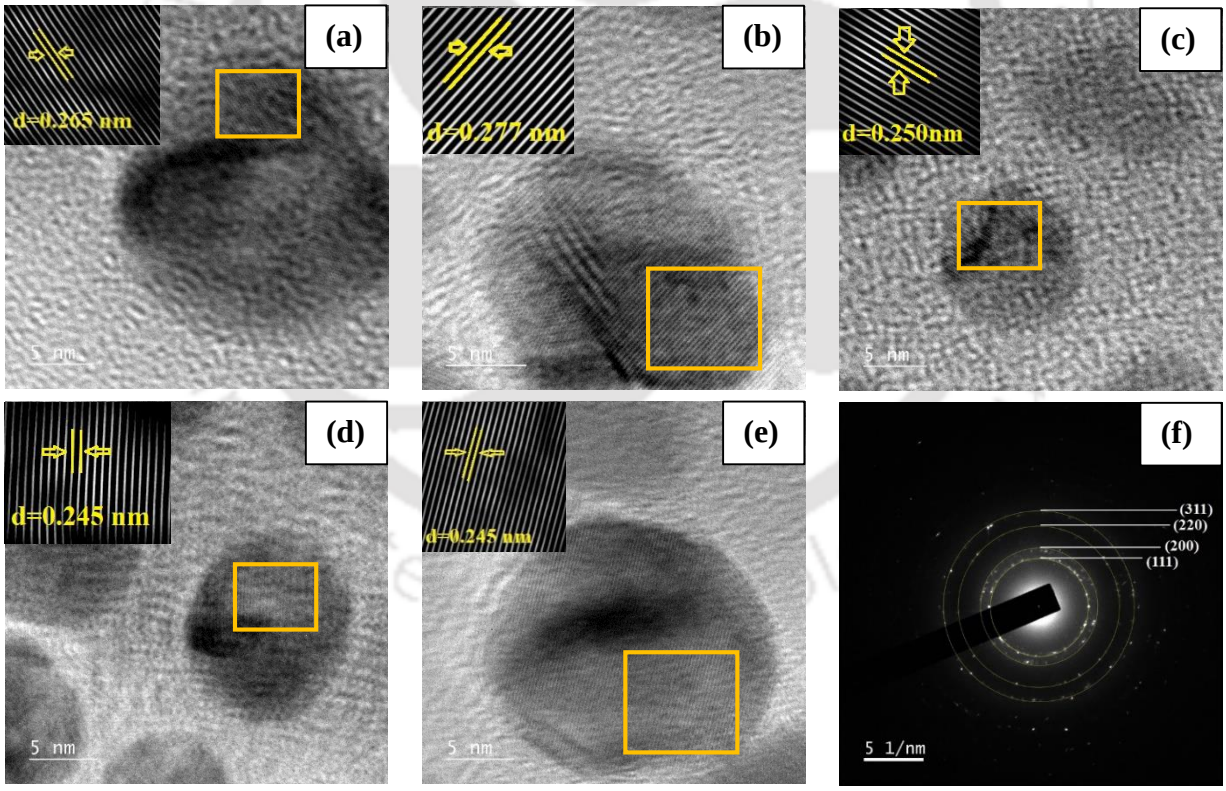

Fig. 5.4. HRTEM images of Ag NPs on carbon-coated copper TEM grid at different substrate temperatures on a 5 nm scale. (a) for RT, (b) for 100, (c) for 200, (d) 300, and (e) for 400 ℃, (f) SAED pattern of Ag NPs for 200 ℃ substrate temperature.

5.3.3 XRD Analysis

Formation of Ag NPs is further confirmed by XRD studies. The XRD spectra of Ag NPs are shown in Fig. 5.5. For all substrate temperatures except room temperature, four XRD peaks at 38.4°, 44.2°, 64.6° and 77.5° are observed. These peaks are corresponding to the (111), (200), (220), and (311) planes of silver, respectively (JCPDS 4-0783). Only two weak diffraction peaks at 38.4° and 44.2° corresponding to (111) and (200) planes are observed for RT deposited films. Decrease in the intensity of peaks in XRD for RT films is due to formation of smaller size NPs and lower interparticle separation. For all the films, the (111) peak is most intense which is due to lowest surface energy for formation of this material [46]. The crystallite sizes of the silver nanostructured films are estimated by using the Debye -Scherrer's formula, defined as $D = 0.9\lambda/\beta \cos\theta$, where D is the average crystallite size and λ is the X-ray wavelength (1.5406 Å). β and θ are the full width at half maxima of the XRD peak and the diffraction angle of the corresponding XRD peak. The most intense peak corresponding to the (111) plane is used to calculate the crystallite size. The average crystallite size increases from 4.1 to 8.5 nm with an increase in the substrate temperature from RT to 300 ℃ and further decreases to 7 nm for 400 ℃. The calculated values of interplanar distance *d* are 2.35, 2.04, 1.44, and 1.23 Å, corresponding to (111), (200), (220), and (311) planes of silver, respectively. The diffraction peak in XRD are same as obtained from SAED for the Ag NPs fabricated on carbon grid indicating that growth process is similar on two substrates.

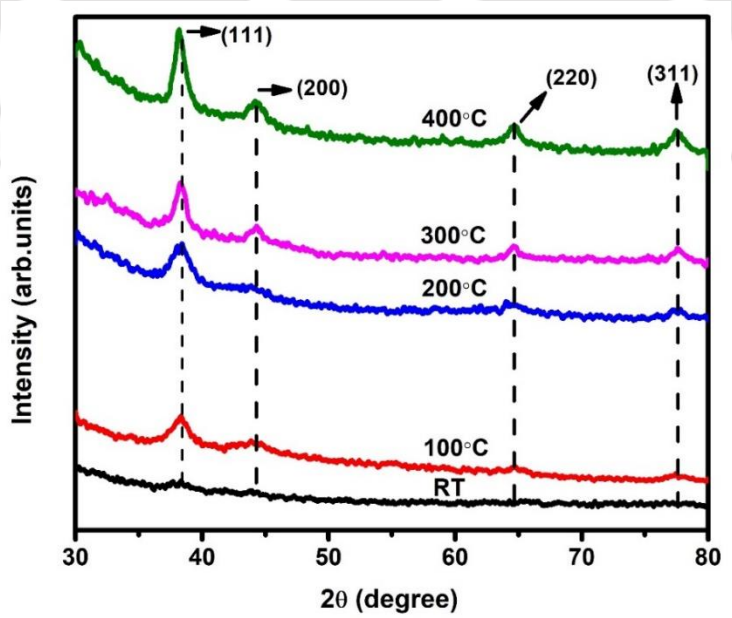

Fig. 5.5. XRD spectra of Ag NPs with substrate temperature variation.

5.3.4 UV-Vis-NIR analysis

To study the localized plasmonic nature due to formation of NPs, absorbance spectra is measured. The absorbance spectra of Ag NPs' after subtracting the glass substrate effect is shown in Fig. 5.6. Absorbance spectra is characterized by a peak corresponding to LSPR nature of Ag NPs. An enhancement in absolute absorbance of Ag NPs is observed with increase in substrate temperature of Ag precursor films. The LSPR peak position of Ag NPs is around 474 nm for room temperature (RT) films. As substrate temperature is increased from RT to 300 ℃, the LSPR peak shifts towards the higher wavelength. With further increase in substrate temperature to 400 ℃, the LSPR peak shifted slightly back towards the peak for RT film. The observed shifts in LSPR peak positions are related to changes in the microstructure, mainly change in particle size and inter-particle separation. Similar observations for particle size and LSPR peak with change in substrate temperature is reported for silver nanoparticle grown by Pulse Laser Deposition (PLD) [47]. For the substrate temperature < 300 ℃, the redshift and increase in intensity of LSPR peak are caused by the increase in the average particle size as measured from FESEM images as well as crystallite size from XRD. However for substrate temperature 400 ℃, the peak in absorbance spectra re-tracked back to lower wavelength due to observed decrease in particle size. The variation in LSPR peak position and the particles size with the substrate temperature is shown in Fig. 5.6 (b), which indicates a linear relationship between particles size and LSPR peak position.

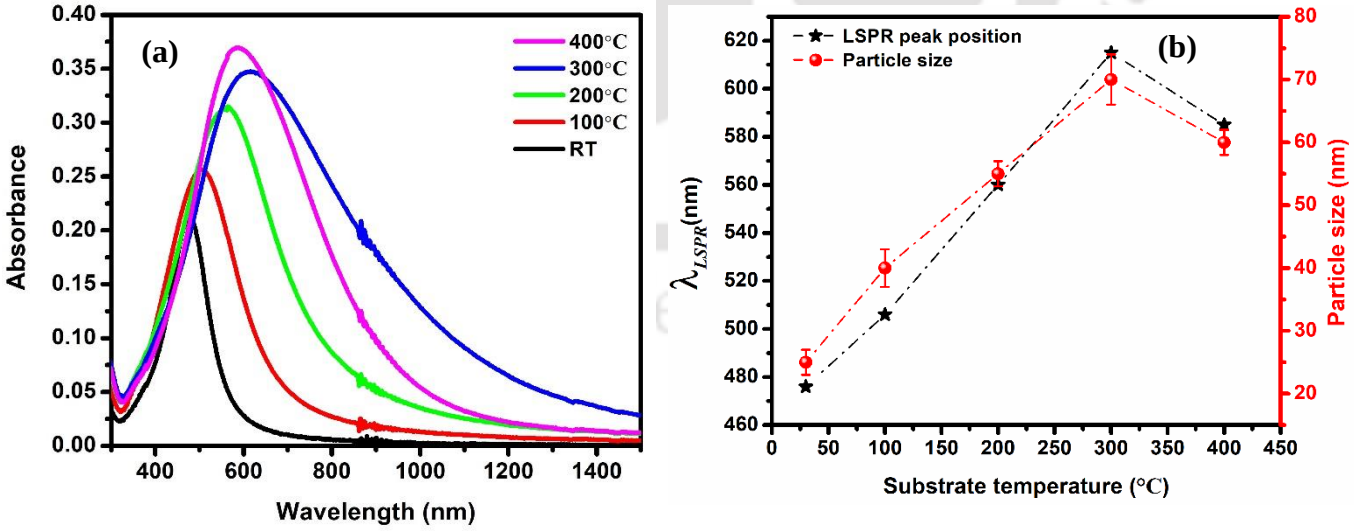

Fig. 5.6 (a) Absorbance spectra of Ag NPs at different substrate temperatures, (b) Variation in LSPR peak and particle size from FESEM with substrate temperature.

5.3.5 Photoluminescence (PL) analysis

Photoluminescence emission spectra of the Ag NPs grown at different substrate temperature under the excitation wavelength of 320 nm are shown in Fig. 5.7 (a). An asymmetric PL emission peak centered at 443 nm is observed for all the samples. The PL peak intensity has enhanced with increase in substrate temperature from RT- 300 ℃. However, for 400 ℃, small decrease in PL peak intensity is observed. Beside this, the peak position remains unchanged with substrate temperature. Similar observations with change in substrate temperature is reported for silver nanoparticle grown by PLD [48]. The PL peak intensity for these NPs depends upon their interaction with the incident photons, which is controlled by the size shape and interparticle separation. To further confirm the nature of dependence, PL peak and particle size calculated from FESEM data are plotted as a function of substrate temperature as shown in Fig. 5.7 (b). The peak intensity is directly related to size of Ag NPs.

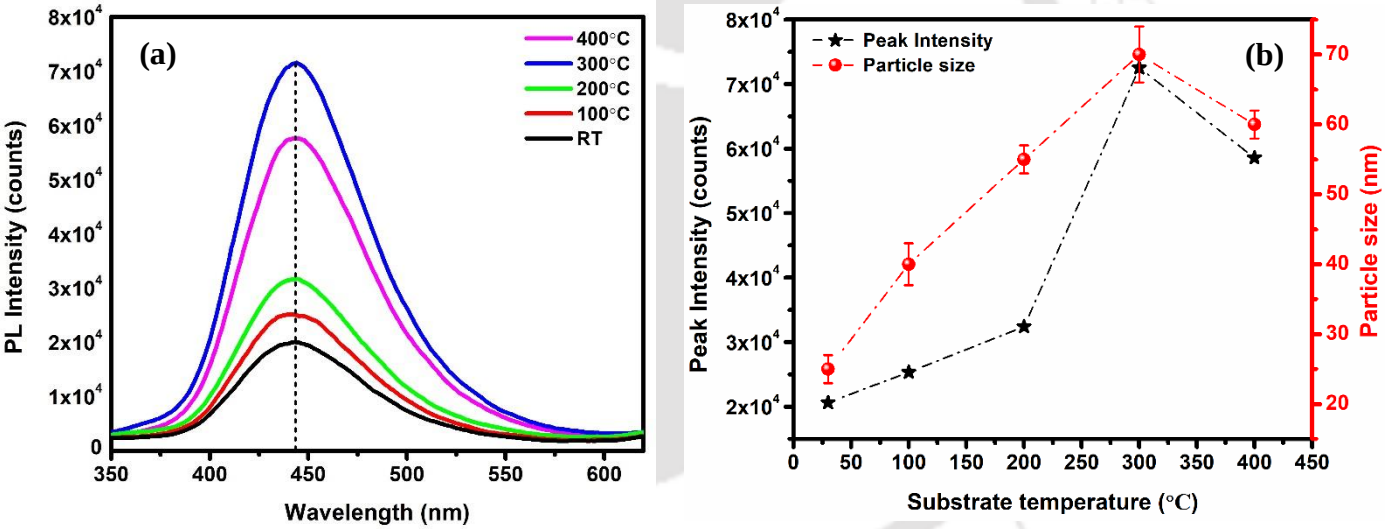

Fig. 5.7. (a) PL spectra of Ag NPs with substrate temperature variation, (b) variation in peak intensity and particle size from FESEM with substrate temperature.

The broadening and asymmetry of PL peak suggests that PL spectra has more than one component. Therefore, PL spectra was de-convoluted and best fitted with two Gaussian peaks; a high intensity peaks at 436 nm and a relatively low intensity peak at 474 nm (see Fig. 5.8 a-e). High intensity peak at 436 nm (peak 1) is attributed to the radiative recombination of an electron from an occupied *sp*-band with holes in the valance *d* band [24,49–51]. The low intensity peak at 474 nm (peak 2) is close to the peak in the absorbance spectra corresponding to LSPR. Similar peak has also been reported in the literature [24,43].

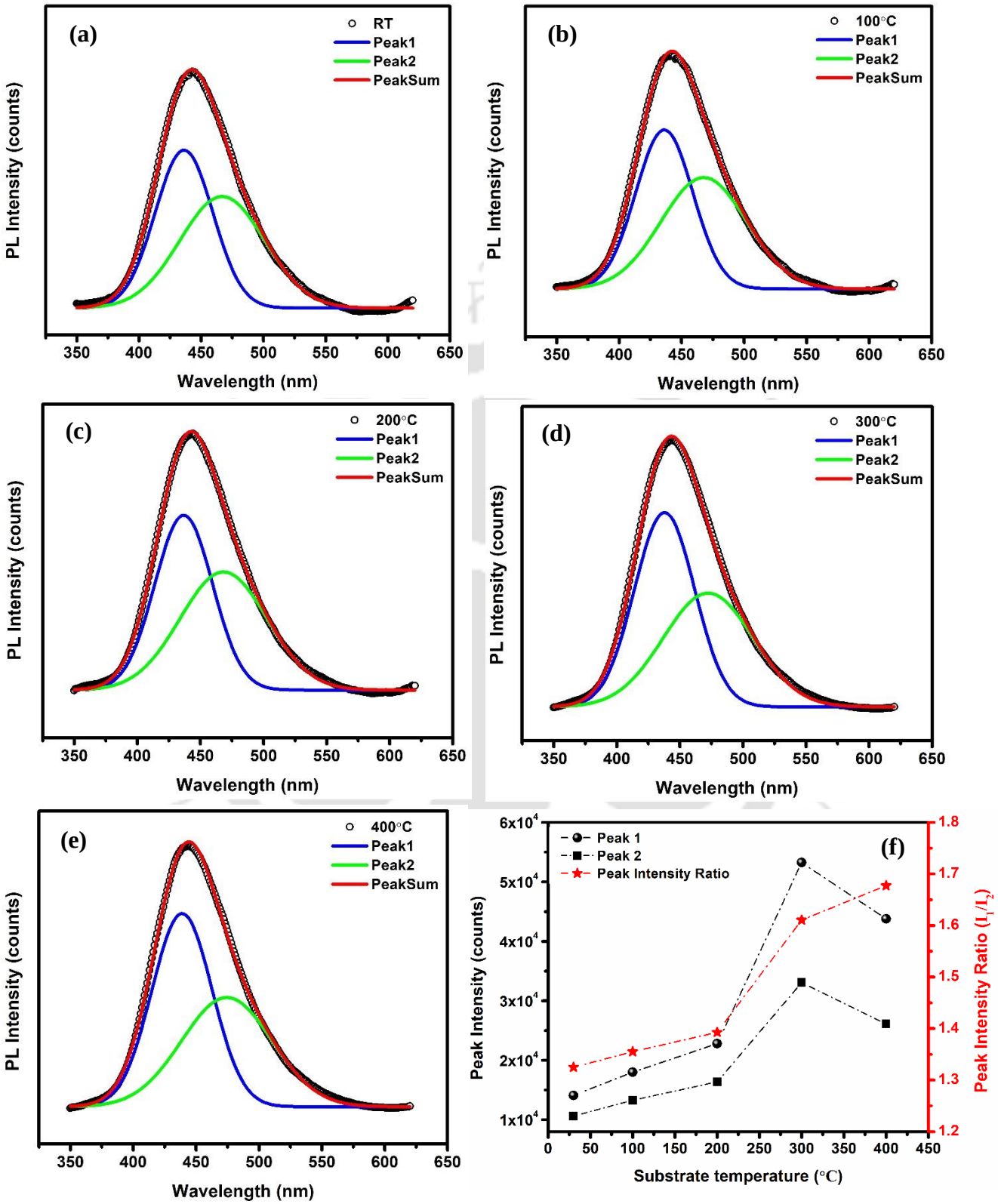

Fig. 5.8. (a-e) De-convoluted PL spectra of Ag NPs with substrate temperature variation, (f) variation in peaks intensity ratio with substrate temperature.

Though there is slight shift in the LSPR peak position in the absorbance spectra with particle size, in de-convoluted PL spectra, the position of these two peaks are independent of particle size. To further investigate the contribution of interband transition and LSPR of Ag NPs in PL, the intensity of both peaks (peak 1 & peak2) and relative intensity of two peaks is also plotted, which is shown in Fig. 8 (f).The intensity of both peaks increase in accordance with particle size suggesting that the contribution of both mechanism is increasing however an increase in relative peak ratio with the substrate temperature indicate dominant contribution of the interband transitions compared to the LSPR.

5.3.6 Raman spectroscopy analysis

Fig. 5.9 shows the Raman spectra of the Ag NPs grown at different substrate temperatures. It was observed that all samples show intense Raman peak at 1587 cm^{-1} and several low intensity peaks at lower wavenumbers. For the clear visualization of these low intensity peaks, Raman spectra was de-convoluted and one of these spectra is shown in Fig. 5.10 (a). The de-convoluted Raman spectra have the Raman Peaks at 1908, 1765, 1587, 1443, 1346, 1144, 1004, 670, 500, 228 cm^{-1}. The similar Raman spectra for the Ag NPs is reported in the literature [52].

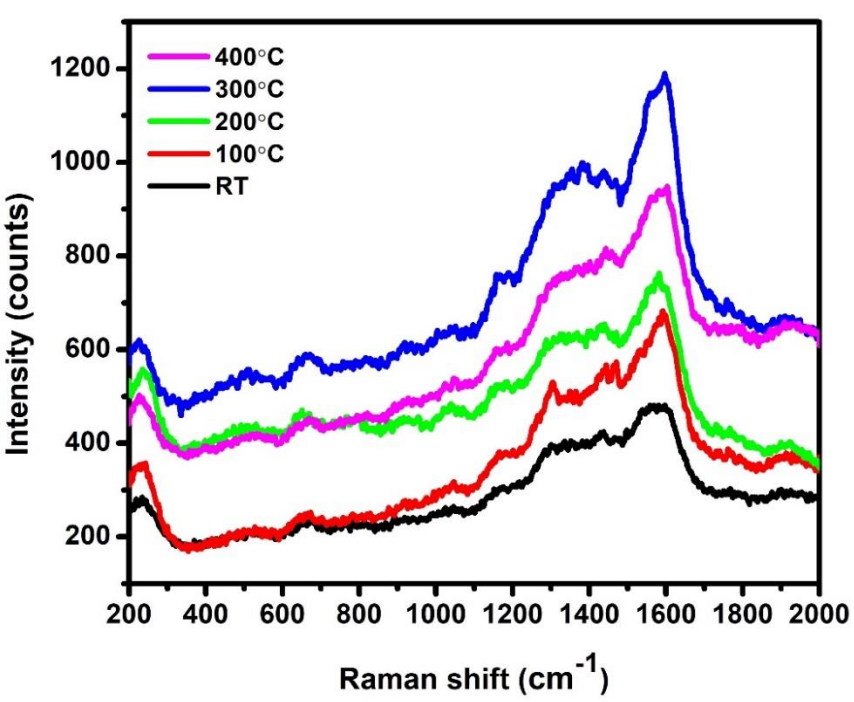

Fig. 5.9. Raman spectra of Ag NPs with substrate temperature variation.

As the substrate temperature increases from RT-300 ℃, the Raman peak at 1587 cm^{-1} (Peak1) becomes sharper and more distinguishable, implying that an increase in particle size leads to increase in scattering from the surface of Ag NPs by the localized field enhancement. For substrate temperature 400 ℃, a decrease in Peak1 intensity was observed which can again be attributed to the decrease in particle size compared to the 300 ℃ substrate temperature. The variation in Peak 1 height and the particle size with the substrate temperature is shown in Fig. 5.10 (b). Almost a linear relation is obtained. The calculated values of FWHM from Raman spectra for peak 1 are 102.2 cm^{-1},93 cm^{-1}, 107.09 cm^{-1}, 98.7 cm^{-1}, and 96.4 cm^{-1} for the substrate temperatures RT, 100, 200, 300, 400 ℃, respectively. With increase in particle size, the contribution from multipole absorption in the absorbance spectra of Ag NPs has increased that broadened and redshifted the plasmon peak [53]. Increase in Raman intensity is attributed to higher order plasmon modes contribution as well as enhanced EM field due to increase in particle size. The increase in Raman intensity with the particle size is in agreement with the theoretical prediction of increasing EM field for larger particles [54].

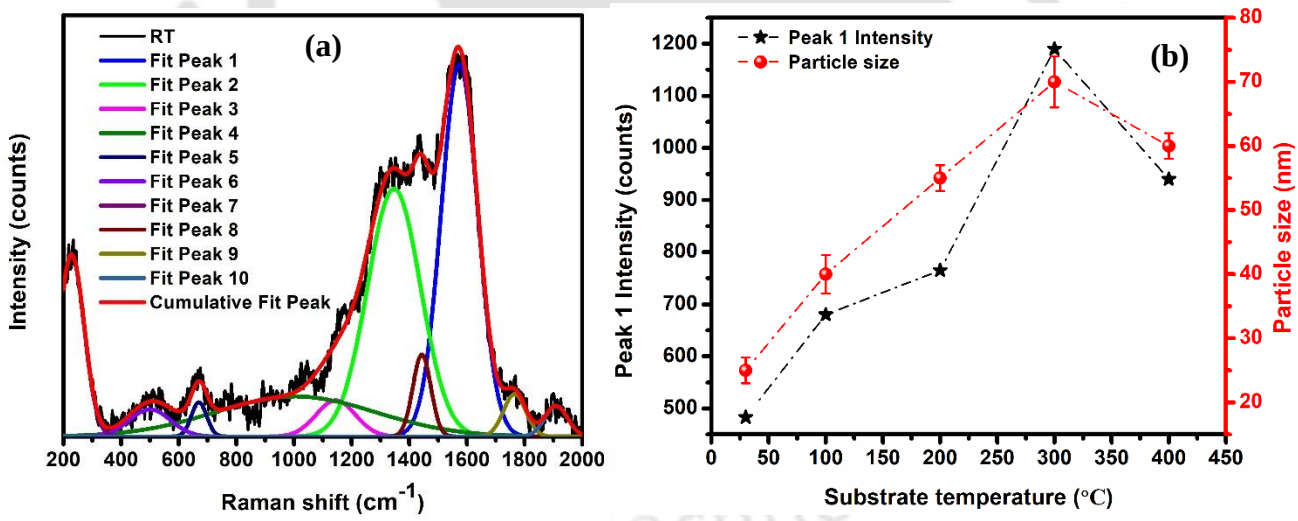

Fig. 5.10. (a) De-convoluted Raman spectra of Ag NPs, (b) variation in peak 1 height and particles size from FESEM with the substrate temperature.

These studies suggest that SERS properties can be tuned by controlling the size of the NPs through optimized substrate temperature. The size controlled NPs on glass substrate can be used as SERS substrate for different device applications as well as study of biological samples.

5.4. Conclusions

In this chapter, we have investigated the influence of substrate temperature on the growth of Ag NPs fabricated on the corning glass substrate by solid-state dewetting of the silver precursor thin films sputtered at different substrate temperatures from RT to 400 ℃. Further the substrate temperature's influence on LSPR, photoluminescence, and Raman spectroscopy of Ag NPs is studied. The change in particle size with the substrate temperature is observed. The LSPR properties of Ag NPs are found to be sensitive to the size. A shift in LSPR peak is observed due to the change in the microstructure of Ag NPs, mainly change in particle size and interparticle distance caused by substrate temperature variation. An asymmetric and broad PL peak is observed at 443 nm and the peak intensity increase with the linear manner with the LSPR of Ag NPs. The de-convoluted PL spectra of Ag NPs shows two peaks around 436 and 474 nm corresponding to their radiative interband transition and LSPR band respectively. The influence of LSPR is also observed in the Raman spectroscopy where an intense and distinguishable Raman peaks is observed at 1587 cm^{-1}. As the substrate temperature increases, the Raman peak becomes sharper and more distinguishable, implying an increase in particle size leads to increase the contribution from multipole absorption in the absorbance spectra of Ag NPs that broadened and redshifted the LSPR peak. Thus a strong influence of the LSPR on the PL and Raman signal is observed. Therefore, this study can be useful to develop various sensors based on these LSPR properties of the Ag NPs.

5.5. References

[1] R. Jin, Y. Cao, C.A. Mirkin, K.L. Kelly, G.C. Schatz, J.G. Zheng, Photoinduced conversion of silver nanospheres to nanoprisms, Science (80-.). 294 (2001) 1901–1903. https://doi.org/10.1126/science.1066541.

[2] P. Gong, H. Li, X. He, K. Wang, J. Hu, W. Tan, S. Zhang, X. Yang, Preparation and antibacterial activity of Fe3O4@Ag nanoparticles, Nanotechnology. 18 (2007) 285604. https://doi.org/10.1088/0957-4484/18/28/285604.

[3] K. Kamakshi, K.C. Sekhar, A. Almeida, J. Agostinho Moreira, M.J.M. Gomes, Tuning the

surface plasmon resonance and surface-enhanced Raman scattering of pulsed laser deposited silver nanoparticle films by ambience and deposition temperature, J. Opt. (United Kingdom). 16 (2014). https://doi.org/10.1088/2040-8978/16/5/055002.

[4] A. Polman, H.A. Atwater, Plasmonics: Optics at the nanoscale, Mater. Today. 8 (2005) 56. https://doi.org/10.1016/S1369-7021(04)00685-6.

[5] Y. Ohko, T. Tatsuma, T. Fujii, K. Naoi, C. Niwa, Y. Kubota, A. Fujishima, Multicolour photochromism of TiO2 films loaded with silver nanoparticles, Nat. Mater. 2 (2003) 29–31. https://doi.org/10.1038/nmat796.

[6] A. Serrano, O. Llorca-Hernando, A. Del Campo, F. Rubio-Marcos, O. Rodríguez de La Fuente, J.F. Fernández, M.A. García, Ag-AgO nanostructures on glass substrates by solid-state dewetting: From extended to localized surface plasmons, J. Appl. Phys. 124 (2018). https://doi.org/10.1063/1.5049651.

[7] C.F. Bohren, Absorption and scattering of light by small particles, John Wiley & Sons, Incorporated, 1983. https://doi.org/10.1088/0031-9112/35/3/025.

[8] M.L. Brongersma, Recent progress in plasmonics, in: Conf. Quantum Electron. Laser Sci. - Tech. Dig. Ser., 2008. https://doi.org/10.1109/QELS.2008.4553160.

[9] A.J. Haes, S. Zou, G.C. Schatz, R.P. Van Duyne, Nanoscale optical biosensor: Short range distance dependence of the localized surface plasmon resonance of noble metal nanoparticles, J. Phys. Chem. B. 108 (2004) 6961–6968. https://doi.org/10.1021/jp036261n.

[10] L. Wang, M. Hasanzadeh Kafshgari, M. Meunier, Optical Properties and Applications of Plasmonic-Metal Nanoparticles, Adv. Funct. Mater. 30 (2020) 2005400. https://doi.org/https://doi.org/10.1002/adfm.202005400.

[11] C. Haynes, C. Yonzon, X. Zhan, R. Duyne, Surface-enhanced Raman sensors: early history and the development of sensors for quantitative biowarfare agent and glucose detection, J. Raman Spectrosc. - J RAMAN SPECTROSC. 36 (2005) 471–484. https://doi.org/10.1002/jrs.1376.

[12] A. Loiseau, V. Asila, G. Boitel-Aullen, M. Lam, M. Salmain, S. Boujday, Silver-based

plasmonic nanoparticles for and their use in biosensing, Biosensors. 9 (2019). https://doi.org/10.3390/bios9020078.

[13] H. Chen, X. Kou, Z. Yang, W. Ni, J. Wang, Shape- and size-dependent refractive index sensitivity of gold nanoparticles, Langmuir. 24 (2008) 5233–5237. https://doi.org/10.1021/la800305j.

[14] A.B. Taylor, P. Zijlstra, Single-Molecule Plasmon Sensing: Current Status and Future Prospects, ACS Sensors. 2 (2017) 1103–1122. https://doi.org/10.1021/acssensors.7b00382.

[15] X.R. Cheng, B.Y.H. Hau, T. Endo, K. Kerman, Au nanoparticle-modified DNA sensor based on simultaneous electrochemical impedance spectroscopy and localized surface plasmon resonance, Biosens. Bioelectron. 53 (2014) 513–518. https://doi.org/10.1016/j.bios.2013.10.003.

[16] K. Nakayama, K. Tanabe, H.A. Atwater, Plasmonic nanoparticle enhanced light absorption in GaAs solar cells, Appl. Phys. Lett. 93 (2008) 1–4. https://doi.org/10.1063/1.2988288.

[17] J.P. Wilcoxon, J.E. Martin, F. Parsapour, B. Wiedenman, D.F. Kelley, Photoluminescence from nanosize gold clusters, J. Chem. Phys. 108 (1998) 9137–9143. https://doi.org/10.1063/1.476360.

[18] W.S. Chang, B. Willingham, L.S. Slaughter, S. Dominguez-Medina, P. Swanglap, S. Link, Radiative and nonradiative properties of single plasmonic nanoparticles and their assemblies, Acc. Chem. Res. 45 (2012) 1936–1945. https://doi.org/10.1021/ar200337u.

[19] M. Yorulmaz, S. Khatua, P. Zijlstra, A. Gaiduk, M. Orrit, Luminescence quantum yield of single gold nanorods, Nano Lett. 12 (2012) 4385–4391. https://doi.org/10.1021/nl302196a.

[20] P. Zijlstra, J.W.M. Chon, M. Gu, Five-dimensional optical recording mediated by surface plasmons in gold nanorods, Nature. 459 (2009) 410–413. https://doi.org/10.1038/nature08053.

[21] H. Wang, T.B. Huff, D.A. Zweifel, W. He, P.S. Low, A. Wei, J.X. Cheng, In vitro and in vivo two-photon luminescence imaging of single gold nanorods, Proc. Natl. Acad. Sci. U. S. A. 102 (2005) 15752–15756. https://doi.org/10.1073/pnas.0504892102.

[22] A. Carattino, V.I.P. Keizer, M.J.M. Schaaf, M. Orrit, Background Suppression in Imaging Gold Nanorods through Detection of Anti-Stokes Emission, Biophys. J. 111 (2016) 2492–2499. https://doi.org/10.1016/j.bpj.2016.10.035.

[23] P. Apell, R. Monreal, S. Lundqvist, Photoluminescence of noble metals, Phys. Scr. 38 (1988) 174–179. https://doi.org/10.1088/0031-8949/38/2/012.

[24] A. Zhang, J. Zhang, Y. Fang, Photoluminescence from colloidal silver nanoparticles, J. Lumin. 128 (2008) 1635–1640. https://doi.org/10.1016/j.jlumin.2008.03.014.

[25] H. Mertens, A. Polman, Plasmon-enhanced erbium luminescence, Appl. Phys. Lett. 89 (2006). https://doi.org/10.1063/1.2392827.

[26] G.T. Boyd, Z.H. Yu, Y.R. Shen, Photoinduced luminescence from the noble metals and its enhancement on roughened surfaces, Phys. Rev. B. 33 (1986) 7923–7936. https://doi.org/10.1103/PhysRevB.33.7923.

[27] A. Lin, D.H. Son, I.H. Ahn, G.H. Song, W.-T. Han, Visible to infrared photoluminescence from gold nanoparticles embedded in germano-silicate glass fiber, Opt. Express. 15 (2007) 6374–6379. https://doi.org/10.1364/OE.15.006374.

[28] M. Eichelbaum, K. Rademann, A. Hoell, D.M. Tatchev, W. Weigel, R. Stößer, G. Pacchioni, Photoluminescence of atomic gold and silver particles in soda-lime silicate glasses, Nanotechnology. 19 (2008) 135701. https://doi.org/10.1088/0957-4484/19/13/135701.

[29] M. Eichelbaum, B.E. Schmidt, H. Ibrahim, K. Rademann, Three-photon-induced luminescence of gold nanoparticles embedded in and located on the surface of glassy nanolayers, Nanotechnology. 18 (2007) 355702. https://doi.org/10.1088/0957-4484/18/35/355702.

[30] K. Imura, H. Okamoto, Properties of photoluminescence from single gold nanorods induced by near-field two-photon excitation, J. Phys. Chem. C. 113 (2009) 11756–11759. https://doi.org/10.1021/jp9018074.

[31] D.-S. Wang, F.-Y. Hsu, C.-W. Lin, Surface plasmon effects on two photon luminescence of gold nanorods, Opt. Express. 17 (2009) 11350. https://doi.org/10.1364/oe.17.011350.

[32] O.A. Yeshchenko, I.M. Dmitruk, A.M. Dmytruk, A.A. Alexeenko, Influence of annealing conditions on size and optical properties of copper nanoparticles embedded in silica matrix, Mater. Sci. Eng. B Solid-State Mater. Adv. Technol. 137 (2007) 247–254. https://doi.org/10.1016/j.mseb.2006.11.030.

[33] J.S. Cho, S. Baek, S.H. Park, J.H. Park, J. Yoo, K.H. Yoon, Effect of nanotextured back reflectors on light trapping in flexible silicon thin-film solar cells, Sol. Energy Mater. Sol. Cells. 102 (2012) 50–57. https://doi.org/10.1016/j.solmat.2012.03.031.

[34] J.N. Anker, W.P. Hall, O. Lyandres, N.C. Shah, J. Zhao, R.P. Van Duyne, Biosensing with plasmonic nanosensors, Nat. Mater. 7 (2008) 442–453. https://doi.org/10.1038/nmat2162.

[35] P. Berini, Surface plasmon photodetectors and their applications, Laser Photon. Rev. 8 (2014) 197–220. https://doi.org/https://doi.org/10.1002/lpor.201300019.

[36] K. Chaudhari, T. Ahuja, V. Murugesan, V. Subramanian, M.A. Ganayee, T. Thundat, T. Pradeep, Appearance of SERS activity in single silver nanoparticles by laser-induced reshaping, Nanoscale. 11 (2019) 321–330. https://doi.org/10.1039/c8nr06497k.

[37] S.A. Razek, A.B. Ayoub, M.A. Swillam, One Step Fabrication of Highly Absorptive and Surface Enhanced Raman Scattering (SERS) Silver Nano-trees on Silicon Substrate, Sci. Rep. 9 (2019) 1–8. https://doi.org/10.1038/s41598-019-49896-2.

[38] S. Wang, L.P. Xu, Y. Wen, H. Du, S. Wang, X. Zhang, Space-confined fabrication of silver nanodendrites and their enhanced SERS activity, Nanoscale. 5 (2013) 4284–4290. https://doi.org/10.1039/c3nr00313b.

[39] D. Cialla-May, X.S. Zheng, K. Weber, J. Popp, Recent progress in surface-enhanced Raman spectroscopy for biological and biomedical applications: From cells to clinics, Chem. Soc. Rev. 46 (2017) 3945–3961. https://doi.org/10.1039/c7cs00172j.

[40] X. Xie, H. Pu, D.W. Sun, Recent advances in nanofabrication techniques for SERS substrates and their applications in food safety analysis, Crit. Rev. Food Sci. Nutr. 58 (2018) 2800–2813. https://doi.org/10.1080/10408398.2017.1341866.

[41] D.K. Bhui, H. Bar, P. Sarkar, G.P. Sahoo, S.P. De, A. Misra, Synthesis and UV-vis spectroscopic study of silver nanoparticles in aqueous SDS solution, J. Mol. Liq. 145 (2009)

33–37. https://doi.org/10.1016/j.molliq.2008.11.014.

[42] Y. Han, R. Lupitskyy, T.M. Chou, C.M. Stafford, H. Du, S. Sukhishvili, Effect of oxidation on surface-enhanced raman scattering activity of silver nanoparticles: A quantitative correlation, Anal. Chem. 83 (2011) 5873–5880. https://doi.org/10.1021/ac2005839.

[43] O.A. Yeshchenko, I.M. Dmitruk, A.A. Alexeenko, M.Y. Losytskyy, A. V. Kotko, A.O. Pinchuk, Size-dependent surface-plasmon-enhanced photoluminescence from silver nanoparticles embedded in silica, Phys. Rev. B - Condens. Matter Mater. Phys. 79 (2009) 1–8. https://doi.org/10.1103/PhysRevB.79.235438.

[44] J.A. Badán, E. Navarrete-Astorga, R. Henríquez, F. Martín Jiménez, D. Ariosa, J.R. Ramos-Barrado, E.A. Dalchiele, Silver Nanoparticle Arrays onto Glass Substrates Obtained by Solid-State Thermal Dewetting: A Morphological, Structural and Surface Chemical Study, Nanomaterials. 12 (2022). https://doi.org/10.3390/nano12040617.

[45] F. Leroy, Ł. Borowik, F. Cheynis, Y. Almadori, S. Curiotto, M. Trautmann, J.C. Barbé, P. Müller, How to control solid state dewetting : A short review, Surf. Sci. Rep. 71 (2016) 391–409. https://doi.org/10.1016/j.surfrep.2016.03.002.

[46] Y.S. Jung, Study on texture evolution and properties of silver thin films prepared by sputtering deposition, Appl. Surf. Sci. 221 (2004) 281–287. https://doi.org/10.1016/S0169-4332(03)00888-2.

[47] K. Kamakshi, J.P.B. Silva, K.C. Sekhar, G. Marslin, J.A. Moreira, O. Conde, A. Almeida, M. Pereira, M.J.M. Gomes, Influence of substrate temperature on the properties of pulsed laser deposited silver nanoparticle thin films and their application in SERS detection of bovine serum albumin, Appl. Phys. B Lasers Opt. 122 (2016) 1–8. https://doi.org/10.1007/s00340-016-6385-0.

[48] K. Kamakshi, J.P.B. Silva, K.C. Sekhar, J. Agostinho Moreira, A. Almeida, M. Pereira, M.J.M. Gomes, Substrate Temperature Effect on Microstructure, Optical, and Glucose Sensing Characteristics of Pulsed Laser Deposited Silver Nanoparticles, Plasmonics. 13 (2018) 1235–1241. https://doi.org/10.1007/s11468-017-0625-y.

[49] J.R. Ansari, N. Singh, R. Ahmad, D. Chattopadhyay, A. Datta, Controlling self-assembly

of ultra-small silver nanoparticles: Surface enhancement of Raman and fluorescent spectra, Opt. Mater. (Amst). 94 (2019) 138–147. https://doi.org/10.1016/j.optmat.2019.05.023.

[50] T. V. Shahbazyan, Theory of plasmon-enhanced metal photoluminescence, Nano Lett. 13 (2013) 194–198. https://doi.org/10.1021/nl303851z.

[51] M. Manoth, K. Manzoor, M.K. Patra, P. Pandey, S.R. Vadera, N. Kumar, Dendrigraft polymer-based synthesis of silver nanoparticles showing bright blue fluorescence, Mater. Res. Bull. 44 (2009) 714–717. https://doi.org/10.1016/j.materresbull.2008.06.033.

[52] G. Naja, P. Bouvrette, S. Hrapovic, J.H.T. Luong, Raman-based detection of bacteria using silver nanoparticles conjugated with antibodies, Analyst. 132 (2007) 679–686. https://doi.org/10.1039/b701160a.

[53] K.L. Kelly, E. Coronado, L.L. Zhao, G.C. Schatz, The Optical Properties of Metal Nanoparticles: The Influence of Size, Shape, and Dielectric Environment, J. Phys. Chem. B. 107 (2003) 668–677. https://doi.org/10.1021/jp026731y.

[54] V.N. Pustovit, T. V. Shahbazyan, Quantum-size effects in SERS from noble-metal nanoparticles, Microelectronics J. 36 (2005) 559–563. https://doi.org/10.1016/j.mejo.2005.02.069.

Chapter 6

Simulation and fabrication of a-Si:H thin film solar cells

6.1 Introduction

Hydrogenated amorphous silicon (a-Si:H) is a semiconducting material explored extensively due to its potential application in thin films solar cells [1–3]. Hydrogenated amorphous silicon (a-Si:H) thin film solar cells are explored as an alternative to c-Si solar cells fabricated by diffusion of p-n junction at high temperature with a series of processing steps [4–7]. However, a-Si:H thin film solar cell efficiency is still below the conventional crystalline silicon solar cells [8]. Nevertheless, several advantages of a-Si:H thin film solar cells include relatively low fabrication cost due to processing at low temperatures and large area deposition on different substrates, including the flexible substrate, which are relatively cheaper than the silicon wafer [9–12].

In a-Si:H thin film solar cells, each individual layer thickness is one significant influencing factor, which controls the fraction of the photon flux that can be absorbed by the cell. In n-i-p solar cells, the carrier lifetime in doped a-Si:H layer is very short and photo carrier generated in these layer do not contribute to photocurrent. Therefore, the thickness of these layer is kept thin to reduce parasitic absorption losses. Nevertheless, finite thickness of these layer is necessary to provide required field in the absorber layer for efficient collection of carrier generated in absorber layer. The electric field depends upon the doping concentration in these layers for a given thickness of absorber layer. The doping has to be increased if thickness of doped layer is reduced. In contrast, the intrinsic layer (a-Si:H i- layer) is the most essential part of (n-i-p) a-Si:H solar cells, where the process of electron-hole generation takes place and these charge carriers get separated by the internal electric field prevailing within the whole i layer. For single junction (n-i-p) a-Si:H thin film solar cells, the thickness of the i-layer is a key factor in achieving a balance between photo generation and collection efficiency, consequently controlling the short circuit current [13–17]. Thin intrinsic layer may result in insufficient photon absorption whereas collection of charge carriers may be reduced if thickness of this layer is large. Therefore, each layer of single junction (n-i-p) a-Si:H thin film solar cells should

be optimized during deposition. Furthermore, it's understood that doping significantly affects device performance. The doping of the emitter layer impacts parameters like series resistance and open circuit voltage. The appropriate level of doping is crucial; low doping can increase series resistance and thus lower fill factor, while high doping contributes to higher open circuit voltage [18–21] but simultaneously decreasing the lifetime of carriers in these layers. Thus, doping optimization is also essential. The best way to optimize each layer's parameter is the numerical modeling using simulation tool [14,22]. This approach helps in saving time, resources and efforts, providing insights into the expected device behavior before the actual fabrication process.

With this motivation, in this chapter, we have numerically modeled single junction n-i-p a-Si:H thin film solar cells and simultaneously fabricated the device prior to implementation of silver nanoparticles for light trapping application. The influence of the emitter layer doping and absorber layer thickness was studied. First, the emitter layer doping is varied from 7.2×10^{19} to 8.4×10^{19} cm^{-3} to match the diborane (B_2H_6) flow rate in p layer which is varied from 8-14 sccm. After optimization of the emitter layer doping of 7.6×10^{19} cm^{-3} using simulation tool, at which device performance matched well with the B_2H_6 flow rate of 10 sccm for the experimentally fabricated solar cells, the absorber layer thickness is varied from 200 nm to 350 nm to study its influence on the performance of the solar cells.

6.2 Simulation details

The single junction n-i-p hydrogenated amorphous silicon (a-Si:H) thin film solar cells were simulated using well-practiced AFORS-HET (Automated For Simulation of Heterostructure, v 2.5) software developed by Helmholtz- Zentrum Berlin (HZB) to accurately evaluate the effect of various parameters on solar cells performance [23–26]. Fig. 6.1 shows the structure of simulated a-Si:H solar cell with *Glass/Ag/AZO/a-Si:H (n) /a-Si:H (i)/ a-Si:H (p)/ITO/ Ag*. For each a-Si:H layer, band tails defect state with exponential distribution and dangling bond defects state with Gaussian distribution were used during the simulation as shown in Fig.6.2. Throughout the optimization, flat band conditions were chosen at front and back contacts. No front and back surface texturing was done. The surface recombination velocity of electrons and holes was set as 10^7 cm/s. The global radiation AM 1.5 spectrum with an incident power density of 100 mW/cm^2 was used as the illuminating source in the present simulation, while the operational temperature was set as 300K. The input parameters used for simulation are listed in Table 6.1 [27–35].

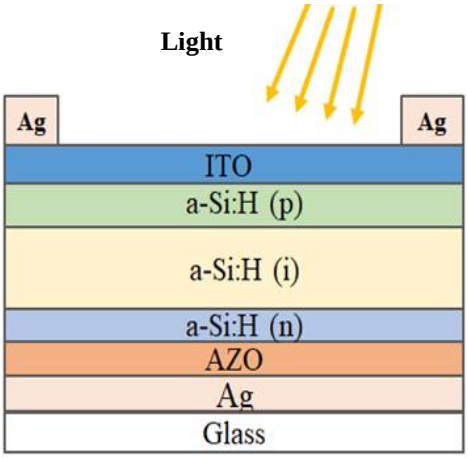

Fig. 6.1 Solar cell structure to be simulated

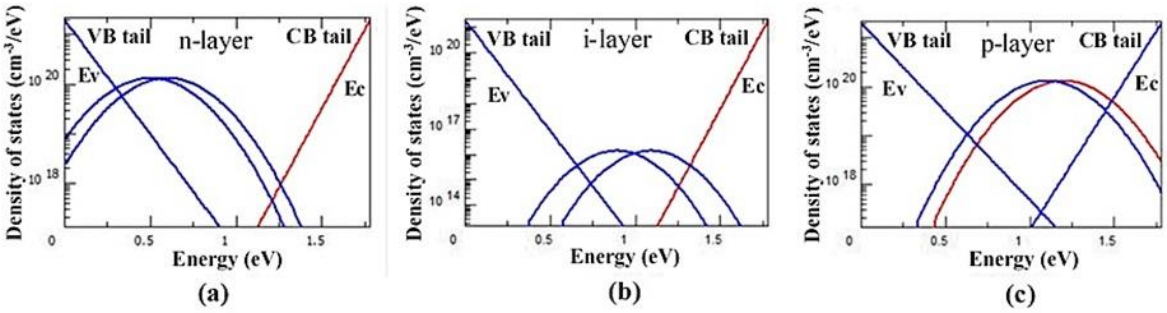

Fig. 6.2 Density of the states of a-Si:H n-i-p layers (a) n-layer (b) i-layer (c) p-layer

Table 6.1 Input parameters used for simulation

Parameters	**a-Si:H (n)**	**a-Si:H (i)**	**a-Si:H (p)**
Layer thickness (nm)	30	200*	10
Dielectric constant	11.9	11.9	11.9
Electron affinity (eV)	3.9	3.9	3.9
Band gap (eV)	1.8	1.7	1.8
Optical band gap (eV)	1.8	1.7	1.8
Conduction band density (cm^{-3})	1×10^{20}	1×10^{20}	1×10^{20}
Valence band density (cm^{-3})	1×10^{20}	1×10^{20}	1×10^{20}
Total trap density in conduction band tail (cm^{-3})	1.36×10^{20}	6.40×10^{19}	1.60×10^{20}
Total trap density in valance band tail (cm^{-3})	1.88×10^{20}	9.40×10^{19}	2.40×10^{20}
Electron mobility ($cm^2V^{-1}s^{-1}$)	20	20	20
Hole mobility ($cm^2V^{-1}s^{-1}$)	5	5	5
Doping concentration of acceptors N_a(cm^{-3})	0	0	7.6×10^{19}*
Doping concentration of donors N_d (cm^{-3})	7.6×10^{19}	0	0
Thermal velocity of electrons (cms^{-1})	1×10^7	1×10^7	1×10^7
Thermal velocity of holes (cms^{-1})	1×10^7	1×10^7	1×10^7
Maximum dangling bond defect density (cm^{-3}/eV)	1.31×10^{20}	1.38×10^{16}	1.31×10^{20}
Layer density ($g.cm^{-3}$)	2.328	2.328	2.328

*Variable parameters

6.3 Experimental details

a-Si:H thin film solar cells were fabricated on the corning glass 1737 substrate with the following structure *corning glass/Ag/AZO/a-Si:H(n)/a-Si:H(i)/a-Si:H(p)/ITO/Ag* using Radio Frequency Plasma Enhanced Chemical Vapor Deposition (RF-PECVD) multi-chamber system. After cleaning the corning glass 1737 substrate as discussed in chapter 2, a silver layer of 100 nm thickness was deposited using rf sputtering system. To prevent the diffusion of silver in solar cells, a thin layer of AZO of 40 nm thickness was deposited over the Ag films using rf sputtering system. After that, the n-i-p layer of a-Si:H were fabricated at 180 ℃ substrate temperature in different (n), (i), (p) chambers. In addition, for doping, phosphine (PH_3, 1% in H_2) and diborane (B_2H_6, 2% in H_2) gases were introduced for a-Si:H(n) layer, and a-Si:H(p) layer. On top of that, 100 nm of ITO layer was deposited using a circular mask of 4 mm diameter (cell area of 0.12 cm^2) by rf sputtering. Finally, front metal grid electrodes were made on cells with silver paste. Using this circular mask of 4 mm diameter during ITO deposition, multiple cells were fabricated for each parameters variation and based on their performance error bars were calculated. The deposition parameters of each layer with the thickness are listed in Table 6.2. The schematic structure of the fabricated solar cell is shown in Fig.6.3.

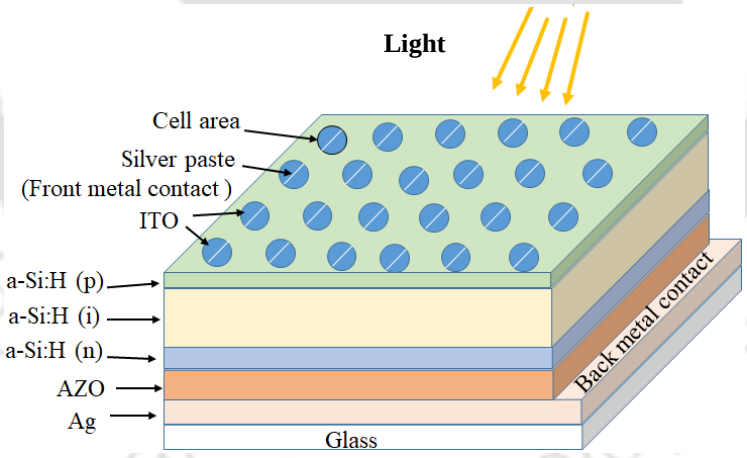

Fig. 6.3 Solar cell structure to be experimentally fabricated

In order to test the performance of the fabricated solar cells, the *I-V* characteristics measurements on a-Si:H solar cells were performed under one sun (AM 1.5G, 100 mW/cm^2) using a solar simulator. The external quantum efficiency (EQE) measurements were performed at room temperature in the wavelength range from 350-900 nm using a calibrated Si photodiode as a reference [36]. Integrated J_{sc} was calculated from the integration of the EQE associated with photon flux over the entire wavelength [37]. All details of these characterization techniques are given in chapter 2.

Table 6. 2 Deposition parameters for each layer of a-Si:H thin film solar cells:

Cell's Layers	Gas flow rate (sccm)					Process pressure (mbar)	Deposition temperature (°C)	RF power (Watt)	Layer thickness (nm)
	Ar	H_2	SiH_4	B_2H_6 (2% in H_2)	PH_3 (1% in H_2)				
ITO	7	-	-	-	-	5.4×10^{-3}	100	80	100
a-Si:H(p)	-	100	5	8-14*	-	6.2×10^{-1}	180	30	10
a-Si:H(i)	-	60	5	-	-	5.6×10^{-1}	180	30	200-350*
a-Si:H(n)	-	50	5	-	10	5.2×10^{-1}	180	30	30
AZO	7	-	-	-	-	5.4×10^{-2}	100	80	40
Ag	7	-	-	-	-	5.4×10^{-2}	100	80	100

*Variable parameters.

6.4 Results and Discussion

6.4.1 Influence of emitter layer doping

The parameters listed in Table 6.1 and Table 6.2 were used as input parameters for the simulation and for the fabrication of the solar cells, respectively. The doping can affect the solar cells performance as it influences the series resistance and the open circuit voltage. The p-layer doping was varied from 7.2×10^{19} to 8.4×10^{19} cm^{-3}. Fig. 6.4 (a) and (b) presents the *J-V* characteristic and spectral response of the simulated solar cell with the variation of p-layer doping.

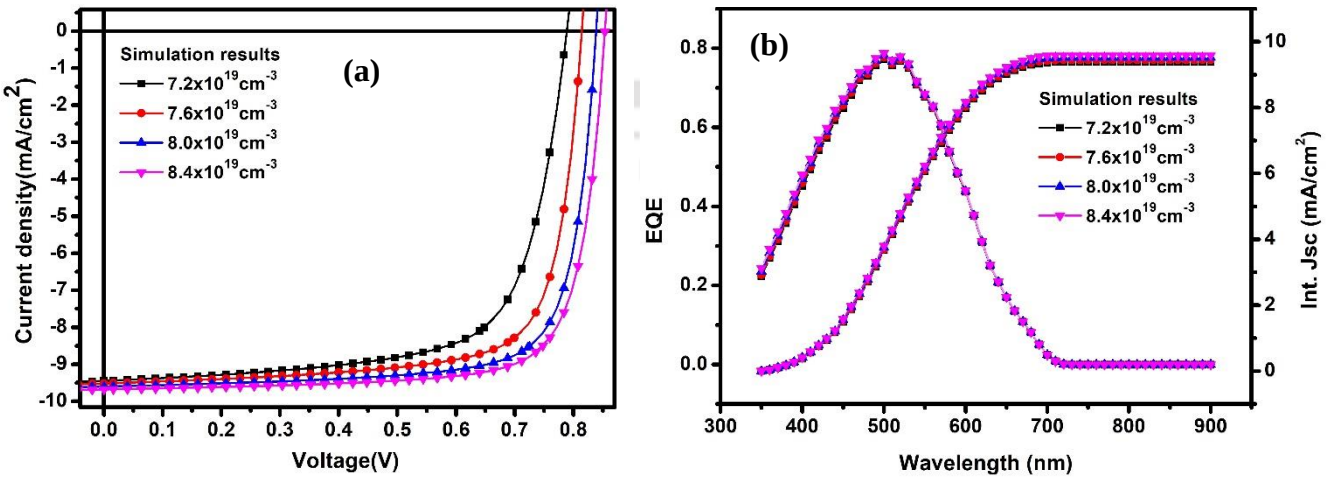

Fig. 6.4 The simulated *J-V* characteristic and spectral response of solar cell with variation in emitter layer doping and 200 nm absorber layer thickness **(**a) *J-V* curve and (b) External quantum efficiency.

Fig. 6.5 (a), (b) shows the *J-V* curve and external quantum efficiency spectra for the four fabricated devices with the variation of emitter layer doping by changing the diborane (B_2H_6) flow rate from 8-14 sccm during the p layer deposition. Fig. 6.6 (a) and (b) shows the external parameters of simulated solar cells and fabricated solar cells as a function of p-layer doping, respectively.

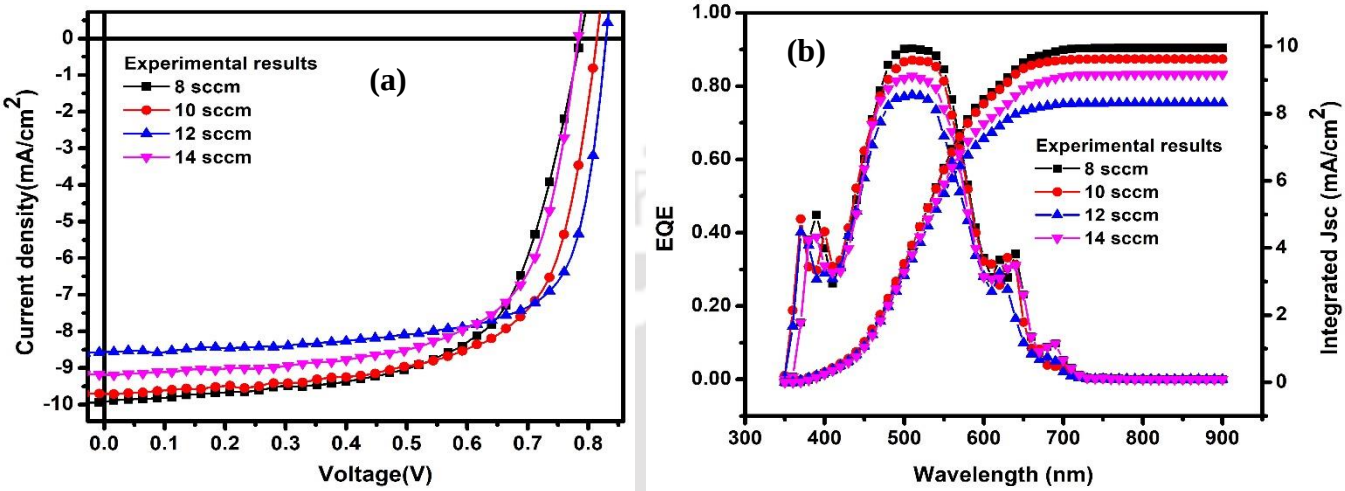

Fig. 6.5 The measured *J-V* characteristic and spectral response of fabricated solar cell with variation in B_2H_6 flow rate in emitter layer and 200 nm absorber layer thickness **(**a) *J-V* curve and (b) External quantum efficiency.

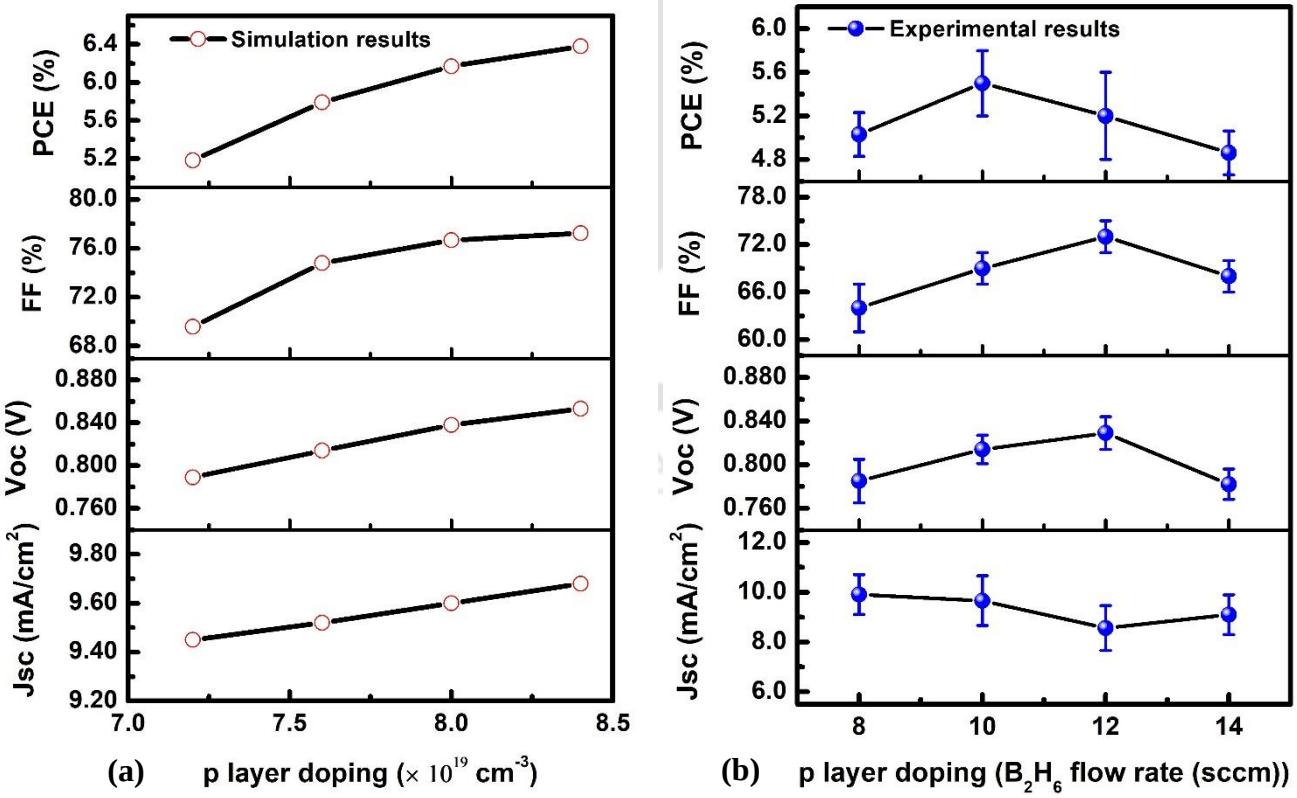

Fig. 6.6 The variation of short circuit current density (J_{sc}), open circuit voltage (V_{oc}), fill factor (*FF*), and power conversion efficiency (*PCE*) as a function of emitter layer doping **(**a) simulated results (b) experimental results.

Simulation results (Fig. 6.6 a) revealed that the J_{sc}, V_{oc}, FF and power conversion efficiency have the same trend throughout the p-layer doping and increase with the increase in the p-layer doping from 7.2×10^{19} to 8.4×10^{19} cm^{-3}. The efficiency increases from 5.2 to 6.4 %, mainly due to an increase in V_{oc} (from 0.789 to 0.854 V) and FF (from 69 to 77%) values. However, no significant change in the J_{sc} values is observed. The doping affected the V_{oc} and *FF* due to the changes of the series resistance and the recombination losses at the p/i interface. Furthermore, Heavy doping provides more free charges [32], which leads to high V_{oc} due to increase in fermi level difference between p doped and n doped layer. No significant change in the values of J_{sc} is also supported by EQE results (Fig. 6.4b)

Experimental results (Fig. 6.6 b) also show the same trend and the output parameters values are similar to simulated results within the error bars. The open-circuit voltage and the fill factor have increased from 0.782 to 0.829 V and 64% to 73%, respectively, with the increase in boron doping of the a-Si: H (p) layer with B_2H_6 flow rate variation from 8 to 12 sccm. On the other hand, the short circuit current density has decreased slightly for the same variation due to a possible increase in the defect density for high doping, which was taken constant in the simulation. An increase in doping concentration in the emitter layer may result in a rise in carrier density and a fall in the fermi energy level of holes, leading to an increase in open-circuit voltage. However, high doping can also increase recombination losses in the emitter region; due to this V_{oc} has slightly decreased at 14 sccm. Cell with p-layer at 10 sccm B_2H_6 flow rate shows best power conversion efficiency. In order to confirm the recombination loss in the emitter region for a high doping concentration of boron for higher B_2H_6 flow rate, external quantum efficiency (EQE) was measured with the variation in B_2H_6 flow rate (Fig. 6.5 b). EQE rapidly decreased at 12 sccm in the short wavelength region, while it exhibited no significant change in the long-wavelength region. This means that the recombination losses have occurred only in the emitter region, which is closely related to increase in defect density in emitter layer at higher B_2H_6 flow rate. For lower B_2H_6 flow rate (8 sccm), $J_{sc}(Exp) > J_{sc}(Sim)$ is due to the less defect density than the simulation while for higher B_2H_6 flow rate (12, 14 sccm) $J_{sc}(Exp) < J_{sc}(Sim)$ indicates higher defect densities than the values in simulation. Further, the values of J_{sc} calculated from *J-V* curve matched well with the integrated J_{sc} calculated from EQE spectra for both simulated and fabricated devices. A close match between the simulated and experimental results was observed for the doping concentration 7.6×10^{19} cm^{-3} and B_2H_6 flow rate 10 sccm for the experimental fabricated cell.

For other doping concentrations and flow rates also, results are in quite good agreement within the error bar. A slight mismatch in these parameters is due to constant defect density taken in the simulation, which is always not true when doping concentration is varied in experiment. Further in a-Si:H, the effective doping concentration increases with the increase in dopant gas flow rate, but the dependence is not linear. In our case also we observed that a two-fold increase in B_2H_6 flow rate corresponds to only about 16% change in doping concentration.

Fig. 6.7 (a) and (b) shows the *J-V* characteristic and external quantum efficiency of the simulated and fabricated solar cell with 7.6×10^{19} cm^{-3} p layer doping concentration for simulation and 10 sccm B_2H_6 flow rate in the p-layer for experimental. Due to higher *FF*, the simulated solar cell has a higher efficiency as compared to the experimental. The experimental solar cells have a comparable value of J_{sc} and V_{oc}. All the external parameters of simulated and experimental solar cells are listed in Table 6.3.

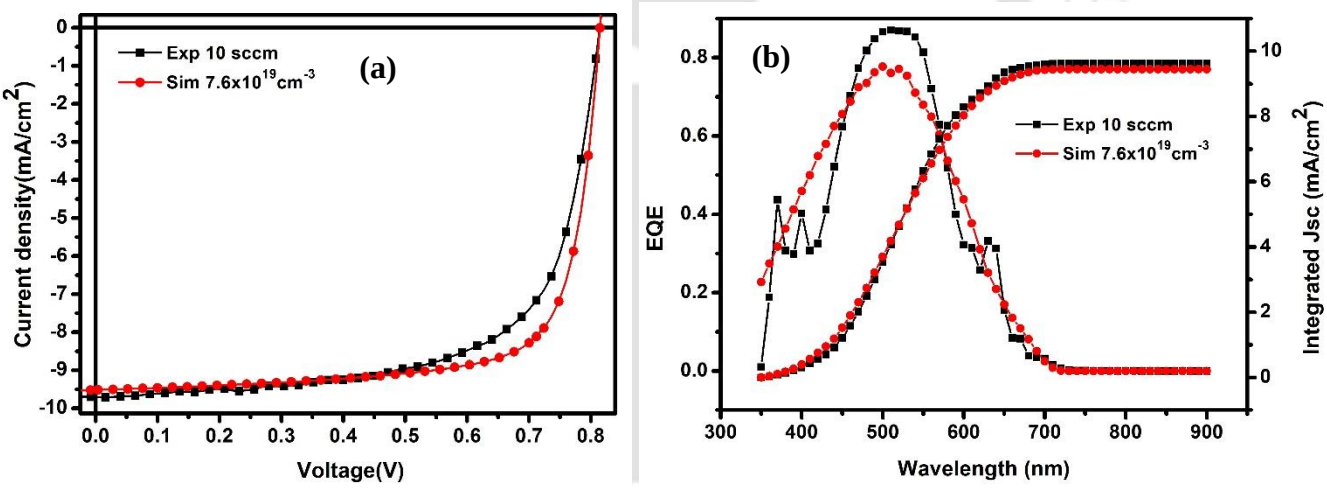

Fig. 6.7 Measured and simulated *J-V* characteristic and spectral response of single-junction n-i-p solar cell with 10 sccm B_2H_6 flow rate and 7.6×10^{19} cm^{-3} doping concentration in emitter layer **(**a) *J-V* curve and (b) External quantum efficiency curve.

Table 6.3 Calculated values of J_{sc}, V_{oc}, *FF*, and power conversion efficiency of fabricated and simulated single junction n-i-p solar cells with 10 sccm B_2H_6 flow rate and 7.6×10^{19} cm^{-3} doping concentration in emitter layer.

(n-i-p) a-Si:H solar cell	**J_{SC} (mA/cm^2)**	**V_{OC} (V)**	**FF (%)**	**PCE (η) (%)**
Experimental	9.66	0.814	69.50	5.50
Simulation	9.52	0.815	74.78	5.79

6.4.2 Influence of absorber layer thickness

The thickness of the i-layer is a crucial parameter that should be thick enough to absorb as many incident photons as possible, and at the same time, it should be thin to prevent the recombination of electron-hole pairs generated within the absorber layer. After optimization of the emitter layer doping of 7.6×10^{19} cm^{-3} using simulation tool, which matched well with the diborane (B_2H_6) flow rate of 10 sccm of the experimentally fabricated solar cells, now we have varied the absorber layer thickness from 200 nm to 350 nm to study its influence on the performance of the solar cells. Fig. 6.8 (a) and (b) shows the *J-V* characteristic and the spectral response of the simulated solar cell with the variation of the absorber layer thickness from 200 nm to 350 nm. *J-V* characteristic and EQE for experimentally fabricated cells are shown in Fig. 6.9 (a), (b).

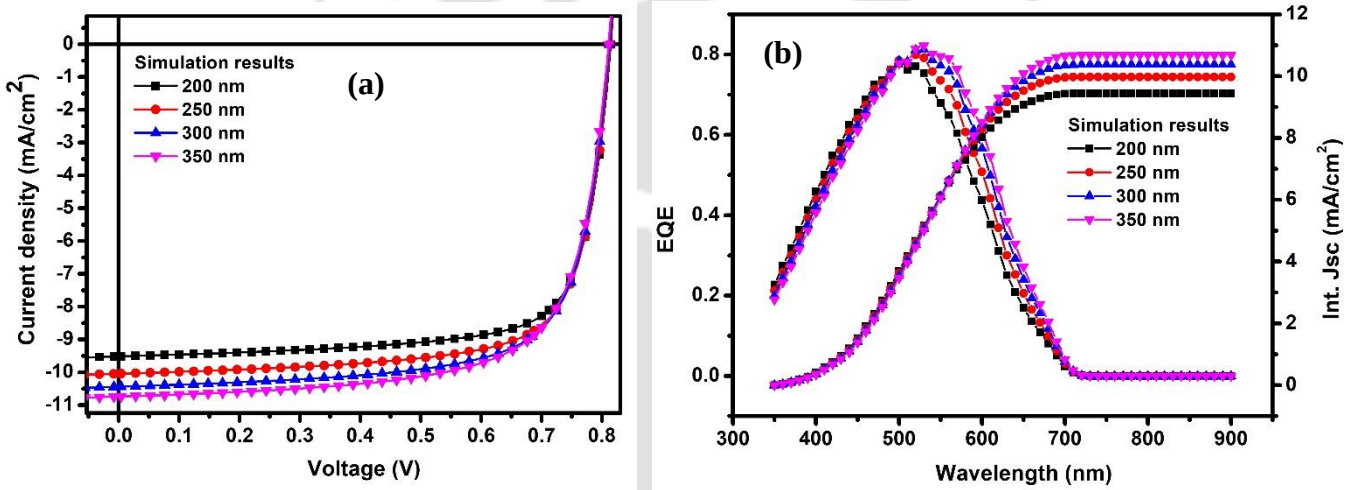

Fig. 6.8 The simulated *J-V* characteristic and spectral response of simulated solar cell with variation in absorber layer thickness and 7.6×10^{19} cm^{-3} p layer doping concentration **(**a) *J-V* curve and (b) External quantum efficiency.

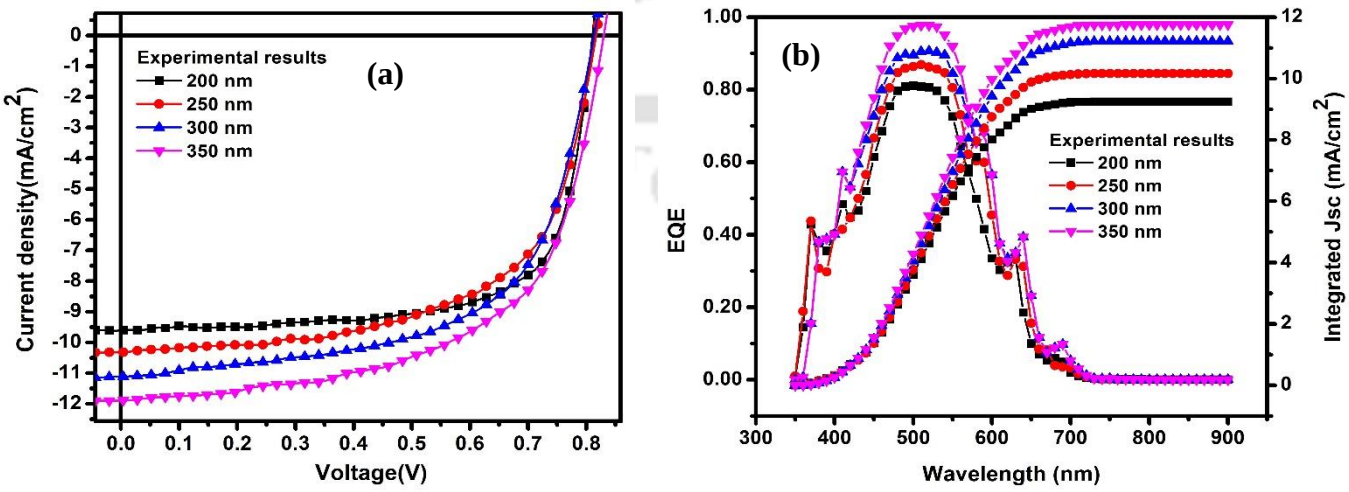

Fig. 6.9 The measured *J-V* characteristic and spectral response of fabricated solar cell with variation in absorber layer thickness and 10 sccm B_2H_6 flow rate in p layer **(**a) J-V curve and (b) External quantum efficiency.

The calculated values of short circuit current density (J_{sc}), open circuit voltage (V_{oc}), fill factor (*FF*), and power conversion efficiency from the J-V curve for the simulated and fabricated solar cells as a function of absorber layer thickness are shown in Fig. 6.10 (a) and (b).

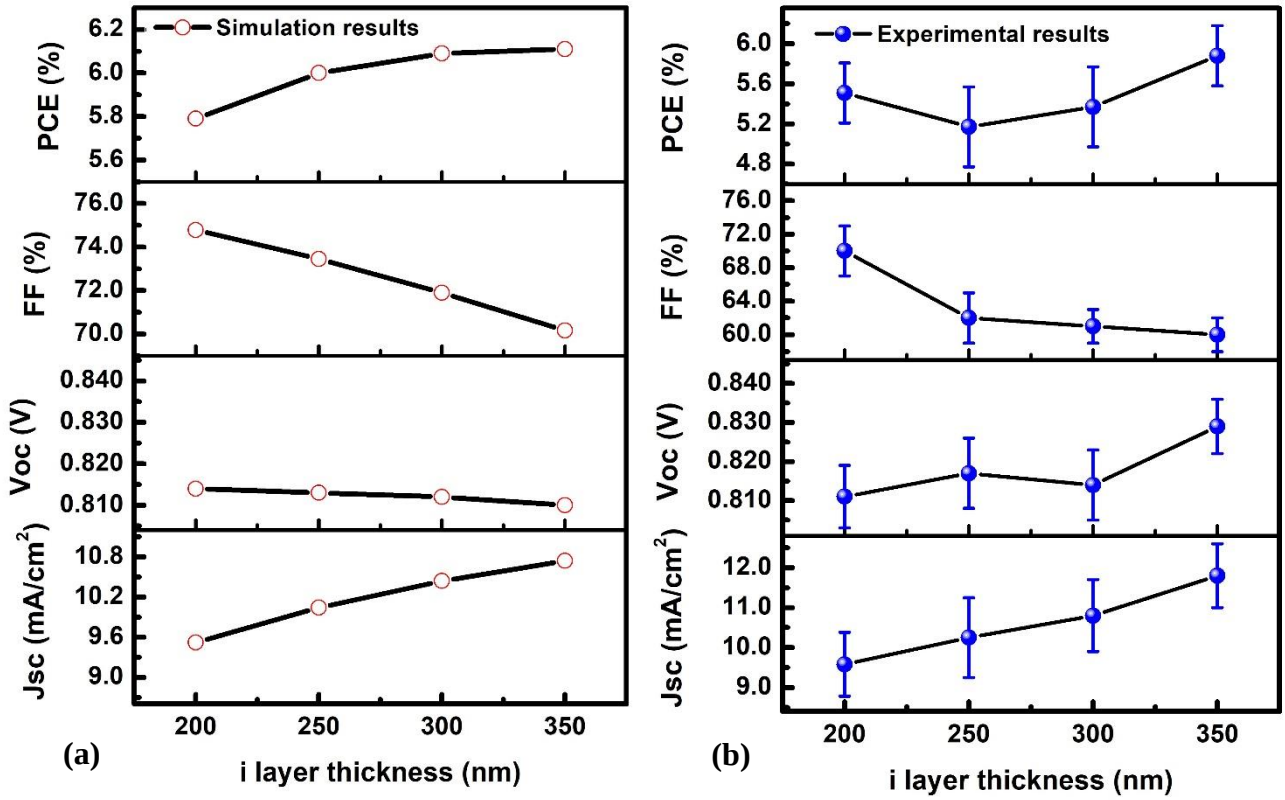

Fig. 6.10 The variation of short circuit current density (J_{sc}), open circuit voltage (V_{oc}), fill factor (*FF*), and power conversion efficiency (*PCE*) as a function of absorber layer thickness **(**a) simulated results (b) experimental results.

For i-layer thickness variation, simulation results (Fig. 6.10 a) show that the short circuit current density (J_{sc}) increases from 9.52 mA/cm^2 to 10.87 mA/cm^2 with variation in i-layer thickness from 200 nm to 350 nm. Since V_{oc} strongly depends on the properties of the doped layer and not much on the i-layer thickness; hence it shows a weak dependence on the i-layer thickness (V_{oc} decrease about by 4 mV when the thickness is increased from 200 nm to 300 nm). In contrast, the fill factor decreases from 75% to 70 % with i-layer thickness [31]. The decrease in fill factor could be caused by either the photo-generated space charges trapped in the valance band instead of the conduction band or by the charges within band states rather than in defects [38]. The decrease in *FF* can also be attributed to the increase in resistive losses at higher current. However, an overall increase in the power conversion efficiency from 5.79 to 6.12 % is observed with an increase in i-layer thickness due to more absorption of light in

the absorber layer, which is also clearly visible in EQE spectra (Fig.6.8b) [31]. The quantum efficiency increases only in the wavelength range from 500-700 nm with the increase in i-layer thickness from 200 nm to 350 nm.

Experimental results (Fig. 6.10 b) are consistent with the simulation having the output parameters values within the error bars. The J_{sc}, and *FF* for both simulation and experiment shows the same trend with the absorber layer thickness. V_{oc} is nearly constant for simulation and varies with in the error bar in experiment. The power conversion efficiency is a calculated parameter from J_{sc}, V_{oc}, *FF*, and also shows similar behaviour for both simulation and experiment.The short circuit current density (J_{sc}) enhanced with the i-layer thickness. The cell with an i-layers thickness of 350 nm shows the highest short circuit current density (J_{sc}) of 11.80 mA/cm^2 compared to other cells of 200, 250, and 300 nm i-layer thickness. On the other hand, the cells with 200 nm absorber layer thickness have a higher *FF* of 70% as compared to 60% for cell with 350 nm i-layer thickness. The power conversion efficiency increases with the absorber layer thickness. The cells fabricated with 350 nm absorber layer thickness exhibit the highest efficiency of 5.9% compared to 200, 250, and 300 nm due to high absorption inside the active layer [35,39], as confirmed by external quantum efficiency spectra, shown in Fig. 6.9 (b). EQE spectra show that the cell with an i-layer thickness of 350 nm has a higher spectral response than other cells because a large portion of the incident light is absorbed by the absorber layer, allowing for more carrier generation and collection, thus increasing solar cell efficiency. The integrated J_{sc} values, calculated from EQE spectra support the values of J_{sc} calculated from *J-V* curve for the both simulated and fabricated devices.

From these studies, a good match is observed with a slight deviation in simulated and fabricated devices due to differences in experimental conditions [40,41]. The experimental results are comparable with the simulation results with in the error bars and can be further used for the improvement of the efficiency with the implementation of silver nanoparticles as plasmonic back reflector in single junction n-i-p a-Si:H thin film solar cells.

6.5. Conclusions

Single junction n-i-p a-Si:H thin film solar cell are simulated using AFORS-HET and also fabricated using radio frequency plasma enhanced chemical vapor deposition (RF-PECVD) multi-chamber system. The influence of the emitter layer doping and absorber layer thickness on solar cell performance is studied. The doping concentration of p layer in simulation and

diborane (B_2H_6) flow rate in fabrication is varied to find the optimum flow rate over which the experimental results match very well. It is observed that the performance of solar cells fabricated using B_2H_6 flow rate of 10 sccm matches well with the simulated results for 7.6×10^{19} cm^{-3} of p-layer doping. The influence of thickness variation of absorber layer for these optimized values in simulation also show a similar trend with the fabricated cells having the comparable values of output parameters of solar cells. From the simulation, a power conversion efficiency of 5.79% is obtained with 200 nm absorber layer thickness and 7.6×10^{19} cm^{-3} p layer doping, while experimentally, 5.50 % power conversion efficiency is achieved with 200 nm absorber layer thickness and 10 sccm B_2H_6 flow rate in p-layer. The simulation results well matched the experimental results, validating the simulation. A small mismatch could be due to variation in layer properties for experimentally fabricated cells.

6.6 References

[1] M. Konagai, Present status and future prospects of silicon thin-film solar cells, Jpn. J. Appl. Phys. 50 (2011). https://doi.org/10.1143/JJAP.50.030001.

[2] M.A. Green, Thin-film solar cells: Review of materials, technologies and commercial status, J. Mater. Sci. Mater. Electron. 18 (2007) 15–19. https://doi.org/10.1007/s10854-007-9177-9.

[3] R.A. Street, Hydrogenated Amorphous Silicon, Cambridge (1991), See Also Ref. 26 (n.d.).

[4] M. Okil, M.S. Salem, T.M. Abdolkader, A. Shaker, From Crystalline to Low-cost Silicon-based Solar Cells: a Review, Silicon. 14 (2022) 1895–1911. https://doi.org/10.1007/s12633-021-01032-4.

[5] M. Stuckelberger, R. Biron, N. Wyrsch, F. Haug, C. Ballif, Review : Progress in solar cells from hydrogenated amorphous silicon, Renew. Sustain. Energy Rev. 76 (2017) 1497–1523. https://doi.org/10.1016/j.rser.2016.11.190.

[6] F. Meillaud, M. Boccard, G. Bugnon, M. Despeisse, S. Ha, F. Haug, M. Stuckelberger, C. Ballif, J. Persoz, J. Schu, Recent advances and remaining challenges in thin-film silicon photovoltaic technology, 18 (2015). https://doi.org/10.1016/j.mattod.2015.03.002.

[7] A. Lambertz, F. Finger, R.E.I. Schropp, U. Rau, V. Smirnov, Preparation and measurement of highly efficient a-Si:H single junction solar cells and the advantages of

μc-SiOx:H n-layers, Prog. Photovoltaics Res. Appl. 23 (2015) 939–948. https://doi.org/https://doi.org/10.1002/pip.2629.

[8] M.A. Green, E.D. Dunlop, M. Yoshita, N. Kopidakis, K. Bothe, G. Siefer, X. Hao, Solar cell efficiency tables (version 62), Prog. Photovoltaics Res. Appl. (2023) 651–663. https://doi.org/10.1002/pip.3726.

[9] R. Madaka, V. Kanneboina, P. Agarwal, Low-Temperature Growth of Amorphous Silicon Films and Direct Fabrication of Solar Cells on Flexible Polyimide and Photo-Paper Substrates, J. Electron. Mater. 47 (2018) 4710–4720. https://doi.org/10.1007/s11664-018-6344-0.

[10] C. Koch, M. Ito, M. Schubert, Low-temperature deposition of amorphous silicon solar cells, Sol. Energy Mater. Sol. Cells. 68 (2001) 227–236. https://doi.org/10.1016/S0927-0248(00)00249-X.

[11] K.B. Alaoui, S. Laalioui, Z. Naimi, B. Ikken, A. Outzourhit, Photovoltaic and impedance spectroscopy characterization of single-junction a-Si : H p – i – n solar cells deposited by simple shadow masking techniques using PECVD Photovoltaic and impedance spectroscopy characterization of single-junction a-Si : H p – i, 095315 (2020). https://doi.org/10.1063/5.0022889.

[12] R. Madaka, V. Kanneboina, P. Agarwal, Exploring the photo paper as flexible substrate for fabrication of a-Si:H based thin film solar cells at low temperature (110 °C): Influence of radio frequency power on opto-electronic properties, Thin Solid Films. 662 (2018) 155–164. https://doi.org/10.1016/j.tsf.2018.07.043.

[13] N.I. Sarkar, H.R. Ghosh, Efficiency improvement of amorphous silicon single junction solar cell by design optimization, ECCE 2017 - Int. Conf. Electr. Comput. Commun. Eng. (2017) 670–675. https://doi.org/10.1109/ECACE.2017.7912989.

[14] F.X.A. Abega, A.T. Ngoupo, J.M.B. Ndjaka, Numerical Design of Ultrathin Hydrogenated Amorphous Silicon-Based Solar Cell, Int. J. Photoenergy. 2021 (2021). https://doi.org/10.1155/2021/7506837.

[15] D. Berrian, M. Fathi, M. Kechouane, Numerical Optimization of a Bifacial Bi-Glass Thin-Film a-Si:H Solar Cell for Higher Conversion Efficiency, J. Electron. Mater. 47 (2018) 1140–1150. https://doi.org/10.1007/s11664-017-5828-7.

[16] D. Hamdani, Y. Cahyono, G. Yudoyono, Darminto, Band gap optimization of thin film a-si:H bifacial solar cells (bfscs) using afors-het, Mater. Sci. Forum. 966 MSF (2019) 409–414. https://doi.org/10.4028/www.scientific.net/MSF.966.409.

[17] I. Benigno, D. Darminto, Effect of Intrinsic Layer Energy Gap and Thicknesses

Optimization on the Efficiency of p-i-n Amorphous Silicon Solar Cell, IPTEK J. Sci. 2 (2017). https://doi.org/10.12962/j23378530.v2i3.a3184.

[18] D. Hamdani, S. Prayogi, Y. Cahyono, G. Yudoyono, D. Darminto, The Effects of Dopant Concentration on the Performances of the a-SiOx:H(p)/a-Si:H(i1)/a-Si:H(i2)/µc-Si:H(n) Heterojunction Solar Cell, Int. J. Renew. Energy Dev. 11 (2022) 173–181. https://doi.org/10.14710/ijred.2022.40193.

[19] W.H. Son, T.Y. Lee, S.Y. Choi, D. Jung, Effect of phosphorus doping on the performance of pin-type a-Si:H thin-film solar cells, Mol. Cryst. Liq. Cryst. 662 (2018) 25–31. https://doi.org/10.1080/15421406.2018.1466237.

[20] L. Hao, M. Zhang, M. Ni, X. Shen, X. Feng, Simulation of a Silicon Heterojunction Solar Cell with a Gradient Doping Emitter Layer, J. Electron. Mater. 48 (2019) 4688–4696. https://doi.org/10.1007/s11664-019-07241-3.

[21] V. Kanneboina, R. Madaka, P. Agarwal, Stepwise tuning of the doping and thickness of a-Si:H(p) emitter layer to improve the performance of c-Si(n)/a-Si:H(p) heterojunction solar cells, J. Mater. Sci. Mater. Electron. 32 (2021) 4457–4465. https://doi.org/10.1007/s10854-020-05187-5.

[22] L. Bechane, N. Bouarissa, K. Loucif, Numerical Simulation and Optimization of the Performances of a Solar Cell (p-i-n) Containing Amorphous Silicon Using AMPS-1D, Trans. Electr. Electron. Mater. 22 (2021) 531–535. https://doi.org/10.1007/s42341-020-00262-4.

[23] R.A. Stangl, a numerical computer program for simulation of (thin film) heterojunction solar cells, (2014) 1–3.

[24] R. Stangl, C. Leendertz, J. Haschke, Numerical Simulation of Solar Cells and Solar Cell Characterization Methods: the Open-Source on Demand Program AFORS-HET, 2010. https://doi.org/10.5772/8073.

[25] R. Stangl, C. Leendertz, General Principles of Solar Cell Simulation and Introduction to AFORS-HET BT - Physics and Technology of Amorphous-Crystalline Heterostructure Silicon Solar Cells, in: W.G.J.H.M. van Sark, L. Korte, F. Roca (Eds.), Springer Berlin Heidelberg, Berlin, Heidelberg, 2012: pp. 445–458. https://doi.org/10.1007/978-3-642-22275-7_13.

[26] R. Varache, C. Leendertz, M.E. Gueunier-Farret, J. Haschke, D. Muñoz, L. Korte, Investigation of selective junctions using a newly developed tunnel current model for solar cell applications, Sol. Energy Mater. Sol. Cells. 141 (2015) 14–23. https://doi.org/10.1016/j.solmat.2015.05.014.

[27] D.E. Carlson, C.R. Wronski, Amorphous silicon solar cell, Appl. Phys. Lett. 28 (1976) 671–673. https://doi.org/10.1063/1.88617.

[28] A. Belfar, Simulation study of the a-Si: H/nc-Si: H solar cells performance sensitivity to the TCO work function, the band gap and the thickness of i-a-Si: H absorber layer, Sol. Energy. 114 (2015) 408–417. https://doi.org/10.1016/j.solener.2015.02.010.

[29] H. Deka, A. Sunaniya, P. Agarwal, Design and Simulation of Highly Efficient One-Sided Short PIN Diode Silicon Heterojunction Solar Cell, IEEE J. Photovoltaics. 12 (2022) 204–212. https://doi.org/10.1109/JPHOTOV.2021.3116016.

[30] M. Sharma, D. Chaudhary, N. Dwivedi, S. Sudhakar, S. Kumar, Simulating the Role of TCO Materials, their Surface Texturing and Band Gap of Amorphous Silicon Layers on the Efficiency of Amorphous Silicon Thin Film Solar Cells, Silicon. 9 (2017) 59–68. https://doi.org/10.1007/s12633-015-9331-6.

[31] A. Belfar, B. Amiri, H. Aït-kaci, Optimization of band gap and thickness for the development of efficient n-i-p+ solar cell, J. Nano- Electron. Phys. 7 (2015) 1–7.

[32] M.I. Kabir, Z. Ibrahim, K. Sopian, N. Amin, Effect of structural variations in amorphous silicon based single and multi-junction solar cells from numerical analysis, Sol. Energy Mater. Sol. Cells. 94 (2010) 1542–1545. https://doi.org/10.1016/j.solmat.2009.12.031.

[33] S. Singh, S. Kumar, N. Dwivedi, Band gap optimization of p-i-n layers of a-Si:H by computer aided simulation for development of efficient solar cell, Sol. Energy. 86 (2012) 1470–1476. https://doi.org/10.1016/j.solener.2012.02.007.

[34] N. Dwivedi, S. Kumar, A. Bisht, K. Patel, S. Sudhakar, Simulation approach for optimization of device structure and thickness of HIT solar cells to achieve ∼27% efficiency, Sol. Energy. 88 (2013) 31–41. https://doi.org/10.1016/j.solener.2012.11.008.

[35] M. Sharma, S. Kumar, N. Dwivedi, S. Juneja, A.K. Gupta, S. Sudhakar, K. Patel, Optimization of band gap, thickness and carrier concentrations for the development of efficient microcrystalline silicon solar cells: A theoretical approach, Sol. Energy. 97 (2013) 176–185. https://doi.org/10.1016/j.solener.2013.08.012.

[36] R. Madaka, V. Kanneboina, P. Agarwal, Enhanced performance of amorphous silicon solar cells (110 °c) on flexible substrates with a-SiC:H(p) window layer and H2 plasma treatment at n/i and i/p interface, Semicond. Sci. Technol. 33 (2018). https://doi.org/10.1088/1361-6641/aac8ca.

[37] V. Kanneboina, R. Madaka, P. Agarwal, High open circuit voltage c-Si/a-Si:H heterojunction solar cells: Influence of hydrogen plasma treatment studied by spectroscopic ellipsometry, Sol. Energy. 166 (2018) 255–266.

https://doi.org/10.1016/j.solener.2018.03.068.

[38] Q. Wang, Fill factor related issues in hydrogenated amorphous Si solar cells, Sol. Energy Mater. Sol. Cells. 129 (2014) 64–69. https://doi.org/10.1016/j.solmat.2014.02.015.

[39] M.I. Kabir, S.A. Shahahmadi, V. Lim, S. Zaidi, K. Sopian, N. Amin, Amorphous silicon single-junction thin-film solar cell exceeding 10 % efficiency by design optimization, Int. J. Photoenergy. 2012 (2012). https://doi.org/10.1155/2012/460919.

[40] G. Ahmad, S. Mandal, A.K. Barua, T.K. Bhattacharya, J.N. Roy, Band Offset Reduction at Defect-Rich p/i Interface Through a Wide Bandgap a-SiO:H Buffer Layer, IEEE J. Photovoltaics. 7 (2017) 414–420. https://doi.org/10.1109/JPHOTOV.2016.2642644.

[41] S.M. Iftiquar, J. Jung, C. Shin, H. Park, J. Park, J. Jung, J. Yi, Light management for enhanced efficiency of textured n-i-p type amorphous silicon solar cell, Sol. Energy Mater. Sol. Cells. 132 (2015) 348–355. https://doi.org/10.1016/j.solmat.2014.09.011.

Chapter 7

Implementation of silver nanoparticle as plasmonic back reflector to improve the performance of a-Si:H thin film solar cells

7.1. Introduction

Thin-film solar cells have emerged as a cost-effective alternative to traditional wafer-based photovoltaics [1]. Particularly, thin-film silicon solar cells offer significant advantages [2], utilizing affordable substrates like glass, plastic foil, or steel [3] due to their low processing temperature requirements [4]. However, they face challenges in achieving high efficiency compared to technologies like crystalline silicon (c-Si), Copper Indium Gallium Selenide (CIGS), and Cadmium Telluride (CdTe), primarily due to incomplete absorption of light beyond the bandgap [5]. Efficient light trapping techniques are essential to address this challenge and enhance light absorption within the device [6–9]. Light trapping structures enable long-wavelength photons to travel greater distances than the device thickness, thus increasing their likelihood of absorption. Recent research has focused on optimizing light trapping schemes in thin-film solar cells, resulting in the identification of promising approaches [7–13]. Random surface texturing is a widely adopted method for light trapping in conventional thin-film Si solar cells. This approach involves texturing the front transparent conducting oxide (TCO) and the rear contact or mirror, especially in superstrate and substrate cell configurations, respectively [14–16]. However, this texturing technique often leads to high surface roughness, contributing to the formation of bulk and surface defects, which in turn increase recombination in the silicon layers and subsequently degrade device performance [17].

Use of metal nanoparticles (MNPs) presents an alternative solution, offering benefits such as low surface roughness [13,18–22] and efficient light scattering when noble metal nanoparticles are excited at their surface plasmon resonance. Surface plasmon resonance is a collective oscillation of the conduction electrons in the metal [23]. The resonance of metallic nanoparticles strongly depends on factors like size, shape, spacing of the metallic particles, and

the dielectric properties of the surrounding medium [24–26]. Light interaction with these nanoparticles at plasmonic resonance results in both scattering and absorption, properties that can be harnessed for effective light trapping. Over time, various light trapping geometries based on periodic or random nanostructures, such as nanowires, nanocones, and nanoparticles, have been successfully demonstrated [27–33]. One particularly promising approach is far-field scattering from subwavelength metallic nanoparticles (NPs) that sustain localized surface plasmon resonances (LSPR) [20,34,35]. Among the metals used, silver nanoparticles (Ag NPs) are a popular choice due to their robust plasmon resonances, large scattering cross-section, potential for low absorption in the visible and near-infrared spectrum, and the ability to precisely control their size and shape using various fabrication methods [26,36].

The positioning of metal NP arrays in solar cells holds significant importance for their photovoltaic application. Metal NPs placed either on the front or rear sides of a solar cell can cause preferential scattering of light into the semiconductor layers. However, placing metal nanoparticles on the rear side of the cell is particularly advantageous. In this configuration, Ag NPs arrays are typically embedded in a thin transparent conductive oxide (TCO) layer situated between the silicon absorbing material and a flat Ag mirror (rear contact). This specific arrangement is referred to as a plasmonic back reflector (Plasmonic BR) [13,18,37–41]. Using silver nanoparticles as a back reflector enhances reflection and scatters light back to the absorber layer, preventing its absorption during the initial pass. Consequently, the absorption of the scattered light by the adjacent active absorbing layer is improved, resulting in an increase in the photocurrent of the solar cell.

With this motivation, in this chapter we have fabricated the Ag NPs by solid state deweting using optimized parameters from our earlier work in different configurations. The structural and optical properties of the Ag NPs on these configurations have been studied. Ag NPs as plasmonic back reflector have been integrated into a-Si:H thin film solar cells to improve the efficiency.

7.2. Experimental Details

Self-assembled silver nanoparticles were fabricated by the SSD of sputtered precursor thin films on different configurations as shown in Fig. 7.1; 1(a) *on corning glass 1737,* 1(b*) corning glass 1737/AZO*, and 1 (c) plasmonic back reflector. The plasmonic back reflector with the structure *corning glass 1737/Ag mirror/AZO/Ag NPs/ AZO* was fabricated on corning glass substrate by sequential deposition of a 100 nm Ag layer, a 40 nm AZO layer and a thin Ag

precursor film of 21 nm using rf sputtering system. The Ag precursor films were deposited using sputtering parameters as follows; Argon flow rate (AFR) of 5 sccm, substrate temperature of 50 ℃, process pressure of 5×10^{-2} mbar, electrode separation of 8 cm and rf power of 40 Watt. The deposition was followed by annealing at 400 ℃ for 1 hour under high vacuum of 10^{-6} mbar, in which self-assembled NPs are formed by solid state dewetting from the topmost Ag thin layer. As a last fabrication step of plasmonic back reflector, a layer of 20 nm of AZO was deposited on top of the Ag NPs. Ag NPs on the corning glass substrate and *corning glass/AZO* substrate were grown in the same way. The flat back reflector with the structure *corning glass 1737/Ag mirror/ AZO* substrate were grown in the same way. The flat back reflector with the structure *corning glass 1737/Ag mirror/ AZO* was deposited in the same manner as plasmonic BR without the NPs as shown in Fig. 1(d)

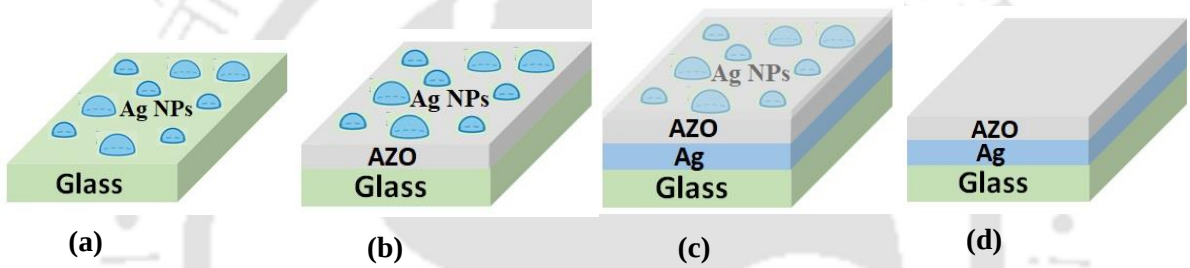

Fig. 7.1 (a) Ag NPs on corning glass substrate, (b) Ag NPs on corning glass/AZO substrate, (c) plasmonic back reflector, and (d) flat back reflector

Hydrogenated amorphous silicon (a-Si:H) solar cells were manufactured with an n-i-p (substrate) configuration, and they were fabricated on both the flat Back Reflector (BR) and the Plasmonic Back Reflector (PBR) at a temperature of 180 ℃. The fabrication process was carried out using a multi-chamber Plasma Enhanced Chemical Vapor Deposition (PECVD) system, with the device structure depicted in Fig. 7.2. The Plasmonic Back Reflector (PBR) was processed before the deposition of silicon layers to ensure that the high temperature required for Ag NPs formation would not adversely affect the a-Si:H layers deposited at lower temperatures. The thickness of the n-i-p layers was maintained at 30 nm, 200 nm, and 10 nm, respectively. Additionally, a 100 nm layer of Indium Tin Oxide (ITO) was deposited using a circular mask with a 4 mm diameter, resulting in a cell area of 0.12 cm^2, through radio frequency (rf) sputtering. To complete the device, front metal grid electrodes were applied to the cells using silver paste. The photograph and cross sectional SEM image of fabricated cell with plasmonic BR is shown in Fig. 7.3.

The specific deposition parameters for each layer are outlined in Table 7.1.

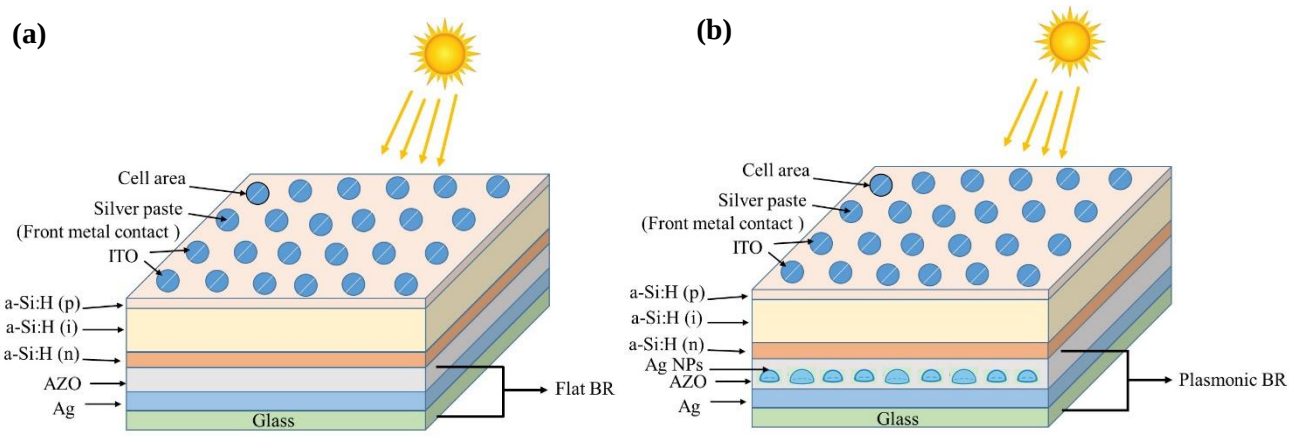

Fig. 7.2 Solar cell structure with (a) flat BR and (b) plasmonic BR

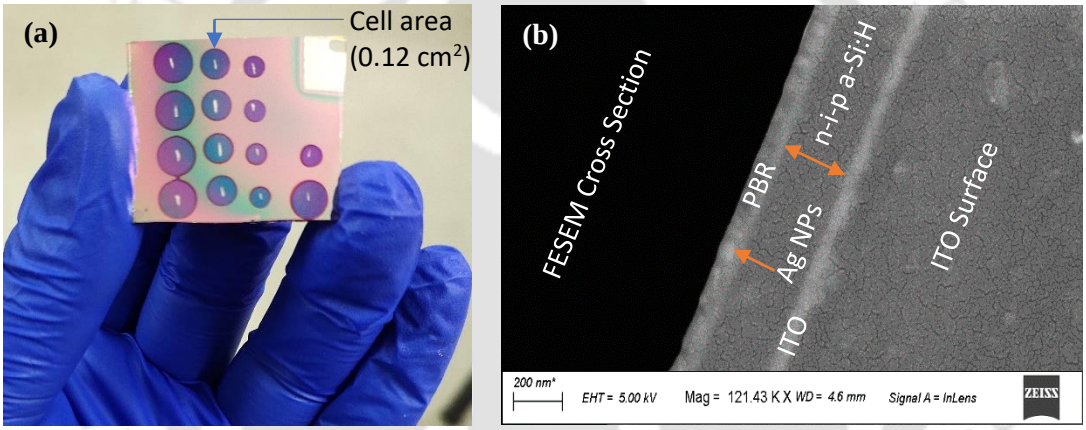

Fig. 7.3 (a) Photograph and (b) cross section SEM image of the fabricated solar cell with plasmonic BR

Table 7.1 Deposition parameters for each layer of a-Si:H thin film solar cells

Cell's Layers	Gas flow rate (sccm)					Process pressure (mbar)	Deposition temperature (°C)	RF power (Watt)
	Ar	H_2	SiH_4	B_2H_6 (2% in H_2)	PH_3 (1% in H_2)			
ITO	7	-	-	-	-	5.4×10^{-3}	100	80
a-Si:H(p)	-	100	5	10	-	6.2×10^{-1}	180	30
a-Si:H(i)	-	60	5	-	-	5.6×10^{-1}	180	30
a-Si:H(n)	-	50	5	-	10	5.2×10^{-1}	180	30
AZO	7	-	-	-	-	5.4×10^{-2}	100	80
Ag	7	-	-	-	-	5.4×10^{-2}	100	80

The thickness of all films/layers was determined by Stylus profilometer. The nanostructure of Ag NPs was characterized by Field Emission Scanning Electron Microscope. Atomic force microscopy (AFM) was done for the surface morphology. The surface coverage, NPs size distribution from the FESEM images were determined by using *image j* software. The absorbance, diffuse and specular reflectance of silver nanoparticles were measured with a double beam UV-Vis-NIR spectrometer equipped with 60 mm integrating sphere and Universal reflectance accessary (URA), in the wavelength range of 300-1500 nm. The specular reflectance measurements were done at incidence angle of 45° from normal of the surface. In order to test the performance of the fabricated solar cells, the *I-V* characteristics measurements on a-Si:H solar cells were performed under one sun (AM 1.5G, 100 mW/cm^2), using a solar simulator. The external quantum efficiency (EQE) measurements were performed at room temperature in the wavelength range from 350-900. All details of these characterization techniques are given in chapter 2.

7.3. Results and Discussion

7.3.1 FESEM analysis

The FESEM images of Ag NPs on corning glass and corning glass/AZO substrate formed by post annealing of Ag precursor films of the thickness 21 nm are shown in Fig. 7.4. From the SEM images, it is clear that the NPs are uniformly distributed over the surface having nearly a regular spherical shape. It is also observed that the size of NPs formed on the AZO is larger than those formed on the bare glass substrate with the average particle size of 110 ± 8 nm and 90 ± 5 nm respectively. Furthermore, the relative number of small particles is reduced in the case of AZO. This indicate the surface properties of the AZO also play a crucial role in the formation of the large size Ag NPs. For this morphological difference, solid state dewetting (SSD) process, which minimize the surface free energies of the film, substrate and film-substrate interface is responsible [42]. The formation of Ag NPs from the thin Ag film under the heat treatment depends upon the process parameters and type of substrate [43–45]. These differences can be attributed to the higher surface free energy of the AZO than the glass.

The particles grown through the SSD process exhibit a broad size distribution. Consequently, a statistical approach is necessary for analysis and its correlation with optical properties. This statistical analysis can be typically achieved through histograms depicting the size distribution of Ag NPs, as shown in Fig. 7.5. These histograms illustrate that the number of small particles decreases while the average particle size increases for the NPs on the AZO. Moreover, the

surface area covered by NPs increases from 26% to 33%, indicating that the NPs formed on AZO also tend to have a flatter morphology compared to those on the bare glass substrate.

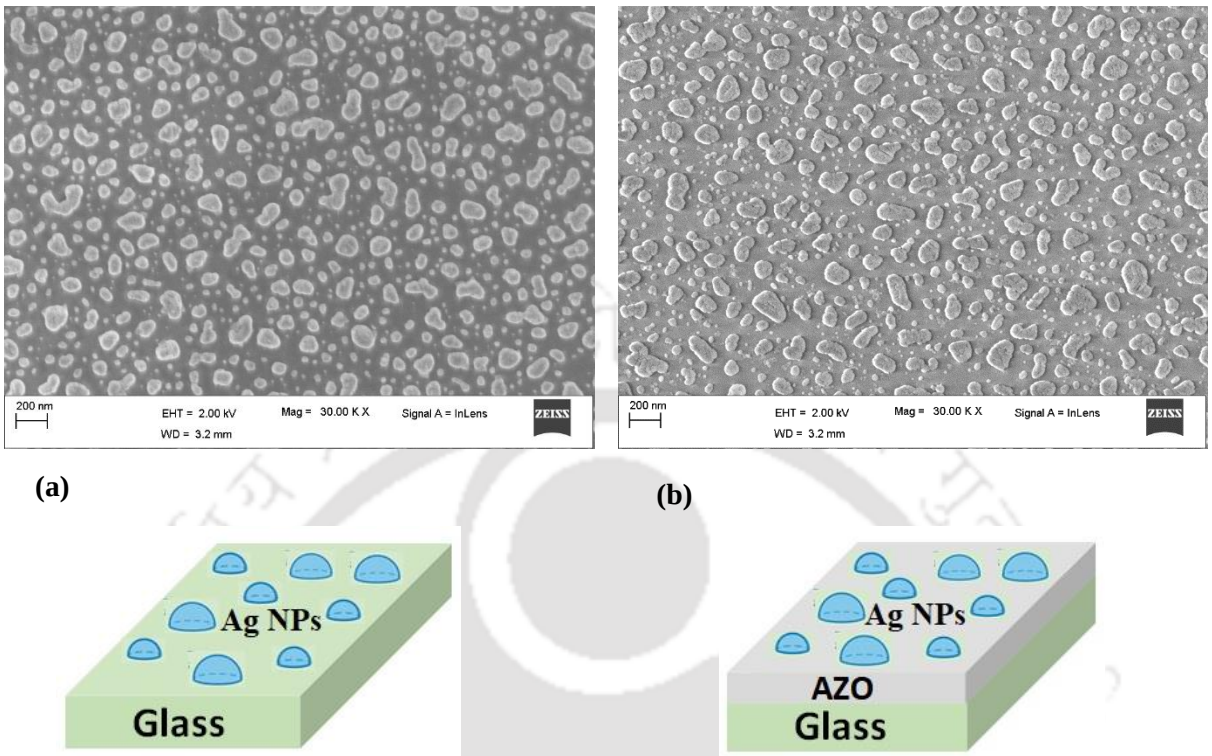

Fig. 7.4 FESEM images of Ag NPs on corning glass (a) and corning glass /AZO (b) formed by annealing at 400 ℃ for 1 h of Ag precursor films of thickness 21 nm on 200 nm scale.

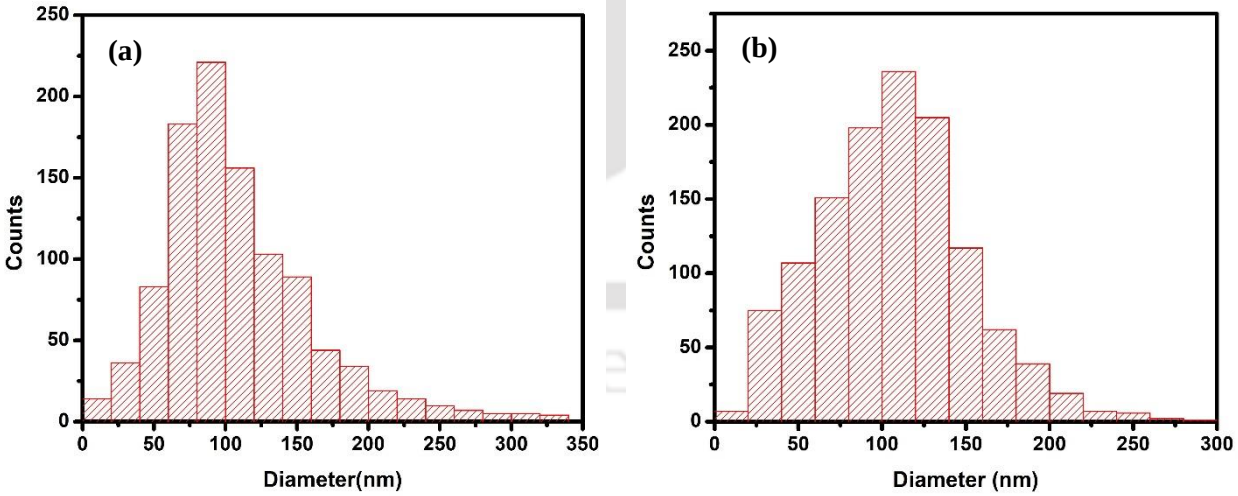

Fig. 7.5 Histogram images of Ag NPs on corning glass (a) and corning glass/AZO (b) formed by annealing at 400 ℃ for 1 h of Ag precursor films of thickness 21 nm.

7.3.2 AFM Analysis

The surface morphology of Ag NPs on both corning glass and corning glass/AZO is depicted in Fig. 7.6, as revealed by AFM images.

These images confirm the even distribution of nanoparticles across the surface. Notably, NPs formed on the glass substrate exhibit an approximately hemispherical shape and tend to flatten on the AZO, with maximum heights reaching around 75 nm [38]. NPs on the bare glass substrate have a lower surface roughness, although the roughness is slightly greater for NPs embedded in the AZO. The root mean square roughness (RMS) measures 15±2 nm for NPs formed on the bare glass substrate and 18±2 nm for those on the AZO. The increased roughness observed for NPs on the AZO is attributed to their larger size and coverage area, in agreement with the FESEM results.

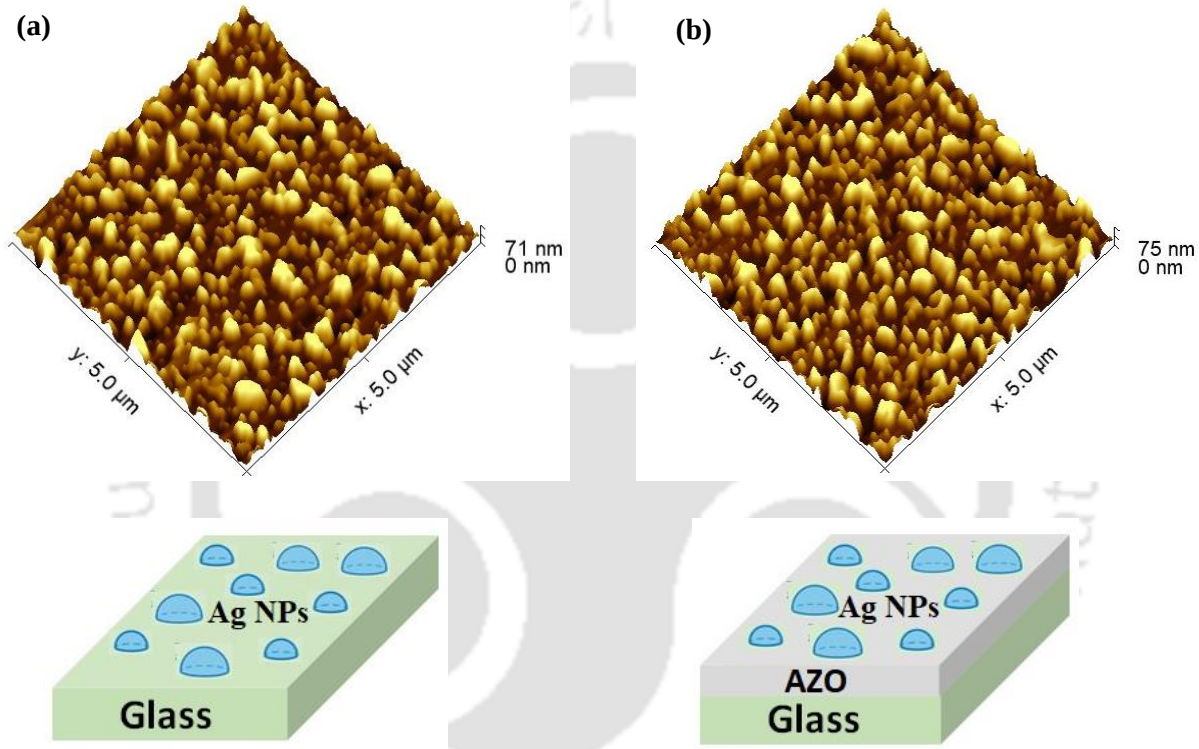

Fig. 7.6 3D AFM images of Ag NPs on corning glass (a) and corning glass/AZO (b) substrate with 5 $\mu m \times 5\ \mu m$ area formed by annealing at 400 ℃ for 1 h of Ag precursor films of thickness 21 nm.

7.3.3 UV-Vis-NIR analysis

The plasmonic properties of Ag NPs, in terms of their absorbance, were measured with a double beam UV-Vis-NIR spectrometer Lambda 950 in the wavelength range of 250-1500 nm and are shown in Fig. 7.7. The spectra only show the characteristics of the Ag NPs and plasmonic back reflector after excluding the background influence of the glass substrate from the raw optical observations. A sharp LSPR peak in the case of Ag NPs on glass and a broad LSPR peak for the Ag NPs on AZO is observed. Furthermore, the LSPR peak is significantly red shifted from 500 nm for NPs on glass to 720 nm for NPs on AZO. This is directly related to the increase in the particle size for NPs on AZO. Additionally, the deposition of Ag NPs on AZO cause an

increase of the effective refractive index of the material surrounding the NPs. This results in spectral broadening of the LSPR peak [26].

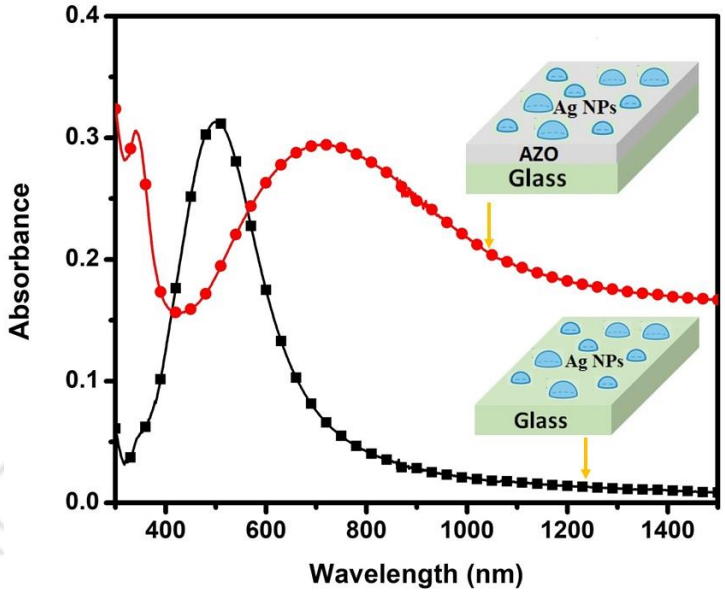

Fig. 7.7 Absorbance spectra of Ag NPs on corning glass substrate and corning glass/AZO.

The light trapping properties of the back reflector (BR) in solar cells are generally characterized by scattering parameters: diffuse reflectance and haze in reflection (the ratio of diffuse to total reflection) [26]. Diffuse reflection, which determines how much light is scattered away from the specular direction, and how many photons are more likely to produce photocurrent and contribute to the external quantum efficiency (EQE), is the primary optical characteristic that assesses the suitability of the plasmonic BR for light trapping. The specular reflectance of the plasmonic BR contributes primarily in the short-wavelength region, where incoming light is not entirely absorbed during the first pass but is more likely to be absorbed in the second pass following specular reflection. On the other hand, diffuse reflectance plays a crucial role in the near-bandgap region of silicon due to a drop in its absorption coefficient, as it enhances the optical path length of incident light, which is essential for light absorption [46]. Fig. 7.8 shows the specular, diffuse, total reflectance and the haze in the reflection of Ag NPs, flat BR and plasmonic BR in the wavelength range of 300-1500 nm. In Fig. 7.8 (a), it is observed that the specular reflectance of the flat BR is higher than that of the plasmonic BR, as well as the Ag NPs on the bare glass substrates, which is related to their surface morphology. In principle, the flat surface contributes more to specular reflection than diffuse reflection. In contrast, Fig. 7.8 (b) shows that the diffuse reflection of the flat BR, i.e., without NPs, is almost negligible, while a substantial increase in diffuse reflection ($R_{diffuse}$) is observed in the presence of NPs on the

glass substrate. The NPs coupled with the flat BR (plasmonic BR) exhibit higher diffuse reflection than those of Ag NPs on the bare glass substrate across the entire wavelength range due to the constructive near-field interaction between the Ag NPs and the AZO. It has been found that the presence of Ag NPs on the AZO, rather than on the bare glass, influences the optical response due to the high refractive index of the surrounding medium of the Ag NPs. In Fig. 7.8 (c), the total reflectance ($R_T = R_{specular} + R_{diffuse}$) of the flat BR, plasmonic BR, and Ag NPs on the glass substrate is depicted. As expected, the flat BR exhibits nearly 100% reflection, which is higher than both Ag NPs on the glass substrate and the plasmonic BR. However, the total reflectance of the plasmonic BR is comparable to that of the flat BR. The haze spectra, represented as the ratio of $R_{diffuse}$ and R_T, for the flat BR, PBR, and Ag NPs on the glass substrate are shown in Fig. 7.8 (d). The flat BR exhibits a lower haze value due to its negligible diffuse reflectance and higher total reflection. The haze of plasmonic BR is higher than the Ag NPs on the glass substrate however in the wavelength region 900-1500 the haze values of plasmonic BR and Ag NPs on the glass substrate is almost similar.

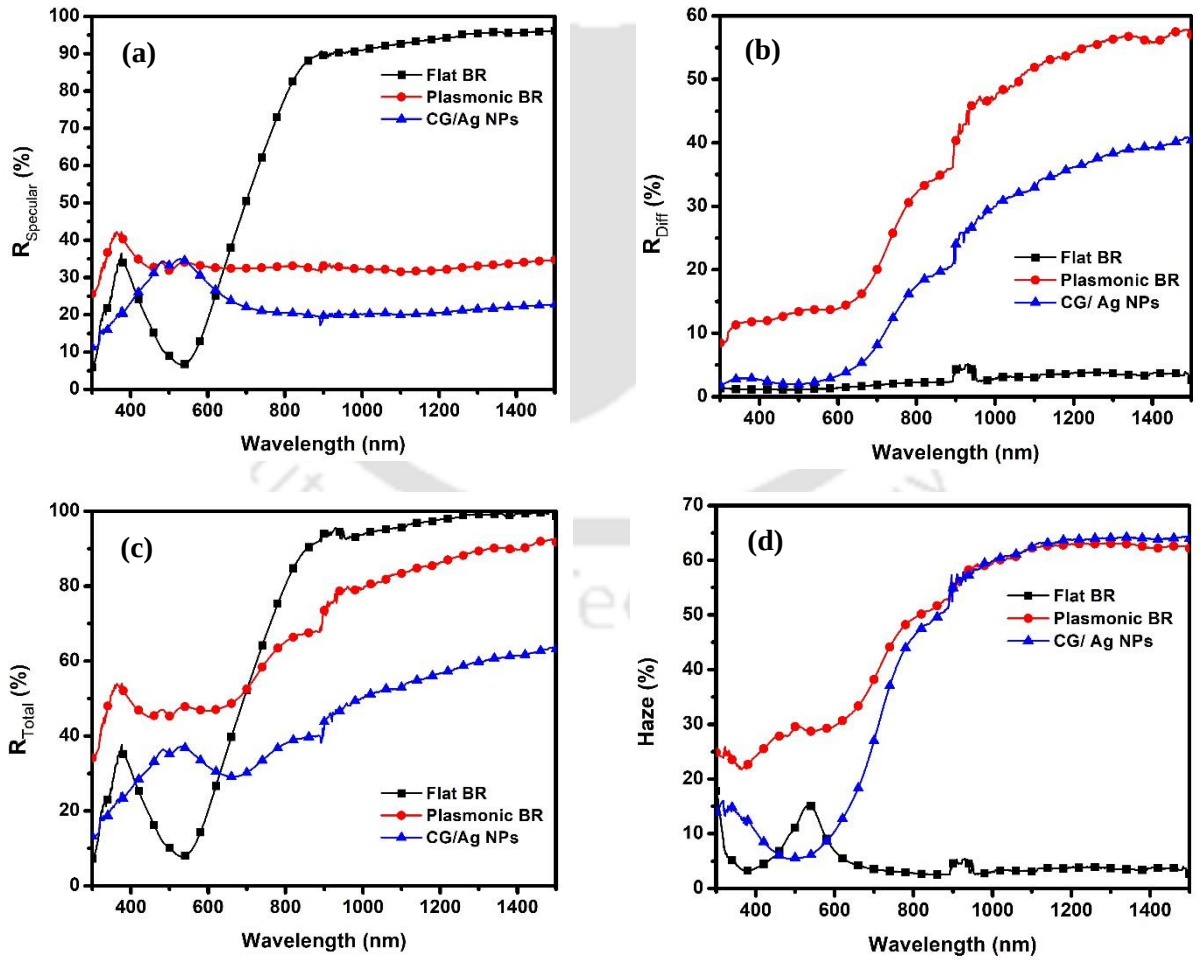

Fig. 7.8 (a) Specular reflectance, (b) diffuse reflectance spectra, (c) total reflectance, and (d) haze in reflection of flat plasmonic BRs and Ag NPs on corning glass substrate.

7.3.4 Current-Voltage and External quantum efficiency measurements on a-Si:H thin film solar cells

Fig. 7.9 illustrates the current-voltage (J-V) curve and external quantum efficiency (EQE) curve of the solar cells deposited on plasmonic back reflectors (BRs), which are compared with a reference planar device deposited on a flat BR (consisting of 100 nm Ag and 40 nm AZO) but without nanoparticles (NPs). Plasmonic BRs exhibit superior cell performance across the entire wavelength range. For shorter wavelengths (below 570 nm), the enhancement in external quantum efficiency (EQE) is primarily attributed to the front surface texturing of the solar cell induced by Ag NPs embedded in the plasmonic back reflector [46]. In this spectral range, all incident light is absorbed within the silicon layers during the initial pass without interaction with the NPs. Conversely, for wavelengths beyond 570 nm, the EQE enhancement is associated with the strong light scattering induced by the Ag NPs. This scattering effect results in an increased optical path within the photovoltaic layer when compared to the flat back reflector configuration. Moreover, the Ag NPs significantly enhance absorption at longer wavelengths. Therefore, the primary factor contributing to the observed EQE enhancements in the red to near-infrared (NIR) region is the light scattering facilitated by the Ag NPs. The power conversion efficiencies (η) of the a-Si:H thin-film solar cell with the flat BR and a-Si:H with plasmonic BR are 5.6% and 8.4%, respectively. The open-circuit voltage (V_{oc}) is 0.814 *V* for the solar cell with the flat BR and 0.820 *V* for the one with the plasmonic BR. The fill factor (*FF*) varies from 70.5% to 72.7%, and the short-circuit currents (J_{sc}) are 9.6 mA/cm² for the solar cell with the flat BR and 14.2 mA/cm² for the one with the plasmonic BR. Hence, the key factor contributing to the increased efficiency of the a-Si:H thin-film solar cells is the enhancement of J_{sc}.

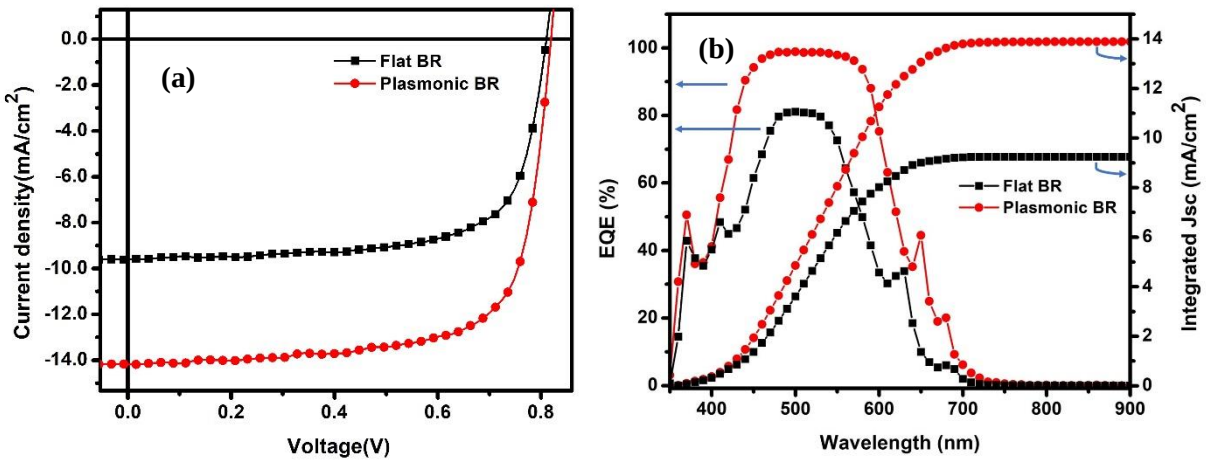

Fig. 7. 9 (a)J-V curve and (b) External quantum efficiency curve of a-Si:H solar cells with flat BR and plasmonic BR.

The use of Ag NPs as a plasmonic BR in a-Si:H solar cells results in a substantial boost in the photocurrent, with an enhancement factor of up to 47%. The values of output parameters of a-Si:H thin film solar cells with flat BR and Plasmonic BR are listed in table 7.2.

Table 7.2 Calculated values of Jsc, Voc , FF, and efficiency with Flat BR and plasmonic BR

(n-i-p) a-Si:H solar cell	J_{SC} (mA/cm^2)	V_{OC} (V)	FF (%)	PCE (η) (%)
Flat BR	9.6	0.814	70.5	5.6
Plasmonic BR	14.2	0.820	72.7	8.4

7.4 Conclusions

We have successfully demonstrated the use of silver nanoparticles as plasmonic back reflector in thin film solar cells for light trapping application to achieve high efficiency. The silver nanoparticles were fabricated by solid state dewetting of Ag thin films on different substrate configuration. The structural and optical properties of the Ag NPs on these different substrate configuration was studied. It was observed that the size of the Ag nanoparticles formed on the AZO substrate was larger than those formed on the bare glass substrate, with average particle sizes of 110 nm and 90 nm, respectively. In the case of Ag nanoparticles on glass, a sharp localized surface plasmon resonance (LSPR) peak at 500 nm was observed. This peak experienced a redshift, shifting from 500 nm to 720 nm, and broadened for the Ag nanoparticles on the glass/AZO substrate. The Ag nanoparticles with a plasmonic BR configuration exhibited excellent light trapping properties, characterized by high values of diffuse reflection and haze in reflection across the visible and near-infrared (NIR) wavelength range. This led to a broadband enhancement in the quantum efficiency of a-Si:H thin-film solar cells fabricated on the plasmonic BR. This enhancement can be attributed to both the front surface texture induced by the shape of the nanoparticles and plasmon-assisted scattering. As a result of these improvements, there was a substantial gain in short-circuit current density (J_{sc}) of 4.6 mA/cm² (47%) when compared to solar cells with a flat back reflector. The a-Si:H thin-film solar cells with plasmonic BRs demonstrated an overall efficiency (η) of 8.4%, a notable improvement from the 5.6% efficiency of a-Si:H thin-film solar cells with flat BRs. Importantly, these enhancements did not lead to any deterioration in other output parameters such as open-circuit voltage (V_{oc}) and fill factor (*FF*) of the solar cells. In summary, our results emphasize the

effectiveness of using metal nanoparticles in a plasmonic BR configuration for light trapping in thin-film solar cells, ultimately leading to improved performance.

7.5 References

[1] M. Okil, M.S. Salem, T.M. Abdolkader, A. Shaker, From Crystalline to Low-cost Silicon-based Solar Cells: a Review, Silicon. 14 (2022) 1895–1911. https://doi.org/10.1007/s12633-021-01032-4.

[2] J. Ramanujam, D.M. Bishop, T.K. Todorov, O. Gunawan, J. Rath, R. Nekovei, E. Artegiani, A. Romeo, Flexible CIGS, CdTe and a-Si:H based thin film solar cells: A review, Prog. Mater. Sci. 110 (2020) 1–20. https://doi.org/10.1016/j.pmatsci.2019.100619.

[3] R. Madaka, V. Kanneboina, P. Agarwal, Exploring the photo paper as flexible substrate for fabrication of a-Si:H based thin film solar cells at low temperature (110 °C): Influence of radio frequency power on opto-electronic properties, Thin Solid Films. 662 (2018) 155–164. https://doi.org/10.1016/j.tsf.2018.07.043.

[4] R. Madaka, V. Kanneboina, P. Agarwal, Low-Temperature Growth of Amorphous Silicon Films and Direct Fabrication of Solar Cells on Flexible Polyimide and Photo-Paper Substrates, J. Electron. Mater. 47 (2018) 4710–4720. https://doi.org/10.1007/s11664-018-6344-0.

[5] M.A. Green, E.D. Dunlop, M. Yoshita, N. Kopidakis, K. Bothe, G. Siefer, X. Hao, Solar cell efficiency tables (version 62), Prog. Photovoltaics Res. Appl. (2023) 651–663. https://doi.org/10.1002/pip.3726.

[6] C. Sun, Z. Wang, X. Wang, J. Liu, A Surface Design for Enhancement of Light Trapping Efficiencies in Thin Film Silicon Solar Cells, Plasmonics. 11 (2016) 1003–1010. https://doi.org/10.1007/s11468-015-0135-8.

[7] P.M. Voroshilov, C.R. Simovski, P.A. Belov, A.S. Shalin, Light-trapping and antireflective coatings for amorphous Si-based thin film solar cells, J. Appl. Phys. 117 (2015). https://doi.org/10.1063/1.4921440.

[8] C. Haase, H. Stiebig, Thin-film silicon solar cells with efficient periodic light trapping

texture, Appl. Phys. Lett. 91 (2007). https://doi.org/10.1063/1.2768882.

[9] R.H. Franken, R.L. Stolk, H. Li, C.H.M. Van Der Werf, J.K. Rath, R.E.I. Schropp, Understanding light trapping by light scattering textured back electrodes in thin film n-i-p -type silicon solar cells, J. Appl. Phys. 102 (2007). https://doi.org/10.1063/1.2751117.

[10] Z. Ouyang, S. Pillai, F. Beck, O. Kunz, S. Varlamov, K.R. Catchpole, P. Campbell, M.A. Green, Effective light trapping in polycrystalline silicon thin-film solar cells by means of rear localized surface plasmons, Appl. Phys. Lett. 96 (2010). https://doi.org/10.1063/1.3460288.

[11] H. Sai, H. Jia, M. Kondo, Impact of front and rear texture of thin-film microcrystalline silicon solar cells on their light trapping properties, J. Appl. Phys. 108 (2010). https://doi.org/10.1063/1.3467968.

[12] J. Müller, B. Rech, J. Springer, M. Vanecek, TCO and light trapping in silicon thin film solar cells, Sol. Energy. 77 (2004) 917–930. https://doi.org/10.1016/j.solener.2004.03.015.

[13] S. Cao, D. Yu, Y. Lin, C. Zhang, L. Lu, M. Yin, X. Zhu, X. Chen, D. Li, Light Propagation in Flexible Thin-Film Amorphous Silicon Solar Cells with Nanotextured Metal Back Re fl ectors, (2020). https://doi.org/10.1021/acsami.0c05330.

[14] X. Yan, S. Venkataraj, A.G. Aberle, Modified surface texturing of aluminium-doped zinc oxide (AZO) transparent conductive oxides for thin-film silicon solar cells, Energy Procedia. 33 (2013) 157–165. https://doi.org/10.1016/j.egypro.2013.05.053.

[15] F.J. Haug, A. Naqavi, C. Ballif, Diffraction and absorption enhancement from textured back reflectors of thin film solar cells, J. Appl. Phys. 112 (2012). https://doi.org/10.1063/1.4737606.

[16] U. Palanchoke, V. Jovanov, H. Kurz, R. Dewan, P. Magnus, H. Stiebig, D. Knipp, Influence of back contact roughness on light trapping and plasmonic losses of randomly textured amorphous silicon thin film solar cells, Appl. Phys. Lett. 102 (2013). https://doi.org/10.1063/1.4793415.

[17] C. Battaglia, J. Escarré, K. Söderström, L. Erni, L. Ding, G. Bugnon, A. Billet, M.

Boccard, L. Barraud, S. De Wolf, F.J. Haug, M. Despeisse, C. Ballif, Nanoimprint lithography for high-efficiency thin-film silicon solar cells, Nano Lett. 11 (2011) 661–665. https://doi.org/10.1021/nl1037787.

[18] C. Zhang, Y. Song, M. Wang, M. Yin, X. Zhu, L. Tian, H. Wang, X. Chen, Z. Fan, L. Lu, D. Li, Efficient and Flexible Thin Film Amorphous Silicon Solar Cells on Nanotextured Polymer Substrate Using Sol–gel Based Nanoimprinting Method, Adv. Funct. Mater. 27 (2017). https://doi.org/10.1002/adfm.201604720.

[19] V.E. Ferry, A. Polman, H.A. Atwater, Light trapping in plasmonic solar cells, Opt. InfoBase Conf. Pap. 18 (2011) 237–245. https://doi.org/10.1364/ls.2011.lwe3.

[20] Y.H. Jang, Y.J. Jang, S. Kim, L.N. Quan, K. Chung, D.H. Kim, Plasmonic Solar Cells: From Rational Design to Mechanism Overview, Chem. Rev. 116 (2016) 14982–15034. https://doi.org/10.1021/acs.chemrev.6b00302.

[21] H.A. Atwater, A. Polman, Plasmonics for improved photovoltaic devices, Nat. Mater. 9 (2010) 205–213. https://doi.org/10.1038/nmat2629.

[22] K.R. and Catchpole, A. Polman, Plasmonic solar cells, Opt. Express. 16 (2008) 21793–21800.

[23] W.J. Ho, Y.Y. Lee, S.Y. Su, External quantum efficiency response of thin silicon solar cell based on plasmonic scattering of indium and silver nanoparticles, Nanoscale Res. Lett. 9 (2014) 1–8. https://doi.org/10.1186/1556-276X-9-483.

[24] M. Singh, P. Agarwal, Growth dynamics and its correlation with plasmonic properties of silver nanoparticles grown by solid state dewetting, Mater. Res. Bull. 167 (2023) 112380. https://doi.org/10.1016/j.materresbull.2023.112380.

[25] L. Wang, M. Hasanzadeh Kafshgari, M. Meunier, Optical Properties and Applications of Plasmonic-Metal Nanoparticles, Adv. Funct. Mater. 30 (2020) 2005400. https://doi.org/https://doi.org/10.1002/adfm.202005400.

[26] S. Morawiec, M.J. Mendes, S. Mirabella, F. Simone, F. Priolo, I. Crupi, Self-assembled silver nanoparticles for plasmon-enhanced solar cell back reflectors: Correlation between structural and optical properties, Nanotechnology. 24 (2013). https://doi.org/10.1088/0957-4484/24/26/265601.

[27] J. Kim, J.H. Yun, H. Kim, Y. Cho, H.H. Park, M.M.D. Kumar, J. Yi, W.A. Anderson, D.W. Kim, Transparent conductor-embedding nanocones for selective emitters: Optical and electrical improvements of Si solar cells, Sci. Rep. 5 (2015) 1–8. https://doi.org/10.1038/srep09256.

[28] P.S. Chandrasekhar, H. Elbohy, B. Vaggensmith, A. Dubey, K.M. Reza, V.K. Komarala, Q. Qiao, Plasmonic silver nanowires for higher efficiency dye-sensitized solar cells, Mater. Today Energy. 5 (2017) 237–242. https://doi.org/10.1016/j.mtener.2017.07.005.

[29] M. Law, L.E. Greene, J.C. Johnson, R. Saykally, P. Yang, Nanowire dye-sensitized solar cells, Nat. Mater. 4 (2005) 455–459. https://doi.org/10.1038/nmat1387.

[30] J. Zhu, C.M. Hsu, Z. Yu, S. Fan, Y. Cui, Nanodome solar cells with efficient light management and self-cleaning, Nano Lett. 10 (2010) 1979–1984. https://doi.org/10.1021/nl9034237.

[31] M.J. Mendes, S. Morawiec, I. Crupi, F. Simone, F. Priolo, Colloidal self-assembled nanosphere arrays for plasmon-enhanced light trapping in thin film silicon solar cells, Energy Procedia. 44 (2014) 184–191. https://doi.org/10.1016/j.egypro.2013.12.026.

[32] M.J. Mendes, A. Araújo, A. Vicente, H. Águas, I. Ferreira, E. Fortunato, R. Martins, Design of optimized wave-optical spheroidal nanostructures for photonic-enhanced solar cells, Nano Energy. 26 (2016) 286–296. https://doi.org/10.1016/j.nanoen.2016.05.038.

[33] Z. Xu, H. Qiao, H. Huangfu, X. Li, J. Guo, H. Wang, Optical absorption of several nanostructures arrays for silicon solar cells, Opt. Commun. 356 (2015) 526–529. https://doi.org/10.1016/j.optcom.2015.08.069.

[34] H.A. Atwater, A. Polman, Plasmonics for improved photovoltaic devices, Nat. Mater. 9 (2010) 205–213. https://doi.org/10.1038/nmat2629.

[35] V.E. Ferry, M.A. Verschuuren, M.C. Van Lare, R.E.I. Schropp, H.A. Atwater, A. Polman, Optimized spatial correlations for broadband light trapping nanopatterns in high efficiency ultrathin film a-Si:H solar cells, Nano Lett. 11 (2011) 4239–4245. https://doi.org/10.1021/nl202226r.

[36] A. Araújo, M.J. Mendes, T. Mateus, A. Vicente, D. Nunes, T. Calmeiro, E. Fortunato,

H. Águas, R. Martins, Influence of the Substrate on the Morphology of Self-Assembled Silver Nanoparticles by Rapid Thermal Annealing, J. Phys. Chem. C. 120 (2016) 18235–18242. https://doi.org/10.1021/acs.jpcc.6b04283.

[37] W. Zi, X. Ren, F. Xiao, H. Wang, F. Gao, S.F. Liu, Ag nanoparticle enhanced light trapping in hydrogenated amorphous silicon germanium solar cells on flexible stainless steel substrate, Sol. Energy Mater. Sol. Cells. 144 (2016) 63–67. https://doi.org/10.1016/j.solmat.2015.08.024.

[38] H. Tan, R. Santbergen, A.H.M. Smets, M. Zeman, Plasmonic light trapping in thin-film silicon solar cells with improved self-assembled silver nanoparticles, Nano Lett. 12 (2012) 4070–4076. https://doi.org/10.1021/nl301521z.

[39] A. Araújo, M.J. Mendes, T. Mateus, J. Costa, D. Nunes, E. Fortunato, H. Águas, R. Martins, Ultra-fast plasmonic back re fl ectors production for light trapping in thin Si solar cells, Sol. Energy. 174 (2018) 786–792. https://doi.org/10.1016/j.solener.2018.08.068.

[40] S. Morawiec, M.J. Mendes, F. Priolo, I. Crupi, Materials Science in Semiconductor Processing Plasmonic nanostructures for light trapping in thin- fi lm solar cells, Mater. Sci. Semicond. Process. 92 (2019) 10–18. https://doi.org/10.1016/j.mssp.2018.04.035.

[41] G. Mokari, H. Heidarzadeh, Efficiency Enhancement of an Ultra-Thin Silicon Solar Cell Using Plasmonic Coupled Core-Shell Nanoparticles, (2019) 1041–1049.

[42] C. V Thompson, Solid-State Dewetting of Thin Films, (2012). https://doi.org/10.1146/annurev-matsci-070511-155048.

[43] F. Leroy, Ł. Borowik, F. Cheynis, Y. Almadori, S. Curiotto, M. Trautmann, J.C. Barbé, P. Müller, How to control solid state dewetting : A short review, Surf. Sci. Rep. 71 (2016) 391–409. https://doi.org/10.1016/j.surfrep.2016.03.002.

[44] A. Serrano, O. Llorca-Hernando, A. Del Campo, F. Rubio-Marcos, O. Rodríguez de La Fuente, J.F. Fernández, M.A. García, Ag-AgO nanostructures on glass substrates by solid-state dewetting: From extended to localized surface plasmons, J. Appl. Phys. 124 (2018). https://doi.org/10.1063/1.5049651.

[45] J.A. Badán, E. Navarrete-Astorga, R. Henríquez, F. Martín Jiménez, D. Ariosa, J.R.

Ramos-Barrado, E.A. Dalchiele, Silver Nanoparticle Arrays onto Glass Substrates Obtained by Solid-State Thermal Dewetting: A Morphological, Structural and Surface Chemical Study, Nanomaterials. 12 (2022) 1–27. https://doi.org/10.3390/nano12040617.

[46] S. Morawiec, M.J. Mendes, S.A. Filonovich, T. Mateus, S. Mirabella, H. Águas, I. Ferreira, F. Simone, E. Fortunato, R. Martins, F. Priolo, I. Crupi, Broadband photocurrent enhancement in a-Si : H solar cells with Plasmonic back Broadband photocurrent enhancement in a-Si : H solar cells with plasmonic back reflectors, (2014). https://doi.org/10.1039/C3NR06768H.

Chapter 8

Summary, Conclusions and Future Scope

The aim of the work presented in this thesis was synthesis of the silver nanoparticles by solid state dewetting (SSD) in a controlled manner and to characterize these using different methods for their light trapping application in a-Si:H thin film solar cells to enhance its efficiency. During synthesis of silver nanoparticles, we have studied the influence of different deposition parameters on the growth, microstructure of silver nanoparticles and on their plasmonic, dielectric, photoluminescence, and light trapping properties. Hydrogenated amorphous silicon (a-Si:H) thin film solar cells were first simulated and then fabricated on corning glass 1737 substrate prior to implementation of silver nanoparticles. Finally, silver nanoparticles as plasmonic back reflector with excellent light trapping properties were incorporated in a-Si:H thin film solar cell to improve the performance. We have achieved a few new results, which are not reported in literature prior to this work. The summary of the chapters and overall conclusion of the thesis work and future research scopes are given in the following sections.

8.1 Thesis summary

Influence of deposition time on the growth of silver precursor film (as deposited samples) and silver nanoparticles grown by solid state dewetting of these silver precursor films (annealed samples) was studied. Surface morphology and growth dynamics of silver nanoparticles were studied using atomic force microscopy (AFM) with advanced statistical analysis. The thickness of the as-deposited films (Ag precursor silver films) was found to be in the range of 12 to 50 nm for the deposition time of 30-120 seconds, respectively. After annealing, the nanoparticles with nearly circular shape was obtained for lower precursor film thickness deposited for shorter time, while higher thickness resulted in the transformation of nanoparticles into irregular shapes and formation of island of silver agglomerates instead of Ag NPs. Height-height correlation function (HHCF) and power spectral density function (PSDF) were extracted from AFM data. The interface width (w) and lateral correlation length (ξ) were found to scale with the thickness (or deposition time) as $w \sim t^{\beta}$, $\xi \sim t^{1/z}$ respectively. The surface behavior accessed from advanced statistical analysis like HHCF, PSDF, and 2D FFT was changed from self-affine surface for the as-deposited samples (Ag precursor films) to mounded surface for annealed

samples (Ag NPs) due to the formation of the nanoparticles by the solid-state dewetting. No LSPR peak was observed from as deposited sample while post annealing samples (Ag NPs) showed a peak in the wavelength range 400-600 nm corresponding to the LSPR nature due to formation of nanoparticles. A correlation between LSPR peak (λ_{LSPR}) position and peak width (Γ_{LSPR}) of the annealed samples (Ag NPs) with the particle size and growth parameters (ξ and w) was observed.

The effect of RF power variation on the microstructure of silver nanoparticles, and its dielectric and plasmonic properties was also studied. Increase in RF power not only increased the thickness of the film but also the size of the NPs depended on the RF power used for deposition of precursor films. Film deposited at 80 Watt did not transform into Ag NPs. This structural changes induced by the rf power variation showed the great impact on the dielectric properties and optical constants. The peak of the imaginary part of pseudo dielectric function, attributed to the LSPR of Ag NPs, moved to lower energies as the RF power increased, primarily due to thicker precursor films resulting in larger particle sizes. A corresponding shift in the LSPR peak was also noted in the UV-Vis-NIR absorbance spectra. Further, thick films deposited at high RF power exhibited no LSPR peak in SE or UV-Vis absorbance spectra, due to the presence of a continuous silver film even after annealing. This change in microstructure from nanoparticle formation to continuous films was also reflected in the values of void fraction and surface roughness calculated from SE using Bruggeman Effective Medium Approximation (BEMA). The microstructural change induced by rf power variation, affected the intraband, interband transitions, and LSPR properties of Ag NPs. The plasma energy evaluated from the Drude model, corresponding to intraband transition, showed an increase with the increase in the rf power due to the structural transition from the nanoparticles to the bulk film.

Influence of substrate temperature on the silver nanoparticles growth and its plasmonic, photoluminescence properties and Raman spectroscopy was studied. The average size of the nanoparticles was found to vary with the variation in substrate temperature from room temperature (RT) to 400°C though the thickness of precursor film was constant. The LSPR properties of Ag NPs was found to be sensitive to NPs size; a shift in LSPR peak was observed due to change in Ag NPs' microstructure, mainly particle size and interparticle distance. An asymmetric and broad PL peak was observed at 443 nm and the peak intensity increased linearly with the LSPR of Ag NPs. The de-convoluted PL spectra of Ag NPs exhibited two peaks around 436 and 474 nm corresponding to their radiative interband transition and LSPR

band respectively. The influence of LSPR was also observed in the Raman spectroscopy, where intense and distinguishable Raman peaks are observed at 1587 cm^{-1}. The Raman peaks became sharper and more distinguishable with increase in substrate temperature, implying an increase in particle size leads to increase in the contribution from multipole absorption. Enhancement in PL peak intensity and Raman peak intensity was found to be in accordance with the LSPR of Ag NPs. Thus a strong influence of the LSPR on the PL and Raman signal was observed.

Prior to implementation of silver nanoparticles as plasmonic back reflector hydrogenated amorphous silicon (a-Si:H) thin film solar cells with (*n-i-p*) substrate structure were simulated and fabricated. Influence of p- layer doping in simulation and diborane flow rate in experiment on solar cell efficiency was studied. Further, the effect of *i*- layer thickness on solar cell efficiency was studied in both simulation and experiments. The open circuit voltage (V_{oc}) was influenced by the doping of the emitter layer and high doping results in significant improvement in external parameters like V_{oc}, and FF resulting in an overall increase in power conversion efficiency of the solar cells. The short circuit current density (J_{sc}) has increased with the absorber layer thickness and consequently increase the power conversion efficiency. The values of V_{oc}, J_{sc}, FF and η (%) fabricated solar cells were similar to those of simulated solar cells. From the simulation, a power conversion efficiency of 5.79% was obtained with 7.6×10^{19} cm^{-3} p layer doping and absorber layer thickness of 200 nm, while experimentally, 5.50% power conversion efficiency was achieved with 10 sccm diborane (B_2H_6) doping concentration in p-layer for same absorber layer thickness. The J_{sc} and V_{oc} values were same.

After optimization of parameters of Solar cells (*n-i-p*) using simulation and experiment, silver nanoparticles were incorporated as plasmonic back reflector for light trapping a-Si:H thin film solar cells. Plasmonic BR showed the excellent light trapping with the high values of the diffuse reflectance and the haze in the reflection in the entire visible and NIR wavelength range. The solar cell characteristics clearly demonstrated the enhanced performance of the a-Si:H thin-film solar cell with a plasmonic back reflector (BR) compared to a flat BR. The conversion efficiencies (η) of the a-Si:H thin-film solar cell with flat BR and a-Si:H with plasmonic BR was 5.6% and 8.4%, respectively. The values of open-circuit voltage (V_{oc}) were 0.814 V and 0.820 V for the solar cell with flat reflector and plasmonic back reflector respectively. The fill factor (FF) varied slightly, and the short-circuit current density values (J_{sc}) were 9.6 mA/cm^2 and 14.2 mA/cm^2 for the solar cell with flat reflector and plasmonic back reflector respectively.

8.2 Thesis conclusions

- The growth of the Ag NPs by solid state dewetting is greatly influenced by deposition parameters like deposition time (chapter 3), rf power (chapter 4), and substrate temperature (chapter 5).
- Plasmonic properties like LSPR peak position and broadening of Ag NPs (annealed samples) depend upon the size of Ag NPs while Ag precursor films (as deposited samples) did not show the plasmonic nature.
- The dielectric properties and optical constants (*n* and *K*) are affected by the microstructure of Ag NPs.
- Photoluminescence (PL) properties and Raman signal follow one to one relation with the Ag NPs size.
- An enhancement of 47% in the short circuit current density and 50% in power conversion efficiency of a-Si:H thin film solar cells is obtained with the implementation of silver nanoparticle as plasmonic back reflector.

8.3 Scope for future work

Present thesis is mainly focused on the growth of silver nanoparticle for light trapping application in a-Si:H thin film solar cells to improve the performance. Some of the future research scopes based on the present thesis could be followings:

- Since *a-Si:H* thin film solar cells can be fabricated on flexible substrate therefore the growth of silver nanoparticles can also be explored on the flexible substrate to use them as plasmonic back reflector for efficiency improvements.

- Since silver nanoparticles in plasmonic back reflector configuration shows excellent light trapping not only in Visible but also in NIR region therefore they can be used further in microcrystalline (*μc-Si:H)* and nanocrytalline hydrogenated silicon (*nc-Si:H)* thin film solar cells for light trapping application.

- The application of Ag NPs is not limited to the solar cells. Ag NPs grown by solid state dewetting can also be explored as SERS substrate for bio sensing applications.

APPENDIX

1. Height Height Correlation Function

Height-height correlation function (HHCF) can be defined as the statistical average of the mean square of height difference between the two points, separated by distance r, and is written as [1]

$$H(r,t) = \langle |h(r+r',t) - h(r',t)|^2 \rangle \tag{A.1}$$

Where $h(r',t)$ is the surface height at position r' and time t measured by AFM and $h(r+r',t)$ is that at point $(r+r',t)$.

For self-affine surface, HHCF can be expressed by exponential correlation model in the scaling form [1]

$$H(r,t) = 2w^2\left[1 - \exp\left\{-\left(\frac{r}{\xi}\right)^{2\alpha}\right\}\right] \tag{A.2}$$

Where w is the interface width (or RMS roughness), ξ is lateral correlation length and α is roughness exponents.

HHCF behaves differently for the two different regions (for $r \ll \xi$ and $r \gg \xi$) depending on the relative value of r and correlation length ξ. Now $eq.(A.2)$ can be expressed as

$$H(r,t) \sim \begin{cases} 2w^2 & {}^{r}/_{\xi} \gg 1 \\ (mr)^{\,2\alpha_{local}} & {}^{r}/_{\xi} \ll 1 \end{cases} \tag{A.3}$$

Here m is the local slope, which identifies the mode of growth (stationary/non-stationary) and is related to interface width w and lateral correlation length ξ as $m = \left(\sqrt{2}w\right)^{1/\alpha_{local}}/\xi$. Here α_{local} is the local roughness exponent. The roughness exponent is local (α_{local}) for the region $r \ll \xi$ and is global (α) for the region $r \gg \xi$.

2. Power Spectral Density Function

The power spectral density function (PSDF) of a surface profile is Fourier transform of the surface heights. A suitable model for the PSDF of a self-affine surface is given by [1]

$$P(k,t) = \frac{1}{(2\pi)^d}\left|\langle h(r,t)e^{-ikr}\rangle\right|^2 \quad \text{(A.4)}$$

Where $P(k,t)$ is PSDF in reciprocal space and $h(r,t)$ is the surface height at position r and time t measured by AFM, d is the dimension of surface.

3. Drude Model

For the metallic thin films, the dielectric function is dominated by the intraband transitions of free electrons which can be described by the Drude model [2]

$$\varepsilon_{Drude}(E) = \varepsilon_\infty - \frac{{E_p}^2}{E^2 + iE\Gamma_{\text{Drude}}} \quad \text{(A.5)}$$

Where $E_p = \hbar\omega_p$ and Γ_{Drude} are plasma energy and broadening which are related to the scattering. Here ω_p is the plasma frequency which is related to the effective mass of the electron (m^*) and free electron density (N_e) and can be defined as $\omega_p = \sqrt{N_e e^2/\varepsilon_0 m^*}$. The parameter ε_∞ accounts for the net contribution from the positive ion cores and the value of the ε_∞ varies in the range from 1-10.

4. Lorentz Model

Though the Drude model describe the free electron contribution with the plasma frequency and the damping constant. However it neglects the band structure effects which describes the interband transitions of electron is used to account for the interband transitions [2]

$$\varepsilon_{Lorentz}(E) = \frac{f{E_0}^2}{({E_0}^2 - E^2 - iE\Gamma_{\text{Lorentz}})} \quad \text{(A.6)}$$

Where f is the oscillator strength E_0 is the oscillator position and Γ_{Lorentz} is the oscillator width.

5. Gauss Oscillator

LSPR properties of the metal nanoparticles are well described by the Gauss oscillator. The contribution to the dielectric constant due to the Gauss oscillator is defined as [3,4]

$$\varepsilon_{1Gauss}(E) = \frac{2A}{\sqrt{\pi}}\left[D\left(\frac{E+E_0}{\sigma}\right) - D\left(\frac{E-E_0}{\sigma}\right)\right] \quad \text{(A.7)}$$

$$\varepsilon_{2Gauss}(E) = A\left[exp\left\{-\left(\frac{E-E_0}{\sigma}\right)^2\right\} - exp\left\{-\left(\frac{E+E_0}{\sigma}\right)^2\right\}\right] \quad \text{(A.8)}$$

Where A is the amplitude of the oscillator, E_0 is the oscillator peak position and D is the operator (Dawson function) [4]. The broadening (B_r) of the peak is related to Full width at Half maxima (FWHM) $\sigma = B_r/2\sqrt{\ln 2}$.

6. Effective Medium Theory

The silver nanostructure layer is having mixed volume fraction of void and silver therefore to calculate the void fraction and surface roughness, an effective medium approximation (EMA) is used [4]

$$\sum_{i=1}^{n} f_i \frac{\varepsilon_i(E) - \varepsilon(E)}{\varepsilon_i(E) + 2\varepsilon(E)} = 0 \quad \text{(A.9)}$$

Where f_i is the volume fraction and $\varepsilon_i(E)$ is the dielectric function of the i^{th} phase. In our SE modelling, the two phases are Ag NPs and voids respectively.

7. Deconvolution of Raman data using Multiple Peak Fitting

The purpose of deconvolution is to fit to a measured Raman spectrum well-defined peaks to which a physical meaning can be attributed, plus a continuous background. To deconvolute a Raman spectrum with the Origin software, several parameters have to be chosen:

1. The range (i.e. the lower and upper wavenumber limit values) of the spectrum over which the fit will be performed.

2. The kind of baseline to be used in order to isolate the Raman-related peaks.

3. The number of peaks to fit to the Raman spectra.

4. The shape of peaks, i.e. if they have a Gaussian or Lorentzian shape (or a mixture of both).

5. The centre position (i.e. frequency), the width and the height of each peak.

The deconvolution is performed by the Origin software (Origin Pro 8.5) with an algorithm based on the Levenberg-Marquardt (L-M) method, which adjusts the parameters of a set of peaks to fit to a measured spectrum. The parameters adjusted for each input peak are frequency, height, width at half height, and possibly the ratio of Gaussian/Lorentzian line shape.

Gaussian Function

$$y = y_0 + \frac{A\, e^{\frac{-4\ln(2)(x-x_c)^2}{w^2}}}{w\sqrt{\frac{\pi}{4\ln(2)}}} \quad \text{(A.10)}$$

Where y_0 is base, x_c is the center, w is the full width half maxima (FWHM), and A is amplitude.

Lorentzian Function

$$y = y_0 + \frac{2\,A\,w}{\pi\,4\,(x - x_c)^2 + w^2} \quad \text{(A.11)}$$

Where y_0 is offset, x_c is the center, w is the width, and A is area.

References

[1] M. Pelliccione, T.-M. Lu, Evolution of thin film morphology, Springer, 2008.

[2] J. Liu, J. Lin, H. Jiang, H. Gu, X. Chen, C. Zhang, G. Liao, S. Liu, Characterization of dielectric function for metallic thin films based on ellipsometric parameters and reflectivity, Phys. Scr. 94 (2019). https://doi.org/10.1088/1402-4896/ab1606.

[3] M.N.M.N. Perera, D. Schmidt, W.E.K. Gibbs, S. Juodkazis, P.R. Stoddart, Effective optical constants of anisotropic silver nanoparticle films with plasmonic properties, Opt. Lett. 41 (2016) 5495–5498. https://doi.org/10.1364/OL.41.005495.

[4] H. Fujiwara, Spectroscopic Ellipsometry: Principles and Applications, 2007. https://doi.org/10.1002/9780470060193.

LIST OF PUBLICATIONS

1. **Manvendra Singh Gangwar,** and Pratima Agarwal "Simulation and fabrication of a-Si:H thin film solar cells: a comparative study of simulation and experimental results". ***J Mater Sci: Mater Electron*** **35**, 487 (2024). https://doi.org/10.1007/s10854-024-12149-8.
2. **Manvendra Singh Gangwar**, and Pratima Agarwal "Enhancement in the performance of a-Si:H thin-film solar cells by light trapping from plasmonic back reflector". ***Plasmonics*** (2024). https://doi.org/10.1007/s11468-024-02191-x.
3. **Manvendra Singh Gangwar,** and Pratima Agarwal "Influence of microstructure on dielectric function and plasmonic properties of silver nanoparticles grown by solid state dewetting: a spectroscopic ellipsometry study". ***Phys. Scr.*** **98**, 105944 (2023). https://doi.org/10.1088/1402-4896/acf796.
4. **Manvendra Singh Gangwar,** and Pratima Agarwal "Growth dynamics and its correlation with plasmonic properties of silver nanoparticles grown by solid state dewetting". ***Mater. Res. Bull.*** **167**, 112380 (2023). https://doi.org/10.1016/j.materresbull.2023.112380.
5. **Manvendra Singh Gangwar,** and Pratima Agarwal "Plasmon-enhanced photoluminescence and Raman spectroscopy of silver nanoparticles synthesized by physical route". ***J. Phys.: Condens. Matter*** **35,** 325301 (2023). https://dx.doi.org/10.1088/1361-648X/acd1cd.
6. **Manvendra Singh Gangwar,** and Pratima Agarwal "Effect of the annealing temperature on the growth of the silver nanoparticles synthesized by physical route". ***AIP Conf. Proc.*** **2369**, 020100 (2021). https://doi.org/10.1063/5.0061110.
7. **Manvendra Singh Gangwar,** Ankit Kumar Singh and Pratima Agarwal, "Synthesis and characterization of metallic nanoparticles on different substrates for light trapping applications in thin film solar cells". ***AIP Conf. Proc.*** **2220**, 020167 (2020). https://doi.org/10.1063/5.0001410.

List of Publications (*not related to thesis*)

8. Juhi Kumari, Pilik Basumatary, **Manvendra Singh Gangwar,** and Pratima Agarwal "Molybdenum oxide (MoO_{3-x}) as an emitter layer in silicon based heterojunction solar cells" ***Materials Today: Proceedings*** **39** 1996–1999 (2021), https://doi.org/10.1016/j.matpr.2020.08.527

Papers presented in Conferences/Workshops (National & International):

1. **Manvendra Singh Gangwar**, and Pratima Agarwal "Effect of the microstructure on the optical properties of silver nanoparticles investigated by spectroscopic ellipsometry", at the International Symposium on Semiconductor Materials and Devices (ISSMD 2022), 16-18 December, 2022, School of Electronics Engineering, Kalinga Institute of Industrial Technology (KIIT), Bhubaneshwar, Odisha. **(Oral)**
2. **Manvendra Singh Gangwar**, and Pratima Agarwal "Dynamic scaling study of the silver nanoparticles for light trapping application in thin film solar cells", at North-East Research and Conclave (NERC 2022), 20-22 May, 2022, IIT Guwahati, Assam, India. **(Oral)**
3. **Manvendra Singh Gangwar**, and Pratima Agarwal "Growth dynamics of silver nanoparticles for light trapping application in thin-film solar cells", at the International Conference on Current Trends in Advanced Materials and their Applications for Societal Development (ICTAMASD 2022), 8-10 March, Dr. Harisingh Gour Vishwavidyalaya, Sagar, M.P. **(Poster)**
4. **Manvendra Singh Gangwar**, and Pratima Agarwal "Role of silver nanoparticle as plasmonic back reflector to improve the performance of a-Si:H thin film solar cells", at the Research and Industrial Conclave (RIC 2022), 20-23 January, 2022, IIT Guwahati. **(Oral)**
5. **Manvendra Singh Gangwar**, and Pratima Agarwal "Photocurrent enhancement in a-Si:H solar cells with silver nanoparticles as plasmonic back reflector", at the XXI International Workshop on Physics of Semiconductor Devices (IWPSD 2021), 14-17 December, IIT Delhi. **(Poster)**
6. **Manvendra Singh Gangwar**, and Pratima Agarwal "Synthesis, characterization and implementation of silver nanoparticles in a-Si:H thin film solar cells for light trapping application", at the international conference on Recent Advances and Innovations in Solar Energy (RAiSE 2021), 2-4 December 2021, IIT Madras. **(Poster)**
7. **Manvendra Singh Gangwar**, and Pratima Agarwal**,** "Effect of the Annealing Temperature on the Growth of the Silver Nanoparticles Synthesized by Physical Route", 2nd National Conference on physics and chemistry of materials, Govt. Holker Science College, Indore, M.P, December 14-16, 2020**. (Poster)**
8. **Manvendra Singh Gangwar**, Ankit kumar Singh and Pratima Agarwal**,** "Synthesis and characterization of metallic nanoparticles on different substrates for light trapping

applications in thin film solar cells", 3rd International Conference on Condensed Matter & Applied Physics, Govt. Engineering College, Bikaner, Rajasthan, October 14-15, 2019. **(Poster)**

9. **Manvendra Singh Gangwar**, and Pratima Agarwal, "Synthesis of metallic nanoparticles on different substrates to study their effects in thin film solar cells for light trapping applications", Resrarch Conclave IIT Guwahati, 14-17 March 2019. **(Poster)**
10. **Manvendra Singh Gangwar**, and Pratima Agarwal**,** "Growth study of metallic nanoparticles on different substrates for light trapping in thin film solar cells", 2nd National Conference on Hard and Soft Condensed Matter Physics, Tezpur University, Assam, 4-6 March, 2019. **(Poster)**

Conferences & Workshops attended (National & International):

1. International conference on light matter interaction (ICLMIN-2021), 19-21 May, 2021, Indira Gandhi Centre for Atomic Research, Kalpakkam, Tamilnadu, India.
2. 2-Day INUP Familiarization Workshop on "Nanofabrication Technologies", 28-29 January, 2019, NIT Silcher, Assam.
3. International conference on Renewable and Alternate Energy (ICRA-2018), 4-6 December, 2018, Assam Science and Technology University, Guwahati, Assam, India.
4. Short term workshop on "Silicon PV System: Fundamentals, Design and Metrology", 10 -14 September, 2018, CSIR-National Physical Laboratory Delhi, Delhi.
5. 4th National Workshop on "NEMS/MEMS & Theranostic Devices", 26-28 February, 2018, IIT Guwahati, Guwahati, Assam.
6. One-Day Workshop on **"**Vacuum technology and its application in optical science", 19th August, 2017, IIT Guwahati, Guwahati, Assam.

Awards/Honors:

1. **Best Poster Award** (2nd position) in the International Conference on Current Trends in Advanced Materials and their Applications for Societal Development (ICTAMASD 2022), 8-10 March, Dr. Harisingh Gour Vishwavidyalaya, Sagar, M.P.
2. **Best Oral Award** (2nd position) in the Research and Industrial Conclave (RIC 2022), 20-23 January, 2022, IIT Guwahati.
3. **Best Poster Award** (1st position) in the international conference on Recent Advances and Innovations in Solar Energy (RAiSE 2021), 2-4 December 2021, IIT Madras.